Transport of suspended particles in turbulent open channel flows

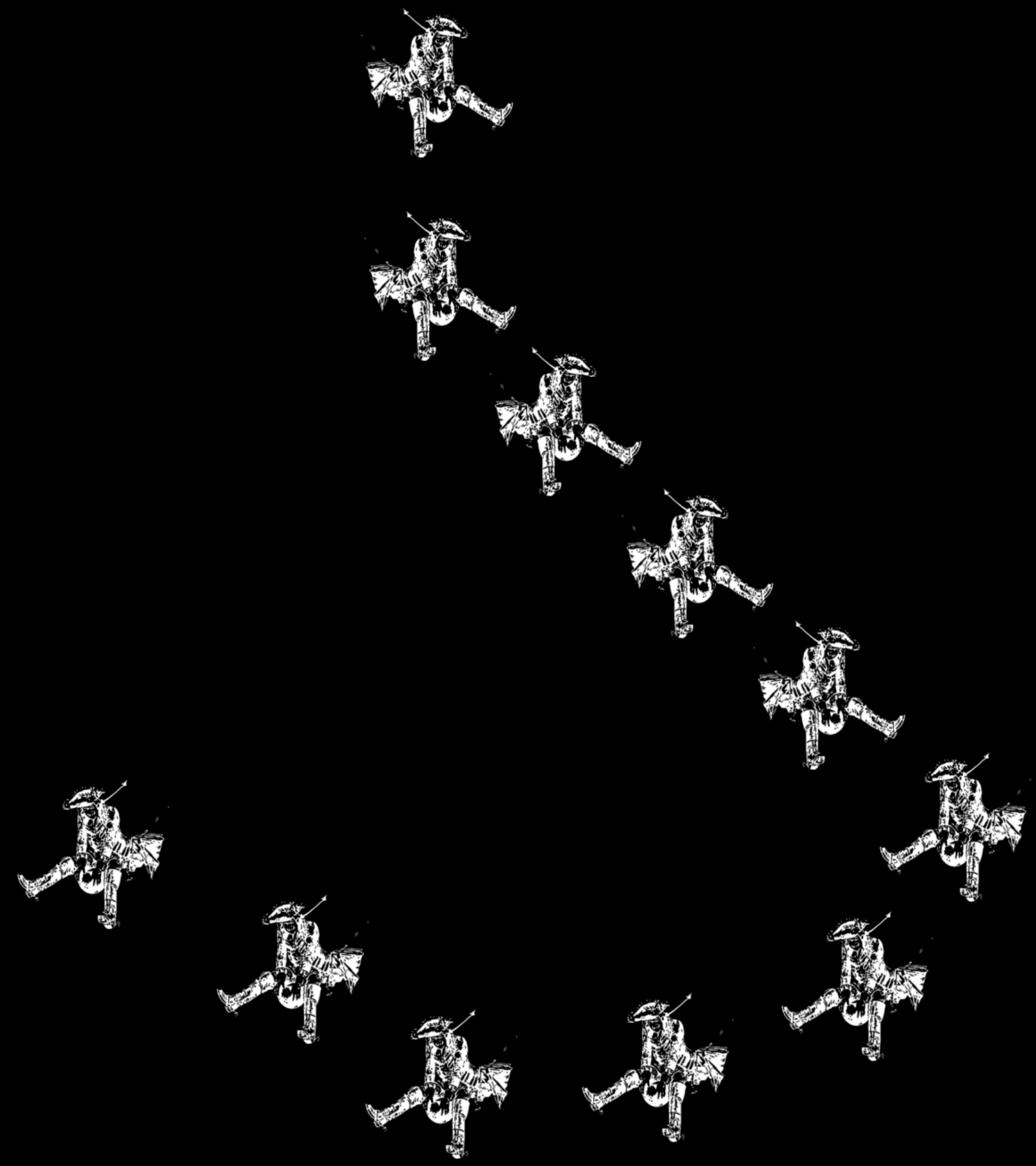

Alexander Breugem

Transport of suspended particles in turbulent open channel flows

Alexander Breugem

Uitnodiging

U bent van harte welkom op de openbare verdediging van mijn proefschrift:

Transport of suspended particles in turbulent open channel flows

op woensdag 11 januari
om 15.00 uur in de Senaatszaal
van de Aula van de TU Delft,
Mekelweg 5 in Delft.

Om 14.30 uur geef ik een korte toelichting op mijn promotiewerk.

Aansluitend aan de promotie is er een receptie.

Tevens bent u van harte welkom om mijn promotie te komen vieren
vanaf 21.00 uur in
Café de Wijnhaven
Wijnhaven 22, in Delft.

Met vriendelijke groet,

Alexander Breugem
alexanderbreugem@yahoo.co.uk
+32 4 88 159 456

Transport of suspended particles in turbulent open channel flows

Transport van gesuspendeerde deeltjes in turbulente open kanaalstromingen

Transport of suspended particles in turbulent open channel flow

Proefschrift

ter verkrijging van de graad van doctor
aan de Technische Universiteit Delft,
op gezag van de Rector Magnificus prof.ir. K.C.A.M. Luyben,
voorzitter van het College voor Promoties,
in het openbaar te verdedigen op woensdag 11 januari 2012 om 15.00 uur

door

Willem Alexander BREUGEM
civiel ingenieur
geboren te Schiedam

Dit manuscript is goedgekeurd door de promotoren:
Prof.dr.ir. W.S.J. Uijttewaal
Prof.dr.ir. G.S. Stelling

Samenstelling promotiecommissie:

Rector Magnificus	voorzitter
prof.dr.ir. W.S.J. Uijttewaal	Technische Universiteit Delft, promotor
prof.dr.ir. G.S. Stelling	Technische Universiteit Delft, promotor
prof. V.I. Nikora	University of Aberdeen
dr.ir. R. Uittenbogaard	Deltares
prof.dr.ir. J.C. Winterwerp	Technische Universiteit Delft
prof.dr. R.F. Mudde	Technische Universiteit Delft
dr.ir. J.S. Ribberink	Universiteit Twente

This research has been supported by STW, Deltares and KIWA Water Research

Printed by Gildeprint drukkerijen, the Netherlands

ISBN 978-94-6108-255-8

“It is the theory which decides what we can observe”

Albert Einstein

Abstract

"Transport of suspended particles in turbulent open channel flows"

In many civil engineering problems, the turbulent transport of sediment particles is important. The physical processes are still rather poorly understand, particularly in non-equilibrium situations and for higher sediment concentrations, where particle-fluid and particle-particle interactions become important.

Therefore, the objectives of this study are directed to a better understanding of the physical processes of sediment transport, in particular to the instantaneous flow structures that govern sediment transport. It is not only aimed to study equilibrium sediment transport processes, but also non-equilibrium processes. Furthermore, it is the objective to validate the use of a particle laden direct numerical simulation (DNS) for suspended sediment transport. Eventually the results of this study should contribute to the further development of experimental methods for investigating two-way coupling in suspended sediment transport processes and to the development of two-fluid numerical models.

In order to fulfill these objectives, an experimental study was performed in a turbulent open channel flow using particles image velocimetry (PIV) to measure the fluid velocity field, while the particle locations and velocities were measured simultaneously using particle tracking velocimetry (PTV). The particles were fed to the flow near the free surface at different distances from the measurement section. In this way, the development of the sediment concentration and the sediment particle velocities toward an equilibrium situation could be studied.

It was found that that in equilibrium conditions, the particles are transported up in ejections (second quadrant structures Q2; $u' < 0$,$v' > 0$), while they moved down equally often in inward interaction (third quadrant Q3; $u' < 0$,$v' < 0$) and sweeps (fourth quadrant Q4; $u' > 0$,$v' < 0$) structures. Because of this, the particles are mainly found in velocity structures with a velocity lower than average, which leads to particles velocities that are lower than the mean fluid velocity. The occurrence of particles in these flow structures was related to the occurrence of hairpin vortices in the turbulence. In particular, the particles are found upstream and beneath the head of the hairpin vortices. It was found that the individual coherent structures are all more efficient in transporting sediment vertically than they are in transporting horizontal momentum. However, Q2 structures are more efficient in transporting sediment than the other ones. Because of the predominant influence of Q2 structures for vertical transport in an equilibrium situation, the eddy diffusivity of the sediment is higher than the eddy viscosity. In the non-equilibrium case of this study where particles are introduced near the free-surface, the opposite happens. The particles were mostly close to the free surface and moved downwards faster than their still water settling velocity, because they were mainly found in downward flow structures, especially Q4 structures. Therefore, the particles have a velocity that is faster than the average fluid velocity in this situation. The Q4 structures that transport particles down can be related to the upstream side and the outside of the hairpin vortices.

In this situations, the predominant vertical transport by Q4 events, which are less efficient in transporting sediment downward than Q2 events are in transporting sediment upward, makes that the eddy diffusivity is now smaller than the eddy viscosity.

It was further found that higher order corrections to the gradient diffusion law, which take into account the non-linearity of the sediment concentration profile over size of the order of the size of the turbulent eddies, did hardly change the predicted sediment fluxes. The fact that particles encountered turbulent velocity fluctuations that are slightly larger than average in equilibrium conditions and slightly smaller in non-equilibrium conditions has only a minor influence on the observed values of the ratio between the eddy diffusivity and the eddy viscosity.

If was found that the results of a direct numerical simulation (DNS), in which the movement of individual point-particles was calculated from the particle equation of motion, compared well with the results of the experiment, provided that a sufficiently strong resuspension mechanism was used at the bed. The details of this resuspension mechanism hardly influenced the results of the simulations. This agreed with the experimental finding that similar results were obtained for two different regimes (with bed load and without bed load), when the experimental results were properly scaled.

An experiment was performed using refractive index matching in order to study two-way coupling effects in suspended sediment transport. In this experiment, silica gel particles in a sodium iodide solution provided a high optical transparency, and allowed PIV measurements of the fluid velocities for bulk volume concentrations up to 0.42 %. It was found that for the present flow conditions (relatively large particle size compared to the Kolmogorov length scale, low density ratio of 1.14, low settling velocity compared to the shear velocity), two-way coupling effects were hardly detected in the mean flow and turbulence. However, a slight decrease (up to 10 %) of the measured eddy viscosity was found, which can be attributed to density stratification effects by the suspended sediment. Two-point correlation functions were used to show that the length scales of the turbulent flow structures were unaffected by the presence of the suspended sediment.

Alexander Breugem
December 2011

Samenvatting

“Transport van gesuspendeerde deeltjes in turbulente open kanaalstromingen”

In veel civieltechnische problemen is het transport van gesuspendeerde deeltjes belangrijk. De fysische processen die een rol spelen in het transport van deze deeltjes worden echter nog slecht begrepen. Dit is het vooral het geval voor situaties die niet in evenwicht zijn en voor hogere sediment concentraties, wanneer terugkoppelingseffecten van de deeltjes op de stroming en interacties tussen verschillende deeltjes belangrijk worden.

Daarom is het doel van deze thesis het verkrijgen van meer inzicht in supensietransportprocessen, vooral met betrekking tot de instantane structuren die het transport bepalen. Hierbij wordt het transportproces bestudeerd in evenwichtssituaties en in situaties die niet in evenwicht zijn. Daarnaast is het een doel van deze thesis het gebruik van een directe numerieke simulatie (DNS) met deeltjesbeweging te valideren voor toepassing in sedimenttransportproblemen. De resultaten van deze studie zullen op termijn leiden tot betere experimentele methodes om de interacties tussen sediment en turbulentie te bestuderen en tot een betere modellering van sedimenttransport met behulp van tweefase modellen.

Om deze doelstellingen te behalen, is een experiment uitgevoerd in een turbulente open kanaal stroming met behulp van“particle image velocimetry” (PIV) om het stromingsveld te meten, terwijl gelijktijdig de beweging van de individuele sedimentdeeltjes werd gemeten met behulp van “particle tracking velocimetry” (PTV). De deeltjes werden bij het vrij oppervlak op verschillende afstanden van de meetsectie aan de stroming toegevoegd. Op deze manier kan de ontwikkeling naar een evenwicht bepaald worden voor de sedimentconcentratieprofielen en de deeltjessnelheid.

Er werd gevonden dat de deeltjes in evenwichtscondities omhoog worden getransporteerd door “ejections” (Q2; tweede kwadrant gebeurtenissen, $u' < 0$, $v' > 0$), terwijl de deeltjes door zowel “inward interactions” (Q3, derde kwadrant gebeurtenissen, $u' < 0$, $v' < 0$) als “sweeps” (Q4, vierde kwadrant gebeurtenissen, $u' > 0$, $v' < 0$) omlaag worden getransporteerd. Hierdoor worden de deeltjes vooral aangetroffen in turbulente structuren met een lager dan gemiddelde snelheid, wat leidt tot een deeltjessnelheid die lager ligt dan de gemiddelde vloeistofsnelheid. Het belang van specifiek deze structuren voor deeltjestransport werd verklaard met het optreden van haarpinwervels in de turbulentie. Meer in het bijzonder werden de deeltjes onder en bovenstrooms van de kop van deze wervels aangetroffen.

De individuele structuren bleken allemaal veel efficiënter te zijn in het transporteren van deeltjes dan in het transporteren van horizontale impuls. De Q2 structuren bleken echter beduidend efficiënter in het transporteren van deeltjes dan de overige structuren. De dominante invloed van de Q2 structuren voor verticaal sedimenttransport in evenwichtssituaties leidt tot een turbulente diffusiviteit die groter is dan de turbulente viscositeit.

In de situatie waarin er geen evenwicht was en waarin het meeste sediment zich bij het vrij oppervlak bevond, vond verticaal transport vooral plaats door Q4 structuren. Hierdoor daalden de deeltjes met een snelheid groter dan de valsnelheid in stilstaand water. De concentratie van deeltjes in Q4 structuren leidde tot een deeltjessnelheid, die hoger was dan de gemiddelde vloeisstofsnelheid. Deze Q4 structuren kunnen gerelateerd worden aan de bovenstroomse en de bovenkant van de haarpinwervels. Omdat de Q4 structuren minder efficiënt zijn in het transporteren van sediment dan de Q2 structuren, is in deze situatie de turbulente viscositeit hoger dan de turbulente diffusiviteit.

Hogere-orde correcties op de gradiënt-diffusiewet, waarin rekening gehouden werd met de niet-lineariteit van het concentratieprofiel over afstanden vergelijkbaar met de grootte van de turbulente structuren, bleek de voorspelde sedimentfluxen nauwelijks te beïnvloeden. Verder bleek het feit, dat de deeltjes in evenwichtssituaties door iets sterkere turbulente fluctuaties getransporteerd worden dan buiten evenwicht, slechts een kleine invloed te hebben op de geobserveerde verhouding tussen de turbulente viscositeit en diffusiviteit.

De resultaten van een DNS, waarin voor ieder afzonderlijk deeltje een bewegingsvergelijking werd opgelost, bleken goed overeen te komen met de experimentele resultaten, zolang een voldoende sterk suspensiemechanisme werd gebruikt bij de bodem. De details van dit mechanisme bleken niet van invloed op de gevonden resultaten. Dit komt overeen met het feit, dat gelijkaardige resultaten werden gevonden in experimenten met en zonder bodemtransport, mits deze resultaten correct werden geschaald.

Er werd een experiment uitgevoerd met behulp van "refractive index matching" om de invloed van de terugkoppeling van de deeltjeskrachten op de turbulentie te bepalen. In dit experiment werden silicageldeeltjes in een natriumiodideoplossing gebruikt. Deze materialen zorgden voor een hoge optische transparantie, zodat PIV metingen mogelijk waren tot een bulk concentratie van 0.42 %. Er werd gevonden dat in de gebruikt condities (grote deeltjes in vergelijking met de Kolmogorov lengteschaal, lage relatieve dichtheid van 1.14, lage valsnelheid in vergelijking met de schuifspanningssnelheid) er nauwelijks terugkoppelingseffecten van de deeltjes werden geobserveerd in de gemeten stromings- en turbulentieprofielen. Er werd echter een kleine afname (maximaal 10 %) van de turbulente viscositeit gemeten, die door dichtheidsstratificatieëffecten wordt veroorzaakt. Tweepuntscorrelatiefuncties laten zien dat de turbulente lengteschalen ook niet veranderen door de aanwezigheid van het sediment.

Alexander Breugem
December 2011

Resumen

"Transporte de partículas suspendidas en un canal abierto con turbulencia"

En la ingeniería civil existen muchos problemas importantes en relación al transporte turbulento de partículas pequeñas. Actualmente no se entiende bien los procesos físicos, especialmente en situaciones fuera de equilibrio y para las concentraciones altas de sedimento, donde las interacciones partícula-fluido y partícula-partícula son importantes.

Por eso, uno de los objetivos de esta tesis es obtener más conocimiento de los procesos físicos del transporte de sedimentos, especialmente con respeto a las estructuras instantáneas del flujo que causan el transporte vertical de sedimento. No solamente se estudia el transporte en condiciones de equilibrio, si no también fuera de equilibrio. También se tiene como objetivo validar el uso de una simulación numérica directa (DNS) para el transporte de sedimentos en suspensión. Los resultados del estudio darán finalmente mejores métodos experimentales para el estudio del transporte de sedimento en altas concentraciones y modelos bi-fluidales para la predicción del transporte de sedimentos.

Para obtener esos objetivos, se hizo una prueba en un canal abierto con turbulencia usando un velocímetro de imagen de partículas ("particle image velocimetry", PIV) para medir el campo de velocidad del fluido y se utilizó al mismo tiempo un velocímetro de detección de partículas ("particle tracking velocimetry", PTV) para medir el lugar y el movimiento de partículas de sedimento individuales. Las partículas eran inyectadas cerca de la superficie libre a una distancia variada del área de medida. En ese forma, se pudo estudiar el desarrollo de las concentraciones y velocidades del sedimento hasta una situación de equilibrio.

Se encontró que en equilibrio las partículas son elevadas por "expulsiones" (estructuras del segundo cuadrante; Q2 ,$u' < 0$ y $v' > 0$), miéntras que son bajadas por "interacciones internas" (estructures del tercer cuadrante; Q3 ,$u' < 0$ y $v' < 0$) y "barridas" (estructures del cuarto cuadrante; Q4 ,$u' > 0$ y $v' < 0$). Eso causa que las partículas se encuentren en estructuras con una velocidad más baja del promedio. De ese manera, las partículas tienen una velocidad más baja que la velocidad promedio de la corriente. La acumulación de las partículas en dichas estructuras se puede explicar por la presencia de vórtices en forma de horquilla en la turbulencia. Más especificamente, se encuentran las partículas abajo y en contra de la corriente de dichas estructuras.

Se descubrió que todas las estructuras son más eficientes en transportar partículas que en transportar impulso. De todas maneras, parece que las estructuras Q2 son más eficientes transportando sedimento que las otras estructuras. Por la gran influencia de las estructuras Q2 en equilibrio, la difusividad turbulenta es mayor que la viscosidad turbulenta.

Fuera de equilibrio, cuando las partículas todavía se encuentren cerca de la superficie libre, pasa lo contrario. Las partículas bajan más rápido que su velocidad terminal, porque se encuentran básicamente en las estructuras Q4. Por eso tienen una velocidad que es más alto que la velocidad promedio del agua. Esas estructuras Q4 se pueden relacionar con lugares en el parte superior y aguas abajo de las vórtices en forma de horquilla. La gran influencia de las estructuras Q4, que son menos eficientes en transportar las partículas que las estructuras Q2, causa que la difusividad turbulenta sea más baja que la viscosidad turbulenta.

Se investigaron también unas correcciones sobre la ley de difusión de gradiente, que toman en cuenta, que el perfil de la concentración de sedimento es non-lineal sobre la escala de tamaño de las estructuras turbulentas. Pareció que el transporte de partículas casi no depende de esas correcciones. Además, el hecho que las fluctuaciones en la velocidad vertical de los granos sea más grande que la fluctuación de la velocidad del flujo tiene solo una pequeña influencia en la diferencia entre la viscosidad turbulenta y la difusividad turbulenta.

Se encontró que los resultados de una simulación numérica directa (DNS), en la cual se calculó el movimiento de las partículas individuales a través de la ecuación del movimiento de las partículas, coinciden bien con las pruebas, cuando el mecanismo de resuspención está usado cerca del fondo y es suficientamente fuerte. Los resultados del cálculo casi no dependen de los detalles de dicho mecanismo. Eso se corrobora con el hecho que los resultados experimentales eran iguales en dos régimens diferentes (sin transporte en el fondo y con transporte en el fondo), cuando los resultados experimentales estaban a una escala apropiada.

Se hizo una prueba para determinar la influencia de las partículas sobre la turbulencia en concentraciones altas usando correspondencia del índice refractivo ("Refractive index matching"). En dicha prueba, partículas de gel de sílice en una solución de yoduro sódico formaba una mezcla con una alta transparencia. Esa mezcla permitió mediciones del flujo usando PIV hasta una concentración de sedimentos de 0.42 %. En las condiciones presentes (baja densidad especifica de 1.14), las partículas tenían una influencia muy pequeña sobre los perfiles de velocidad y de la turbulencia. Se encontró que la viscosidad turbulenta se disminuyó (hasta 10 %), lo cual se atribuye a la estratificación de la densidad. Por último, se usaron correlaciones entre dos puntos para mostrar que las escalas de longitud en la turbulencia tampoco cambian con la adición de sedimentos.

Alexander Breugem
Diciembre 2011

Contents

Chapter 1

Introduction

1.1. Transport of natural sediment

In many problems in hydraulic engineering, the transport of particles needs to be considered. In the natural environment, sand and silt on the bottom of rivers, estuaries or a coastal sea are transported by waves and currents. In rivers, the transport of sediment may lead to the formation of large dunes during a river flood, thus enhancing the high water levels and causing safety problems in the surrounding areas. Scour can occur around obstacles such as bridge pillars and groynes, and in severe cases this scour might lead to failure of the structure. Sediment can also be transported into harbors or deposit in water ways (such as in the inner side of a river bend), leading to safety hazard for ship traffic and high dredging costs. Furthermore, the presence of suspended sediment due to dredging works can influence the turbidity of the water (fig. 1.1), which can have strong ecological consequences. Therefore, regulations exist in many countries on the changes in turbidity due to man made structures.

Equally important is the transport of particles in man-made water systems. Particles can be found in drinking water systems, where they can cause severe water quality problems and in

Figure 1.1: The influence of dredging works on the turbidity; source: http://watercenter.unl.edu

sewer systems, where deposition of particles is highly undesirable. During dredging, sediment particles are transported in high concentrations and stored in a hopper where the sediment deposits. Efficient prediction and control of these processes might limit the costs of dredging operations.

Depending on particle behavior, transport is traditionally subdivided in categories like bed load transport, suspended sediment transport and wash load (e.g. Jansen *et al.*, 1994). Bed load occurs for particles that are mostly in direct contact with the bed, either sliding or rolling over other particles, or saltating, which means hopping in mall steps along the bottom. Different criteria were proposed for the thickness of this layer, for example Einstein's one, which states that for situations without bed forms, the bed load is limited to a layer with a thickness of two particle diameters from the bottom (see Jansen *et al.*, 1994, page 113).

Suspended sediment transport includes those particles that are suspended in the flow and that are not in contact with the bottom for a significant amount of time. An arbitrary, but frequently used criterion (e.g. Niño *et al.*, 2003) is that suspended sediment transport consists of those particles that do not touch the bottom for a streamwise distance of least one hundred particle diameters. Wash load is a subclass of suspended sediment transport, reserved for those sediment particles that never interact with the bed, and therefore are not important for morphological changes.

The distinction between bed load and suspended load is important. When sediment is mostly transported in suspension, the sediment transport does not need to be in equilibrium with the local flow conditions (e.g. Galappatti & Vreugdenhil, 1986), whereas bed load is assumed to adapt instantaneously to the flow conditions. Here, equilibrium transport is defined as the transport that would occur in a uniform flow in an infinitely long flume. In such a situation, erosion and deposition are in equilibrium. In situations, where the adaptation length or time scales of the sediment concentration are small compared to the length and time scales of the mean flow, non-equilibrium transport occurs. It is important in some of the above mentioned applications, such as the flow near groyne fields or downstream variations in river bed material composition. In this thesis, we will focus on suspended sediment transport and we will not consider bed load.

From the above, it is clear that turbulent sediment laden flows occur in many situations of great practical importance. Therefore, it is important to have a good insight in the behavior of these flows and not only in equilibrium situations in a uniform flow, where most research so far has focused on, but also in non-equilibrium situations. With this insight, it is possible to develop models that provide results applicable to a wider range of conditions than the empirical relations commonly used in engineering practice such as those from Engelund-Hansen (see for example Raudkivi, 1976).

To obtain more insight, it is necessary to consider more details of the turbulent transport process such as the interaction of individual sediment particles with turbulent flow structures. This can be done by performing detailed experiments or detailed numerical simulations. The latter can be achieved by using a direct numerical simulation (DNS) to calculate the flow and turbulence in combination with particle tracking to calculate the movement of a large number of individual particles. These particle laden DNS simulations have been very successful for simulating particle laden gas flows (Uijttewaal & Oliemans, 1996; Portela *et al.*, 2002), but they have never been validated for sediment transport. It is therefore highly desirable that the latter approach is validated for use in suspended sediment transport problems.

In most of the above mentioned flows, the sediment concentration tends to be quite high, such that two-way coupling (the influencing of the flow and turbulence by the presence of sediment particles) and four-way coupling (the influence on the motion of a particle by other particles) can become important. However, most detailed sediment transport investigations at present have focused on low sediment transport concentrations and covered a limited parameter space, because of experimental difficulties. It is therefore necessary to improve current experimental methods to make high concentration sediment transport experiments feasible and to use these experiments to obtain insight into high concentration flows.

1.2. Aims and limitations

The issues addressed in the preceding section lead to the four main goals of this thesis:

1. To identify the instantaneous flow structures that govern the vertical transport of sediment, which (in an averaged sense) are commonly interpreted as diffusion. Insight in the dynamics of these structures may be used to develop better Reynolds averaged sediment transport models.
2. To provide insight into suspended sediment transport for non-equilibrium conditions. This provides additional insight on the length and time scales for a sediment concentration profile to develop toward an equilibrium, which is of vital importance in some practical models, such as depth-averaged sediment transport models (Galappatti & Vreugdenhil, 1986).
3. To validate a particle laden DNS without any kind of scaling by means of an experiment.
4. To further develop the experimental methods needed to provide insight in high concentration flows, and use these to obtain more insight into two-way coupling.

We will limit ourselves to a steady, uniform, low Reynolds-number open channel flow with a smooth bottom, knowing that this situation does not fully represent a natural river. This appears to be the most feasible situation for the numerical simulations as well as the experiment. Hence, we will not consider more complex flows such as bends, mixing layers, gradually varying flows, secondary currents or density stratification, nor do we consider the influence of short waves, all of which are important in many real life situations.

Here, the focus will be on the suspended sediment transport in a regime, where bed forms do not occur. The bottom layer, where bed load transport occurs, is considered as a source of sediment for the outer layer, without studying in detail what is going on there. For the sediment, we will use monodispersed, spherical particles, instead of graded sediment, which is found in many applications.

1.3. Outline of this thesis

This thesis starts with an overview of the relevant physical processes in chapter 2, describing first the structure of the turbulence in an open channel flow and the individual coherent structures (the hairpin vortex packets), followed by a Lagrangian description of the forces that act on an individual particle. An Eulerian continuum description of sediment transport is presented in section 2.3. This chapter is concluded with an overview of two-way and four-way coupling, which are processes that start to become important, when the sediment concentration increases.

In chapter 3, the experimental setup, flow conditions and the used sediment particles are described for a low concentration sediment transport experiment. This is followed by a description of the data processing technique that allows for the discrimination between tracer particles that track the fluid motion and sediment particles. It was used to measure the velocities of both phases separately with respectively particle image velocimetry (PIV) and particle tracking velocimetry (PTV). This is followed by a description of a second experiment performed on a smaller scale that was specially designed to perform a high concentration experiment using refractive index matching in order to make the sediment particles invisible and hence ensure the optically accessibility during high concentration conditions. We conclude with a description of the statistical techniques used to process the measured fluid and particles velocities, which include the identification of vortical motions by swirling strength and the determination of conditionally averaged properties using linear stochastic estimation (LSE).

In chapter 4, we present the results of an experiment for a fully developed situation, where the sediment transport is in equilibrium with the hydrodynamic conditions. Here, we study fluid and particle velocity profiles as well as turbulence profiles, and concentration profiles. Special attention is paid to the momentum and mass balances, which provide insight in the vertical motion of the sediment. This chapter is ended with a preliminary comparison between experiments and DNS in an equilibrium situation (objective 3 in section 1.2). This is followed in chapter 5 by an analysis of experiments where the sediment had not yet reached equilibrium conditions (objective 2 in section 1.2). A more detailed view of the flow structures that are responsible for transporting the particles by using quadrant analysis and spatial conditional averages is described in chapter 6, (objective 1 in section 1.2). In chapter 7, the use of refractive index matching to measure the change of the fluid flow (two-way coupling) at high particle concentrations is described (objective 4 in section 1.2).

Conclusions will be drawn in chapter 8 and in this chapter, recommendations will be given for future research as well as for the application of the results of this work in current engineering practice.

Chapter 2

Overview of the physical processes in turbulence-particle interaction

In this chapter, the theoretical background of sediment transport is presented. The main objective is to show that a combination of a two-fluid model and the gradient diffusion closure results in the same equations as the traditional advection-diffusion equations for suspended sediment transport, but with some extra correction terms for processes that are normally neglected. Although the derivation to obtain this results is lengthier and more difficult than the traditional one (based on a analogy between turbulent and molecular diffusion), it is felt that the present approach provides additional value for four reasons. First, because it is is based on fundamental principles (the use of continuity and momentum balances in combination with formal averaging). Second, because it provides more detailed information about the physical processes that are going on (especially on the importance of the fluid velocity at the particle locations). Third, because it shows extra physical effects that do not occur in the traditional derivation (such as the difference in the average particle and fluid velocity), and finally because it shows which effects are being neglected in the common derivation (e.g. extra transport if the mixing length over which the particles are transported is not small compared to the length scale over which the sediment concentration changes). From this derivation, some physical processes that are known to be very important in gas-particle flows (such as turbophoresis) are shown to be negligible for suspended sediment transport.

In this chapter, the structure of open channel flow is reviewed in section 2.1, with special attention to the characteristics flow structures in open channel flows, the hairpin vortices. This is followed by a description of the forces on a single particle and the interaction between a single particle and turbulent flow structures in section 2.2. In section 2.3, continuum modeling of sediment transport based on a two-fluid approach is presented. Finally, the influence of high sediment concentrations is discussed in section 2.4.

2.1. Open channel flow turbulence

2.1.1. Introduction

In virtually every situation where sediment transport occurs, the flow is turbulent. Therefore, it is important to understand the characteristics of turbulence. In the present section, the characteristics of turbulence in open channel flows without sediment are reviewed. This review will focus on the flow in a stationary, uniform two-dimensional open-channel without secondary currents, where the mean flow and turbulence characteristics are relatively well understood.

There are some characteristics of turbulence, which are important for all turbulent transport processes. First of all, turbulent flows are irregular and show a wide range of fluctuations, which means that statistical tools are needed in order to describe the turbulence. Second, turbulence has the tendency to mix substances efficiently. In general "turbulent diffusion" is much more efficient than molecular diffusion. The efficiency of the turbulent mixing depends on the intensity of the turbulent fluctuations and on the length and time scales on which these fluctuations occur. Turbulent diffusion was placed between quotation marks here, because it is not a real diffusion processes, but rather advection by turbulent motions. These turbulent flow structures have an intermittent character and consist of structures covering a range of length and time scales. These structures can remain coherent for substantial times, and can show quite similar shapes in many different situations, and therefore knowledge about these flow structures might help to improve our understanding of turbulent transport and its modeling.

Fluid motion (both turbulent and laminar) is described with the continuity equation for an incompressible fluid and a momentum balance (the Navier-Stokes equations):

$$\frac{\partial u_{f,i}}{\partial x_i} = 0 \tag{2.1}$$

$$\frac{\partial u_{f,i}}{\partial t} + u_{f,j}\frac{\partial u_{f,i}}{\partial x_j} = -\frac{\partial}{\partial x_i}\frac{p_f}{\rho_f} + \nu_f\frac{\partial^2 u_{f,i}}{\partial x_j^2} \tag{2.2}$$

Here, $u_{f,i}$ is the instantaneous fluid velocity in the i direction, ρ_f and ν_f the density and kinematic viscosity of the fluid and p_f the fluid pressure. In these and all further equations, the Einstein summation convention is used. In principle, the Navier-Stokes equations can be solved numerically, if sufficient initial and boundary conditions are prescribed. The solution than includes the mean flow and the turbulence implicitly. However, this can only be done for low Reynolds numbers, because the range of scales present in the flow increases rapidly with Reynolds number, and hence the necessary computational resources to resolve all these scales hamper the use of DNS. Therefore, for many practical applications "Reynolds averaging" is applied to the Navier-Stokes equations. To do so, the instantaneous fluid velocity is decomposed in an ensemble averaged and a fluctuating part: $u_{f,i} = \langle u_{f,i}\rangle + u'_{f,i}$ and the decomposed term is substituted in eq. 2.2, which are then also averaged. The result is the Reynolds Averaged Navier-Stokes and continuity equations:

$$\frac{\partial \langle u_{f,i} \rangle}{\partial x_i} = 0 \tag{2.3}$$

$$\frac{\partial \langle u_{f,i} \rangle}{\partial t} + \langle u_{f,j} \rangle \frac{\partial \langle u_{f,i} \rangle}{\partial x_j} = -\frac{\partial}{\partial x_i} \frac{\langle p_f \rangle}{\rho_f} - \frac{\partial \langle u'_{f,i} u'_{f,j} \rangle}{\partial x_j} + \nu_f \frac{\partial^2 \langle u_{f,i} \rangle}{\partial x_j^2} \tag{2.4}$$

These equations have the same form as the Navier-Stokes equations, but now using averaged velocities rather than instantaneous ones, and with one extra term containing $\langle u'_{f,i} u'_{f,j} \rangle$: the Reynolds stresses. These stresses represent the influence of the turbulence on the mean flow. The presence of the Reynolds stresses in these equation means that extra unknows were introduced and hence the Reynolds Averaged Navier-Stokes equations cannot be solved without a closure relation for the Reynolds stresses. One of the key subjects in turbulence research is to develop closure relations that express the Reynolds stresses as function of mean flow quantities.

2.1.2. Mean flow and Reynolds stress characteristics

In the present section, we will consider stationary, uniform flow in a straight open channel. In order to do so, we will use a laboratory coordinate system (fig. 2.1) with x the streamwise, y the wall normal and z the spanwise direction. The components of the velocity vector in these directions are denoted respectively with u, v and w. In such a uniform open channel flow, all $\frac{\partial}{\partial t}$, $\frac{\partial}{\partial x}$ and $\frac{\partial}{\partial z}$ terms in the Reynolds averaged Navier-Stokes equations (eq. 2.4) are equal to zero with the exception of the streamwise pressure gradient generated, which is the force driving the flow and which comes from the free surface slope. In this situation, the streamwise momentum balance (eq. 2.4) reduces to:

$$\frac{d\langle u'_f v'_f \rangle}{dy} + \nu_f \frac{d^2 \langle u_f \rangle}{dy^2} = \frac{1}{\rho_f} \frac{dp}{dx} \tag{2.5}$$

The viscous stress term (second on the left hand side) is only important very close to the wall. This implies that the Reynolds shear stress is a linear function of the wall normal distance in the outer layer (defined as the layer above $y/h = 0.2$). It is zero at the free surface and equal to $u_*^2 = \tau_b/\rho_f$ (τ_b is the shear stress at the bottom), when it is extrapolated to the wall.

In this situation, the mean streamwise flow velocity over a smooth bottom is described by the law of the wall:

$$u^+ = \frac{1}{\kappa} \ \ln(y^+) + A \tag{2.6}$$

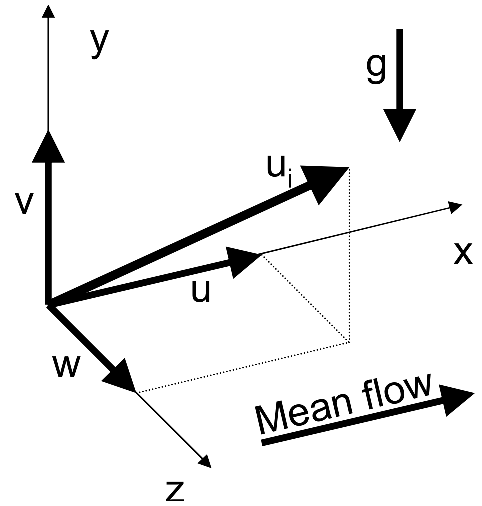

Figure 2.1: The laboratory coordinate system used in this thesis.

, with $\kappa = 0.41$ and $A = 5.29$, as found by Nezu & Rodi (1986). Here, rescaling in wall units is done $u^+ = \langle u_f \rangle / u_*$ and $y^+ = y u_* / \nu_f$. Strictly speaking, this law is only valid in the inner layer, which extends from $y^+ = 30$ to $y/h = 0.2$. Above this region, the velocity is found to be somewhat higher than predicted by the law of the wall (called the law of the wake), except for very low Reynolds numbers ($Re_* = u_* h/\nu_f \lessapprox 500$; Nezu & Rodi 1986). The Reynolds shear stress can be related to the velocity gradient through the "so-called" eddy viscosity ϵ_{xy} using equation 2.5 and 2.6 (e.g. Nezu & Nakagawa, 1993):

$$\epsilon_{xy} = \frac{\langle u'_f v'_f \rangle}{d\langle u_f \rangle / dy} = \kappa u_* h \, \frac{y}{h} \, (1 - \frac{y}{h}) \tag{2.7}$$

Obviously, the parabolic eddy viscosity profile is only strictly valid in the inner layer, although at very low Reynolds numbers, it can be used for a larger part of the water column (Nezu & Rodi, 1986). The eddy viscosity is often modeled using the mean velocity gradient and a length scale, the mixing length l_m:

$$\epsilon_{xy} = l_m^2 \frac{d^2 \langle u \rangle}{dy^2} \tag{2.8}$$

Using eq. 2.6 and 2.7, the following distribution, which is called the Bakhmetev distribution, can be derived for the mixing length:

$$\frac{l_m}{h} = \kappa \frac{y}{h} \left(1 - \frac{y}{h}\right)^{1/2} \tag{2.9}$$

The mixing length is a typical length scale over which momentum is transported vertically. Physically, the apparent vertical diffusion of streamwise momentum (here modeled using an eddy viscosity) is the average result of vertical advection of streamwise momentum by many individual flow structures. In the next section, these individual flow structures will be reviewed.

2.1.3. Coherent structures

In recent years, much research on turbulent flows has been performed using improvements in measurement techniques and computational power. With these improved resources, it has now become possible to obtain quantitative data on the shape of the flow structures in turbulent boundary layers. In this way, more insight in the structure of turbulent flows can be obtained, which in turn can be used to improve the computational modeling. The main result of this research is that a turbulent boundary layer is built up from packets of hairpin shaped vortices. These vortices and their alignment in packets are described in this section.

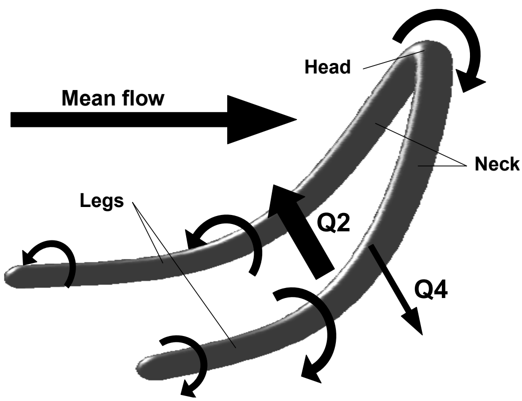

Figure 2.2: Schematic image of a hairpin vortex

It is known for many years that the dominant vortical structure in a boundary layer has a hairpin-like shape (e.g. Head & Bandyopadhyay, 1981). Note that these vortices are identified with various names representing similar shapes, such as hairpins, canes, omegas, lambdas and horseshoes, but in this thesis, they will all be referred to as hairpin vortices. A hairpin vortex consists of two streamwise vortices of opposite sign parallel to the wall forming the legs of the vortex, an inclined region, called the neck and at the top a spanwise vortex rotating in the same direction as the mean shear (fig. 2.2). According to Hagen & Kurosaka (1993) the flow inside the neck of the hairpin vortex is directed away from the wall. Considering the turbulent fluctuations in the vertical plane, the flow induced by the hairpin vortex shows a strong ejection (Q2) between the legs and neck, and a weaker sweep (Q4) beside the hairpin vortex. Here, the quadrants (Willmarth & Lu, 1972) are defined as follows (fig. 2.3): Q1 (outward interaction: $u' > 0$ and $v' > 0$), Q2 (ejection: $u' < 0$ and $v' > 0$, Q3 (inward interaction: $u' < 0$ and

$v' < 0$), and Q4 (sweep: $u' > 0$ and $v' < 0$). Robinson (1991) found that the symmetrical hairpin shape was actually quite scarce in instantaneous events, but rather that most vortices were asymmetric, only consisting of one half of the idealized hairpin. The advection velocity of the vortex head is on average equal to the local fluid velocity (Wu & Christensen, 2006) with deviations proportional to the turbulence intensity.

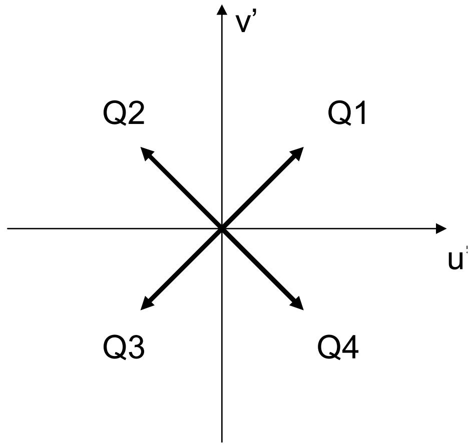

Figure 2.3: Definition of the different quadrants

Zhou *et al.* (1999) simulated the formation of a hairpin vortex related to a high Re-stress event using DNS ($Re_* = 150$). They found that a high Reynolds stress event can develop into a hairpin vortex. In this process, a hairpin vortex is elongated by the mean shear and straightens because of self-induction (see appendix A) and therefore it develops into an omega-like shape. The induced fluid motion between the vortex's legs forms an ejection (Q2 event), which in its turn causes the hairpin head to move upwards. They found that because of self-induction, kinks develop in the legs of the vortex, which are bent inward. At this location, a particularly strong ejection exists between the legs. When this ejection meets the high-velocity fluid above it, a shear layer develops, which rolls up into a secondary vortex downstream of the primary vortex, with its head closer to the wall. The same process is repeated for the legs of the secondary vortex, thus forming a tertiary vortex and so on leading to the alignment of several hairpin vortices in groups (fig. 2.4).

The alignment of several hairpin vortices in groups was found experimentally by Adrian *et al.* (2000) in their PIV measurements of a turbulent boundary layer. They called this phenomenon a “hairpin vortex packet” (fig. 2.4). Because the upstream vortices are formed by the legs of the older vortices, the oldest hairpin of a group is highest in the water column. The different hairpin vortices together cause a low momentum region beneath their heads and between their legs, which shows as a triangular shape with a characteristic angle of 12°, with a layer of high shear formed by a row of hairpin vortex heads on top. These triangular regions are also found in high Re-number turbulence (Hommema & Adrian, 2003), indicating that groups of hairpin vortex packets may be an important characteristic of any turbulent boundary layer. Statistical evidence for the hairpin vortex packet model has appeared in literature in the form of correlation functions (Liu *et al.*, 2001; Ganapathisubramani *et al.*, 2005) and conditionally averaged velocity fields (Christensen & Adrian, 2001).

Adrian *et al.* (2000) inferred that a turbulent boundary layer consists of multiple hairpin vortex packets passing over each other. Young packets, will generally be found near the bottom and therefore, they will move relatively slow, whereas older packets are found at higher elevations and will move faster. It was suggested (Hutchins *et al.*, 2005) that these older packets are detached from the wall, and that their vertical dimension scales with the boundary layer depth. This agrees with the findings of del Álamo *et al.* (2006), who found that many vortices exist which do not extend with their legs to the wall region.

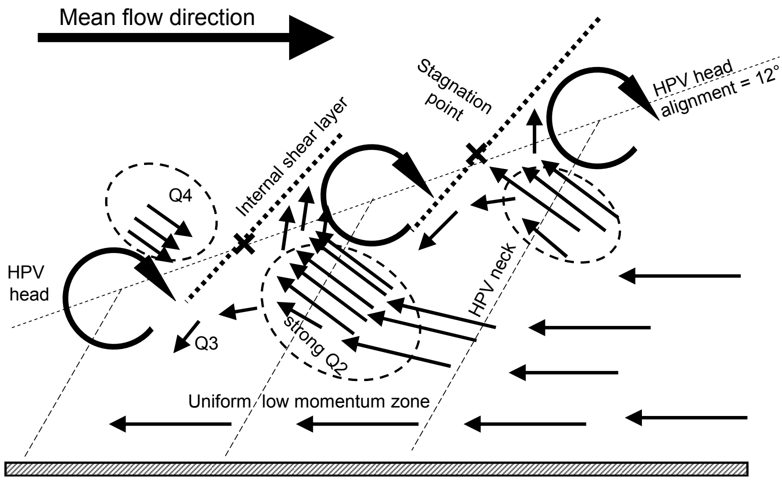

Figure 2.4: Schematic representation of a hairpin vortex packet consisting of three hairpin vortices and the induced flow field by these hairpin vortices (side view, in a frame with the same velocity as the hairpin vortex packet)

Little work has been done in obtaining averaged velocity and turbulence profiles using knowledge on these coherent structures. Based on the attached eddy hypothesis, scaling laws for the normal and shear Reynolds stresses have been obtained (e.g. Nickels *et al.*, 2007). These show that the $\langle u'^2 \rangle(y)$ and $\langle w'^2 \rangle(y)$ are generated by all eddies with a height greater than y, whereas $\langle v'^2 \rangle(y)$ and $\langle u'v' \rangle(y)$ depend only on those eddies that have their center at a height of approximately y, i.e. these stresses depend on the local coherent structures. Note that the term eddy is used here and further on to refer to the hairpin vortex and the flow field it induces. The occurrence of hairpin vortices also explains the experimentally observed occurrence of a negative skewness in the streamwise velocity fluctuations and a positive skewness of the wall normal ones (e.g. Wei & Willmarth, 1991). The reason is that the combination of the induced flow by both legs and the head of the vortex causes Q2 events, which are stronger than other events. Thus extreme values will be stronger in the low velocity structures than in the high velocity structures (thus giving a negative skewness for the streamwise velocity fluctuations), and they will also be stronger in the upward velocity fluctuations than in the downward velocity fluctuations (thus giving a positive skewness for the wall normal velocity fluctuations).

The previous results have been obtained in relatively simple flows over a smooth bottom. However, similar coherent structures have also been found in more complex flows, such as a flow over rough walls (Tomkins, 2001; Hofland, 2005), over wavy walls (Nakagawa & Hanratty, 2001) and behind a backward facing step (Lesieur *et al.*, 2003). Therefore, it can be expected that insight obtained from detailed turbulence measurements in relatively simple flows might have a broader range of application.

2.1.4. Eulerian and Lagrangian length and time scales

A consequence of the coherence of the turbulent flow structures discussed in the preceding section is that they exhibit certain length and time scales. These scales are important for the motion of sediment particles, because they occur in the equations that are used to determine the turbulent diffusion coefficients for sediment (section 2.3.3). The length and time scales can be determined either in a fixed frame of reference (Eulerian) or a moving one (Lagrangian).

Usually, the Eulerian integral length L_E and time scales T_E are used to characterize the large scale motions. These are defined as:

$$L_E = \int_0^\infty R[u'_i(x)u'_j(x_k + r_k)]dr_k \tag{2.10}$$

$$T_E = \int_0^\infty R[u'_i(t)u'_j(t + \tau)]d\tau \tag{2.11}$$

Here R is either the spatial or the temporal correlation function. The Eulerian integral length scale can be interpreted physically as a characteristic size of an eddy, and the integral time scale is the time such an eddy needs to be advected by the mean flow along a fixed point. These time and length scales can be related using Taylor's hypothesis, which states that turbulence is advected along a fixed point by the mean flow without deforming. With the requirement $u' \ll \langle u \rangle$, this gives $T_E \approx L_E/\langle u \rangle$. Measurements (Kim & Adrian, 1999; Liu *et al.*, 2001) suggest that the streamwise integral length scale for the streamwise velocity fluctuations can exceed many boundary layer depths. On the other hand, the wall normal scale of the streamwise fluctuations ($\int R[u'(y_0)u'(y)]dy$) as well as both the streamwise and the wall normal scale of the wall normal fluctuations scale with the water depth, but do not exceed it. This can be related to the hairpin vortex packets from the previous section. Apparently, the long streamwise length scales are related with long zones of uniform streamwise momentum (Adrian *et al.*, 2000) due to the induction of many aligned hairpin vortices in a packet. The wall normal velocity on the other hand, changes its direction with every new vortex, and thus its streamwise integral length scale ($\int_0^\infty R[v'(x)v'(x+r_x)]dr_x$) is related with the distance between the hairpin vortices. The wall normal length scales (($\int_0^h R[u'(y_0)u'(y)]dy$ and $\int_0^h R[v'(y_0)v'(y)]dy$) depend on the wall normal dimensions of the packets, which according to Adrian *et al.* (2000) are located one above the other.

The Lagrangian integral time scale is defined as:

$$T_L = \int_0^\infty R[u_i'(x_k(t))u_j'(x_k(t+\tau)]d\tau \tag{2.12}$$

This is the time scale found in a reference frame moving with a fluid particle. Many investigations in homogeneous isotropic turbulence use the term "Eulerian time scale" as the time scale in a frame moving with the average advection velocity, even though this is a Lagrangian quantity. Here, we will refer to this time scale as the moving Eulerian time scale $T_{M,E}$, which can be found from the maxima of two-point space-time correlations $R[u_i'(x_k, t)u_j'(x_k + r_k, t + \tau)]$. Kraichnan (1964) uses the following thought experiment to argue that the Lagrangian integral time scale should always be smaller than the moving Eulerian one. Imagine a flow field that is advected passively (without changing). In such a flow field, the latter time scale is infinite, whereas the former is not, because the particles still follow a trajectory through this flow field, where they encounter different eddies thus leading to a changed correlation along their path. DNS simulations (Squires & Eaton, 1991) and measurements (Sato & Yamamoto, 1987) indeed showed the ratio between the Lagrangian and moving Eulerian timescale to be $T_L/T_{M,E} \approx 0.3 - 0.8$ in isotropic turbulence, where this ratio decreases with increasing Reynolds numbers. Wang & Maxey (1993) called $T_L/T_{M,E}$ the "structure parameter", and they suggest that it is one of the key parameters in modeling turbulent diffusion. Physically, the moving Eulerian time scale (also called the eddy decay time) indicates the time an eddy needs to decay. The Lagrangian time scale (also called eddy turnover time) is the time a fluid particle needs to be advected through an eddy.

Reliable expressions for the Lagrangian integral time scale as function of Eulerian quantities are rare. Based on the idea that it is the time a particle needs to transverse an eddy, it should be of the order L/u' (Philip, 1967; Hinze, 1975). Here, L is a characteristic size of an eddy, which can be estimated with an integral length scale, and u' is the rms of the velocity fluctuations as a characteristic fluid velocity inside an eddy. For the wall normal dispersion in an open channel flow, it seems plausible to use the scales based on the wall normal velocity fluctuations for estimation of T_L, thus $L_y = \int R_{vv}dy$ and $\langle v'^2\rangle^{1/2}$.

Oesterlé & Zaichik (2004) suggested to obtain T_L from equating the eddy viscosity (eq. 2.7) to Taylor's (1921) diffusion coefficient (eq. 2.47) in a shear flow, i.e. they assumed that the wall normal turbulent diffusion of streamwise momentum is equal to the wall normal diffusion of a scalar. From this they found:

$$T_L = -\frac{\langle u'v'\rangle}{\langle v'^2\rangle d\langle u\rangle/dy} \tag{2.13}$$

They further found that the time scale calculated with this equation compare very well with data from fluid particle tracking in a DNS. Using the definition of the mixing length (eq. 2.8) we find that this equation can be written in the L/u' form of the phenomenological result of Philip (1967) and Hinze (1975):

$$T_L = \frac{(-\langle u'v'\rangle)^{1/2}}{v'_{rms}}\left(\frac{l_m}{v'_{rms}}\right) = \left(-R[u'(x)v'(x)]\frac{u'_{rms}}{v'_{rms}}\right)^{1/2}\left(\frac{l_m}{v'_{rms}}\right) \tag{2.14}$$

Equation 2.13 will be used in the following, when an estimation of the Lagrangian time scale is needed.

2.1.5. Conclusion

In the preceding, the background of turbulence in an open channel flow was discussed. It was clarified that turbulence consists of structures that show coherence in space and time. In open channel flow, the characteristic model of these structures is a hairpin vortex, which normally aligns in groups in the streamwise direction. Such a group is called a hairpin vortex packet. The occurrence of these hairpin vortex packets, together with the fluid motions these vortices induce, explains many of the phenomenological knowledge of the burst cycle in wall bounded flows, such as the occurrence of sweeps and ejections.

The characteristics of the mean flow and turbulence profiles are an average of an ensemble of these hairpin vortices. Further, the combined influence of these vortices lead to characteristic length and time scales in the turbulence. The turbulent transport of sediment is determined by a combination of the turbulence intensity and the length and time scales of the turbulence. A consequence of the occurrence of these flow structures is that turbulence is intermittent, which means that the structures have length and time scales that vary over a large range. Therefore, turbulent diffusion differs from molecular diffusion, which occurs on such small length scales that it can be considered a continuous process on our scales of interest.

2.2. Physics of particle motion

In this section, the forces acting on an individual suspended sediment particle are addressed. The Lagrangian approach has some consequences for the interpretation of the relative motion between particles and fluid and the interaction between particles and coherent flow structures. Interpolating and averaging the forces on the particles at fixed points leads to an Eulerian continuum description, which will be discussed in the next section.

In this thesis, we are mainly interested in particles found in suspended sediment transport in rivers. These typically consist of fine sand ($60\ \mu m < d_p < 200\ \mu m$) and medium sand ($200\ \mu m < d_p < 600\ \mu m$) with a density $\rho_p = 2650\ kg/m^3$. Smaller particles (silt) are not considered, because they are mainly transported as wash load and thus not important for river morphology and because they can become cohesive. Larger sand particles are generally to heavy to be suspended, and are thus mostly transported as bed load. In this work, particles are assumed to be spherical for simplicity.

		River	Experiment using natural sand	Experiment using light particles
$\langle u_f \rangle$	$[m/s]$	1.0	1.0	0.2
h	$[m]$	5.0	0.1	0.05
u_*	$[cm/s]$	5.0	5.0	1.0
Re	[-]	5,000,000	100,000	10,000
Re_*	[-]	250,000	5,000	500
λ_{kolm}	$[mm]$	0.21	0.08	0.22
τ_{kolm}	$[ms]$	45	6	50
$T_L \approx h/u_*$	$[s]$	100	2	5
d_p	$[mm]$	0.2	0.2	0.35
ρ_p	$[kg/m^3]$	2650	2650	1035
v_T	$[mm/s]$	25	25	2
τ_p	$[ms]$	4.9	4.9	8.9
$u_*/\lvert v_T \rvert$	[-]	2.0	2.0	5.0
τ_p/τ_{kolm}	[-]	0.11	0.77	0.18
τ_p/T_L	[-]	$4.9\ 10^{-5}$	$2.4\ 10^{-3}$	$1.8\ 10^{-5}$
d_p/λ_{kolm}	[-]	0.9	2.5	1.6
ρ_p/ρ_f	[-]	2.65	2.65	1.035
Re_p	[-]	5.0	5.0	0.7

Table 2.1: Parameters for typical river and for typical laboratory experiments

For future reference, typical values for various parameters of the flow and sediment in a river are given in table 2.1. In this table, also the typical parameters for a flume experiment using real sand (such as Coleman, 1981) are given for comparison, as well as typical parameters for an experiment in which a smaller particle density is used in order to reduce the flow velocities (as performed in the present thesis). This table shows that sediment particles have a density of the same order of magnitude as the fluid and a diameter comparable to the Kolmogorov length scale. Fall velocities (v_T) are typically significantly smaller than the friction velocity u_*.

2.2.1. Particle equation of motion

The fluid force on a particle can be considered as composed of two different components: one due to fluid stresses that are present in the undisturbed flow, the other due to the fluid stresses from a disturbance flow generated by the no-slip boundary at the particle surface. These fluid stresses can be divided in normal and shear stress working on the particle surface. The disturbance flow field can be calculated analytically using a complete viscous approximation by neglecting the advection terms in the Navier-Stokes equations, which is valid for $Re_p \ll 1$, where $Re_p = |u_{rel}|d_p/\nu_f$ and u_{rel} the relative velocity of the particle ($\vec{u}_p - \vec{u}_f$). The resulting disturbance flow is shown in fig. 2.5. It can clearly be seen that the disturbance flow field of the particle is quite large (up to $5d_p$), and that the flow field is symmetrical in the completely viscous approximation.

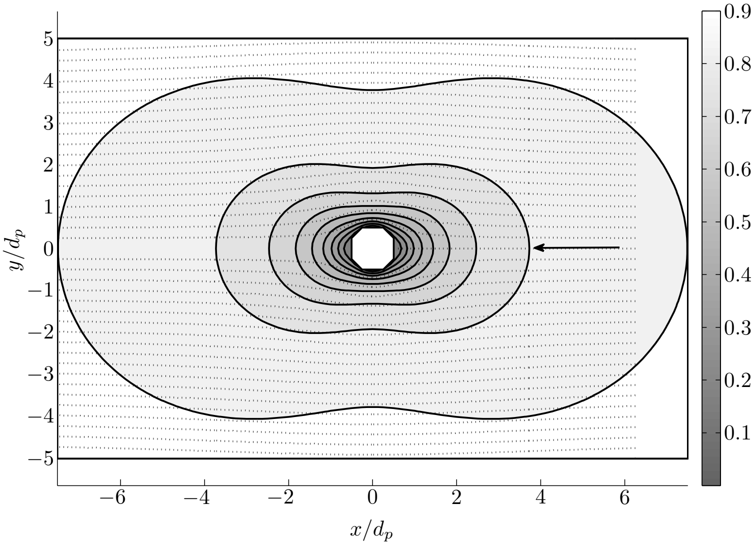

Figure 2.5: Disturbance flow (seen in a frame moving with the particle) around a spherical particle moving to the right in an otherwise undisturbed flow. This disturbance flow is calculated using a completely viscous approximation ($Re_p = 0$). Contours with a spacing of 0.1 u_f/u_p give the magnitude of the disturbance flow, streamlines give its direction.

Maxey & Riley (1983) derived the equation of motion for a solid sphere by integrating the stresses due to the undisturbed and the disturbed velocity field, the latter calculated with a completely viscous approximation. They assumed $Re_p \ll 1$ and $d_p/L \ll 1$ (with L a characteristic length scale of the undisturbed flow). Particle rotation, particle-particle and particle-boundary interactions were neglected. This result in the following equation:

$$m_p \frac{du_{p,i}}{dt} = \underbrace{\frac{1}{2} m_f \left[\frac{d}{dt} \left(u_{p,i} - \frac{1}{40} d_p^2 \nabla_j^2 u_{f,i} \right) - \frac{Du_{f,i}}{Dt} \right]}_{\text{Added mass}} + \underbrace{m_f \frac{Du_{f,i}}{Dt}}_{\text{Pressure gradient}}$$
$$\underbrace{-3\pi d_p \mu_f \left(u_{p,i} - u_{f,i} - \frac{1}{24} d_p^2 \nabla_j^2 u_{f,i} \right)}_{\text{Stokes drag}} + \underbrace{(m_p - m_f) g_i}_{\text{Buoyancy and gravity}} \quad (2.15)$$
$$\underbrace{-\frac{3}{2} \frac{\pi d_p^2 \mu_f}{\sqrt{\pi \nu_f}} \int_0^t d\tau \frac{\frac{d}{d\tau} \left(u_{p,i}(\tau) - u_{f,i}(\tau) - \frac{1}{24} d_p^2 \nabla_j^2 u_{f,i}(\tau) \right)}{\sqrt{t-\tau}}}_{\text{Basset history force}}$$

In this equation m_p is the mass of the particle, calculated with $m_p = 1/6\pi d_s^3 \rho_p$, m_f, the mass of a fluid particle with the same size as the particle, u_p the particle velocity and and u_f the fluid velocity at the particle location x_p. The acceleration due to gravity is denoted as g_i and the dynamic viscosity of the fluid as μ_f. Accelerations in a frame moving with the particle and with the fluid are notated respectively with $\frac{du}{dt}$ and $\frac{Du}{Dt}$. The Basset history force is usually neglected, even for density ratios of the order one, where the instantaneous value of this force can be significant in comparison with the other forces (Armenio & Fiorotto, 2001). Nevertheless, this seems a good approximation, because the net dispersion of particles due to this force is on average negligible (Mei *et al.*, 1991; Michaelides, 1997; Armenio & Fiorotto, 2001). The $\nabla_j^2 u_{f,i}$ terms are called the Faxén force. Basically, they are a correction to account for any non-uniformity in the undisturbed flow field averaged over the surface of the sphere. This leads to an increase in the drag, added mass and Basset forces in a turbulent flow. They are usually negligible for small particles (compared to the Kolmogorov length scale), and it is assumed that this applies to sediment particles as well.

The assumption that $Re_p \ll 1$ does not hold for sediment transport (table 2.1). In case $Re_p = O(1)$, the disturbance flow around a particle field can be calculated analytically using a linearized advection term, which is called Oseen's correction (Batchelor, 1967). The disturbance flow field calculated using this method is shown in fig. 2.6. In this case, a steady wake develops at the downstream side of the particle, whereas in the viscous case, the disturbance flow field is symmetrical (fig. 2.5). A modified equation of motion can be obtained by integrating the fluid stresses on the particle due to this modified disturbance flow field. However, in practice an empirical correction (e.g. Michaelides, 2003) is used to account for the drag force for $Re_p < 85$. This expression has the form $F_{drag} = (1 + f(Re_p))F_{Stokes}$, where F_{Stokes} is the term marked 'Stokes drag' in eq. 2.15 and:

$$f(Re_p) = 0.15 Re_p^{0.687} \quad (2.16)$$

Neglecting the Faxén and Basset history force and including the non-linear drag from equation 2.16, we can write equation 2.15 as:

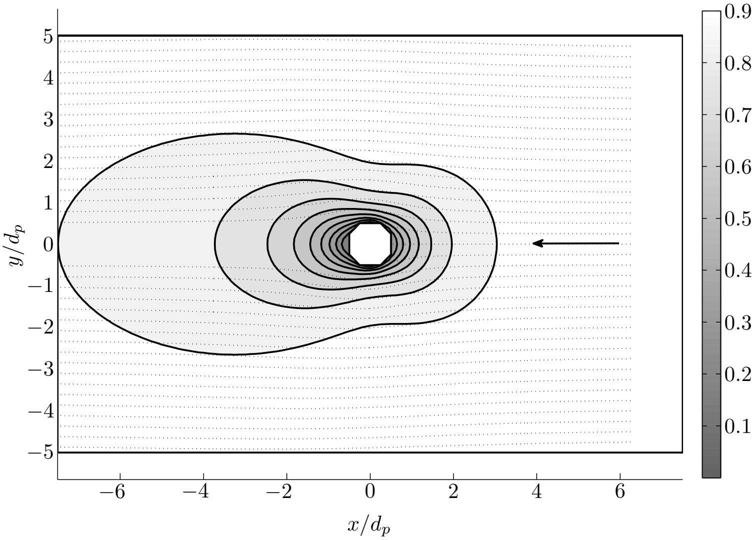

Figure 2.6: Disturbance flow (seen in a frame moving with the particle) around a spherical particle moving to the right in an otherwise undisturbed flow. This disturbance flow is calculated using Oseen's correction ($Re_p = 0.7$). Contours with a spacing of 0.1 u_f/u_p give the magnitude of the disturbance flow, streamlines give its direction.

$$\frac{du_{p,i}}{dt} = \frac{1}{\tau_p}(u_{p,i} - u_{f,i} - u_{T,i}) + \beta\frac{Du_{f,i}}{Dt} \tag{2.17}$$

With:

$$\beta = \frac{3\rho_f}{2\rho_p + \rho_f} \tag{2.18}$$

Furthermore, the terminal velocity $u_{T,i} = [0, v_T, 0]$ is defined as (note that a downward velocity is positive):

$$v_T = \frac{(\rho_p - \rho_f)gd_p^2}{18\rho_f\nu_f(1 + f(Re_p))} \tag{2.19}$$

The particle time scale τ_p is given by:

$$\tau_p = \frac{d_p^2}{18\nu_f(1 + f(Re_p))}\frac{\rho_p + \rho_f/2}{\rho_f} = \frac{v_T}{g}\left(\frac{\rho_p + \rho_f/2}{\rho_p - \rho_f}\right) \tag{2.20}$$

In these equations, the added mass force is still retained (leading effectively to an increased particle time scale), even though Armenio & Fiorotto (2001) found in their DNS results that it is negligible for sediment particles.

According to equation 2.17, a particle in a steady flow will tend to attain the velocity of the fluid, apart from a settling component due to gravity. It adapts with a characteristic time scale

τ_p. In accordance with eq. 2.17, we can define a non-dimensional parameter, called the Stokes number $St = \tau_p/\tau_f$ based on the particle time scale and a characteristic time scale of the fluid τ_f. If St_{kolm} (using the Kolmogorov time scale as fluid time scale) is smaller than one, then the particle follows all turbulent fluctuations. For a particle to be able to follow the energetic large scale fluid motion, its Stokes number based on the Lagrangian integral time scale should be smaller than one. In table 2.1, it can be seen that both these conditions are fulfilled for sediment particles in a river as well as in a laboratory experiment. Hence, sediment particles will follow the flow and turbulent fluctuations well, with the exception of a net relative velocity due to gravity.

Equation 2.15 does not include lift forces. The disturbance flow field around a particle in a shear flow can become asymmetric when inertia is taken into account. In that situation, there can be a net force on the particle acting perpendicular to the flow direction, called lift. The expression by Saffman (1965) is an asymptotic expansion for a particle in a simple linear shear flow with shear rate $\partial u_f/\partial y$ far from the wall and is only valid for $Re_p \ll \sqrt{Re_G} \ll 1$ where the shear Reynolds number is defined as $Re_G = d_p^2|\partial u_f/\partial y|/\nu_f$. It reads:

$$F_{ls,y} = 1.61\rho_f d_p^2 \left(u_p - u_f\right) \sqrt{\left|\frac{\partial u_f}{\partial y}\right| \nu_f} \,\mathrm{sign}\left(\frac{\partial u_f}{\partial y}\right) \tag{2.21}$$

McLaughlin (1993) derived a correction to the Saffman lift force for arbitrary values of Re_p and Re_G of the form $F_{l,y} = J(Re_p, Re_G)F_{ls,y}$. A comparison of this approximation with the results of a three-dimensional numerical simulation by Kurose & Komori (1998) clearly demonstrates the validity of this approach.

Far away from the wall, the vertical lift force is not important for sediment transport, because the average velocity gradient is small. Furthermore, the lift force can be expected to be zero on average. The reason is that the relative velocity of the particle in the streamwise direction is on average zero.

Very close to the wall, eq. 2.21 is also not valid anymore. Corrections to eq. 2.21 for a particle close to the wall have been derived by McLaughlin (1993) and Cherukat & McLaughlin (1994). These expressions show that the lift force on a particle near the wall may decrease or increase compared to eq. 2.21, depending on the precise values of Re_p and Re_G. For a stationary particle at the wall, Leighton & Acrivos (1985) derived the following equation for the lift force:

$$F_{l,y} = 0.576\rho_f d_p^4 \left(\frac{\partial u_f}{\partial y}\right)^2 \tag{2.22}$$

Using this equation, it can be shown that the lift force on a particle in the viscous sublayer has a similar order of magnitude as the downward force due to gravity minus buoyancy, and hence that lift forces might be expected to play a significant role in the entrainment of small particles from the viscous sublayer.

2.2.2. Particle transfer functions

Because equation 2.15 is linear[1] if the fluid velocity at the particle locations is prescribed, we can use superposition in order to get the transfer function for the particle velocity fluctuation spectrum $\eta(\omega)$:

$$\eta(\omega) = \frac{E_p(\omega)}{E_f(\omega)} \tag{2.23}$$

Here, $E_p(\omega)$ is particle velocity fluctuation spectrum, $E_f(\omega)$ the fluid velocity spectrum on the particle's location and ω the frequency. The results of this transfer function (fig. 2.7) shows clearly the behavior of the different forces (Coimbra & Rangel, 2001). In the low frequency region (significantly lower than τ_p^{-1}), the particle completely follows the fluid motion ($\eta(\omega) = 1$). In the high-frequency limit, the force is completely determined by the fluid acceleration coming from the added mass and pressure gradient terms in the Maxey & Riley (1983) equation. In this region, $\eta(\omega) = \beta^2$. This means that for heavy particles (e.g. solid particles in gas), the spectral response goes to zero, but for neutrally buoyant particles, it remains one, meaning that for the latter neither high nor low frequency fluctuations are damped.

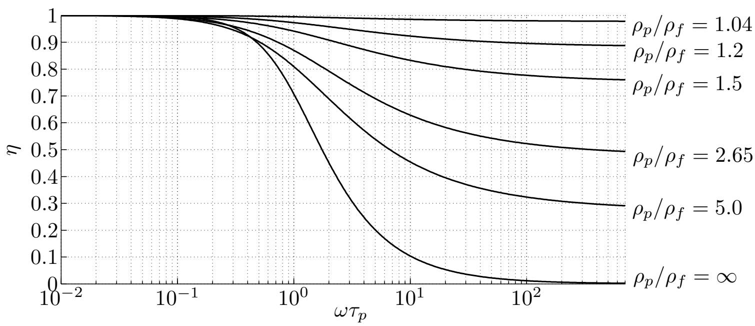

Figure 2.7: Transfer function for particles with ρ_p/ρ_f and the same τ_p

The results of these transfer functions can be used to derive a relation between the fluid velocity fluctuations and the particle velocity fluctuations, which can be used to show that for sediment transport, the sediment particles (typical diameters and densities are given in table 2.1) follow

1. For this, the non-linear correction of eq. 2.16 needs to be neglected. However, the Basset force is a linear operator and can be included in the calculation of a transfer function, but is neglected hear in accordance with section 2.2.

the fluid velocity fluctuations they encounter very well. The relations between the fluid and particle velocity fluctuations have the form:

$$\langle u'^2_{p,i} \rangle_p = \gamma_p \langle u''^2_{f,i} \rangle_p \tag{2.24}$$

$$\langle u'_{p,i} u''_{f,i} \rangle_p = \gamma_{pf} \langle u''^2_{f,i} \rangle_p \tag{2.25}$$

$$\tag{2.26}$$

In these equations, $u''_f(x_p) = u_f(x_p) - \langle u_f \rangle_p$, thus $u''_f(x_p)$ are the fluid velocity fluctuations as seen by a particle. These equations are valid for the normal stresses as well as for the shear stresses. Assuming an exponential function for the Lagrangian velocity correlation function, the following relation for the transfer coefficients γ_p and γ_{pf} can be derived:

$$\gamma_p = \frac{\beta^2 + T_f/\tau_p}{1 + T_f/\tau_p} \qquad \text{Hinze (1975)} \tag{2.27}$$

$$\gamma_{pf} = \frac{\beta + T_f/\tau_p}{1 + T_f/\tau_p} \qquad \text{Simonin } et\ al. \text{ (1993)} \tag{2.28}$$

Here, T_f is the integral time scale of the turbulence seen by the particles. In these relations, the inverse Stokes number T_f/τ_p determines the behavior of the particles. For very large values T_f/τ_p (thus particles with a very small time scale), γ_p and γ_{pf} approach 1, which means that the particles follow the fluid exactly. This is the case for sediment particles, where using the data from table 2.1 it can be found that $\gamma_1 = 0.9999$ for typical river conditions, and similar values for γ_p are found for laboratory experiments. Furthermore, the influence of the density ratio is visible in these relations. A decreasing density for a given Stokes number, gives an increased response of the particles (an increasing value of γ_p and γ_{pf}). In case the particle density equals the fluid density, $\gamma_p = 1$, irrespective of the Stokes number. Note however, that the validity of this statement is limited by the additional constraint in the derivation of eq. 2.15 that $d_p/\lambda_{kolm} \ll 1$.

Using eq. 2.28, it is also possible to calculate the relative velocity fluctuations of the particle:

$$\langle u'^2_{rel,i} \rangle = \langle u'^2_{p,i} \rangle_p + \langle u''^2_{f,i} \rangle_p - 2\langle u'_{p,i} u''_{f,i} \rangle_p = \frac{\beta^2 - 2\beta + 1}{1 + T_f/\tau_p} \langle u''^2_{f,i} \rangle_p \tag{2.29}$$

this relation shows that for Stokes numbers going to zero, the relative velocity fluctuations also go to zero. The same holds when the fluid density ratio equals the particle density. For typical sediment transport conditions (table 2.1) $\langle u'^2_{rel,i} \rangle / \langle u''^2_{f,i} \rangle_p$ is $O(10^{-5})$, and hence the fluctuations in the relative particle velocity can be considered small.

2.2.3. Turbulence structure interaction

In the preceding section, it was shown that suspended sediment particles follow the fluid flow velocities they encounter almost exactly, with the exception of a mean drift due to gravity. In this section, the effect of the interaction between a single particle and a coherent flow structure is analyzed.

Strongly inhomogeneous particle concentration distributions have been observed in gas-particle flows (Fessler *et al.*, 1994). The inhomogeneity is ascribed to preferential concentration (Eaton & Fessler, 1994). This term is used to describe the phenomenon that particles heavier than the fluid are swept out of vortices into straining regions, due to their inertia. Preferential concentration can lead to a difference between the fluid velocity statistics on the particle location and the overall fluid velocity statistics. It is strongest when $St_{kolm} \approx 1$, but absent for very small and large Stokes numbers. In case gravity plays a role, the particles swept out of vortices preferentially concentrate in downgoing fluid regions (Wang & Maxey, 1993), thus increasing the apparent settling velocity, even though the relative velocity remains unchanged (fig. 2.8). It was demonstrated that apparent settling velocities could increase with 50 % of the settling velocity in undisturbed conditions.

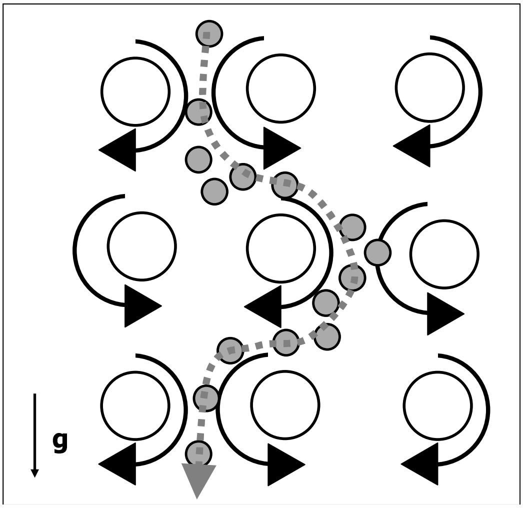

Figure 2.8: Mechanism leading to an increased apparent settling velocity

A priory, one might think that these effects are less important for sediment particles, because the inertial force that ejects particles out of a vortex is then counterbalanced by an inward fluid pressure gradient. Furthermore, the Stokes numbers for sediment particles are much smaller than one, which means that the particles follow the flow velocity almost exactly (section 2.2.2). However, increased apparent settling velocities have also been observed for glass particles in water (Yang & Shy, 2003) despite the small density ratio. They found experimentally that the relative increase in the apparent settling velocity $|v_S|/|v_T| - 1$, with v_S the apparent settling velocity, increased with decreasing values of $|v_T|/u_{kolm}$. Hence the increase in the apparent settling velocity was strongest for low still water settling velocities.

Maxey & Corrsin (1986) calculated the motion of particles in a flow field that consisted of many vortices. These vortices were arranged in a rectangular grid in such a way that two vortices next to each other had an opposite vorticity. From now on, this flow field, which is similar to the flow field shown in fig. 2.8, will be called a cellular flow field. In this situation, they found that the behavior of hypothetical inertialess but settling particles that are randomly distributed in these cellular flow fields can be divided into two groups. First, there is a group of particles that sample the downward flow zones similar as happened in fig. 2.8 and therefore have a significantly increased apparent settling velocity. Just as found by Yang & Shy (2003), the relative increase of the apparent settling velocity ($|v_S|/|v_T|$) increases with a decreasing still water settling velocity. This increased apparent settling velocity was also found for inertialess settling particles in a single vortex (Dávila & Hunt, 2001). The percentage of particles that shows an increased settling velocity increases from zero (when the still-water settling velocity is zero) to 100% (when the settling velocity equals the characteristic velocity of the cellular flow). Second, there is a group of particles that gets trapped in a circulating flow field and that therefore has a decreased apparent settling velocity. It appears that the average of the apparent settling velocity over all particles in this situation is equal to the still water settling velocity. However, in case the initial sediment concentration is not homogeneous, the average apparent settling velocity is not equal to the still water settling velocity. The net result depends on the distribution of the particles over the distinct flow structures. Finally, it was found that this trapping cannot occur for finite inertia particles, because they are swung out of the trapping zones into the zones of descending fluid flow, and thus in this situation, there is always an increase of the apparent settling velocity (Maxey & Corrsin, 1986).

To summarize, it appears that sediment particles are not necessarily homogeneously distributed in a flow field and that this inhomogeneity can influence mean particle velocities. The inhomogeneity is due to the particle's weight and their distribution over the different flow structures. The strongest changes in the apparent settling velocities for the lowest still water settling velocities compared to a typical velocity scale of the turbulence.

2.2.4. Conclusion

In the preceding, the particle equation of motion was addressed in the context of sediment transport. It was found that far from any boundary, the forces of importance for such particles are the drag force, the fluid pressure gradient and gravity. For these particles, the drag force needs to be corrected, because $Re_p = O(10)$.

Sediment particles have a density slightly larger than the density of the fluid and a timescale in which it adapts to the fluid velocity, which is smaller than all the time scales in the turbulence. A consequence of these two properties is that sediment particles will follow the flow well, except for a mean drift due to gravity.

The fluid velocity statistics at the particles do not need to be equal to the overall fluid statistics. Due to the particles' gravitational weight (and an additional influence of its inertia), particles in a turbulent flow can favor downward flow structures, which leads to an increased apparent settling velocity, even though the instantaneous relative velocity between fluid and particle does not change.

2.3. Continuum particle transport models

2.3.1. Introduction

In the preceding section, particle motion was studied from a Lagrangian viewpoint, i.e. the momentum of a single particle was considered. However, for practical applications, the Lagrangian approach is not always feasible and an Eulerian continuum approach is preferred for modeling purposes. This approach will be discussed in the present section.

Sediment transport can be modeled using an advection-diffusion equation:

$$\frac{\partial C}{\partial t} + (\langle u_j \rangle - u_{T,j}) \frac{\partial C}{\partial x_j} - \frac{\partial}{\partial x_j} D_{ij} \frac{\partial C}{\partial x_j} = 0 \tag{2.30}$$

Here, C is the volume concentration, u_j the velocity of the sediment-water mixture, and D_{ij} a diffusion coefficient tensor. This equation is basically a Reynolds averaged continuity equation for sediment, in which the $\langle c' u'_j \rangle$ terms that arise from Reynolds averaging are modeled with a gradient diffusion term [2]. Applying eq. 2.30 to a stationary, uniform open channel flow yields:

$$D_{yy}(y) \frac{dC}{dy} + v_T C = 0 \tag{2.31}$$

This equation states that in a uniform flow, an equilibrium exist with an upward sediment flux due to turbulent diffusion and a downward flux due to the settling of the particles. In order to calculate a concentration profile, a closure relation for the turbulent diffusion coefficient D_{yy} is needed. Usually, the assumption is made that the diffusivity of sediment is proportional to the "diffusivity" of streamwise momentum, i.e. $D_{yy} = \beta \epsilon_{xy}$, where β is the inverse of the turbulent Prandtl-Schmidt number and ϵ_{xy} the eddy viscosity. For a uniform channel flow, a parabolic eddy viscosity (eq. 2.7) can then be used to provide the diffusion coefficient. With this diffusion coefficient eq. 2.31 can be integrated to give the Rouse equation for the suspended sediment concentration distribution:

2. The advection velocity is taken out of the derivative, because the fluid-sediment mixture is usually assumed to be incompressible.

$$\frac{C(y)}{C(y_0)} = \left(\frac{h-y}{y} \frac{y_0}{h-y_0} \right)^{\frac{v_T}{\beta \kappa u_*}} \tag{2.32}$$

Here $C(y_0)$ denotes the concentration at the reference height y_0. It is necessary to prescribe this, because according to equation 2.32, the sediment concentration becomes infinite at $y = 0$, which is of course not physical. Equation 2.32 works quite well in practice despite the assumptions that were made in the derivation of this equation that lack apparent justification:

- The analogy between turbulent and molecular diffusion leads to the gradient diffusion closure, even though the intermittent character of the turbulence differs strongly from the continuous character of molecular diffusion.
- The proportionality between the eddy viscosity and eddy diffusivity is not obvious.
- It assumes that $C(y_0)$ can be known for various conditions.

In the following, the continuum equations for sediment transport will be derived using a more fundamental approach. It has the advantage that more insight is obtained in what the different terms in eq. 2.30 represent, which can be used to improve these models.

2.3.2. Two-fluid flow equations

To go from the motion of individual particles to a continuum formulation, two-fluid models can be used (see Elghobashi, 1994; Enwald *et al.*, 1996; Minier & Peirano, 2001, for a derivation). These models describe sediment transport as two interpenetrating fluids, one for the continuum phase (i.e. the water) and another for the dispersed phase (i.e. the sediment). For both continua, mass and momentum balances are derived using concentration weighted averaging. A concentration weighted average of a quantity X_a in phase a is defined as $\langle X_a \rangle = \langle X_a \alpha_a \rangle / \langle \alpha_a \rangle$. Here, α_a is the phase indicator function, which is equal to 1 if at time t and position $\vec{x}$, phase a is present, and zero otherwise. The volumetric concentration of phase a is then defined as the average of the phase indicator function of that phase: $C_a \equiv \langle \alpha_a \rangle$. This means that the concentration is an averaged quantity by construction, and no fluctuations of the concentration exist. The advantage of using concentration weighted variables is that less cross-correlation terms arise than when Reynolds averaging is used, which can make it easier to develop closure relations. Furthermore, density weighted quantities are the quantities that are obtained from PIV/PTV measurements such as those in this thesis. The density weighted two-fluid continuity and momentum equations are respectively:

$$\frac{\partial C_k}{\partial t} + \frac{\partial C_k \langle u_{k,j} \rangle_k}{\partial x_j} = 0 \tag{2.33}$$

$$\underbrace{\frac{\partial C_k \langle u_{k,i}\rangle_k}{\partial t} + \frac{\partial C_k \langle u_{k,i}\rangle_k}{\partial x_j}\langle u_{k,j}\rangle_k}_{\text{advection}} = \tag{2.34}$$
$$\underbrace{-C_k g_i}_{\text{gravity}} - \underbrace{\frac{1}{\rho_k}\frac{\partial C_k \langle p_k\rangle_k}{\partial x_i}}_{\text{normal stresses}} + \underbrace{\frac{1}{\rho_k}\frac{\partial C\langle \tau_{k,ij}\rangle}{\partial x_j}_k}_{\text{shear stresses}} + \underbrace{f(k)C_p F_{f\to p}}_{\text{interaction term}}$$

In this equations, the subscript k is used as an indicator for the phase (no summation is implied in terms with multiple ks). This subscript can take the values p for the particle phase, and f for the fluid phase. The mean volume concentrations of fluid and particle, denoted here with a C_k, need to obey the additional constraint that $C_p + C_f = 1$. Concentration weighted averaging over a particular phase is denoted by $\langle\rangle_k$. In these equations p_k is the normal stress and $\tau_{k,ij}$ the shear stress in phase k. For the fluid phase, these terms are equal to respectively the fluid pressure and the sum of viscous and Reynolds shear stresses. For the particle phase, these terms are equal to the fluid pressure and the shear stress at the particle-fluid interfaces to which the stresses due to particle-particle interaction (such as collisions) are added. These particle-particle interactions are neglected for the moment, but will be discussed in 2.4.3. In the interaction term, $F_{f\to p}$ is the force of the fluid on the particle due to the development of a disturbance flow field, such as the drag, added mass, lift and Basset history force (see 2.2.1). Here, $f(k)$ is an indicator function , which is 1 for the particle phase and -1 for the fluid phase. In this way, the equations are in accordance with Newton's third law.

We will now apply these equations to sediment transport. More detailed derivations can be found in e.g. Greimann *et al.* (1999). For low sediment concentrations (one-way coupling), which is assumed in this section, eq. 2.33 and 2.34 reduce to the Reynolds averaged Navier-Stokes equations (eq. 2.4) for the fluid phase. For the sediment phase, the continuity equation yields, (with the average volume concentration of the sediment from now on denoted as C):

$$\frac{\partial C}{\partial t} + \frac{\partial C\langle u_{p,j}\rangle_p}{\partial x_j} = 0 \tag{2.35}$$

Here, $u_{p,i}$ and $u_{f,i}$ are the respective particle and fluid velocities in the i-direction. Concentration weighted ensemble averaging over the fluid and particle phase is indicated with $\langle\rangle_f$ and $\langle\rangle_p$ respectively. The concentration averaged momentum balance for the sediment phases in the i-direction can be obtained by including the drag and added mass terms from eq. 2.15 in the interaction term and performing some algebra. Lift, Faxén and Basset forces are neglected in this equation. Subsequently, because for the low St-numbers, the time in which a particle adapts to the changed mean flow is very short and the advection terms in eq. 2.34 can be neglected. The relative velocity in the drag force can be written as function of the particle and fluid velocities (Simonin *et al.*, 1993), reading:

$$\begin{aligned}\langle u_{rel,i}\rangle_p &= \langle u_{p,i}\rangle_p - \langle u_{f,i}\rangle_p \\ &= \langle u_{p,i}\rangle_p - \langle u_{f,i}\rangle_f - \langle u'_{f,i}\rangle_p\end{aligned} \tag{2.36}$$

In the second line, $\langle u_{f,i}\rangle_p$ is expressed as the difference between the mean fluid flow velocity $\langle u_{f,i}\rangle_f$ and an extra term ($\langle u'_f\rangle_p$), which takes into account that the fluid velocity fluctuations at the particle location do not need to be zero on average. This $\langle u'_f\rangle_p$ term is called the drift velocity. Combining this leads to the following equation for the momentum of the sediment motion:

$$C\langle u_{p,i}\rangle_p = C\langle u_{f,i}\rangle_f + Cu_{T,i} + C\langle u'_f\rangle_p - (\gamma_{ij} - \beta)\tau_p \frac{\partial C\langle u'_{f,i}u'_{f,j}\rangle_f}{\partial x_j} \tag{2.37}$$

Here, $\gamma_{ij} \equiv \langle u'_{p,i}u'_{p,j}\rangle_p / \langle u'_{f,i}u'_{f,j}\rangle_f$ and β is calculated according to eq. 2.18. In eq. 2.37, on the left hand side one can find the average particle flux. On the right hand side, one finds the different contributions to this flux, viz. advection by the mean flow, settling due to gravity, the drift velocity (due to the non-zero average of the fluid velocity fluctuations at the particle location) and the influence of the fluid Reynolds stresses. We will apply eq. 2.37 first to the vertical momentum balance. The term due to the fluid Reynolds stresses can then be split into in a turbophoretic and a diffusion like term as:

$$-(\gamma_{yy} - \beta)\tau_p \frac{\partial C\langle u'^2_{f,y}\rangle_f}{\partial y} = \underbrace{-(\gamma_{yy} - \beta)\tau_p C \frac{\partial \langle u'^2_{f,y}\rangle_f}{\partial y}}_{\text{turbophoresis}} + \underbrace{-(\gamma_{yy} - \beta)\tau_p \langle u'^2_{f,y}\rangle_f \frac{\partial C}{\partial y}}_{\text{diffusion like}} \tag{2.38}$$

By dividing this equation by C, it is possible to identify apparent velocities due to turbophoresis $u_{d,t}$ and the diffusion like term $u_{d,d}$:

$$v_{d,t} = -(\gamma_{yy} - \beta)\tau_p \frac{\partial \langle v'^2_f\rangle_f}{\partial y} \tag{2.39}$$

$$v_{d,d} = -(\gamma_{yy} - \beta)\tau_p \langle v'^2_f\rangle_f \frac{1}{C}\frac{\partial C}{\partial y} \tag{2.40}$$

The turbophoresis term denotes that particles with a finite inertia tend to move to regions of low fluid turbulence (Young & Leeming, 1997), whereas the diffusion-like term accounts for an increased turbulent diffusion flux due to the particles' inertia. These two terms clearly depend on three parameters: the density ratio parameter β, the particle time scale τ_p, and γ_{yy}. In accordance with eq. 2.28, γ_{yy} is approximately one for small Stokes numbers (section 2.2.2). Apparently, the turbophoresis and diffusion-like term are only important for relatively large particle time scales. As can be seen in table 2.1, the particle time scale is very small compared to the integral time scale for sediment transport in the field and in the laboratory, and hence the diffusion-like term will not be important. Using equation 2.39 in combination with an empirical relation from (Nezu & Nakagawa, 1993) to estimate the gradient of the velocity fluctuations, it can be estimated that for sand particles in a river, as well as laboratory sediment transport experiments (using the parameters from table 2.1), the turbophoretic velocity is less than 1 % of the settling velocity at $y/h = 0.1$.

Neglecting the turbophoresis and the diffusion-like term is thus justified for suspended sediment transport. This results in two very simple equations that can be obtained from eq. 2.37 for the momentum balance in the streamwise and wall normal directions:

$$\langle u_p \rangle_p - \langle u_f \rangle_f = \langle u_f' \rangle_p \tag{2.41}$$

$$\langle v_p \rangle_p = \langle v_f \rangle_f + \langle v_f' \rangle_p - v_T \tag{2.42}$$

Equation 2.41 shows that in the streamwise direction, there can be a difference between the mean fluid and the mean particle velocity if the particles do not sample the streamwise fluid fluctuations homogeneously, i.e. if the particles are preferentially distributed in either slower or faster than average turbulence structures. Only if this happens, $\langle u_f' \rangle_p$ is different from zero. Equation 2.42 shows that the mean wall normal velocity of the particles, is equal to the mean fluid velocity added to the difference in the drift and settling velocity. The mean particle velocity is important to know, because the mean particle flux is equal to $C\langle v_p \rangle_p$. In many applications, the vertical fluid velocity is zero. Then the mean particle velocity depends on the difference between the settling due to gravity (v_T) and the drift velocity $\langle v_f' \rangle_p$. In practical applications, eq. 2.42 can be used together with the continuity equation for the sediment (eq. 2.35), for modeling sediment transport in inhomogeneous situations.

In an equilibrium situation, $\langle v_p \rangle_p = 0$ and eq. 2.42 reduces to:

$$\langle v_f' \rangle_p = v_T \tag{2.43}$$

Equation 2.43 shows that in an equilibrium situation, the particles need to be located on average in upward moving flow structures, because the average of the vertical fluid velocity fluctuations at the particle's location is positive (i.e. upward). Hence, it can be concluded that in an equilibrium the downward flux due to gravity (the settling of the sediment particles with respect to the surrounding fluid) is compensated by an upward flux, that occurs because particles are encountered on average in upward flow structures. The drift term $\langle v_f' \rangle_p$ comes from the drag force in the wall normal momentum balance for suspended sediment (eq. 2.34). Thus the net downward working force acting on the particles due to gravity minus buoyancy is compensated by an on average upward directed drag force, which has two components (both directed upwards):

1. The drag force that exists due to the relative motion of the particle with respect to the surrounding fluid, caused by gravity. In eq. 2.43 this force is included in the settling velocity.
2. A mean upward drag force on the particles, which exists, because the particles are found on average in upward flow structures. This is the drift term in eq. 2.43.

Simonin *et al.* (1993) related the drift term to the turbulent diffusion flux. In fact, he stated that $\langle v'_f \rangle_p = \langle c'v' \rangle / C$, where $\langle c'v' \rangle$ is the turbulent diffusion flux. This can be explained as follows: Imagine a flow with high sediment concentrations near the wall and lower concentrations higher in the water column. In this situation, an upward flow structure will transport many particles upward, whereas a downward flow structure will transport less particles downward. Taking the average velocity that the particles encounter will then lead to a positive drift (because there are much more particles in the upward than the downward flow structure). In the next section, a closure for the turbulent diffusion flux is derived.

2.3.3. Turbulent diffusion closure

In eq. 2.42, a closure is needed for the drift velocity in terms of mean variables such as concentration and turbulent Reynolds stresses. In the preceding section, it could be seen that it is this drift which keeps the particles suspended, while they are being pulled down by gravity. The velocity drift is the average of many instantaneous flow structures by which the particles are transported. Because this process shows some analogies with molecular diffusion, it is called turbulent diffusion, even though it is actually not a diffusion process. Note that because the drift velocity is related to the turbulent diffusion flux F, with $\langle u'_f \rangle_p = F / \langle C \rangle$, we use the flux rather than the drift velocity in this section.

In order to gain more understanding of the turbulent diffusion process, we start by describing the transport as the result of many instantaneous displacements. This can be done with a random walk approach, similar as was done as long ago as 1921 in Taylor's pioneering approach to derive diffusion coefficients in a homogeneous, isotropic turbulence. This derivation shows how the combined occurrence of advection of particles leads to turbulent diffusion of particles. Using this approach has the advantage that the effect of intermittency in the turbulence is explicitly included in the equations for the turbulent diffusion flux. Especially, this approach has the advantage that one does not need to assume that the turbulent transport only occurs on length scales that are smaller than the turbulent length scales.

A random walk in a one-dimensional domain is considered, where the derivation from Bazant (2005) is followed. In such an approach, the transport of sediment particles is schematized as the occurrence of many discrete steps, that have a random displacement Δy during a time interval Δt. The probability density function of these random steps is given by $P(\Delta y)$. Now, the sediment concentration $C_{n+1}(y)$ after $n+1$ steps at a height y is related to the concentration at all other locations $y' = y - \Delta y$ steps one time step before (see the schematic representation in fig. 2.9). This can be expressed mathematically with Bachelier's equation:

$$C_{n+1}(y) = \int P(\Delta y) C_n(y - \Delta y) d\Delta y \tag{2.44}$$

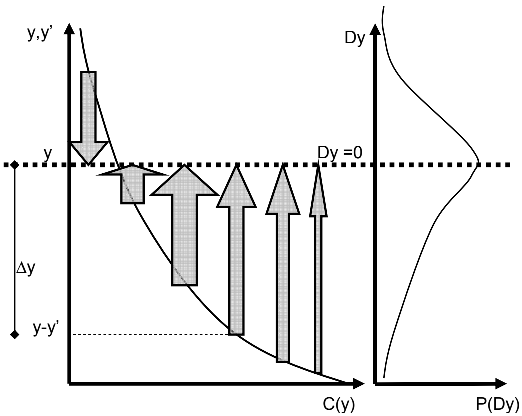

Figure 2.9: Schematic depiction of the flux of particles with respect to a reference level y in a random walk

In this equation, the effect of the occurrence of a range of length scales in the turbulence and thus the influence of intermittency is implicitly included. This equation is simplified by approximating $C_n(y - \Delta y)$ with a Taylor series, which after some algebra leads to (see Bazant, 2005):

$$\frac{\partial C(t,y)}{\partial t} = \sum_{n=1} (-1)^n \tilde{D}_n \frac{\partial^n C(t,y)}{\partial y^n} \tag{2.45}$$

Here $\tilde{D}_n = k_n/(n!\Delta t)$, with k_n the n^{th} order cumulant. Using the 1-d continuity equation $\partial C/\partial t = -\partial F_y \partial y$, we can write the total flux F_y for a random walk as:

$$F_y = -\frac{-k_1}{\Delta t} C + \frac{k_2}{2\Delta t}\frac{dC}{dy} - \frac{k_3}{6\Delta t}\frac{d^2C}{dy^2} + \frac{k_4}{24\Delta t}\frac{d^3C}{dy^3} + HOT \tag{2.46}$$

Thus, the gradient diffusion model can be obtained from a random walk approach, and apparently it is a first order description of turbulent diffusion. However, it is only strictly valid when the displacements of the sediment particles caused by the turbulent eddies are small compared to the length scales over which the sediment concentration changes.

It is insightful to compare this diffusion model with a mixing length model. A mixing length model assumes that the upward flux is equal to the concentration at one mixing length below

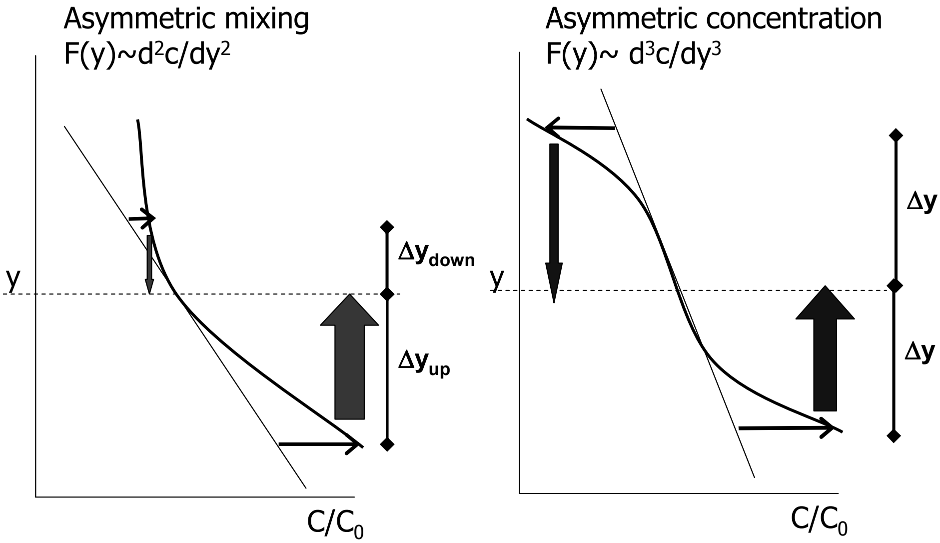

Figure 2.10: Concept of long range turbulent diffusion transport

the point of observation, multiplied by a characteristic velocity. The downward flux comes from the concentration at one mixing length above that point. In the present random walk model, the mixing length is equal to the standard deviation of the step lengths and the velocity scale is this mixing length divided by Δt. Here, Δt can be seen as a kind of integral time scale. The extra terms on the right hand side of 2.46 correct the flux for the fact that the particles do not all come from the location one mixing length away, but actually from a range of locations nearby. Two of these phenomena are shown in fig. 2.10. First, if the step length distribution is positively skewed (which means that the probability that a particles comes from far below the point of reference is higher than that it comes from far above) an extra flux occurs if the concentration profile deviates from linearity. The extra flux is the results of the stronger than linear increase in the concentration far below the reference point. No extra flux occurs in case the concentration distribution is linear. The reason for this is that in this case, the increase of the flux due to the higher concentration on one side of the reference is exactly balanced by the more frequent transport (needed in a skewed probability distribution with a zero mean) from the opposite side. The second term corrects for the kurtosis of the distribution, i.e. whether most steps are shorter than the mixing length (a kurtosis lower than 3) or longer. In case of an asymmetry in the concentration profile around the point of reference, this can give an extra upward or downward flux (fig. 2.10). Wyngaard & Weil (1991) showed that the asymmetry in the length scales can be related to the skewness in the velocity fluctuations. In case of a positive skewness in the wall normal velocity fluctuations, there exist some strong upward flow structures, which transport sediment up from a farther distance, than the distance from which the sediment is transported downward.

Thus to conclude, it appears that a possible explanation for the experimentally found difference between the eddy diffusivity and the eddy viscosity (section 2.3.1) might be found in the transport of sediment by eddies that are large compared to the distance over which the sediment concentration varies. A similar hypothesis was proposed by Nielsen & Teakle (2004). They took a similar d^3C/dy^3 term into account in their derivation from a mixing length approach. The difference between their derivation and the present one is that in their derivation a positive d^3C/dy^3 always yields an increased upward sediment flux.

2.3.4. Diffusion coefficients for suspended sediment transport

Unfortunately, the formulations derived in the previous section do not give much information about the relation between the diffusion coefficient and the turbulence quantities. In the present section, we will discuss this relation. The focus will be on the first order transport term (the standard gradient diffusion term). A relation between the turbulent diffusion coefficient and turbulence quantities was obtained by Taylor (1921), who considered the turbulent diffusion process in homogeneous turbulence as a random walk with correlated steps in time (rather than space):

$$\begin{aligned} D_2 &= \frac{1}{2}\frac{d}{dt}\langle \Delta L'^2 \rangle = \langle \Delta L' \frac{d}{dt} \Delta L' \rangle = \int_0^t \langle v'_f(t) v'_f(t-\tau) \rangle d\tau \\ &= \langle v'^2_f \rangle \int_0^t R_{L,yy}(\tau) d\tau \end{aligned} \tag{2.47}$$

Here, $R_{L,yy}(\tau) = \langle v'(t_0)v'(t_0+\tau)\rangle / (v_{rms}(t_0)v_{rms}(t_0+\tau)$ is the Lagrangian time correlation function (section. 2.1.4). For small times $R_{L,yy}(\tau) \approx 1$, which means that $\langle \Delta L'^2(t) \rangle \sim t^2$ and hence the particle transport is governed by advection. For large times $t \ll T_L$, the integral in equation 2.47 reduces to the Lagrangian time scale T_L (see section 2.1.4) and $\langle \Delta L'^2(t) \rangle \sim t$. Thus the long term diffusion coefficient reduces to:

$$D_2 = \langle v'^2_f \rangle T_L \tag{2.48}$$

Now the gradient diffusion transport term is known as function of the turbulence statistics. However, the Lagrangian time scale is very difficult to determine experimentally and theoretically (see section 2.1.4). Therefore, it is usually assumed that the vertical diffusion coefficient of sediment is proportional to the diffusion coefficient of streamwise momentum (the eddy viscosity), thus:

$$D_2 = \beta \epsilon_{xy} \tag{2.49}$$

Indeed, good results where obtained by Oesterlé & Zaichik (2004), who determined the Lagrangian time scale from this assumption and found that it compared well with DNS results (see section 2.1.4). There is however no known theoretical justification for this approach. In fact, this assumption is doubtful, as one can easily see that the coherent flow structures that are responsible for transporting momentum (those with high values of $u'v'$) do not necessarily have to be the same as the ones responsible for transporting sediment vertically (those with high values of v'). Most investigations on sediment transport have focused on determining the proportionality coefficient β. This coefficient represents the ratio between the turbulent diffusion of sediment particles and momentum. Determining β experimentally has not been a very successful approach, as both values higher (e.g Nezu & Azuma, 2004; Muste *et al.*, 2005) and lower (e.g Cellino & Graf, 1999) than one have been found for β. Especially, the focus has always been on its determination in equilibrium conditions, and no information exist on its applicability in non-equilibrium situations.

Using a Langevin equation approach, Simonin *et al.* (1993) found that $\langle v_p' v_f' \rangle_p$ should be used as the Reynolds stress in eq. 2.48. In 2.2.2, it was shown that for suspended sediment transport $\langle v_p' v_f' \rangle_p \approx \langle v_f'^2 \rangle_p$. Thus any differences between the particle velocity fluctuations and the fluid velocity fluctuations at the particle location are not an explanation for a value of β that differs from one. It is however possible that the difference between the turbulence statistics at the particle locations and those in the complete flow field might account for the differences between the diffusion of sediment and momentum. In this way, it seems also possible that difference between the Lagrangian time scale of the sediment particles and the one of the fluid accounts for the difference in the diffusion of sediment particles and fluid momentum. If for example particles are found in larger than average flow structures, the turbulent diffusion of the particle would be larger than the turbulent diffusion of momentum. Note that the crossing trajectories effect (Csanady, 1963), which leads to a decrease of the turbulent time scales of the particles compared to the one of the fluid because particle fall out of the turbulent eddies, is only important if $v_T > v'_{rms}$ (Wang & Stock, 1993). Hence, it is not important for suspended sediment transport, where $v_T < v'_{rms}$. Similarly, the direct effect of the particle time scale on the Lagrangian timescale is negligible, because for suspended sediment transport the particle time scale is very small compared to the integral fluid time scale (as shown in section 2.3.2).

In the following, it will be investigated whether the difference in the turbulent diffusion of sediment particles and that of momentum are similar in equilibrium and non-equilibrium situations. Furthermore, the above mentioned hypotheses for the difference between the turbulent diffusion of sediment particles and that of momentum are investigated.

2.3.5. Conclusion

Various hypotheses for the difference in the diffusion coefficient for the sediment and momentum were formulated:

- The transport of momentum differs from the transport of suspended particles, because different turbulent structures are important for the transport of momentum (for which both u' and v' need to be high), than for the transport of particles (for which in principle only v' is important).
- Additional transport occurs because the concentration cannot be approximated with a linear relation over the size of the eddies that transport sediment, in combination with complicating turbulence phenomena as intermittency and bursts.
- Additional transport is caused by the fact that the turbulence statistics (velocity fluctuations, and integral length scales) at the particle locations have different statistical properties than the complete flow field has.

2.4. Concentration dependence of particle-turbulence interaction

2.4.1. Introduction

In the preceding section, dilute sediment concentrations were assumed (one-way coupling). However, in most situations of practical importance, the concentrations can be quite large, especially near the bottom. If the sediment concentration is sufficiently high, the influence of the suspended particles on the fluid flow starts to become observable, which is called two-way coupling. This influence exists because of Newton's third law, which states that a particles exerts a force on the fluid equal and opposite to the force the fluid exerts on the particles. If the sediment concentration increases further, the particles start to influence each other, either through collisions, or due to hydrodynamic interactions (the interactions between the disturbance flow fields of two or more different particles). This is called four-way coupling.

The exact effects of two-way and four-way coupling are not known. Suspended particles are reported to have increased (Best *et al.*, 1997) or decreased (Righetti & Romano, 2004) the turbulence level in a flow, particles can alter the mean flow (e.g. Coleman, 1981), and the presence of particles in the bottom layer changes the effective bottom roughness (Kaftori *et al.*, 1998). For flows with suspended sediment transport, it has been suggested that an analogy with stratified flows might be used to explain the changes in the mean flow and turbulence (Villaret & Trowbridge, 1991). A more detailed overview of the experimental findings can be found in chapter 7, when the present experimental results are compared with those in the literature. In the present section, the theoretical background of two-way coupling is discussed.

2.4.2. Two-way coupling

Introduction

In this section, the average effect of two-way coupling is discussed using a continuum description of sediment similar as used in section 2.3. We will derive the two-way coupling effects from the two-fluid flow equations, in contrast to most sediment transport literature (e.g. Zhou & Ni, 1995), who derive two-way coupling effects for suspended sediment transport using an equation for the sediment-water mixture, rather than considering sediment and fluid equations separately. In this section, we will first discuss the effects of changes in the fluids continuity equation (thus a fluid flow generated by a net sediment flux). Then, we will consider the effect of the presence of sediment particles on the mean momentum equations. Finally, we will consider the effect of the particles on the fluid turbulence.

On a microscopic scale, two-way coupling is the result of all the disturbance flows (see section 2.2) generated by the particles. In some instances the details of the microscopic flow might be of importance. Hetsroni (1989) collected data from various sources and found that particles in a gas can increase turbulence levels if $Re_p \rangle 400$, and he attributed this to vortex shedding from the wake of the particles. The influence of the microscopic flow field might also explain the experimentally found influence of the particle size (Gore & Crowe, 1989). They found that the turbulence is increased in the presence of particles is $d_p > 0.1L$, and decreased otherwise. In many situations, especially when $d_p/\lambda_{kolm} \ll 1$ and $Re_p < 400$, the exact details of the disturbance flow are not important. For typical sediment transport conditions, only the second criterion is fulfilled (table. 2.1). Nevertheless, the influence of the details of the disturbance flow fields of the particles will be neglected here. In this case the two-fluid continuity and momentum equations (eq. 2.33 and 2.34) for the fluid phase become respectively:

$$\frac{\partial(1-C)}{\partial t} + \frac{\partial(1-C)\langle u_{f,j}\rangle_f}{\partial x_j} = 0 \tag{2.50}$$

$$\begin{aligned}\frac{D(1-C)\langle u_{f,i}\rangle_f}{Dt} = &- \frac{\partial(1-C)\langle u'_{f,i}u'_{f,j}\rangle_f}{\partial x_j} - \frac{1}{\rho_f}\frac{\partial\langle p_f\rangle}{\partial x_i} \\ &- \nu_f \frac{\partial^2(1-C)\langle u_{f,i}\rangle_f}{\partial x_j^2} - \frac{C}{1/6\pi d_p^3 \rho_f}\langle F_{f\to p}\rangle_p\end{aligned} \tag{2.51}$$

In the latter equation, $F_{f\to p}$ is the fluid force on a single particle, due to the disturbance flow field generated by the no slip conditions at the particles' surfaces (the drag, added mass and Basset history force in eq. 2.15). According to Newton's third law, an equal but opposite force act from the particles on the fluid. The effect of the changed momentum equation is discussed further on, after discussing the effect of the changes in the continuity equation.

Effect through fluid continuity equation

A direct consequence of the continuity equation is that a net particle flux in a closed reservoir results in a fluid flow in the opposite direction, because the mixture volume is conserved. The magnitude of this fluid flow is of $\langle u_f\rangle_f = C/(1-C)\langle u_p\rangle_p$. Batchelor (1972) showed that this reverse flow is the main contribution to explain hindered settling of sediment particles in still water in a closed reservoir (e.g. Richardson & Zaki, 1954). Batchelor (1972) further showed that in case of hindered settling, the downward volume flux consists of both particles and fluid in the disturbance flow area, thus the upward fluid flux is increased by a factor of four (for $Re_p \approx 0$) in comparison with a point-particle approach. The insightful two-fluid description of hindered settling by Thacker & Lavelle (1977), which of course does not include the influence of the fluid in the disturbance flow area, indeed shows a less severe hindered settling for low concentrations than Batchelor's (1972) analysis. Addressing the return flow as the main cause for hindered settling raises very strong doubts on the current practice (introduced by Lavelle & Thacker, 1978) to include the hindered settling velocity in the advection-diffusion model (2.31) that describes a sediment concentration profile in a fully developed situation, where the mean wall normal particle velocity $\langle v_p \rangle_p$ is zero. According to eq. 2.33, there is no upward fluid flow and hence one of the main causes of hindered settling does not exist. In a situation, where there is a net deposition of sediment, there will be an upward fluid flux causing some hindered settling. However, this upward fluid flux is smaller than found for hindered settling in still water, because the net downward particle flux is decreased by the upward particle flux due to turbulent diffusion.

In principle hindered settling in non-equilibrium flows can be accounted for by using the complete two-fluid flow equations (eq. 2.50 and 2.51), rather than the Navier-Stokes equation (eq. 2.2) to calculate the fluid flow and in a sediment transport simulation. However, eq. 2.51 should be modified to include the net fluid flux due to the disturbance flow field of the particles in order to get correct results.

Effects trough fluid mean momentum equation

After discussing the effect of continuity on two-way coupling, we now discuss the effect of the particles on the fluid momentum equation. In a uniform open channel flow, the fluid and particle momentum balance (eq. 2.34) in the wall normal direction can be written as:

$$\begin{aligned}(1-C)\left(\frac{\partial\langle p_f\rangle - g\rho_f}{\partial y} + \rho_f\frac{\partial(1-C)\langle v_f'^2\rangle}{\partial y}\right) + \frac{C}{1/6\pi d_p^3}\langle F_{f\to p}\rangle_p = 0\\ C\left(\frac{\partial\langle p_f\rangle - g\rho_p}{\partial y} + \rho_p\frac{\partial C\langle v_p'^2\rangle}{\partial y}\right) - \frac{C}{1/6\pi d_p^3}\langle F_{f\to p}\rangle_p = 0\end{aligned} \tag{2.52}$$

Here, it was assumed that $d(1-C)/dy = 0$, which is valid when $C \ll 1-C$, which is still satisfied for suspended sediment transport conditions. The buoyancy force on the particles in the second equation comes from the $d\langle p_f\rangle/dy$ term. Because the fluid force on the particles is equal and opposite to the particles' force on the fluid, we can eliminate these terms by adding the two previous equations. After neglecting the vertical fluid fluctuations (i.e. using the hydrostatic assumption) the sum of these equations can be reduced to the very familiar result that the fluid pressure gradient depends on the weight of the mixture (which is valid as long as there are no contact forces between the sediment particles):

$$\frac{\partial \langle p_f \rangle}{\partial y} = -\left(\rho_f(1-C) + \rho_p C\right) g \tag{2.53}$$

A consequence of this equation is that the increased mixture density causes the fluid pressure to increase. If we substitute eq. 2.53 back into eq. 2.52, we find the increase in the fluid pressure ($C(\rho_p - \rho_f)g$) balances exactly the mean force of the particles on the fluid, which in this situation is basically the drag on the particles. In an equilibrium situation, there is a mean upward drift velocity, which means that the particles are more often found in upward than in downward structures, and in this way there can exist a mean upward drag on the particles (see the preceding section for details). Thus:

$$\frac{\langle F_{f\to p} \rangle_p}{1/6\pi d_p^3} = (1-C)\left(\rho_p - \rho_f\right) g \tag{2.54}$$

A direct consequence of the increased fluid pressure gradient is that the buoyancy force on the particle increases with increasing sediment concentration (this effect is also accounted for in the two-fluid hindered settling model of Thacker & Lavelle, 1977). Hence, the still water settling velocity decreases when sediment concentrations increase as:

$$v_T = (1-C) v_{T0} \, \frac{1 + f(Re_p)}{1 + f(Re_{p,0})}, \tag{2.55}$$

with v_{T0} the settling velocity of a single particle in a otherwise particle free fluid, and $Re_{p,0}$ the particle Reynolds number of this single particle. This equation shows that there is an effect of hindered settling for high sediment concentrations even in an equilibrium sediment concentration profile. This effect is caused by the increase buoyancy force on the particles when sediment concentrations increase. However, the strength of the effect is smaller than when hindered settling is applied. Here the decrease in the settling velocity is proportional to $1 - C$. When a complete hindered settling relation is used (such as Richardson & Zaki, 1954), the change in the settling velocity is proportional to $(1-C)^n$, with $n \approx 5$.

Effect on fluid turbulence

Having investigated the influence of the particles on the mean momentum balances, we will now discuss its influence on the turbulence. For this purpose, we will use the results obtained by Minier & Peirano (2001, section 8.5.5). They proposed the following Reynolds stress equation for a two-way coupled flow:

$$\frac{D\langle u'_{f,i}u'_{f,j}\rangle_f}{Dt} = P_{ij} + DIFF_{ij} + PS_{ij} - \epsilon_{ij} - \frac{C\rho_p}{(1-C)\rho_f}\left(\langle u'_{f,j}\rangle_p \frac{\langle F_{f\rightarrow p,i}\rangle}{m_p} + \langle u'_{f,i}\rangle_p \frac{\langle F_{f\rightarrow p,j}\rangle}{m_p} + \left\langle u'_{f,i}\frac{F'_{f\rightarrow p,j}}{m_p}\right\rangle + \left\langle u'_{f,j}\frac{F'_{f\rightarrow p,i}}{m_p}\right\rangle\right) \tag{2.56}$$

Here, P_{ij} is the production term, $DIFF_{ij}$, the viscous, turbulent and pressure diffusion, PS_{ij} the redistribution due to pressure strain correlations ϵ_{ij} the dissipation of Reynolds stresses, which are all defined in the same way as in the one-way coupled Reynolds stress equation (e.g. Libby, 1996). The influence of the particles is accounted for in the last four terms, where $F_{f\rightarrow p,i}$ is the force from a single particle on the fluid, and m_p the mass of a particle. The two-way coupling effect consists of two separate effects; one due to the inhomogeneous sampling of the mean fluid force by the particles, and one by the correlation between the fluid velocity and fluid-particle force fluctuations. The contribution from the mean force on the particles (i.e. from the $\langle u'_{f,j}\rangle_p \frac{\langle F_{f\rightarrow p,i}\rangle}{m_p}$ term) is discussed first for a uniform open-channel flow. Using eq. 2.54, the mean fluid force on a particle can be shown to be related to the increase of the density of the mixture due to presence of suspended sediment (as long as there are no direct forces due to particle-particle interactions). Then this term reduces to the buoyancy terms due to the mean fluid force on the particles in the y direction ($BUOY_{iy}$ and $BUOY_{jy}$):

$$BUOY_{iy} = -\langle u'_{f,i}\rangle_p C\left(\frac{\rho_p - \rho_f}{\rho_f}\right) g_y \tag{2.57}$$

Thus apparently, this term represents density stratification due to the presence of suspended sediment. The importance of this effect for sediment laden flow has already been recognized for quite some time (Villaret & Trowbridge, 1991), but it was based on a analogy explanation, rather than a formal derivation from two-fluid flow equations. Therefore, the limitations of this formulation (especially the necessity to assume the absence of particle-particle contact forces) had not been recognized.

To estimate the importance of the buoyancy term, commonly the flux Richardson number (Ri_f) is used. This is defined as the ratio between the buoyancy ($BUOY_{yy}$) and the turbulence production term (P_{ii}) in the balance equation for the turbulent energy (which can be obtained from eq. 2.56 by summing the three equations for the diagonal components $\langle u'^2_{f,i}\rangle$):

$$Ri_f = \frac{(\rho_p/\rho_f - 1)\, gC\langle v'_f\rangle_p}{\langle u'_f v'_f\rangle_f \frac{d\langle u_f\rangle_f}{dy}} \tag{2.58}$$

In case $Ri_f < 0$, the stratification is unstable and extra turbulence will be produced. This occurs, when the turbulent diffusion flux is in the same direction as gravity (g_y). If $Ri_f > 0$, the situation is stable and turbulence will be damped. According to stability analysis, the maximum value of Ri_f that can occur is 0.25 (e.g. Libby, 1996), above this value all turbulence is damped.

In an equilibrium situation, most suspended sediment can be found near the bottom (see eq. 2.32), and thus a stable stratification exists ($Ri_f > 0$). Then the physical explanation of the damping due to the particles can be explained as follows. For an equilibrium situation to exist (section 2.3), the particles need to be concentrated in upward flow structures ($\langle v'_f \rangle_p > 0$). There is a mean upward force of the fluid on the particles (due to the fluid drag and buoyancy), which equilibrates the downward force due to gravity. Hence there is an average downward force of the particles on the fluid (Newton's third law), which act on the upward flow structures. Thus the upward flow structures are decelerated, leading to a damping of the turbulence. Note here that the stratification depends on the direction of the drift velocity (i.e. the turbulent diffusion flux) and not a priori on the concentration gradient.

The $\langle u'_{f,j} F'_{f \to p,i} / m_p \rangle$ term is negligible for suspended sediment transport, because the relative velocity fluctuations are negligible (section 2.2.2). However, this effect is important in many investigations for particles in gas in the literature (such as Squires & Eaton, 1990; Elghobashi & Truesdall, 1993; Boivin *et al.*, 1998). Thus, because the mechanisms that are important for two-way coupling in sediment laden fluid flows are different from those in particle laden gas flows, it is not a priori correct to use results from gas-particle flows for suspended sediment transport. An example is the well-known diagram by Elghobashi (1991), which states that two-way coupling becomes important from $C_{vol} = 10^{-6}$. However, two-way coupling effects have never been observed for suspended sediment transport at this low concentrations.

Finally, the presence of suspended sediment particles could also have an influence on the dissipation of turbulence (ϵ_{ij} in eq. 2.56 Crowe, 2000). This might occur, because the particles cause a disturbance flow field in the turbulence (see 2.2.1), which might interact with the energy cascade and then leads to changes in the turbulence dissipation.

2.4.3. Four-way coupling

In case the sediment concentration increases even further than those concentration where two-way coupling is significant, the interaction between the particles themselves starts to become important. This is called four-way coupling. In gas-solid flow and in liquid-solid flows with very large particles (such as gravel), particle-particle interactions occur in the form of collisions. For smaller particles in a fluid on the other hand, particles only touch each other at very high concentrations and four-way coupling occurs via hydrodynamic interactions.

Schmeeckle *et al.* (2001) investigated the collisions of settling natural sand particles and glass beads with a wall, and found that some particle rebound occurs only for $St_c > 39$ and that the collisions are not significantly damped by the interstitial fluid for $St_c > 105$. Here St_c is a Stokes number they defined as:

$$St_c = \frac{\rho_p}{\rho_f} \frac{d_p v_T}{9\nu_f} \tag{2.59}$$

For natural sediment, this means that some rebound occurs from a particle diameter of 1 mm (an order of magnitude larger than typical suspended sediment; table 2.1). Elastic rebounding of a particle, occurs for $d_p > 1.5$ mm. For smaller particle sizes, viscous damping is dominant and a settling particle does not rebound when it touches the wall.

Because collisions are not important for suspended sediment transport, the rest of this section focuses on hydrodynamic interactions. In these hydrodynamic interactions, the disturbance flow fields (see fig. 2.5 and 2.6) created by two or more interacting particles lead to a change in the fluid force acting on these particles. Analytical results for these interactions have been obtained in two asymptotic regimes, viz. when particles are relatively far apart ($\Delta x/d_p > 2$), or when they are very close ($\Delta x/d_p \ll 1$), where Δx is the inter-particle distance.

It can be seen from fig. 2.5 and 2.6 that hydrodynamic interactions starts to be important for inter-particle distances $\Delta x = n_p^{1/3}$ smaller than five particle diameters (with n_p the number density of the particles). This leads to a concentration of at least $C = \pi/6(d_p/\Delta x)^3 = 4.2\ 10^{-3}$ for four-way coupling to become important. An equation of motion for two nearby particles ($Re_p \ll 1$) similar to eq. 2.15 has been derived (Ardekani & Rangel, 2006) for $\Delta x/d_p > 2$. This equation shows that the drag force for two nearby particles decreases, thus leading to an increased settling velocity. An increased settling velocity for two particles has indeed been observed experimentally (Wu & Manasseh, 1998).

This effect becomes stronger if the particles are closer together. Therefore, it is necessary to consider the probability that particles approach each other closely, rather than to consider the mean inter-particle distance in order to determine the strength of four-way coupling. This is important, because the former leads to a scaling proportional to C for four-way coupling at low concentrations, whereas just considering the mean inter-particle distance would lead to a much weaker effect with a scaling proportional to $C^{1/3}$ as was shown in the hindered settling analysis of Batchelor (1972). Unfortunately, no closed expression for the mean drag force on a particles as function of the concentration was given in that paper. Such an expression could be used to determine the settling velocity as a function of the sediment concentration and could thus be included in eq. 2.43 to model the influence of hydrodynamic interactions on the sediment concentration profile.

When the inter-particle distances become smaller than the particle diameter, the liquid between the two particles is squeezed out of the gap between them when they approach each other. This process is called lubrication. Of course, this only happens instantaneously for a short time. The result of such hydrodynamic interactions is comparable to a plastic collision, and leads to a significant dissipation of turbulent kinetic energy (ten Cate *et al.*, 2004).

From this short review, it is clear that our understanding of four-way coupling effects for dispersed solid-liquid flows is still very limited. Especially, the theoretical results are only valid for very small particles with $Re_p \ll 1$ in an otherwise quiescent fluid. Very little results exist for applying these effects to larger particles or turbulent flows (an exception is the DNS from ten Cate *et al.*, 2004) and it seems that these effects have never been included in a Reynolds averaged model.

2.4.4. Conclusion

In this section, the influence of increasing sediment concentrations on the mean fluid flow and turbulence (two-way coupling) and on the interactions between individual particles (four-way coupling) was discussed. For two-way coupling, the mechanisms that are of importance for sediment transport are:

- The occurrence of net return fluid flow due to a net sediment flux and their disturbance flow field. This return flow is only important in non-equilibrium situations such as hindered settling of sediment in an undisturbed flow. In equilibrium sediment transport conditions, no net sediment flux exists. It is therefore questionable to include a hindered settling model in the calculation of the settling velocity that is used for the determination of an equilibrium sediment concentration profile using eq. 2.43.
- The presence of sediment leads to an increase in the fluid pressure and the vertical fluid pressure gradient. This increased pressure gradient manifests itself in a buoyancy force that increases with increasing sediment concentrations and hence a decreased settling velocity. In combination with a net turbulent diffusion flux of the sediment, the increased fluid pressures can lead to a damping of turbulence similar as found in stratified flows.
- It is possible that the presence of the disturbance flow fields of the particles interferes with the energy cascade of the turbulence, thus leading to a change (either an increase or decrease) of the turbulent energy dissipation.

With respect to four-way coupling, it is shown that for typical suspended sediment transport conditions, particle collisions are not important, except for concentration close to complete packing (approximately 60 %). Instead, hydrodynamic interactions can be important at larger sediment concentrations, which can lead to a decreased drag force with increasing concentrations and hence increased settling velocities. Hydrodynamic interactions between very nearby particles (lubrication) may have an influence that is similar to that of completely plastic collisions, and may lead to additional dissipation of turbulence.

2.5. Consequences for experimental research

It is the objective of this study to investigate experimentally sediment transport and its relation with coherent flow structures. We will do so for both non-equilibrium and equilibrium situations, since it is not known whether in these situations the same flow structures are important for particle transport.

In order to do so, a measurement technique is needed that can provide detailed information of the fluid velocity at the locations of the particles, since it was shown that the fluid velocity at the particle locations determines the turbulent transport of sediment. Further, this measurement technique needs to provide spatial fluid flow information, such that the coherent flow structures can be measured, which were shown to be an important characteristic of a turbulent open channel flow. The method chosen in this thesis is a combination of PIV (particle image velocimetry), which measures the fluid flow field in a two-dimensional plane and PTV (particle tracking velocimetry), which measures both the velocities and locations of individual sediment particles a the same instant in time as the PIV fluid flow measurements.

Further insight into these detailed physical processes can also be obtained from DNS simulations in combination with tracking the motion of many individual particles. However, this technique has never been verified against experimental data for the conditions that apply to this study (fluid-particle density ratio of the order one in a horizontal open channel flow). Therefore, the experiment is set-up such that a direct comparison without any additional scaling is possible. A preliminary comparison between experimental results and the DNS simulation is performed in chapter 4.

It was shown that the important physical processes at high sediment concentrations (two-way coupling and four-way coupling by hydrodynamic interaction) are still rather poorly understood. More detailed investigations in simple flow configurations are necessary in order to understand the influence of various parameters of the physical system (particle-fluid density ratio, sediment concentration, particle diameter to turbulent length scales, and particle Reynolds number) on these processes. Experimental equipment is therefore required that can measure detailed flow information at high sediment concentrations. Therefore, the feasibility of refractive index matching in combination with PIV for sediment transport is investigated in section 3.3.1 and chapter 7 by performing a small scale high concentration sediment transport experiment, measuring the changes in the fluid and turbulence statistics due to the presence of the sediment particles.

Chapter 3

Experimental setup and data processing[1]

3.1. Introduction

In this chapter, the experimental set-up is described that was used for the two different experiments that were performed. First, a low concentration experiment is addressed. Special attention is given to the choice of the flow conditions and sediment particles, which had to be done in such a way that a one-to-one comparison with a DNS was possible. This is followed by a description of the algorithm that is used to discriminate sediment particles from tracers in order to measure the velocities of the fluid and the particles simultaneously. Then, a description of a smaller scale experiment in a high concentration flow using refractive index matching is given. The objective of this experiment was to measure the two-way coupling effects of the particles on the flow and hence only fluid velocity measurements were done. This chapter is ended with a description of some of the statistical techniques used in the data processing.

3.2. Low concentration experiment

3.2.1. Experimental design

It is one of the objectives of this study to validate a particle laden DNS with an experiment. This experiment must be designed so that its parameters (Reynolds number, particle diameter and density ratio) are equal to those used in the DNS and thus the validation can be performed without having to use any scaling. Because a DNS is not feasible for large Reynolds numbers (typically, the upper limit is 10,000), the experiment needs to be performed at this Reynolds number, which means that severe restrictions exist for the flow velocity in the experiment. It was found experimentally, that the fastest flow that could be obtained at this Reynolds number in the present experimental facility was about 0.3 m/s, which corresponds to $u_* \approx 1.5\ cm/s$.

1. Parts of this chapter were previously published as: W.A. Breugem and W.S.J. Uijttewaal (2007), "PIV/PTV for suspended sediment transport measurements in an open channel flow", Hydraulic Measurements & Experimental Methods Conference (HMEM 2007), Lake Placid, NY, USA

The particles need to be suspended at these low flow velocities. In order to keep the particles suspended, the Rouse number u_*/v_T should be large enough (typically around 5), which means that the settling velocity should not exceed 3 mm/s, and hence natural sediment could not be used. This is not a sufficient criterion, because for particles substantially smaller than the thickness of the viscous sublayer (i.e $d+ = d_p u_*/\nu_f \ll 5$), much higher u_*/v_T are needed to keep them in suspension (up to values of 20 e.g. Niño *et al.*, 2003). Also, these small particles are more likely to result in bed forms than larger particles (Raudkivi, 1976, fig. 5.1). Therefore, it is advantageous to use larger particles with a low density, rather than smaller particles with a higher density. These larger particles have the additional advantage that phase discrimination techniques based on the particle size (described in section 3.2.4) can be applied more easily with larger size differences between dispersed particles and flow tracers. The disadvantage of using relatively large particles is that the point particle approximation ($Re_p < 1$ and $d_p/l_{kolm} < 1$), which was used to derive the Maxey & Riley (1983) equation that is used in the DNS, is not completely fulfilled. Note however that sediment particles in natural systems such as rivers and estuaries do not fulfill the criteria for being a point-particle either (table 2.1).

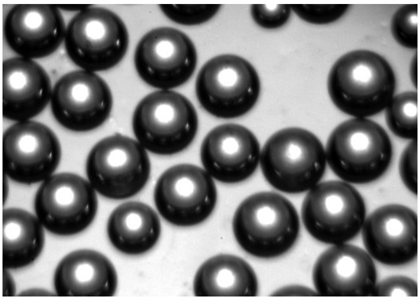

Figure 3.1: Microscopic picture of polystyrene particles (Magnification 150 x)

In order to fulfill the above mentioned restrictions on the settling velocity, spherical polystyrene particles 347 μm ($\sigma = 45$ μm) were used as pseudo-sediment (fig. 3.1). A histogram of their size is shown in fig. 3.2. These particles had a density ρ_p of 1035 kg/m^3. A terminal velocity v_T of 2.2 mm/s was measured, which compares well with the theoretical estimate of 2.1 mm/s ($Re_p = v_T d_p/\nu_f = 0.71$). For these particles, a mean flow velocity of 0.20 m/s was sufficient, which in combination with a water depth of 0.05 m remained below the maximum Reynolds number set by the DNS.

3.2.2. Experimental setup

The experiments were performed in an open channel, with a length of 23.5 m a width of 0.495 m and a height of 0.50 m (Fig. 3.3). The walls and bottom were made of glass in order to have a hydraulically smooth boundary. The water was pumped from a buffer into the flume. At the

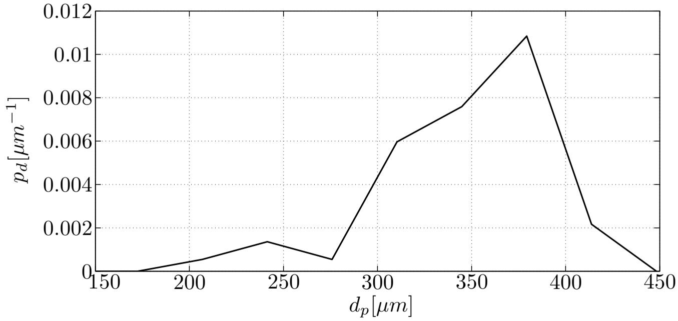

Figure 3.2: Histogram of the particle diameters of the polystyrene spheres

downstream side, the water level was controlled with an adjustable weir, followed by three pipes allowing the water to return to the buffer. In order to perform the fluid velocity measurements, the water was seeded with 10 μm hollow glass spheres ($\rho = 1100\ kg/m^3$).

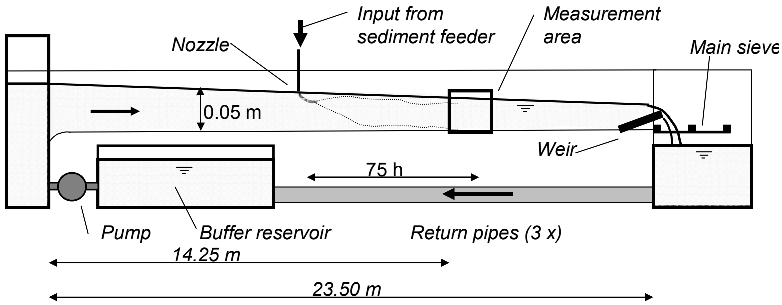

Figure 3.3: Experimental setup for the low concentration experiment.

The particles were fed to the channel with a particle feeder that consisted of two vessels (fig. 3.4). In the first vessel ($V = 80\ l$), a mixer was used to mix the particles with the water, using baffles and a specially adapted bottom shape to obtain a homogeneous mixture. This sediment mixture was pumped into a second smaller vessel, from which it was led into the channel. The concentration of the mixture after it had left the mixing vessel was measured with an infrared turbidity meter (Oslim) with a sample frequency of 10 Hz, in order to check the stationarity of the concentration influx. In order to obtain a constant mixture discharge, the water level in the second vessel was held constant by letting the surplus flow in a third vessel from which the mixture was pumped back to the mixing vessel. The sediment mixture entered the channel through a nozzle with an inner diameter of 1 cm at the channel's centerline and its center located at 0.7 cm below the free surface. The inflow velocity was manually adjusted to the channel velocity. Preliminary tests, in which the mixture flowing from the nozzle was collected for a concentration measurement showed that no demixing occurred in the second vessel and that concentration of the mixture coming from the nozzle was constant and correlated well with the turbidity measurement ($R^2 = 0.79$). Downstream of the weir, the sediment particles were collected using a sieve.

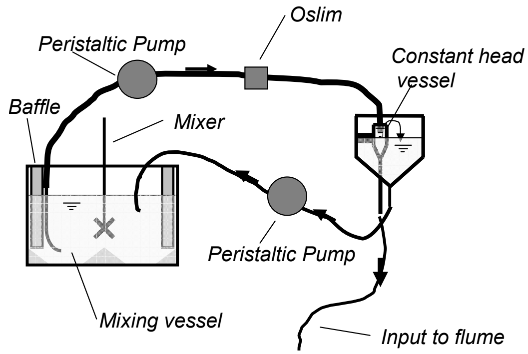

Figure 3.4: Equipment used for mixing sediment and introducing it into the flume.

The measurement section was located at a distance of 14.25 m from the channel entrance. At this location, a combination of both PIV and PTV was used to measure the velocities of the polystyrene particles and the fluid. A 50 mW double pulsed Nd-YAG laser was used to illuminate the particles in the measurement area. A light sheet was made with a cylindrical lens and two spherical lenses and its width was set to 1.0 mm with an adjustable slit. A 1 cm wide glass plate was put on the free surface in a streamlined device to let the laser light penetrate the free surface without being disturbed. Images were recorded with a Kodak Megaplus ES 1.0 1008×1018 pix^2, 15 Hz CCD camera with a 55 mm lens ($f\# = 2.8$ or 4). The time between the two image frames was adjusted to obtain particle displacements of about 25 pixel between two frames with the objective to increase the signal to noise ratio. In this situation, displacements of the particles with respect to the ambient fluid are still of the same order as the experimental accuracy, which is of the order of 0.1 pixel for the PIV algorithms used here. Note that the time between the frames is still significantly smaller than the Kolmogorov timescale, which means that the error made by approximating the particle movement as a straight line will be small. At the bottom of the measurement section, a 1 cm wide strip of absorbing fluorescent paint was applied in combination with an optical filter in front of the camera, to avoid laser light reflections from the bottom. For the calibration procedure, in which the physical dimensions of the measurement area matched with the dimensions of the image, we used a 7 cm wide white plastic plate with black markers on a regular grid with a typical spacing of 2.5 mm. This plate had its own foot piece, which was used to place it into the flow after the measurements at the location of the laser light sheet. Preliminary testing had shown that small deviations of the spanwise location hardly affected the calibration procedure as long as the plate was parallel to the flume walls.

3.2.3. Description of the experimental conditions

Different experimental situations were studied, which were all variations on a reference case. This basic case fulfills all the requirements defined in 3.2.1 for a direct comparison with a DNS, which means that the Reynolds number is 10,000. This is obtained with a flow velocity of 0.2 m/s and a water depth of 0.05 m. The sediment is suspended well, because $u_*/v_T \approx 5$, and it is introduced far enough upstream (160 water depths) for a fully developed situation to exist (see chapter 5).

Two sets of variations to this reference case were made. First, the Reynolds number was increased by increasing the flow velocity (leading to an increased u_*/v_T). Parameters for these experiments are shown in table 3.1. Secondly, the distance from the sediment introduction point was varied in six cases from 16 to 280 water depths, providing insight into the process of obtaining equilibrium conditions and into the length scales for the adjustment process. These cases are described in chapter 5. All conditions for these experiments are shown in table 3.2.

		Basic case		Increased flow velocity	
Dataset		CWF	$x_{in}/h = 160$	CWF	$x_{in}/h = 160$
$u_*\langle u'v'\rangle$	[cm/s]	0.91	0.92	1.66	1.66
$u_*\langle u\rangle$	[cm/s]	0.93	0.93	1.66	1.66
h	[cm]	4.96	4.96	4.8	4.8
T	[$^\circ C$]	19	19	18	18
Re_*	[-]	439	443	755	755
τ_{p+}	[-]		0.75		2.32
d_{p+}	[-]		3.13		5.51
u_*/v_T	[-]		4.3		8.3
Re_p	[-]		0.72		0.69
nr of files		1200	7500	1200	6000
nr of particles			47,400		59,193

Table 3.1: Experimental conditions of the various fully developed cases

Finally it was checked that introducing the sediment at only one spanwise location, which is not sufficient for laterally fully developed conditions to exist, did not cause any bias in the results. To do so, an experiment was performed, in which the sediment was introduced simultaneously at four different spanwise locations. The statistics from this experiment did not show any differences with the data obtained using only one injection point, when they were properly scaled.

For each case, measurements were done at a frequency of 15 Hz during 20 s and at 2 Hz during 150 s. In this second series, the time interval between two velocity measurements (0.5 s) was significantly larger than the Eulerian integral timescale, estimated as $h/\langle u\rangle \approx 0.25$ s for the $Re = 10,000$ case, which means that all velocity measurements in this set are statistically independent. Because of the large number of samples, the measurement period for a set was

Dataset		CWF	$x_{in}/h = 16$	CWF	$x_{in}/h = 20$	CWF	$x_{in}/h = 25$	$x_{in}/h = 35$	$x_{in}/h = 75$	CWF	$x_{in}/h = 280$
$u_*\langle u'v'\rangle$	[cm/s]	1.02	1.02	1.01	0.92	0.92	0.86	1.02	1.02	0.92	0.87
$u_*\langle u\rangle$	[cm/s]	1.03	0.98	1.01	1.01	0.95	0.95	1.00	0.99	0.95	0.89
h	[cm]	5.0	5.0	5.2	5.2	4.9	4.9	5.0	5.0	4.8	4.8
T	[$°C$]	20	20	20	20	19	19	20	20	17.5	17.5
Re_*	[-]	506	506	522	476	442	413	506	506	416	416
τ_{p+}	[-]		0.96		0.78		0.65	0.96	0.96	0.70	0.62
d_{p+}	[-]		3.56		3.21		2.93	3.56	3.56	3.01	2.85
u_*/v_T	[-]		4.68		4.22		4.05	4.68	4.68	4.51	4.26
Re_p	[-]		0.76		0.76		0.72	0.76	0.76	0.67	0.67
nr of files		1,200	4,500	1,200	3,600	1,200	2,700	4,500	4,500	1,200	6,000
nr of particles			27,936		105,584		50,385	63,405	34,785		29,900

Table 3.2: Experimental conditions of the various developing cases

about one and half hour. Before and after the measurement, the water levels were determined at five different locations in order to ensure that flow conditions had been stationary. For comparison, also four sets of 300 double images were recorded at a frame rate of 2 Hz for the flow in the channel, without the nozzle and any sediment input, which will be denoted as the clear water flow (CWF).

3.2.4. Phase discrimination for PIV/PTV application

Basically, two approaches can be used for the simultaneous measurement of particle and fluid velocities. Some investigations (e.g. Poelma, 2004) have used fluorescent tracers in combination with at least two cameras. Each phase scatters light of a different color, hence they can be recorded separately using an optical filter. In case the size difference between tracers and sediment particles is large enough, this property can be used for discrimination. Kiger & Pan (2000) used a median filter (basically a low-pass filter) to eliminate tracer images from a two-phase flow image. The tracer images were then obtained by subtracting the particle image from the complete image. They showed using synthetic images that the errors in the particle and fluid velocities by using this technique are below 0.1 pixel/frame, which is the typical accuracy of PIV. Khalitov & Longmire (2002) on the other hand determined the size and intensity for each particle and then used a threshold based on a histogram of these data to distinguish each particle separately based on their intensity and size.

In most investigations, the image size of the tracer is enlarged by either defocussing or using diffraction of the tracer's image in the diaphragm in order to obtain a tracer size of 2 pixels, which is the minimum needed to prevent peak locking (Raffel *et al.*, 1998). With a sediment particle image size of at least three times the tracer image size (Kiger & Pan, 2000), this leads to a required minimum particle image diameter of 6 pixels, which for our experiment results in a minimum particle size of 0.3 mm. This is fulfilled by the polystyrene particles that were used. Note that the enlargement of the tracer image size does not affect the dispersed phase images, as the depth of field of an object increases linearly with its size, which means that the dispersed particles are still completely focused.

We adopted the median filtering technique of Kiger & Pan (2000) in combination with defocussing as it is easily implemented and combines accurate results with low processing time. This algorithm consists of the following steps:

1. The recorded image (Fig. 3.5a.) is filtered with a median filter with a filter size of 7 x 7 pixels. This eliminates the tracer as well as small scale noise from the image, rendering the sediment particles only. From now on, the resulting image will be called the sediment image (Fig. 3.5b.).
2. The sediment image is subtracted from the original image. This leads to an image of the tracers. However, some leftovers of the brightest sediment particles are still visible in this image.
3. A median filter with a filter width of 7 pixels is applied to the subtracted image in order to determine the location of the sediment particle leftovers and is then subtracted from the result of the preceding step. The result is called the tracer image (Fig. 3.5c.).
4. A PIV algorithm (LaVision, 2002) is applied to the tracer image with first a 64 x 64 window (50 % overlap) and then two 32 x 32 window (final iteration with 75 % overlap) iterations. The results are post-processed with a median filter to eliminate vectors that differ significantly from their neighbors. This results in 126 x 126 vectors with distance of 0.37 mm between each other. The number of good vectors was about 90 %, compared to 95 % for data without sediment particles. Peak locking was found to be negligible as the histogram of the subpixel displacements did not show any abnormalities.
5. A PTV algorithm developed by Eindhoven University of Technology (van der Plas *et al.*, 2003) was applied to the sediment image. This algorithm uses the centroid of the particles to determine the particle velocities, where the mean velocity profile of the fluid from the PIV measurements was used as an initial guess for the particle velocities, with a maximal allowed deviation of 10 pixels/frame. Particles at the edge of the measurement area are eliminated, because they generally result from the inability of the median filter to eliminate tracers at the edge of the image. A histogram of the subpixel displacements of the particles showed negligible bias to integer displacements (peaklocking).
6. Errors due to lens distortion were eliminated with a third-order polynomial fit to a picture of a calibration grid. The final result is shown in (Fig. 3.5d.)

The algorithm differs from the method of Kiger & Pan (2000) from step 3 on. In the original method, the elimination of the sediment leftovers is left to the PIV post-processing. In the present investigation it is explicitly filtered out.

The centroid based PTV algorithm was used, because it is an easy and fast method, which appears to yield an accuracy comparable to more advanced methods (Poelma, 2004). We used some noise-free synthetic PIV images to confirm that this algorithm also performs well for over-exposed particle images.

However, accuracy tests using synthetic images might give a false impression of the accuracy.

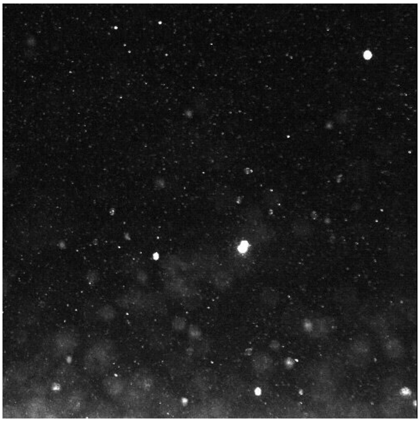

(a) Raw image with both sediment and tracers

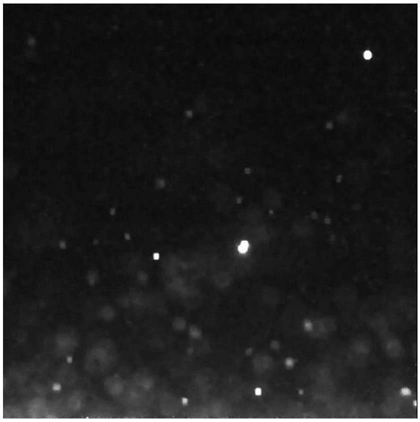

(b) Result of applying median filter

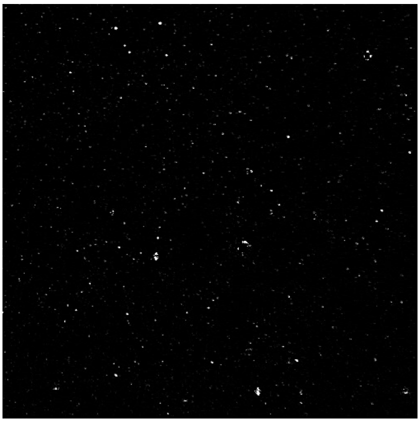

(c) Tracer image after eliminating sediment leftovers

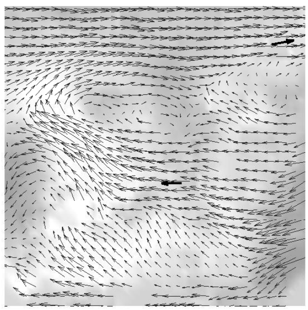

(d) Final calculated velocity field and sediment movement

Figure 3.5: Results of the image processing algorithm. The contrast in the images has been enhanced four times in (a) and (b) and eight times in (c). Therefore, even rather weekly illuminated particles appear bright.

When looking at true two-phase images (fig. 3.5a), these are obviously more complicated than synthetically generated two-phase flow images, as the former also shows many weakly illuminated particles and blurred spots. These are basically particles that are not in the laser light sheet, but that are illuminated by the reflected light from streaks of sediment on the channel bottom (Kiger, personal communication). Indeed, an experiment at a high velocity such that the streaks are no longer present, shows a decrease of optical disturbances.

The sediment particles that are not in the image plain should not be included in the PTV analysis, as the perspective error will cause them to have larger velocities when they are closer to the camera (and vice versa) thus leading to an apparent increase in particle turbulence. Moreover, they also lead to a wrong concentration profile. Therefore, the PTV processing was performed for various intensity thresholds until the sediment concentration normalized by the concentration at $0.30h$ did not change anymore (fig. 3.6). Additionally, we corrected the sediment images for the inhomogeneous light sheet by calculating the average intensity profile from the clear water flow and using the correction $I_{cor}(x,y) = \frac{I_{tracer,75}}{I_{tracer}(y)} I_0(x,y)$. Here, $I_{tracer}(y)$ is the average tracer intensity profile, $I_{cor}(x,y)$ and $I_0(x,y)$, the corrected and uncorrected image intensities respectively. $I_{tracer,75}$ is the intensity in the average tracer image, below which 75 % of the pixels are. Using only the tracer data for rescaling the light intensities of the sediment image does not cause any serious difficulties, because the variation in the light sheet intensity is expected to be the same for tracers only and a situation with a low sediment concentration. This approach would have been problematic if an increase in thickness and decrease in intensity of the laser light sheet would occur with increasing penetration due to the sideways scattering of light from the suspended particles. However, such an increase in light sheet thickness only occurs at concentrations that are one order of magnitude higher than in the present experiment (Poelma, 2004).

With the high enough threshold setting, the particle turbulence profiles did hardly change (less than 0.1 pix/frame in the rms velocities) with a further increase of the threshold. The concentration profiles measured in this way correlated well with those measured one meter downstream using an optical turbidity meter (Foslim).

3.3. High concentration experiment

In many sediment transport situations, the volume concentrations that are found can be rather large (up to a percent or more). With this regime, two-way coupling and even four-way coupling are expected to be important (see section 2.4), the occurrence of which make detailed experimental data highly desirable. Unfortunately, the use of optical techniques is not feasible at this high particle concentrations as the sediment-water mixture starts to become opaque. Therefore, detailed sediment transport experiments have been limited to rather low concentrations of the order of 10^{-4} (e.g. Best *et al.*, 1997; Muste & Patel, 1997; Kiger & Pan, 2002). The maximum

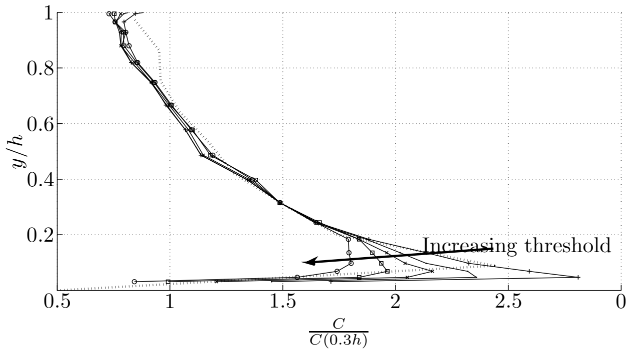

Figure 3.6: Normalized concentration profiles with different threshold settings for the PTV processing, where the threshold that was actually used had + signed markers. The concentration profile measured with the Foslim is shown as a dashed line.

concentrations that were reached in this way were of the order of 10^{-3}, (Righetti & Romano, 2004; Nezu & Azuma, 2004; Muste *et al.*, 2005), which is still an order of magnitude smaller than the ones found in practice.

In order to overcome the limitation of the current PIV/PTV technique to low sediment concentrations, refractive index matching (e.g. Budwig, 1994) was used. In this technique, the refractive index of either the dispersed or the continuous phase is adapted to match the other phase. In this way, a ray of light can pass any particle-fluid interface without refraction thus making the particles invisible. Yet, fluid velocity measurements are still feasible by using a non-matched tracer. The hydrodynamic effects of the invisible sediment particles on the fluid can thus be visualized.

Just as in the large scale experiment, we wanted to have experimental conditions that can be matched one-to-one with a direct numerical simulation (DNS) in which the particles are tracked through the Maxey & Riley (1983) equation. This yields once again the constraints that $Re_{*,max} \approx 500$ for using DNS, and $u_*/v_T \approx 5$, for particles to get suspended, where the particles should not be too small compared to the viscous sublayer (see 3.2.1).

In the present work, a high concentration refractive index matched experiment is performed, with the aim to demonstrate the feasibility of this approach for further research. This experiment will be limited to measuring the fluid flow properties under the influence of the high sediment concentration. Because it is only intended to measure the fluid velocities, and not simultaneously the particles velocities, no requirements were put on the size difference between the particle and tracer image. In the following, possible fluid-particle combinations for refractive index matching are described, followed by a description of the choices that were made for the used experimental setup and the matching procedure.

3.3.1. Refractive index matching materials

Various combinations of fluids and solid materials have been considered for the purpose of making a transparent suspension (see Budwig, 1994, for an overview). For the present experiment, we are limited to only those combinations that have similar properties as sediment in water, i.e. $\rho_p/\rho_f = O(1)$, $\nu_f \approx 10^{-6} m^2/s$, and for which particles in the sub-millimeter range are readily available. This leads to the following possible combinations:

- Borosilicate glass (Chen & Fan, 1992), fused silica or silica gel (Chen, 1991) can be used in combination with a sodium iodide (NaI) solution. This material is rather safe and not flammable, with the largest disadvantage the costs (± 100 EUR/l for the NaI solution). However, these costs are still manageable, when a small setup with a rather small volume of fluid is used. The densities here are 2100 kg/m^3 to 2400 kg/m^3 for the silicon based materials and 1600 kg/m^3 to 1800 kg/m^3 for the NaI solution. This means that particles of approximately 200 μm are needed, in combination with flow velocities of approximately 0.55 m/s. The smaller density difference between fluid and particles, makes the experiment easier to perform, because larger particles can be used to fulfill the scaling requirements. Because of the lower density difference, the Richardson number (see section 2.4.2, eq. 2.58) will be quite low and hence two-way coupling effects due to density stratification are expected to be rather weak.
  The iodide ions in the solution react slowly under the influence of light and oxygen forming I_3^- ions, which give a reddish color to the solution and limit its transparency. Hence, sodium thiosulphate ($Na_2S_2O_3$) has to be added to the solution in order to remove the I_3^- ions and to guaranty the transparency of the solution.
- Fluorinated Ethylene Propylene (FEP), a kind of Teflon with a refractive index of 1.338 in combination with a sodium chloride (NaCl) solution was considered for refractive index matching. The densities of the material are 1872 kg/m^3 and 1030 kg/m^3 respectively. This leads to an experiment with 130 μm particles ($U = 0.6\ m/s$) to fulfill the above requirements. The advantage of this material is that the materials are safe to use and that the NaCl solution's refractive index is not very sensitive to temperature variations, which makes temperature control easier. Preliminary tests to verify the feasibility for refractive index matching, did not result in complete invisibility of the FEP grains. Moreover, the FEP is sold as 2 mm pallets, rather than powder and grinding resulted in fibers instead of spherical particles. Furthermore, suspending the FEP fibers in the water appeared very difficult due to the material's hydrophobic properties. Therefore, it was considered not suitable for the present experiment.
- Glass spheres in a benzyl alcohol/ethanol solution has been used for refractive index matching with a refractive index of 1.51 (Cui & Adrian, 1997; van Wageningen, 2006). The densities of the material are 2450 kg/m^3 and 950 kg/m^3 respectively. To fulfill the above specification, particles of 150 μm should be used ($U = 0.75\ m/s$). The main disadvantage of this material is that the benzyl alcohol is hazardous when inhaled and

flammable. This means that ventilation is necessary and a spark-free pump needs to be used. Moreover, the ethanol has the tendency to evaporate, making it difficult keep the experiment stable for longer periods.

- Perspex (PMMA) or glass in combination with Paracymene (Haam *et al.*, 2000) or turpentine/tetralin (Liu *et al.*, 1990), have characteristics and disadvantages very similar to a benzyl alcohol/ethanol solution.

From the preceding, a NaI solution seems the best working fluid for our laboratory application. Preliminary refractive index matching tests with Borosilicate glass spheres were unsuccessful, due to the presence of small air bubbles inside these spheres, which probably are a remainder of the production process. Therefore, we performed the experiment with somewhat amorphous (the shape actually was rather similar to those of natural sand particles) silica gel particles with a diameter of 360 μm and a fall velocity of 7.0 mm/s.

3.3.2. Fine tuning of the refractive index matching technique

To match the refractive index as accurately as possible, different techniques have been proposed in the literature. Many of them rely on having a larger sample of the material such as a rod or a plate, and then use the lens like properties (van Wageningen, 2006) or the light reflections (Budwig, 1994) of this material. For granular materials, these methods are only possible if a sample with a larger size can be obtained.

A method that is specially suited to granular materials is the measurement of the turbidity of a sample (Koh *et al.*, 1994) with a photo diode. In this method, the quantity that is measured (the turbidity) is also the one that determines the feasibility of the experiment. This method is therefore adopted here. We sent the laser beam through a small fluid-sediment sample (4 cm x 4 cm x 4 cm) with different sodium iodide concentrations and we measured the turbidity of the mixture as function of the sodium iodide concentration to determine the optimal one for the experiment. In this way, the refractive index of the solution could be matched well to the one of the silica gel. In such a well matched solution, the silica gel particles become completely invisible (fig. 3.7). It was estimated that the refractive index of the silica gel and the solution differed at most 3 10^{-4} in the experiment. After the $C_{vol} = 0.4\%$ experiment, a camera calibration was performed using a picture of a calibration grid in the sediment laden flow. This calibration yielded the same results as a clear water calibration before the experiment, thus showing that the optical disturbance by the suspended silica gel particles was indeed minimal. However, it appeared in the PIV images, that the light intensity scattered from the tracers had decreased significantly when the silica gel was added and that the tracer particle images had become blurred. At higher concentrations, the scattered light intensity was not sufficient, which resulted is an increased peak locking. Apparently, the small refractive index mismatch between silica gel and NaI solution had a stronger effect on the very small tracer particles than on the larger calibration grid image.

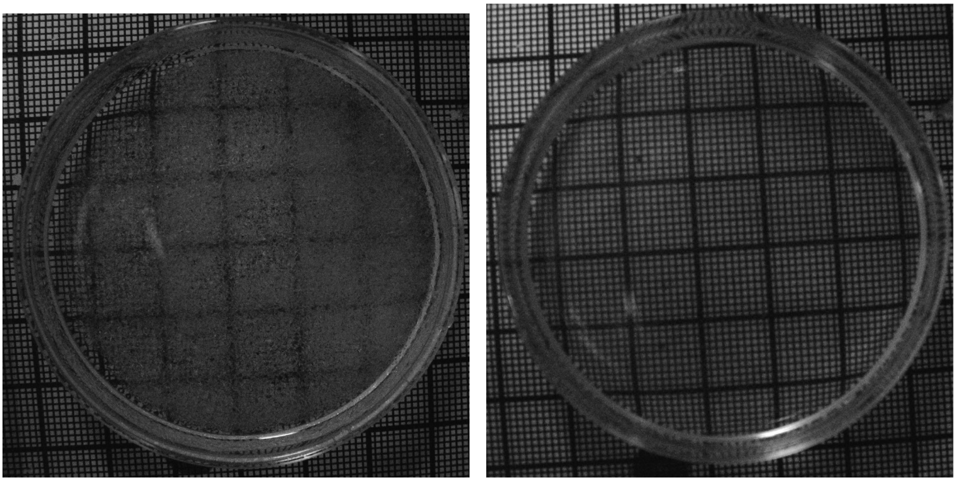

(a) Silica gel in water (b) Silica gel in RI matched NaI solution

Figure 3.7: Comparison of the optical disturbance of an eight millimeter silica gel layer in a (a) non-matched and (b) matched solution.

3.3.3. Experimental setup

As can be seen in section 3.3.1, the settling velocity of the silica gel particles is significantly higher than the one of polystyrene in 3.2, which means that higher flow velocities need to be used. In order to keep the Reynolds number low enough, smaller water depths have to be used resulting in supercritical flows ($Fr = u/\sqrt{gh} > 1$). However, this decreased water depth is required anyhow in order to keep the fluid volume limited, which is required for the control of the refractive index (i.e. the temperature) and to keep the costs manageable. This is not a serious disadvantage, because turbulence statistics do not differ significantly between subcritical and supercritical flows (Nezu & Nakagawa, 1993), except near the free surface, where the vertical velocity fluctuations are increased because of the stronger waves that exist at the free surface in supercritical flows.

For this experiment, a new flume was designed and built (figure 3.8), with a length of 3 m, and height and width of 10 cm, with the side walls and the bottom made of glass, to allow for optical access. In order to make the water depth in the experiment low enough, a control gate was placed at the upstream side, and the flume was placed on two in height adjustable supports, in order to get an inclined bottom. The typical experimental water depth is 2 cm, which gives a B/h ratio of 5. To prevent any disturbances at the inflow, a honey comb, was placed just downstream of the control gate. To keep the volume of fluid and sediment needed for an experiment as small as possible, the flume was designed to recirculate the sediment particles as well. Therefore, a torque flow pump was used and care was taken to eliminate all location were sediment could deposit. For temperature control ($\pm 0.1°C$), a 750 liter vessel of water (2.1

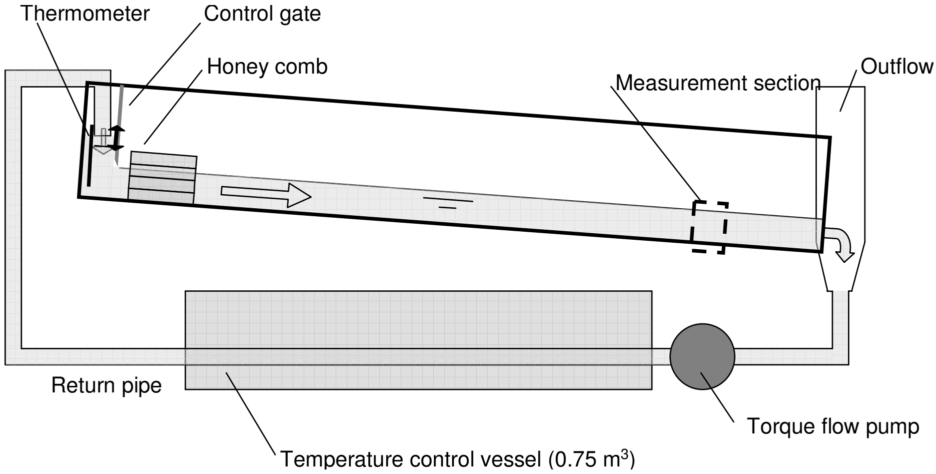

Figure 3.8: Experimental setup for the refractive index matching experiment

m x 0.6 m x 0.6 m) was placed downstream of the pump, through which a stainless steel return pipe (inner diameter of 4 cm) was running. A digital platinum thermometer with an accuracy of $\pm 0.01°C$ is used to monitor the temperature at the flume entrance. Water levels in the flume are measured from a connection made in the side walls of the flume, that are constructed every 0.50 m at a height of 1 cm above the flume's bottom.

The measurement section is located at 2.75 m from the inflow section, i.e. at 135 water depths, which appears long enough to get a fully developed situation. Here PIV was used to measure the fluid and turbulence properties, with a measurement frequency of 15 Hz, which is high enough for each double image pair to be statistically independent ($T_E \approx h/U = 0.04\ s$, $T_{sample} = 0.067\ s$). The laser light is directed upward through the flume's bottom with a mirror. It appeared that the refractive index matched silica gel, sometimes still scattered a large amount of light, which impeded good measurements. In order to circumvent that problem, fluorescent melamine resin based polymer coated with Rhodium B ($d_p = 10\ \mu m$, $\rho_p = 1500\ kg/m^3$) were used as flow tracers in combination with a 550 nm high pass optical filter in front of the camera. These tracers have a maximum light absorption at 550 nm and a maximum emission at 590 nm. Suspended in a high density fluid, the tracer particles have a rise velocity of 2 $\mu m/s$ and a particle time scale of 6.7 $10^{-6} s$, which both can be considered negligible and hence these particles serve as proper fluid tracers.

The flow velocity in the experiments was 0.6 m/s, with a fluid depth of 16 mm in the measurement section, yielding $Re_* \approx 700$. A 49.4 % NaI solution was used as working fluid, for which we measured a density of 1581 kg/m^3. Details of the matching procedure used to determine this concentration are described in section 3.3.2. This fluid has a refractive index of 1.447 at 16 $°C$ for light of 532 nm wave length (calculated with the empirical expression of Narrow

		Exp 01		Exp 02		
		CWF	conc03	CWF	conc01	conc02
$u_*\langle u\rangle$	$[cm/s]$	2.7	2.97	2.9	2.8	2.7
$u_*\langle u'v'\rangle$	$[cm/s]$	2.8	2.9	3.0	2.9	2.9
h	$[cm]$	1.6	1.6	1.6	1.6	1.6
Re_*	$[-]$	412	389	453	439	445
T	$[°C]$	15.8	15.8	16.6	16.6	16.6
τ_p	$[-]$		5.60		5.94	5.94
d_p+	$[-]$		8.44		8.76	8.76
u_*/v_T	$[-]$		4.09		4.17	4.17
Re_p	$[-]$		2.07		2.10	2.10
C_{mass}	$[\%]$		0.76		0.24	0.49
C_{vol}	$[\%]$		0.67		0.21	0.43
ρ_p/ρ_f	$[-]$		1.14		1.14	1.14
nr of files	$[-]$	1200	1200	1200	1800	1800

Table 3.3: Experimental conditions of the various high concentration cases

et al., 2000). The viscosity of this fluid was $\nu_f = 1.2\ 10^{-6}\ m^2/s$ (calculated with the method of Abdulagatov *et al.*, 2006), which in very similar to the viscosity of water. The silica gel particles were sieved to a range of $300 - 425\ \mu m$, and have a material density of 2240 kg/m^3 and a refractive index of 1.44. However, silica gel is porous and absorbs fluid. Therefore, the density of the particles in the experiment (i.e. of the particle with voids and the fluid the particle had absorbed) reduced to 1802 kg/m^3. This value was determined by determining the porosity inside the particles from the materials bulk density, the estimated void fraction and the silica gel's material density. Subsequently, the porosity inside the particles that is not filled with fluid was measured. With these data, the density of the particles can be estimated as the mass of the particles and the absorbed fluid divided by the volume of the non-filled pores, the pores filled with fluid and the silica gel. Using this value for the particle density, the settling velocity of these silica gel particles in a sodium iodide solution was calculated to be 6.7 mm/s, which agreed well with the measured value of 7.0 mm/s . In the experiment $u_*/v_T \approx 5$. Three different cases were measured, with volume concentrations ranging from 0.22% to 0.67%. The latter was the upper limit for a useful transparent suspension. Detailed data of the experimental cases are shown in table 3.3.

The PIV images were processed with a multiple iteration 32 x 32 pixel 75 % overlap interrogation window, yielding 127 x 113 velocity vectors with a distance of $y+ \approx 4$. The velocity data were post-processed using a median filtering technique.

3.4. Data post-processing

3.4.1. Statistics

In this work, statistics of the fluid velocities were calculated from the PIV vector fields by averaging over all PIV images, which were taken with a time interval that was large enough for each image to be statistically independent of the previous one. From images of the average velocity and turbulence fields, it was verified that the flow was homogeneous and that velocity and turbulence gradients in the streamwise direction were zero (up to experimental precision). Then averages were taken over all data rows in the flow field in order to obtain profiles of mean flow and turbulence.

For the sediment particles, profiles of a quantity X were calculated on an irregular grid by taking averages over all particles in a bin (here n_p is the number of particles):

$$\langle X \rangle_p = \frac{\sum_i n_p X_i}{\sum_i n_p} \tag{3.1}$$

It is easy to see that the averages obtained in this way correspond to the concentration weighted averages used in the two-fluid model equations (see section 2.3.2). Note that because even in the high concentration cases, the concentration were that low that $1 - C \approx 1$. Therefore, the obtained averages of the PIV velocity fields were equal to the density weighted fluid field averages.

A vertically stretched grid was used to calculate the particle statistics, in order to anticipate as well as possible with the irregular distribution of the particles. It was stretched such that the grid cells were larger, where the concentration gradient and the number of particles were smallest (the latter was used in order to obtain a sufficient numerical convergence). The elevation of the edges of the grid cells (y_{grid}) were defined using a hyperbolic tangent, that was the same as used in the DNS simulations (section 4.4):

$$Y_{grid} = h\left(\frac{\tanh \alpha y_k}{\tanh \alpha} + 1\right) \tag{3.2}$$

$$y_k = \frac{k}{N} - 1 \tag{3.3}$$

$$k = 0..N+1 \tag{3.4}$$

Here N is the number of grid cells ($N = 20$), h the height of the PIV interrogation window (rather than the complete water depth) and α a coefficient ($\alpha = 1.7$). Note that for the developing case ($x_{in}/h = 16$, table 3.2), where most particles were near the free surface, the grid was turned upside down to have the largest grid spacing near the bottom.

Sediment concentrations were calculated by counting the number of particles in a grid cell, and then dividing by the volume of the grid cell.

Bicubic interpolation was used to obtain fluid velocities at the particle locations. A comparison to the results obtained from bilinear information did not show different results.

In order to check the statistical convergence a percentile bootstrap using 200 iterations was performed on the PIV data of the CWF of the $x_{in}/h = 160$ case (table 3.1) and on the PTV data of the particle-laden $x_{in}/h = 160$ case. The results for the fluid showed that with 95% confidence $\langle u_f \rangle_f$ is within ±0.1 % of the measured value (for the complete profile), $\langle v_f \rangle_f$ within $\pm 0.004 u_*$ (for the complete profile), $\langle u_f'^2 \rangle_f$ within ±0.5 % (for $y/h < 0.9$), $\langle v_f'^2 \rangle_p$ within ±0.5 % (for $y/h < 0.9$), and $\langle u_f' v_f' \rangle_f$ within ±2 % (for $y/h < 0.9$). For the particles, $\langle u_p \rangle_p$ is within ±0.5 % of the measured value (for $y/h > 0.1$), $\langle v_p \rangle_p$ within $\pm 0.05 u_*$ (complete profile), $\langle u_p'^2 \rangle_p$ within ±4 % (for $y/h < 0.8$), $\langle v_p'^2 \rangle_p$ within ±4 % (for $y/h < 0.8$), $\langle u_p' v_p' \rangle_p$ within ±15 % (for $y/h < 0.8$) and C within ±6 % (for $y/h < 0.9$). Because of the lower reliability of the data near the free surface (in combination with the bias due to the boundary layer from the glass plate on the free water surface) and near the bottom, the data in these regions was eliminated from the plots.

The two-dimensional histograms in chapter 6 were calculated using a kernel estimation technique with an quadratic Epanechnikov (1969) kernel. The bin spacing in the histogram was $0.45 u_*$ for the streamwise velocity fluctuations and $0.23 u_*$ for the vertical velocity fluctuations (using 61x61 bins to approximate the two-dimensional probability density function).

3.4.2. Vortex eduction

In the present work, vortices are detected with the aid of swirling strength λ_s (Zhou *et al.*, 1999). This is a fast and easy to use method to determine for each point in the measurement area whether the streamlines show a rotational pattern. It has the advantage compared to using the vorticity that it is not sensitive to shear layers, but only highlights rotational flow patterns. The swirling strength is defined as:

$$\lambda_s = -\min\left(\frac{\partial u_y}{\partial x}\frac{\partial u_x}{\partial y} - \frac{1}{2}\frac{\partial u_x}{\partial x}\frac{\partial u_y}{\partial y} + \frac{1}{4}\left(\left(\frac{\partial u_x}{\partial x}\right)^2 + \left(\frac{\partial u_y}{\partial y}\right)^2\right), 0\right) \tag{3.5}$$

The above analysis also shows that the rotation rate increases if the complex part of the eigenvalue increases. Thus the actual value of the swirling strength has a physical meaning in that the strongest vortices will have the highest swirling strength. Also, it is clear that swirling strength does not indicate the direction of the rotation. When this was required, the sign of the vorticity ω_z was used to determine this.

Good results have been obtained using this method (Zhou *et al.*, 1999). However, there are still some differences between a vortex and a point with large swirling strength. A vortex is expected to to cover a minimum area where the swirling strength is high. In the present analysis, no distinction is made between vortex with a large and a small extend.

The swirling strength was calculated from the gradients of the fluid velocity field. These were calculated with a central difference scheme on the PIV fluid velocity fields, which were first filtered with a 3×3 Gaussian filter in order to decrease the influence of noise.

3.4.3. Linear stochastic estimation

Conditional averaging is a widely used tool in turbulence research for the eduction of turbulent structures. Unfortunately, statistical convergence of such conditional averages is quite slow, because only part of the data can be used. One way to overcome this problem is the use of Linear Stochastic Estimation (LSE; see Adrian, 1994, for a review).

In linear stochastic estimation, the conditional averages are calculated from correlation functions. This has the advantage that the complete dataset is used to calculate the conditional averages, since the complete dataset is also used in the calculation of the correlation functions. A derivation of the equations used for calculating the LSE is given in appendix B. This technique is used to calculate the velocity field in the vicinity of a vortex head, where the swirling strength (section 3.4.2) was used as a condition for the occurrence of a vortex head. Hence the calculated conditional average is $\langle u_i'(\vec{x}_0 + \vec{r}) | \lambda'_{s,cond}(\vec{x}_0) >$. Because the LSE is linear in the condition $\lambda'_{s,cond}$ (appendix B), the exact value for this quantity is not important. It merely acts as a kind of threshold, and therefore a value of $\lambda_{rms}(\vec{x}_0) = 1\ m^2/s^2$ was used. Note that because of homogeneity in the streamwise direction, the standard deviation and correlation function do not change with x and therefore, only a reference height y_0 has to be chosen, rather than a reference point $\vec{x}_0$. The necessary correlation functions were calculated for each PIV velocity field and then averaged over all realizations.

In order to illustrate this technique, the LSE for the streamwise and wall normal velocity fluctuations are plotted together with the corresponding correlation functions in fig. 3.9a and b. It is clear that these correspond. In fact, the LSE is nothing more than the correlation between the fluid velocity field and the swirling strength weighted with the root mean square velocities. The two LSE estimates are combined in fig. 3.9c and in this way, the complete conditionally averaged velocity fluctuation field in the presence of a vortex is obtained.

In this thesis, this technique will be used to consider the flow structures with the capacity of transporting sediment particles up or down. To this end, this methodology will be applied to the drift velocity (i.e. the fluid velocities at the particle locations, see section 2.3.2), in chapter 6. In this way the spatial structure and characteristics length scales of the flow structures for particle transport are encountered. Furthermore, the structures in the complete velocity field are determined for comparison to those structures found responsible for the vertical particle motion.

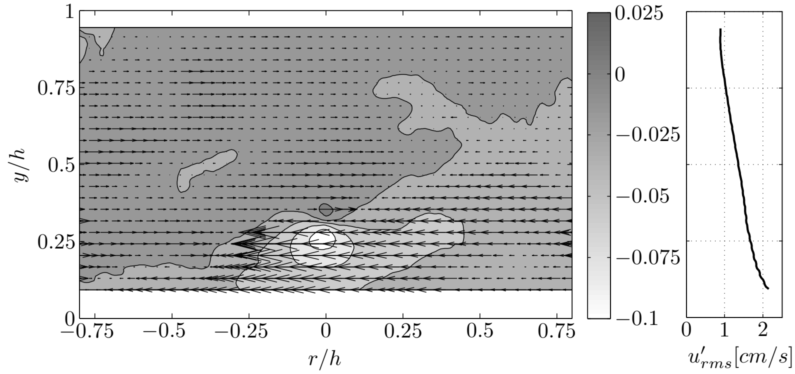

(a) streamwise fluctuations

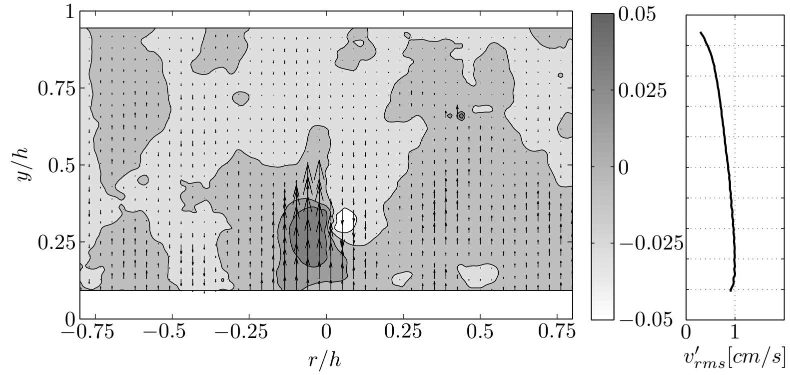

(b) wall normal fluctuations

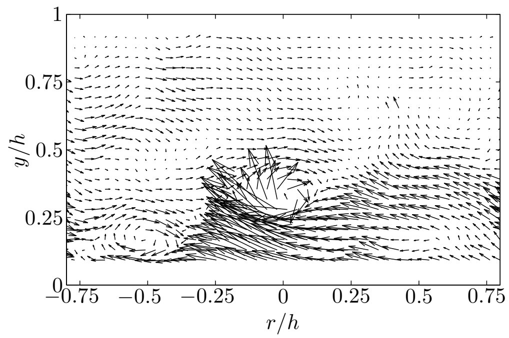

(c) complete conditional average

Figure 3.9: (a) and (b): Correlation contours ($y_0/h = 0.23$) between velocity fluctuations and swirling strength in combination with conditional velocity estimate (arrows). Also shown is the corresponding rms velocity profile. (c): Complete conditional velocity estimate (arrows).

Chapter 4

Fully developed transport of suspended sediment in open channel flow

4.1. Introduction

In the past, many experiments were performed in order to obtain data of suspended sediment concentrations (one of the earliest was Vanoni, 1946). These data were used to validate simple suspended sediment transport models (such as the Rouse equation; eq. 2.32) or for obtaining empirical relations to predict sediment concentrations or fluxes. Almost all of these experiments were limited to (approximately) fully developed conditions, where the suspended sediment was given a sufficient distance to develop toward an equilibrium distribution. However, in many real world problems, situations out of equilibrium are important. Therefore, we will perform an investigation to suspended sediment transport outside equilibrium conditions in this thesis (chapter 5). However, before studying non-equilibrium suspended sediment transport, we will first study equilibrium suspended sediment transport, because of the following reasons:

- It is a simple configuration, which allows for straightforward data acquisition.
- It provides a reference to which the results in non-equilibrium situations can be compared.
- It can be easily compared to the result of previous suspended sediment transport investigations in the literature.
- It is easier to model using simple models (such as the Rouse equation) or complex models (such as DNS simulations).

Apart from laboratory and field investigations, detailed numerical simulations can be used to obtain an understanding of the physical processes occurring in suspended sediment transport processes. A combination of direct numerical simulation (DNS) and particle tracking has been successfully applied many times for the simulation of particle transport in gases (e.g. Uijttewaal & Oliemans, 1996; Portela *et al.*, 2002). The use of DNS has some clear advantages when performed in addition to experiments. Especially for the verification and parametrization of two-fluid models (see chapter 2), the DNS has the advantage that the closure terms can be determined straightforwardly from the resolved fluid and particle motion, whereas they are (virtually) impossible to determine from experiments. In this way, the significance of the variations in the momentum balance of the particle and fluid phase can be assessed, and different models can be tested for relatively poorly understood processes (such as lift forces, see section. 2.2.1). However, as far as we know, this approach has never been applied to suspended sediment transport, and thus one cannot be sure that the results of these models represent the physics accurately. This is especially true for the particle motion, because there is still a significant amount of simplifying assumptions involved in the sense that a particle is considered to be a point-particle that should have a diameter significantly smaller than the Kolmogorov length scale. However, in suspended sediment transport processes, the particles have similar dimensions as the Kolmogorov length scale, thus they are not strictly point-particles. For this reason, the experiment was set-up in such a way that a direct comparison with a particle laden DNS is possible. A preliminary comparison is performed, focusing on the sediment concentration profile and using the experimental data of this chapter to provide recommendations for the comparison between DNS and experiments.

Much of the published research focuses on three problems: the vertical transport processes far from the wall due to turbulent diffusion, the entrainment of sediment from the wall, and the effects of high sediment concentrations on the flow. The most studied of these are the vertical suspended sediment transport process at low sediment concentrations far away from the wall (e.g. Vanoni, 1946; Nezu & Azuma, 2004). In section 2.3, it was shown that the upward sediment flux can be modeled by a gradient diffusion process, with the diffusion coefficient proportional to the eddy viscosity. In many investigations it was found that the coefficient of proportionality between these two (usually denoted as β) differs from one (Cellino & Graf, 1999; Muste *et al.*, 2005; Nezu & Azuma, 2004), but no conclusive value has been found and no convincing physical argument has yet been given why β should be either smaller or larger than one. In section 2.3.3, various hypothesis for the relation between the turbulent diffusion of streamwise momentum and suspended particles are given, two of which will be validated in this chapter. Additionally, it was shown in section 2.3 that the streamwise velocity of the fluid and the particles do not need to be equal, and indeed this was found in many recent experiments (Best *et al.*, 1997; Muste & Patel, 1997; Righetti & Romano, 2004; Kiger & Pan, 2002). In section 2.3.1 it was shown that the velocity difference is related to the particles being located in flow structures with a different velocity than the average flow velocity. This will be investigated in this chapter.

The second problem that arises when modeling sediment transport is the determination of a reference concentration for the near bed suspended sediment concentration (see e.g. Van Rijn, 1984; García & Parker, 1991). In this chapter, the reference concentration will not be investigated explicitly, for two reasons. First, because the resolution and accuracy of the experiment near the bed are not sufficient for high quality data (see section 3.2). Second, because this experiment is not representative for conditions in the field, where the bed consists completely of sediment, whereas in the experiment, it was only partly covered with sediment in one case (see 4.3.1) and not covered at all in the other case. However, because of the difference in bed coverage, we can investigate the influence of the near bed behavior on the sediment turbulence interaction higher in the water column indirectly. More specifically, we want to know whether or not the bed load layer and the suspended sediment transport layer are coupled in any other way than that the bed load layer provides a flux to the outer layer, which can be schematized by providing a reference concentration at a fixed distance from the wall.

The third problem in modeling suspended sediment transport is to determine the influence of the increase of the suspended sediment concentrations on the physical processes and their influence on the particle concentration and the fluid velocity profile (e.g. Coleman, 1981; Best *et al.*, 1997; Cellino & Graf, 1999). According to the theory discussed in section 2.4, the concentrations in the experiment in this chapter are too low for any two or four-way coupling effects to be present, and this will be verified in the present chapter. An experiment with concentrations high enough for two and four-way coupling to be present, will be addressed in chapter 7.

From the previously discussed, we distill the following the objectives of the research presented in this chapter:

- To investigate sediment-particle interaction in a fully developed situation with the focus on the processes occurring away from the bed. In specific the influence of the parameter u_*/v_T is investigated, as well as the effect of the difference in the near bed behavior on the sediment-turbulence interaction higher in the water column.
- To provide material for comparison with non-fully developed situation (addressed in chapter 5).
- To present experimental data of a suspended sediment transport that can be compared directly to a particle laden DNS (without any scaling) and perform a preliminary comparison.

In this chapter, first the experimental setup and parameters of the different cases are presented very briefly. This is followed by a presentation of the results starting with a discussion of the occurrence of streaks of sediment on the bottom of the flume in the two different cases. Then, the measured velocity velocity profiles are discussed, with the main emphasis on the difference between the streamwise fluid and the particle velocities. The turbulence profiles of fluid and particles are studied next. In a subsequent section, the concentration profile and drift velocities are studied, verifying two hypotheses given in section 2.3.3 for the difference between the turbulent transport of momentum and sediment particles. Finally, a short discussion of the comparison between DNS and experimental data is given.

4.2. Experimental setup and parameters

In this chapter, the experiments in a fully developed situation are discussed. In these experiments, the particles are introduced sufficiently far upstream of the measurement section, that a fully developed situation occurs. The experimental setup is described in section 3.2. We will compare two different cases (table 3.1), using the same particles and water depth, but different flow velocities. The two different cases with $u_*/v_T = 4$ and $u_*/v_T = 8$ will in the following be respectively referred to as the “low velocity case” and the “high velocity case”. The different flow velocities lead to differences in two dimensionless particle properties: u_*/v_T and $d+$. Both these parameters double in the high velocity case. The physical importance of these parameters is that the first determines the strength of the turbulent diffusion process and that the latter determines the size of the particle with respect to the viscous sublayer, which has a large influence on the lift of the particles from the wall. Note that the increase in other non-dimensional parameters (Re and St) is less important here since these parameters essentially remain in the same regimes ($Re > Re_{crit}$, $St \ll 1$).

4.3. Results

4.3.1. Bottom streaks

The two velocity cases that were studied differ substantially in the near-bed behavior of the sediment particles. Visual observations showed that in the low velocity case, the bottom of the flume was partially covered with sediment (fig. 4.1), whereas in the high velocity case all the sediment was in suspension and no sediment could be seen on the bottom of the flume. In the former case, the sediment at the bottom was not randomly distributed over the bottom of the flume, but rather it occurred in streaks with high sediment concentrations that were separated by areas without any sediment. Such streaks were also observed by Rashidi *et al.* (1990); Kaftori *et al.* (1995a); Niño & García (1996) and Kiger & Pan (2002). The streaks were not stationary but showed movements in the spanwise direction. The streaks had a very large streamwise extend. Visual observations showed that eventually, they covered the complete flume. Camera recordings showed that each streak remained visible during the complete recording time (of approximately 30 minutes, which corresponds to 350 T_E). This agrees with the findings of Hutchins & Marusic (2007), who studied the streamwise extend of the flow structures near the wall in a turbulent boundary layer and found that they can have very large dimensions (up top 20 times the boundary layer thickness), but such values are normally not found in measurements of velocity correlation functions, because these structures tend to meander in the spanwise direction.

In order to understand the reason of the difference in the near-wall behavior between the two cases, we study the lift force on the particles in the near wall layer. Using eq. 2.22, we can write the following equation for the ratio between the lift force and the net gravitational force on a particle at the wall:

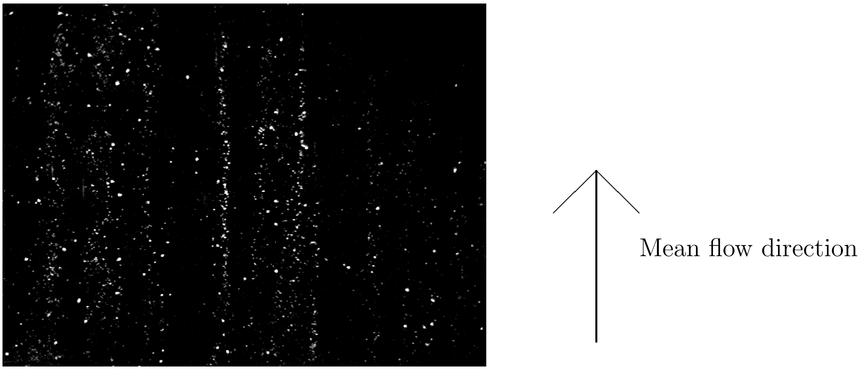

Figure 4.1: Example of streaks occurring in the low velocity case as seen from above. Image enhancement was performed by subtracting a background image taken without sediment transport.

$$\frac{F_l}{F_g} = \frac{0.576\rho_f d_p^4 (du_f/dy)^2}{1/6\pi d_p^3(\rho_p - \rho_f)g} \tag{4.1}$$

At the center of the particle (which was in both cases inside the viscous sublayer see table 3.1), this reduces to:

$$\frac{F_l}{F_g} = \frac{3.46 d_p u_*^4}{\pi \Delta g \nu_f^2} \tag{4.2}$$

For the $u_*/v_T = 4$ case $F_l/F_g = 0.28$, whereas for the $u_*/v_T = 8$ case $F_l/F_g = 2.9$. Thus the flow is that strong that in the latter case, the particles cannot remain on the bed and this explains the different near bed behavior (occurrence of near bed streaks at the lower velocity case, whereas no streaks on the bed are found in the latter case).

The different near-wall behavior between the two cases can give important information on the importance of the sediment transport in the near wall layer, which we will call the “bed load layer” from now on, on the sediment transport in the outer layer, which is defined as the part of the water column outside the bed load layer. Note that the thus defined outer layer does not necessarily have to be the same as the outer layer in turbulent boundary layer flows. It is commonly assumed that bed load and suspended load are decoupled in the sense that the physical processes in the bed load layer do not determine the shape of the concentration profile in the outer layer, but only the near bed reference concentration. This is usually modeled by applying a reference concentration at a certain height away from the wall (eq. 2.32), which is assumed to be the top of the bed load layer. Here we can investigate whether or not these two layers are in fact decoupled, because the two situations have a completely different bed load: non-zero in the low velocity case and zero in the high velocity case. This distinction will be applied in the rest of this chapter.

4.3.2. Mean velocity

In fig. 4.2, the mean streamwise velocity profiles of the fluid and the particles are shown in inner coordinates for both u_*/v_T cases. The friction velocity that was used to normalize the data (table 3.1) was determined by fitting a logarithmic velocity profile (eq. 2.6) to the data. In this figure, the fluid velocity of the corresponding clear water flow and the logarithmic velocity profile (eq. 2.6) are also shown. It shows that the measured fluid velocity profiles agree well with the logarithmic velocity profile. This agreement extends over the whole water depth, rather than only to the logarithmic layer (from $y^+ = 30$ to $y/h = 0.2$). This is in agreement with the results of Nezu & Rodi (1986), who found that for low Reynolds numbers, the velocity data agree with eq. 2.6 for the largest part of the water column.

Furthermore, fig. 4.2 shows that the particle velocity is clearly lower than the fluid velocity in the low velocity case as well as in the high velocity case. The difference between the particle and fluid velocity will be discussed further in this section, when the profile of relative velocity is discussed.

Some small differences are found between the fluid velocities in the particle laden flow and the clear water flow. These differences might be related to two-way coupling effects. The most important reason for two-way coupling in these kind of flows is the increased apparent bed roughness due to the addition of the sediment particles (Kaftori *et al.*, 1998). This means that in the present experiment, we would only expect an effect for the $u_*/v_T = 4$ case, because in the $u_*/v_t = 8$ case, there were no sediment particles on the bottom of the flume (section 4.3.1). If there were any effects of increased bottom friction, one would find an increased friction velocity. Such an increase was however not found (see table 3.1). Furthermore, one would expect the velocity profile in the sediment laden flow to be below the clear water flow, which is not visible in fig. 4.2. If any effect can be seen it this figure, it is an increase in the fluid velocity in the sediment laden case. Higher in the water column, the concentrations in these cases are too low to cause substantial two-way coupling effects (section 2.4.2). Thus it seems that the differences can be explained by experimental uncertainties. Note that a comparison between the two fluid velocities is more ambiguous than the comparison between the fluid and particle velocity profile, because for the former comparison, a different value of u_* needs to be determined for each case. The plotted velocity profiles are very sensitive to the value of u_*, and even a small error can give relatively larger effects. The velocity and particle profile use the same friction velocity, and thus the difference between the two profiles is only to a limited extend influenced by this error.

The profiles of the relative velocity between particles and fluid are shown in fig. 4.3. Here, the average relative velocity u_{rel} is defined as $u_{rel} = \langle u_p \rangle_p - \langle u_f \rangle_f$. The relative velocity indicates

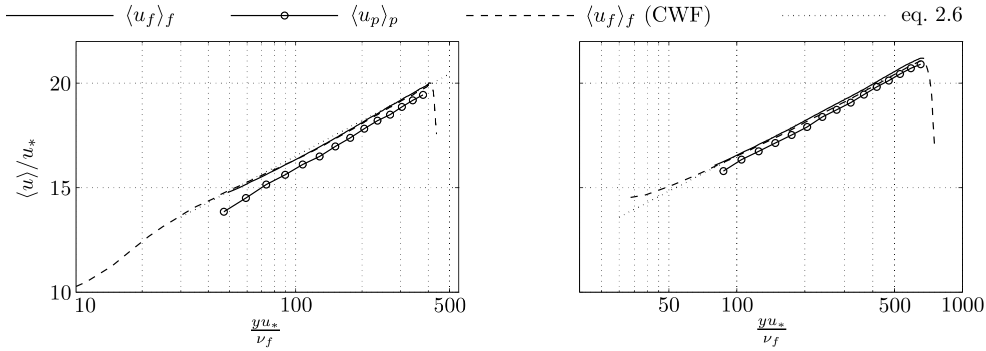

Figure 4.2: Mean streamwise velocity profiles of fluid, particles and corresponding clear water flow. Left: $u_*/v_T = 4$; Right: $u_*/v_T = 8$;

a difference in the average velocity of the two phases. However, it does not necessarily provide information about the instantaneous velocity differences (the slip velocity) between the two phases. As already mentioned before, the particles lag the fluid in the streamwise direction. The velocity difference (scaled with u_*) is larger for the low velocity case (approximately $0.5u_*$) than in the high velocity case (approximately $0.3u_*$). The velocity difference is rather constant over the water column, but increases close to the bed. These results are in line with those found in literature with respect to the magnitude of the velocity differences and the decrease of the relative velocity with increasing u_*/v_T. Kaftori *et al.* (1995b) presented a large dataset using polystyrene particles similar to those in the present experiment. They found u_{rel}/u_* between 0.4 and 0.9 for different situations with u_*/v_T ranging from 1.3 to 40. Similar particles were also used by Nezu & Azuma (2004), who found values of u_{rel}/u_* ranging between 0 and 0.5 for u_*/v_T ranging from 0.8 to 6.8. Kiger & Pan (2002) found u_{rel}/u_* between 0.3 and 0.6 for $u_*/v_T \approx 1.2$ using glass beads in a closed channel. For higher concentration ($C \approx 10^{-3}$) Righetti & Romano (2004) found u_{rel}/u_* between 0.2 and 1.2 for $u_*/v_T \approx 1.1$ and between 0.3 a 0.7 for $u_*/v_T \approx 3.1$. Muste *et al.* (2005) found $u_{rel}/u_* = 1.3$ at $y/h = 0.1$ for $u_*/v_T \approx 1.8$, while no velocity difference between fluid and particles was found for $u_*/v_T \approx 70$. The decrease of the relative velocity with an increasing u_*/v_T and with increasing distance from the wall was also found by Righetti & Romano (2004) and Muste *et al.* (2005). Some investigations (Kaftori *et al.*, 1995b; Nezu & Azuma, 2004; Muste *et al.*, 2005; Righetti & Romano, 2004) have also found that the sediment particles move faster than fluid in the very near wall region ($y+ < 20$). The present experiment does not provide reliable data for this region.

The vertical relative velocity is close to zero (fig. 4.3). It appears that the vertical fluid and particle velocity both have values close to zero (not shown), as one would expect in a fully developed situation.

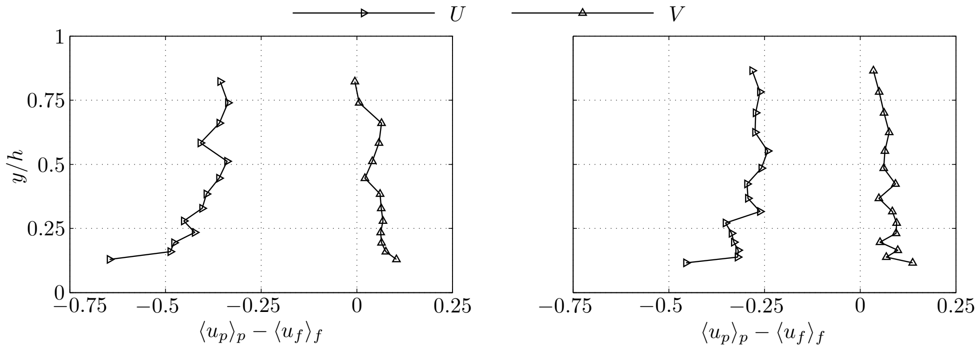

Figure 4.3: Profiles of relative velocity. Left: $u_*/v_T = 4$; Right: $u_*/v_T = 8$;

4.3.3. Turbulence

In fig. 4.4, the profiles of fluctuating streamwise velocity of the fluid and the particles are shown together with the fluctuating fluid velocity profile of the clear water flow. This figure shows that the difference between the streamwise fluid and particle velocity fluctuations is very small. The particle velocity fluctuations seems to be slightly larger than the fluid velocity fluctuations in the low velocity case. The difference between the fluid velocity fluctuations in the sediment laden flow and the clear water flow is negligible, indicating the absence of two-way coupling effects in this situation.

In order to get a clearer view of the dynamics of the turbulence profile, we plotted the profiles of the ratio between particle and fluid velocity Reynolds normal stresses ($\langle u_p'^2\rangle_p/\langle u_f'^2\rangle_f$) in fig. 4.5. In the same figure, we also plotted the ratio between the particle Reynolds normal stress and the fluid Reynolds normal stress at the particle location ($\langle u_p'^2\rangle_p/\langle u_f'^2\rangle_p$). The first ratio confirms what was seen in fig. 4.4, that the streamwise particle fluctuations are up to 8% larger than the fluid velocity fluctuations. This effect is stronger in the low velocity case than in the high velocity cases (where the effects are limited to the upper part of the water column; $y/h > 0.5$). Note that the ratio of the Reynolds normal stresses (used in fig. 4.5) is larger that the ratio of the root mean squared velocities (in fig. 4.4), because of the quadrature involved in the former quantity. Fig. 4.5 also shows that the ratio between the particle Reynolds normal stresses and the fluid Reynolds normal stresses at the particle location is equal to one. Thus in accordance with the theoretical results in section 2.2.2, the particle velocity fluctuations are equal to the fluid velocity fluctuations seen by the particles. This also explains the reason why the particle fluctuations are larger than the fluid velocity fluctuations: they are larger, because the particles encounter larger than average fluid velocity fluctuations. However, the reliability of this finding can to some extend be questioned, since it could partly be influenced by the used experimental technique, which biases the fluid velocity at the particle location toward the particle velocity (this bias error will be discussed in section 4.3.2). The results found here (larger $\langle u_p'^2\rangle_p$ than

$\langle u_f'^2 \rangle_f$) agree with those of Righetti & Romano (2004) and Kaftori *et al.* (1995b), but Best *et al.* (1997) and Nezu & Azuma (2004) found no difference between the two (at least for $y+ > 15$), while Muste & Patel (1997) and Kiger & Pan (2002) found that $\langle u_p'^2 \rangle_p$ was lower than $\langle u_f'^2 \rangle_f$. Thus there is no consensus in the literature whether or not the streamwise particle velocity fluctuations are larger or smaller than fluid velocity fluctuations. This is not surprising given the small magnitude of the effect, which makes its determination very sensitive to experimental errors.

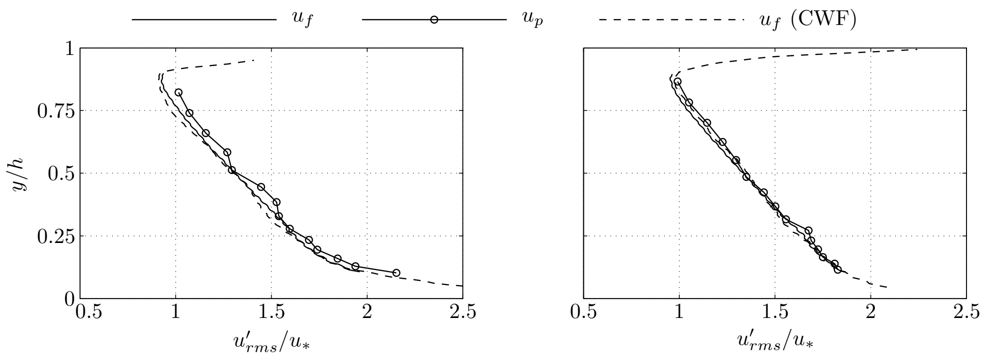

Figure 4.4: Profiles of streamwise fluid and particle fluctuations. Left: $u_*/v_T = 4$; Right: $u_*/v_T = 8$;

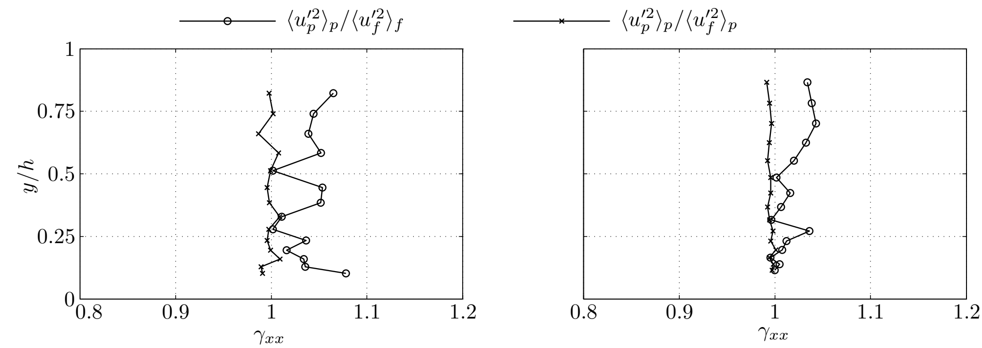

Figure 4.5: Profiles of ratio between streamwise particle and fluid Reynolds normal stresses. Left: $u_*/v_T = 4$; Right: $u_*/v_T = 8$;

The profiles of the vertical fluctuating fluid and particle velocities are shown in fig. 4.6. This figure shows particle velocity fluctuations that are clearly larger than the fluid velocity fluctuations. The difference between the vertical fluid velocity fluctuations in the particle laden and clear water flow are very small (especially in the high velocity case) suggesting once again that no two-way coupling effects occurred. The results are confirmed by fig. 4.7, which shows the ratio between the vertical particle and fluid Reynolds normal stresses ($\langle v_p'^2 \rangle_p / \langle v_f'^2 \rangle_f$). The particle Reynolds normal stresses are 5 to 10% larger than the fluid Reynolds normal stresses. This effect seems to be slightly larger for the low velocity case than for the high velocity case. The ratio of the particle Reynolds normal stresses and the fluid Reynolds normal stresses at the particle location ($\langle v_p'^2 \rangle_p / \langle v_f'^2 \rangle_p$)) shows that the particle velocity fluctuations are slightly smaller (up to 2%) than the fluid velocity fluctuations they encounter. This means that the vertical particle velocity fluctuations are damped even more than expected from the theoretical results in section 2.2.2. This could be related to the fact that the particle are not strictly point-particles, but it also might be the result of experimental noise. Furthermore, this figure suggests that the difference in the velocity fluctuations between particles and fluid are caused by the fact that the particles are found in flow structures with larger than average velocity fluctuation amplitudes. The results agree with those of Righetti & Romano (2004), who also found $\langle v_p'^2 \rangle_p$ to be larger than $\langle v_f'^2 \rangle_f$ as well as an increase in the effect with increasing u_*/v_T and with those of Muste *et al.* (2005). No differences between $\langle v_p'^2 \rangle_p$ and $\langle v_f'^2 \rangle_f$ were found by Best *et al.* (1997) and Nezu & Azuma (2004), while Muste & Patel (1997) and Kiger & Pan (2002) found the opposite result of the particle velocity fluctuations being slightly smaller than the fluid velocity fluctuations.

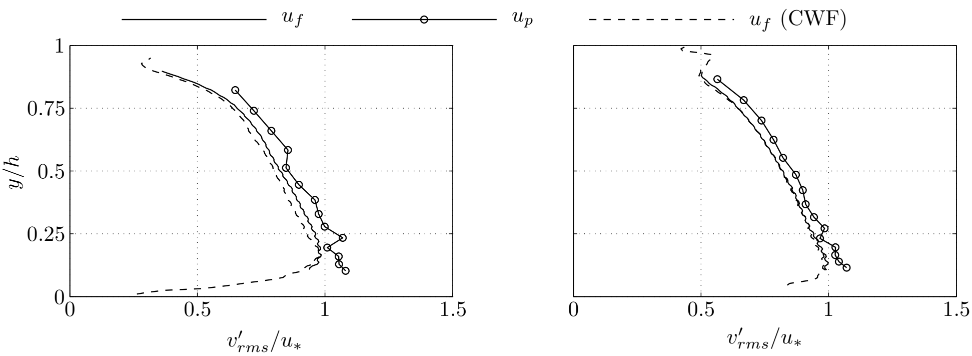

Figure 4.6: Profiles of wall normal fluid and particle fluctuations. Left: $u_*/v_T = 4$; Right: $u_*/v_T = 8$;

The profiles of the Reynolds shear stresses for the particles ($\langle u_p' v_p' \rangle_p$) and fluid ($\langle u_f' v_f' \rangle_f$) are shown in fig. 4.8, together with the Reynolds shear stress profile in the clear water flow. This figure shows that the particle Reynolds stresses have a larger magnitude than the fluid Reynolds stresses at most bins in the water column. The differences between fluid and particle Reynolds stresses have a similar magnitude in the low velocity case as in the high velocity case, in contrast with what was found for the Reynolds normal stresses. The differences between the Reynolds shear stresses in the sediment laden flow and the clear water flow are small. The ratio between fluid and particle Reynolds shear stresses ($\langle u_p' v_p' \rangle_p / \langle u_f' v_f' \rangle_f$) is shown fig. 4.9 together with the ratio between particle Reynolds shear stresses and the fluid Reynolds shear stresses at the particle location ($\langle u_p' v_p' \rangle_p / \langle u_f' v_f' \rangle_p$). The data in this figure are rather noisy. Nevertheless, one can observe that $\langle u_p' v_p' \rangle_p / \langle u_f' v_f' \rangle_f$ is generally larger than one, whereas $\langle u_p' v_p' \rangle_p / \langle u_f' v_f' \rangle_p$ is close

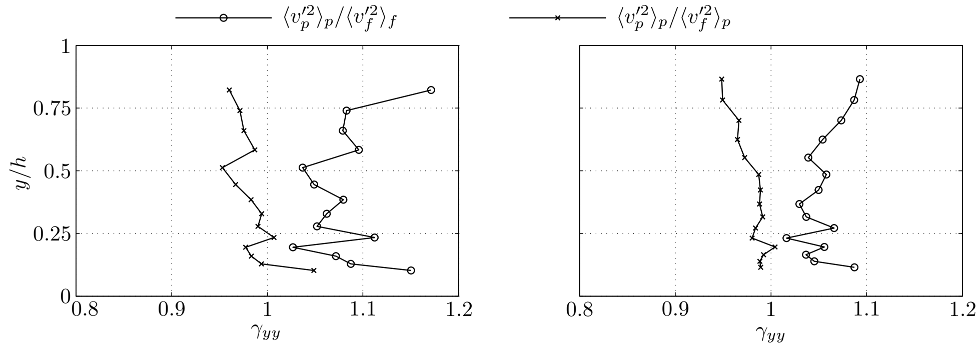

Figure 4.7: Profiles of ratio between wall normal particle and fluid Reynolds normal stresses. Left: $u_*/v_T = 4$; Right: $u_*/v_T = 8$;

to one (especially in the high velocity case). However one cannot observe a clear difference between the low and high velocity cases from this figure. In the literature, much less data of the particle Reynolds shear stresses are reported than for the normal stresses. The only known results are Kiger & Pan (2002) and Righetti & Romano (2004), who both also found that the particle Reynolds stresses are larger than the fluid ones (only for $y/h > 0.2$ in Kiger & Pan, 2002), which agrees with the present findings.

The dependency the Reynolds normal stresses (especially $\langle v_p'^2\rangle_p/\langle v_f'^2\rangle_f$) on u_*/v_T suggest the following mechanism to explain the differences in the fluid velocity fluctuations. Particles are transport upward by vertical flow structures. The structures that transport them upward need to have a vertical velocity larger than v_T (at least when the particles enter these structures), thus the particles are found relatively more often in flow structures with stronger vertical flow (hence the increase in $\langle v_f'^2\rangle_p$ and $\langle u_f'v_f'\rangle_p$ compared to $\langle v_f'^2\rangle_f$ and $\langle u_f'v_f'\rangle_f$) and this effect increases when v_T/u_* increases. However, changes in the streamwise fluctuations encountered by the particles occur only when the streamwise velocity fluctuations are correlated with the vertical velocity fluctuations, which explains the weaker effect on $\langle u_f'^2\rangle_p$ compared to $\langle u_f'^2\rangle_f$.

4.3.4. Concentrations

The sediment concentration profiles for the different cases are shown in fig. 4.10. The profiles were normalized using the concentration at $y/h = 0.25$, rather than the concentration in the lowest bin near the bed, because the concentrations higher in the water column are more reliable (see section 3.2.4). In this figure, the Rouse profile (eq. 2.32) is also shown, using the best-fit values for β, the ratio between eddy diffusivity and eddy viscosity (section 2.3.1). The best-fit values were respectively $\beta = 1.26$ and $\beta = 1.31$ for the low and high velocity case. Using, this best-fit values, the agreement between the Rouse profile and the experimental data is remarkably good. The most important differences are found in the high velocity case in the

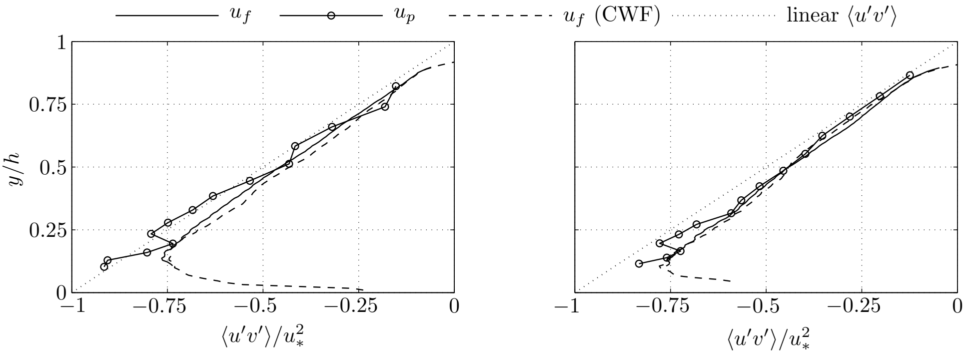

Figure 4.8: Profiles of the particle and fluid Reynolds shear stresses. Left: $u_*/v_T = 4$; Right: $u_*/v_T = 8$;

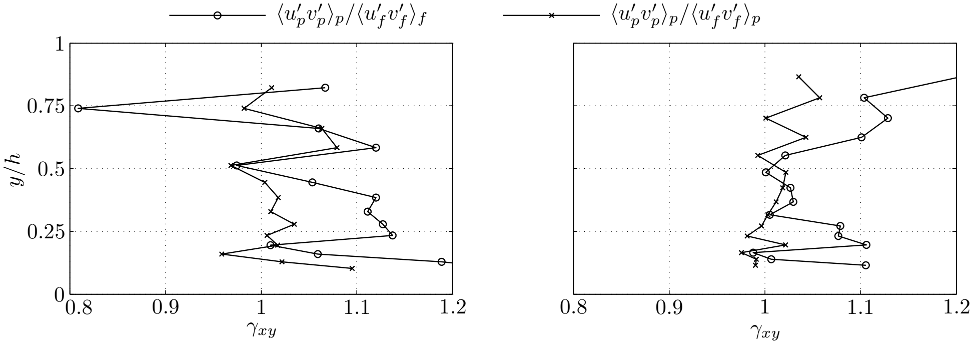

Figure 4.9: Profiles of ratio between particle and fluid Reynolds shear stresses. Left: $u_*/v_T = 4$; Right: $u_*/v_T = 8$;

lower part of the water column (below $y/h = 0.2$). Here, the measured sediment concentrations are lower than those predicted by the Rouse profile. This presumably indicates that the sediment concentration profile was still not completely fully developed near the bed in this situation. In chapter 5, it will be shown that the sediment concentrations are fully developed at $x/h = 160$ in the low velocity case. In the high velocity case, only data exist at $x/h = 160$, thus it is not possible to be certain that the situation is fully developed here. However, one can expect the high velocity case to be less developed than the low velocity case, because one can see from the length scale in which the concentration profile adapts ($L/h = \langle u_f \rangle_f / v_T$) that the length scale needed in the high velocity case is twice as large as in the low velocity case. It is also possible that the low concentrations near the bottom are a bias in the measurement technique, since it was shown in section 3.2.4 that the measured sediment concentrations in this part of the water column depend on the settings of the threshold in the PTV processing.

There is considerable disagreement in the literature on the values of β. Cellino & Graf (1999) found $\beta = 0.5$ a 0.6 for $u_*/v_T = 3.4$. Nezu & Azuma (2004) found values of β ranging from 1.1 to 3.5, with the highest values of β found for the lowest values of u_*/v_T. Their cases with u_*/v_T closest to the values in the present experiment show values of β of 1.1 and 1.2. Muste *et al.* (2005) found β ranging from 1.6 to 2.1 for $u_*/v_T = 1.8$, whereas for $u_*/v_T = 70$, they found values of β in the range of 0.2 to 0.5. Based on the results of different experimental investigation from the literature, Van Rijn (1984) presents an expression for β that increases with increasing v_T/u_*, which is in agreement with the results of recent literature above. The values found in the present investigation are somewhere in the middle of these results, and are in good agreement with the results for the dispersion of a passive scalar, for which values of β are mentioned in the range of 1.1 to 1.4 (e.g. the results cited in Hinze, 1975). In contrast with some of the previous results, the present results do not show a significant dependence on u_*/v_T.

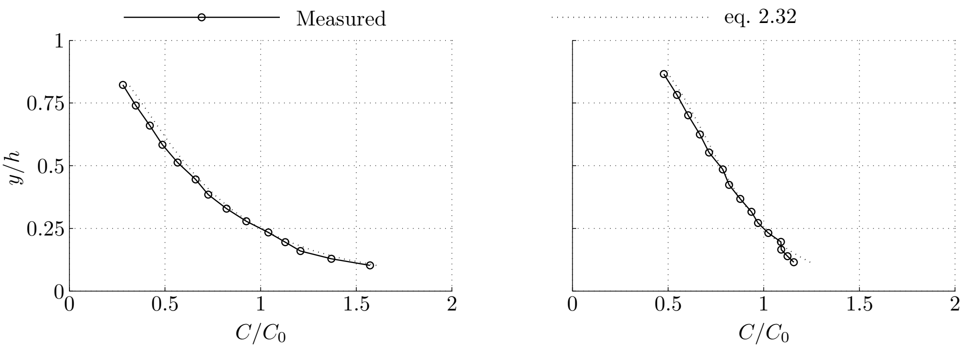

Figure 4.10: Measured concentration profiles and Rouse profile (using best fit values for β). Left: $u_*/v_T = 4$; Right: $u_*/v_T = 8$;

In order to understand the processes leading to the presented concentration profiles, we now study the horizontal and vertical sediment fluxes due to turbulent diffusion. In section 2.3.2, it was shown that the particle flux due to turbulent diffusion is directly related to the drift velocity, which is the average of the fluid velocity fluctuations at the particle location ($v_d = \langle v'_f \rangle_p$). In an equilibrium situation, the vertical drift velocity is equal and opposite to the settling velocity (eq. 2.43). The drift velocities were determined from the experimental data using bicubic interpolation of the fluid velocity fluctuations (determined using PIV) at the particle locations (determined using PTV). The results are shown in fig. 4.11.

The streamwise drift velocities are negative and have the same magnitude as the velocity difference between the fluid and particles (fig. 4.3). This shows that the particles lag the fluid, because they are found in upward moving flow structures emerging from below, which have a lower than average streamwise fluid velocity. The results agree with those found by Kiger & Pan

(2002), who found a streamwise drift velocity of $0.5u_*$, and they also found that the relative streamwise velocity between particles and fluid is equal to the streamwise drift velocity.

The vertical drift velocity shows values close to zero, rather than an upward drift with a value close to the settling velocity as would be expected from section 2.3.2. A determination of the average slip velocity ($\langle v_p - v_f \rangle_p$; not shown) revealed that the measured slip velocity was approximately zero, rather than being equal to the settling velocity. This means that the used experimental technique is not able to resolve the small settling velocity and the upward drift velocities. The reason for this is most likely a bias error in the phase discrimination algorithm (section 3.2.4). The fluid velocities are determined from an image of the tracers, which was determined by subtracting the sediment particle image from the complete image. However, some left-overs of the sediment particles (which move with the velocity of the sediment particles) are still present in fluid velocity image. These left-overs bias the fluid velocity at the particle location toward the particle velocity, thus decreasing the measured slip velocity. Note that there might be an additional effect due to the particle wake (section 2.2.1, fig. 2.5 and 2.6), which has a size that is larger than the distance between the PIV vectors that were used to determine the fluid velocity at the particle location. This can also lead to smaller measured slip velocities. However, the latter effect is not a bias error, but rather a conceptual difficulty, because the sediment particles are not the true point particles that they are assumed to be in the two-fluid theory.

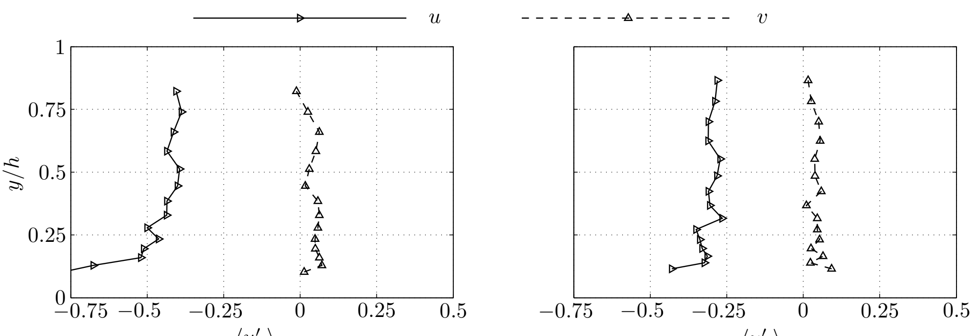

Figure 4.11: Profiles of streamwise and wall normal drift velocity. Left: $u_*/v_T = 4$; Right: $u_*/v_T = 8$;

Because of the impossibility to determine the drift velocities directly, they are determined in this chapter from eq. 2.42 (using the independently determined settling velocity), which can be written as:

$$\langle v'_f \rangle_p = \langle v_p \rangle_p - \langle v_f \rangle_f + v_T \tag{4.3}$$

Using the drift velocity determined from eq. 4.3, the eddy diffusivity was determined from the experimental data using:

$$D_{yy} = -\langle v'_f \rangle_p \frac{C}{dC/dy} \tag{4.4}$$

The results are show in fig. 4.12, together with the experimentally determined eddy viscosity and the parabolic eddy viscosity profile (eq. 2.7). Here, the eddy viscosity was determined from the experimental data using:

$$\epsilon_{xy} = -\frac{\langle u'_f v'_f \rangle_f}{d\langle u_f \rangle_f / dy} \tag{4.5}$$

The velocity and concentration gradients were determined by fitting a fourth order polynomial to the data and determining the derivative of this polynomial analytically. Fig. 4.12 shows that the measured eddy viscosity does not agree completely with the parabolic profile. Especially around $y/h = 0.5$, there is a discrepancy, where the measured values are 15% lower than the parabolic profile. In the low velocity case, the shape of the measured eddy viscosity profile is rather similar to the parabolic profile. In the high velocity case on the other hand, the eddy viscosity is notably different close to the free surface ($y/h > 0.8$), where the eddy viscosity increases significantly. However, this appears to be an artifact of the experiment, related to the small deviation from the logarithmic profile in the fluid velocity profile in this case (fig. 4.2). This deviation is likely to be caused by the internal boundary layer due to the small glass plate on the free surface that was used to allow the laser light to penetrate the flow. Fig. 4.12 further shows that the eddy diffusivity is larger than the eddy viscosity in the whole water column in both cases. This was of course expected, because the value of β that made the Rouse profile fit best to the data (fig. 4.10) was larger than one. In the low velocity case, the shape of the eddy diffusivity profile is rather similar to the eddy viscosity profile. In the high velocity case, there is remarkable difference. Here, the highest diffusivities occur close to the bed, and the lowest high up in the water column. The high eddy diffusivities near the bed are a result of the different concentration profile near the bed (which have a lower gradient than expected from the Rouse profile; fig. 4.10).

Using the experimentally determined eddy viscosity and eddy diffusivity, profiles of their ratio β are plotted in fig. 4.13. As expected, this figure shows again values of β larger than one. It appears that the values of β are also larger than the ones found from the fit of the Rouse profile (which were around 1.3; see fig. 4.10). The reason for this is that in fig. 4.13 the measured eddy viscosity was used, which was seen to be lower than the parabolic eddy viscosity profile that was used in the derivation of the Rouse equation. Thus it is important to know how the values of β were determined to interpret their value. The values of β in previously mentioned investigations of Cellino & Graf (1999) and Muste *et al.* (2005) were obtained from the measured eddy viscosity and eddy diffusivity profiles, while those of Nezu & Azuma (2004) were obtained from a fit of the Rouse profile. When comparing the values measured by Muste *et al.* (2005) with those in fig.4.13 rather than those obtained from a fit of the Rouse profile, we find that they are

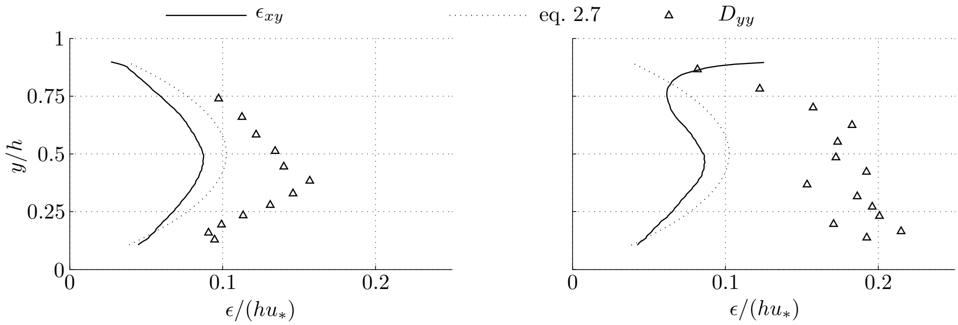

Figure 4.12: Profiles of eddy viscosity and eddy diffusivity. Left: $u_*/v_T = 4$; Right: $u_*/v_T = 8$;

in a similar range. Note that the data in the low velocity case do not show a clear development over the water depth. The data in the high velocity case above $y/h = 0.3$ also do not show a clear development over the water depth. However, below $y/h = 0.3$, the value of β increases strongly toward the bed. The reason for this increased value of β in this case is most likely that the concentration profile is still not fully developed (fig. 4.10). In section 5.3.2, it will be shown that when developing toward an equilibrium, the values of β can increase substantially in the lower part of the water column. The elevation at which this increase occurs decreases with increasing distances from the sediment injection (as a kind of downward traveling wave). A similar increase in the value of β is visible in fig. 4.12 at $x/h = 35$, although at the latter location, it is located somewhat higher in the water column than in the high velocity case. However, the results for β low in the water column are not very reliable, because the largest uncertainty exists here in the determination of the sediment concentrations (see fig. 3.6). From the above, we can conclude that using a constant value of β seems a reasonable approximation in equilibrium conditions.

In section 2.3, various hypotheses were given that could explain the difference between the eddy diffusivity and the eddy viscosity. Two of the hypotheses will be tested here against the data. The third one, which is related to the occurrence of coherent flow structures, will be tested in section 6.2.1. First, we test whether the value of β can be explained by the fact that the concentration profile cannot be approximated as linear over the size of an eddy. In order to do so we use the results from section 2.3.3, where its was shown that a random walk approximation for the vertical sediment fluxes leads to the following high order gradient diffusion relation:

$$\langle u'_{f,y} \rangle_p = D_{yy} \frac{1}{C} \frac{\partial C}{\partial y} + D_{yyy} \frac{1}{C} \frac{\partial^2 C}{\partial y^2} + D_{yyyy} \frac{1}{C} \frac{\partial^3 C}{\partial y^3} \tag{4.6}$$

In the following, we will call the first term on the right hand side of this equation the "first order term", the second one the "second order term" and so on. In order to obtain the higher order diffusion coefficients, we used the approach from Wyngaard & Weil (1991) and inserted

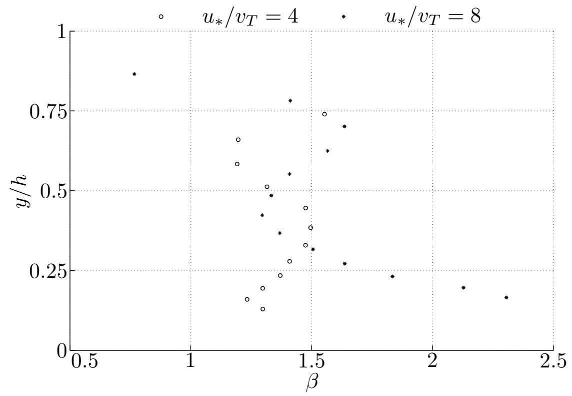

Figure 4.13: Profiles of the ratio between measured eddy diffusivity and measured eddy viscosity. Left: $u_*/v_T = 4$; Right: $u_*/v_T = 8$;

eq. 2.13 from Oesterlé & Zaichik (2004) to calculate the Lagrangian time scales, which yields:

$$D_{yyy} = \alpha_3 S_{vf} \epsilon_{xy}^2 \langle v_f'^2 \rangle^{-1/2} \tag{4.7}$$
$$D_{yyyy} = \alpha_4 F_{vf} \epsilon_{xy}^3 \langle v_f'^2 \rangle^{-1} \tag{4.8}$$

Here, S_{vf} and F_{vf} are the skewness and the excess kurtosis (i.e. the kurtosis minus three) of the vertical velocity fluctuations. Furthermore, α_3, α_4 are proportionality coefficients between respectively the integral under the triple and quadruple velocity fluctuation correlation function and the Lagrangian time scale to the power 3/2 respectively 2. These coefficients were assumed to be equal to one. Note that this result shows directly the relation between the intermittency and bursting in the turbulence (both influence the skewness and the kurtosis in the velocity fluctuations, see section 2.1.3) and the turbulent transport of sediment. Specifically, the asymmetry in the length scales that was shown before to be able to influence the turbulent diffusion, can now be related to the skewness in the velocity fluctuations. In case of a positive skewness in the wall normal velocity fluctuations, there exist some strong upward flow structures that transport sediment from farther away.

For the turbulent diffusion coefficient (D_{yy}), the measured eddy viscosity (obtained from the fluid velocity and Reynolds shear stress profile) was used. The results are shown in fig. 4.14. Note that in this figure in the line called "third order term", only the dc/dy and d^3c/dy^3 term are used and not the d^2c/dy^2. Fig. 4.14 shows that the higher order terms do not lead to significant differences in the calculated vertical sediment fluxes. Hence for suspended sediment transport with values of u_*/v_T of 4 and larger, the effect that the concentration profile is non-linear over the size of the eddies is not important. It might still have an influence at much lower values of

u_*/v_T, where the velocity profile deviates more from linearity, but this cannot be assessed from the current data set.

The second hypothesis that is being tested here is whether the difference in the fluid velocity fluctuations as seen by the particles and the overall fluid fluctuations might lead to increased particle diffusivities. Simonin *et al.* (1993) proposes that the diffusivity of particles can be written as:

$$D_{yy} = \langle v'_f v'_p \rangle_p T_L \tag{4.9}$$

Here, T_L is the Lagrangian integral timescale as seen by the particles. He then assumes that $\langle v'_f v'_p \rangle_p \approx \langle v'_f v'_p \rangle_f$. In section 2.2.2 it was shown theoretically that for suspended sediment transport, $\langle v'_f v'_p \rangle_p \approx \langle v'^2_f \rangle_p$ and indeed in section 4.3.3 it was confirmed that the particle fluctuations are equal to the fluid velocity fluctuations at the particle location (up to experimental precision). From this, one can infer that also $\langle v'_f v'_p \rangle_p$ will be equal to $\langle v'^2_f \rangle_p$. However, in section 4.3.3 it was also shown that $\langle v'^2_f \rangle_p$ was not equal to $\langle v'^2_f \rangle_f$, but 5 to 10% larger. Hence, this effect leads to an increase of the eddy diffusivity of 5 to 10% (eq. 4.9). However, the eddy diffusivity is 50% larger than the measured eddy viscosity (fig. 4.12). Hence this effect can also not explain the difference in the values of the eddy diffusivity and the eddy viscosity, although it might contribute to it.

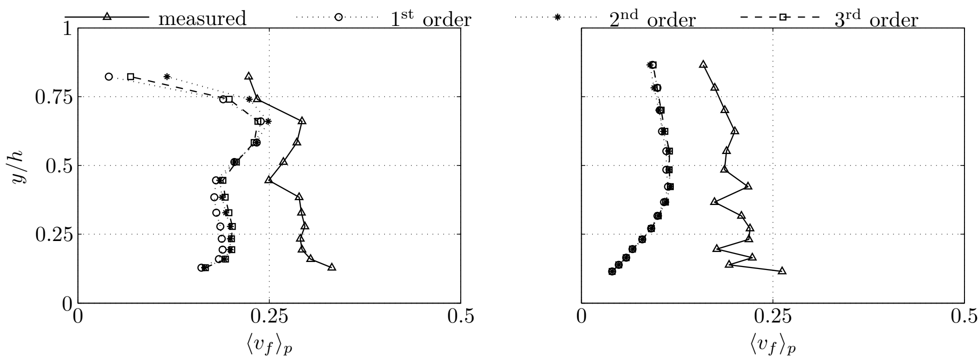

Figure 4.14: Measured vertical drift velocity profile and modeled ones using eq. and 4.6 4.7. Left: $u_*/v_T = 4$; Right: $u_*/v_T = 8$;

4.4. Comparison of DNS with experimental data

In section 4.1, it was argued that the use of a DNS in combination with the simulations of individual sediment particles could be an added value in sediment transport research, but that before such an approach can be used, it still needs to be validated against experimental data. Here, we perform a preliminary comparison between experiment and simulations of the results of the low velocity case. The simulations were performed by Marcos Cargnelutti of Kramers' Laboratory at TU Delft. The DNS solved the Navier-Stokes equation (eq. 2.1 and 2.2) using a finite volume solver with a predictor-corrector approach and a second-order Adams-Bashfort scheme for the time integration. Periodic boundary conditions were used in the streamwise and spanwise direction. A free slip and a no-slip boundary condition were used respectively at the free surface and the bottom. The sediment particles were simulated using eq. 2.17, including the forces of gravity, Stokes drag, added mass and fluid pressure gradients. Two-way and four-way coupling effects were neglected, as well as the Basset history and Faxén forces. The fluid velocity at the particle location was obtained from the DNS using trilinear interpolation. More details of the DNS can be found in Portela & Oliemans (2003) and Cargnelutti & Portela (2007).

The concentration profiles found in the experiment and simulations are shown in fig. 4.15. In this figure, different results from different simulations are shown. In Cargnelutti & Portela (2007), it was found that the results of the DNS depended strongly on the type of resuspension mechanism that was used at the bottom. If no resuspension mechanism was used, all particles eventually ended up at the wall, which is clearly not in agreement with the experimental results. Therefore, three different resuspension mechanisms were tested:

- The use of a virtual wall at one particle diameter from the wall, which prevents the particles from entering the viscous sublayer where the vertical velocity fluctuations are too small to cause particle entrainment.
- The use of a lift force at the wall only using wall lift of Krishnan & Leighton, Jr. (1995).
- The use of a lift force over the complete water column. At the wall, the expression from Krishnan & Leighton, Jr. (1995) is used, away from the wall the lift model of Wang *et al.* (1997).

From fig. 4.15, it is found that the experimental data profiles are well simulated, provided a resuspension mechanism is used. This can be either the use of a virtual wall, or the use of a complete lift force (over the complete water column). Using only the lift force from Krishnan & Leighton, Jr. (1995) at the wall does not give good results, because the lift is not strong and a large number of particles still end up at the wall (the used normalization in fig. 4.15 obscures this aspect). In this case, the sediment concentration gradient is flatter, which means that β is higher in this situation. This is probably caused by the fact that in this situation, particles are only entrained by very strong vertical flow structures, and these structures can transport the particles easier upward, leading to a flatter concentration profile. Note that this mechanism also explains the experimentally observed increase of β with increasing v_T/u_* (see the references in section 4.3.4). In this situation, one then also expects an increase of $\langle v_p'^2 \rangle_p$, compared to $\langle v_f'^2 \rangle_f$.

Using a sufficiently strong lift force, the results are reproduced that well that one can state that β is larger than one in the DNS as well as in the experiments. The remarkable thing is

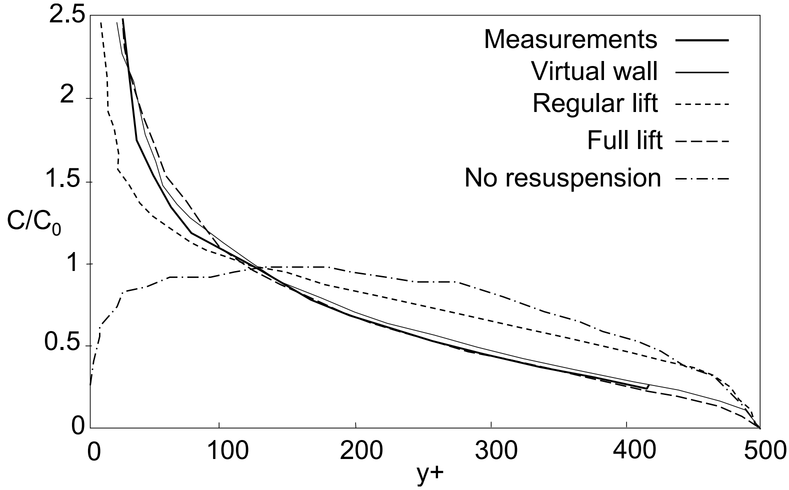

Figure 4.15: Concentration profiles obtained from DNS and experimental concentration profile.

that independent of the details of the used resuspension mechanism (provided it is sufficiently strong), the experimental results are reproduced. This means that the near-wall layer and outer layer are decoupled, and that the outer layer can be well simulated, provided a sufficient particle flux from the wall is provided. This justifies the current modeling approach in many large scale models, where a near wall reference concentration or flux is applied. From this, we can also conclude that the used approximations in the DNS (neglecting Basset and Faxén forces, as well as two and four-way coupling) are justified for the low concentration experiment, since the inclusion of these forces is not needed to obtain a good agreement with the experimental data. This agrees with the results in section 2.3.2 and 2.4.3 as well as with the fact that no two-way coupling effects were found in the experimental data in this chapter. The importance of the lift force is more difficult to assess. It does not seem necessary in the outer layer. The necessity to use lift forces above the wall indicates that the particles need to be taken out of the viscous sublayer. Above the viscous sublayer, the fluid velocity gradients are so small that lift force on the particle is negligible compared to effective gravity and vertical turbulent velocity fluctuations form the main transport mechanism.

From the experimental results in this chapter, one can infer the following recommendations for the comparison of the velocity and turbulence data of the DNS and the experiments. First of all, the mean streamwise relative velocities should be compared in order to view if the velocity difference between fluid and particles is reproduced well. The velocity difference is an important quantity, because it provides important information about which flow structures are sampled by the particles. Just comparing fluid and particle velocity profiles is not sufficient, and it is influenced more heavily by experimental noise (especially in the determination of u_*). Thus comparing fluid and particle velocity profiles, rather than relative velocity profiles will readily give a good comparison, even if the underlying dynamics of the particle movement is not simulated correctly. Secondly, it should be tested whether the increased particle Reynolds stresses (compared to the fluid Reynolds stresses) are found in the simulations, and whether this ratio increases in simulations that show increased values of β. Comparing the ratio between particle and fluid Reynolds stresses, rather than the fluid and particle turbulence profiles, is a more sensitive test to show whether the dynamics of the flow are simulated well. This has the additional advantage that the ratio between the two is not influenced by any experimental errors in the determination of u_*. Finally, the vertical balances leading to the equilibrium concentration profile should be tested. This includes the vertical drift velocity (which should be opposite to the settling velocity) as well as the eddy diffusivity obtained from this drift velocity and the concentration profile. For this quantity, it should be tested whether it is larger than the eddy diffusivity obtained from Reynolds shears stress and mean velocity profiles.

4.5. Summary and conclusion

In this chapter, an experiment was presented measuring suspended sediment transport in a fully-developed situation. Polystyrene particles were used as pseudo-sediment, in order to create an experimental situation that could be compared directly (without any scaling) with the results of a DNS (direct numerical simulation) that simulated the sediment by calculating the movement of a large number of individual sediment particles. Fluid velocities and the velocity and location of individual sediment particles were measured simultaneously using PIV (particle image velocimetry) for the fluid and PTV (particle tracking velocimetry) for the particles. Two different cases were considered with a different fluid velocity and hence a different value of u_*/v_T.

The two cases differed drastically in the near-wall behavior of the sediment. In the low velocity case, the sediment formed streaks on the bottom of the flume, whereas in the high velocity case, all particles were kept in suspension, and no sediment was visible on the bed.

It was found that the average streamwise velocity of the sediment particles was lower than the average fluid velocity. The velocity difference (scaled with u_*) decreases with increasing u_*/v_T. It was found that the particles lag the fluid, because the particles are encountered in velocity structures with a streamwise velocity that is lower than average.

The particle velocity fluctuations were found to be stronger than the fluid velocity fluctuations, especially for the wall normal velocity fluctuations. This effect was slightly stronger for smaller values of u_*/v_T. A comparison of the particle velocity fluctuations with the fluid velocity fluctuations at the particle locations showed that the particle velocity fluctuations are approximately equal to the fluid velocity fluctuations at the particle locations (as can be expected for particles with a low value of the Stokes number). Thus, the increased particle velocity fluctuations compared to the fluid velocity fluctuations are caused by the fact that the particles are found in the strongest vertical flow structures. This seems to be related to the fact that stronger flow structures are needed to lift up the particles.

The observed concentration profiles showed a good agreement with the Rouse profile (eq. 2.32), provided that a value of β (the ratio between the eddy diffusivity and the eddy viscosity) of around 1.3 is used. This value differed little between the low and high velocity case. Thus the sediment diffusivity is found to be higher than the diffusivity of streamwise momentum. It was noted that the values of β found from using a best-fit of the Rouse profile tend to be lower than those found from a direct comparison of the measured eddy diffusivity and measured eddy viscosity. The reason for this is that the measured eddy viscosity is lower than the parabolic eddy viscosity profile, which is assumed in the derivation of the Rouse profile. Two hypotheses were tested for the eddy diffusivity being larger than the eddy viscosity. The first one was that extra sediment is transported, because the concentration profile cannot be approximated by a linear function over the size of a turbulent flow structure. This effect was shown to be negligible for the present range of u_*/v_T. The second hypothesis is that the increased eddy diffusivity is due to the fact that the particles are located in flow structures that have stronger than average velocity fluctuations. This effect was shown to be at most of second order importance, but not strong enough to explain the observed increase in β.

In agreement with what can be expected for the low sediment concentrations in these cases, no clear evidence of two-way coupling was found.

A preliminary comparison of the experimental results with the results of the DNS showed a good agreement between the experimental and the numerically simulated sediment concentration profiles, provided that a sufficiently strong resuspension mechanism is used near the wall. If no resuspension mechanism is used, all particles in the DNS end up at the wall. If a resuspension mechanism is used that is too weak, concentration profiles are found in the DNS with a much higher value of β.

From the fact that experimental results in the two different cases are comparable, we can conclude that the near wall layer does not have a strong influence on the processes higher up in the water column, at least for the present range of values of u_*/v_T. Merely, the wall region is a source of particles to the outer layer, controlling the amount of particles, but not the shape of the sediment profiles. This agrees with current modeling practice, where a separation is made between bed load and suspended load. A boundary condition near the wall (rather than at the wall) is used to calculate the flux of sediment for the suspended sediment calculation. These results agree with the results of the comparison with the DNS, where it was found that the experimental data were reproduced well irrespective of the type of resuspension mechanism used (provided it was strong enough to lift the particles to a level, where the vertical velocity fluctuations have a comparable magnitude as the settling velocity).

Chapter 5

Non-equilibrium sediment transport[1]

5.1. Introduction

Most experimental sediment transport investigations have focused on fully developed conditions, because they are relatively easy to obtain and because the sediment transport equations in this situation simplify considerably. However, in many real world applications (such as the development of a turbid plume from a dredging vessel, changes in the flow cross section, variations in sediment properties, and confluences), the non-uniformity or non-stationarity of the sediment transport is important. This is especially important for morphodynamics, because in a completely fully developed situation, there are no gradients in the sediment transport and hence the bottom morphology will not change. Models that were derived or calibrated for fully developed conditions, are frequently applied to non-uniform and non-stationary situations. This quasi steady approach is expected to yield reasonably good results in those situations, where the sediment concentration and the velocity of the sediment particles adapt rapidly to the flow conditions, i.e. in those situations where the adaptation length and time scales are small compared to the length and time scales over which the mean flow and turbulence change. However, in many situations this is not fulfilled, like for example scour near groynes or bridge piers. In those situations, sediment transport problems become more complicated. It is therefore important to obtain more insight in the behavior of sediment transport at these length and time scales.

In this chapter, an experiment is presented that was set up to investigate the development toward a fully developed situation and we will show which length scales are relevant for this process. In addition, the transport process in a non-homogeneous situation is compared to the turbulent transport in an equilibrium situation as was presented in chapter 4. From this information, it can be seen which turbulent flow structures are important for the adaptation process.

1. Parts of this chapter has been published in modified form in: W.A. Breugem and W.S.J. Uijttewaal, (2006) "A PIV/PTV experiment on sediment transport in a horizontal open channel flow", River Flow 2006, Lisboa, Portugal, pp. 789–798

Here, we study the adaptation process by feeding the sediment to the flow near the free water surface, at different distances from the measurement section in an otherwise uniform flow, thus providing data on the development of a plume of sediment (more details can be found in section 3.2). In this way, non-uniform transport can be studied quite easily. Experimental investigations to flows that vary in time (like Admiraal *et al.*, 2000) or space are more difficult to perform than the present experiment. Also the interpretation in varying flows is more difficult, because the change in the flow conditions have to be accounted for. In the present experiment, the flow and turbulence are uniform in the streamwise direction, so that the focus can be on the adaptation of the sediment to this flow. Note that the concentrations in the experiments were low enough for two-way coupling (see section 2.4) to be negligible.

In this chapter, we focus on single point statistical data. Some statistical data of the spatial structure and the coherent structures responsible for the diffusion process will be shown in chapter 6.

5.2. Approach

In this section, the results of an experiment are discussed, in which velocities of the fluid and individual particles are measured simultaneously using respectively PIV and PTV. As pseudos-sediment particles, polystyrene spheres were used. Because these particles have low settling velocities, the experiment could be performed at a low Reynolds number, while still enough sediment particles remained suspended ($u_*/v_T \approx 5$). The used Reynolds number was low enough for the experiment to be in the range that is currently within reach of DNS simulations.

Sediment mixed with water is introduced close to the free surface in the centerline of the channel. The distances from the sediment introduction to the measurement section ranged from 16 to 280 water depths. A more detailed description of the experimental set-up can be found in section 3.2. The measurement equipment is shown in fig. 3.4 and 3.3. The experimental parameters are shown in table 3.1 and 3.2.

5.3. Results

5.3.1. *Concentration*

The mean velocity profile in wall coordinates is shown in figure 5.1. The friction velocity u_* was determined by fitting the mean fluid profile to the law of the wall. This estimate agrees generally well with the friction velocity obtained from fitting the Reynolds stress profile (see table 3.2). For comparison, the law of the wall (eq. 2.6) is plotted with $\kappa = 0.41$ and $A = 5.29$, as found by Nezu & Rodi (1986). Our data generally compare well with the law of the wall.

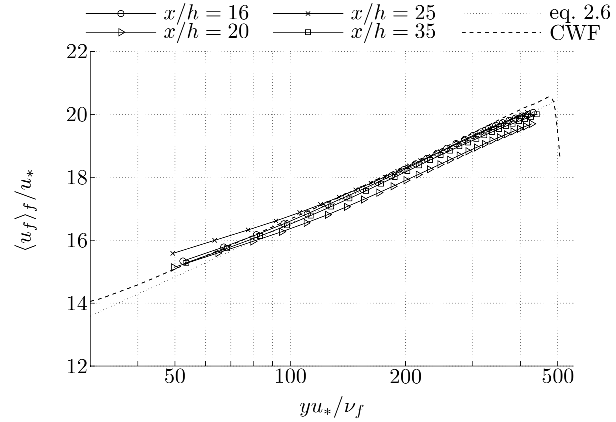

Figure 5.1: Mean fluid velocity profiles in wall coordinates.

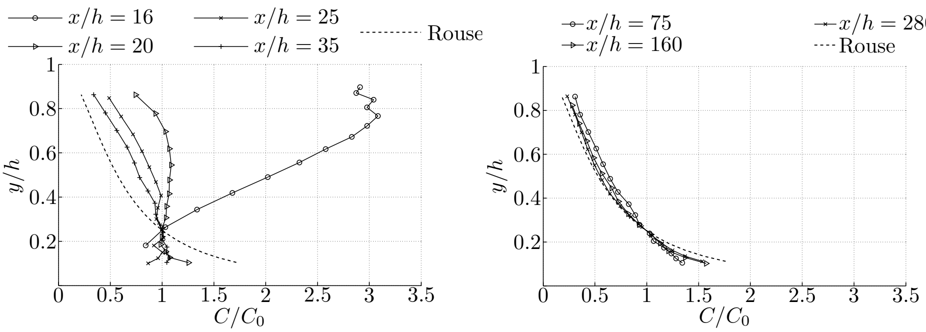

Figure 5.2: Mean sediment concentration profiles at various downstream locations.

The mean sediment concentrations are shown in figure 5.2. The concentrations are normalized with the concentration at $y/h = 0.25$, where the most reliable sediment concentration were obtained (see 3.2.4). Scaling these cases with a reference concentration was done for easy comparison with each other, but there are no physical reasons for choosing this particular elevation for the normalization. For comparison, we also plotted the Rouse distribution (eq. 2.32) with $\beta = 1.0$.

At $x/h = 16$, the sediment is predominantly at the height where it was injected [2]. The sediment particles are descending rapidly. Already at $x/h = 20$, most sediment is distributed reasonably well over the water depth, whereas from $x/h = 25$ on, there is more sediment near the bottom than near the free surface. At $x/h = 75$, the concentration distribution is already quite similar to a fully developed situation, although some small changes are still visible. At $x/h = 160$, the

2. Using eq. 2.13, one can show that the sediment has already been multiple integral time scales (T_L) in the flow at this location since it was introduced. Therefore, it is expected that disturbances due to the sediment introduction are not important at this location.

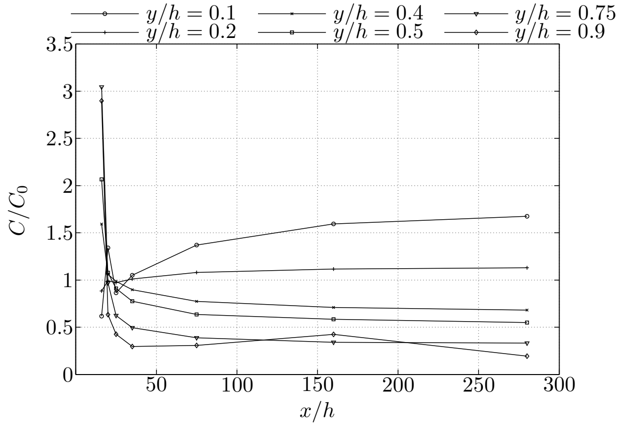

Figure 5.3: Mean sediment concentration as function of the distance from the injection point.

concentration does not differ from the one measured at $x/h = 280$. This fully developed situation will not be discussed any further in this chapter, as it has already been treated in chapter 4. The length scale commonly used to determine the adaptation of a concentration profile is the distance a particle travels in the time it needs to settle to the bottom: $L \approx \langle u \rangle h/v_T$, which for the present experiment is equal to 100 h. Apparently, the adaptation is much faster than this length scale predicts. To obtain a clearer view of the adaptation, the concentrations at various water depths were plotted against the distance from the injection point (fig. 5.3). This figure shows a fast adaptation of the concentrations toward equilibrium in the first 35 water depths from the injection point. Further downstream, the adaptation process appears much slower. Apparently, processes with different time scales determine the adaptation length.

5.3.2. *Vertical velocity*

The development of an equilibrium situation can also be seen clearly in the mean vertical velocity profile (fig. 5.4). The particles have a mean downward velocity of up to $0.45u_*$ in the $x/h = 16$ case, which gradually decreases toward zero at larger distances from the injection point. Already at 35 water depths from the injection point, the vertical particle velocities have become equal to the vertical fluid velocities, which should occur in equilibrium conditions. It is interesting to note that vertical fluid velocities are not completely zero in the particle laden cases, but have a small bias in the same direction as the particle velocity. This is presumably a bias in the phase discrimination algorithm (discussed in detail in section 4.3.4, p. 78).

To obtain more insight into the adaptation process, the relative velocities (i.e. $\langle u_{p,i} \rangle_p - \langle u_{f,i} \rangle_f$) were plotted in fig. 5.5, and the drift velocities ($\langle u'_{f,i} \rangle_p$) were plotted in fig. 5.6. In the latter figure, the vertical drift velocity was calculated in two different ways. First, it was calculated directly by performing a bicubic interpolation of the fluid velocity field measured with PIV at the

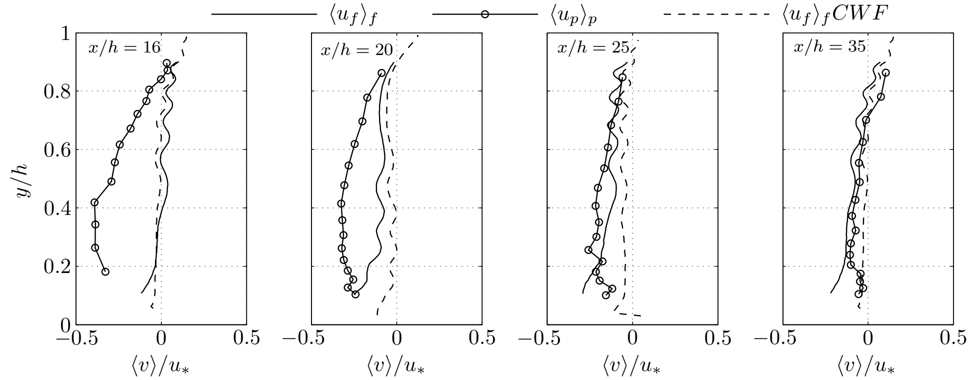

Figure 5.4: Mean vertical velocity profiles.

measured particle locations. From now on, this method will be referred to as the "interpolation method". This method was also used for the calculation of the streamwise drift velocities. In order to verify that these results were not determined by the chosen interpolation method, the drift velocities were also determined using bilinear interpolation, and it was found that the results hardly differed from those obtained with bicubic interpolation. Just as was found in section 4.3.4, the direct estimation of the vertical drift velocity from the fluid velocities interpolated at the particle locations is unreliable due to the bias in the measured fluid velocities near the particles (p. 78). Therefore, we use the vertical sediment momentum equation (eq. 2.42) to calculate the drift velocity from the fluid and particle velocities, in combination with the measured still water particle settling velocity (see 3.2.2), as was done in section 4.3.4 (eq. 4.3). This method will be referred to as the "momentum balance method". Note that a value of zero was used for the vertical fluid velocity (rather than the measured values), because the measured values also contained some bias from the phase discrimination algorithm. The sensitivity of this choice is discussed later. At present, mainly the wall normal velocities are discussed, with only occasional references to the streamwise velocities. A more thorough discussion of the streamwise velocities plotted in these figures is given in the next section.

First of all, it appears from fig. 5.4 that the sediment particles descend rapidly close to the injection point (faster than can be expected if they would only settle due to gravity). It appears from the calculated drift velocities that this increased downward particle velocity is due to the fact that the particles are mostly concentrated in flow structures that have a downward velocity (the drift velocity from the momentum balance method is directed downward). It is known that in a turbulent open channel flow, most downward flow structures also possess a larger than average streamwise velocity (e.g. Nezu & Nakagawa, 1993). If the particles are found mostly in downward flow structures, then they should also predominantly be found in faster than average flow structures. Since there is no slip velocity in the streamwise direction (see section 2.3), they should have a velocity that is larger than the local fluid velocity. This is indeed what

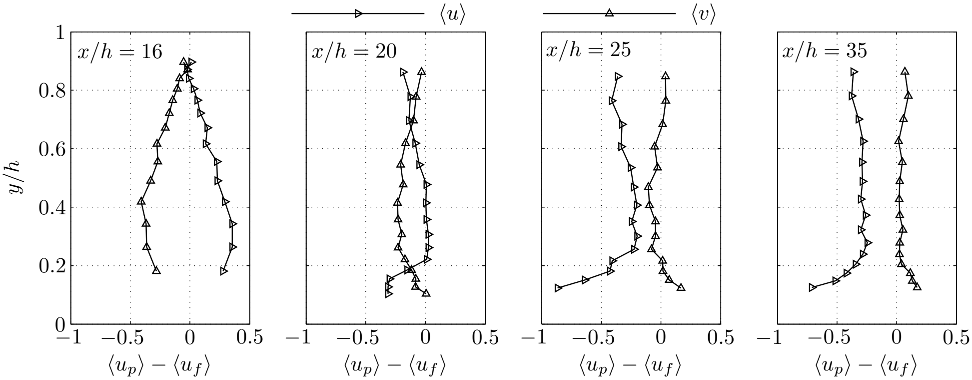

Figure 5.5: Relative velocities $\langle u_p \rangle_p - \langle u_f \rangle_f$.

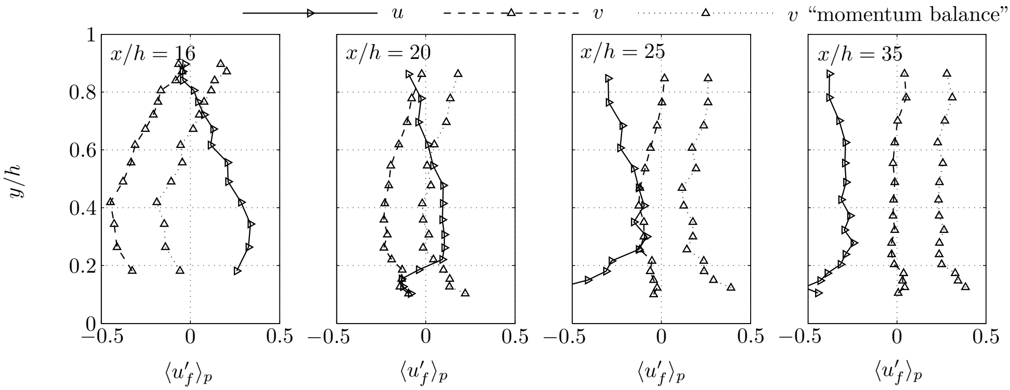

Figure 5.6: Drift velocity.

can be seen in fig. 5.5 and fig. 5.6. Thus the rapid downward motion of the sediment particles close to the injection point is due to the turbulence. In some sense, the situation resembles the increased settling due to turbulence observed in cellular flow fields (Maxey & Corrsin, 1986) and homogeneous isotropic turbulence (Wang & Maxey, 1993, also see section 2.2.3, especially fig. 2.8), where also an increased apparent settling velocity can be found, because the flow field causes the particles to remain mainly in the downward flow structures. A more detailed view of the coherent flow structures that determine this process is shown in chapter 6.

Already at 25 water depths from the injection point, the vertical drift velocity (calculated with the momentum balance method) has changed its sign and is now directed upward (although still smaller than the settling velocity of the particles). This means that at this stage, the particles still move downwards (i.e. an equilibrium situation has not yet been reached), but that the turbulence is causing a small upward flux, which slows down the process of reaching an equilibrium profile. Interestingly, the streamwise relative and drift velocity have also changed its sign at this point, implying that the average particle velocity is lower than the mean fluid velocity, although not as low as is obtained in equilibrium conditions (see section 4.3.2).

It is important to test whether the gradient diffusion hypothesis is valid in this non-equilibrium situation, or that extra effects need to be taken into account. To do so, we first plot the vertical drift velocities calculated with the momentum balance method, in combination with the estimates of the drift velocity obtained from gradient diffusion theory and higher order corrections that account for long range effects (see 2.3.3). The drift velocity according to the gradient diffusion hypothesis can be obtained from:

$$\langle v_f' \rangle_p = D_{xy} \frac{1}{C} \frac{\partial C}{\partial x} + D_{yy} \frac{1}{C} \frac{\partial C}{\partial y} \tag{5.1}$$

In the following, the influence of the streamwise concentration gradient $\partial C/\partial x$ on the vertical drift has been neglected, because $\partial C/\partial x$ estimated from the PTV data is an order of magnitude smaller than $\partial C/\partial y$. The difference between $\partial C/\partial x$ and $\partial C/\partial y$ could be expected by examining the continuity equation (eq. 2.35) in a stationary situation.

We used the same approach as in section 4.3.4 in order to determine the fluxes using a high order gradient diffusion law (eq. 4.6). The results are shown in fig. 5.7.

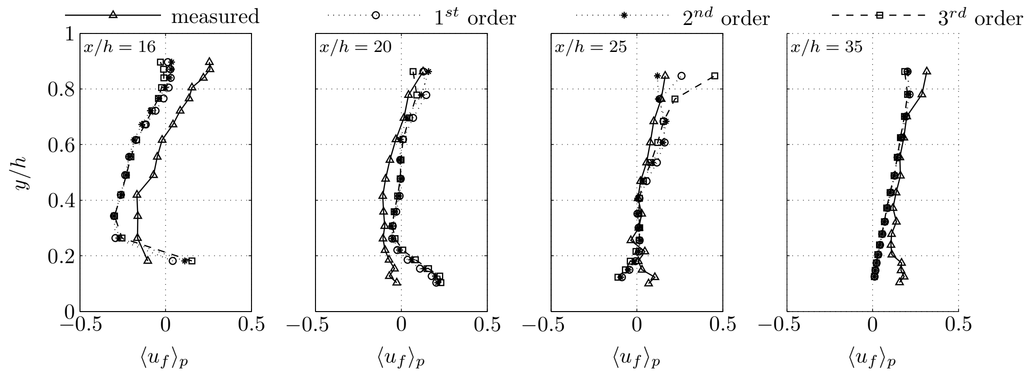

Figure 5.7: Profiles of the experimentally determined vertical drift velocity and the ones obtained from different approximations of a random walk (i.e. the sums of the right hand side terms in eq. 4.6 up to the order noted in the legend).

From this figure it appears that the gradient diffusion hypothesis as such (with the added assumption that the diffusion coefficient for the sediment particles is equal to the eddy viscosity) is not sufficient to model the vertical drift velocities accurately in this situation (just as in a fully developed situation, chapter 4). It appears that the diffusion fluxes are underestimated close to the injection point, while the opposite occurs further away. The measured drift velocities at $x/h = 20$ and 25 are very small. Furthermore, the effect of adding the high order terms is virtually absent. Hence the influence of long range effects is unimportant in this situation. Therefore, the high order terms will be neglected in the following.

The values of the inverse Prandtl-Schmidt number β are plotted in fig. 5.8. It is defined as the eddy diffusivity divided by the eddy viscosity (see section 2.3.3). This figure shows that near the sediment introduction (at $x/h = 16$), D_{yy} is lower than ϵ_{xy} for $0.2 < y/h < 0.7$, which is in clear contrast with the fully developed situation (see section 4.3.4), where the turbulent diffusion coefficient of the sediment is higher than the eddy viscosity. For $y/h < 0.2$ we even find negative β values, which means that the turbulent transport is countergradient here. However, it is not clear whether this data point is reliable. This value might be also an artifact of the used data processing technique. Above $y/h > 0.7$, there is an asymptote in the values of β or in other words, the values of β tend to go to minus infinity and plus infinity. This is related to a change in the concentration gradient at this location (fig. 5.2). Higher up in the water column ($y/h > 0.8$), there is insufficient data to draw a conclusion.

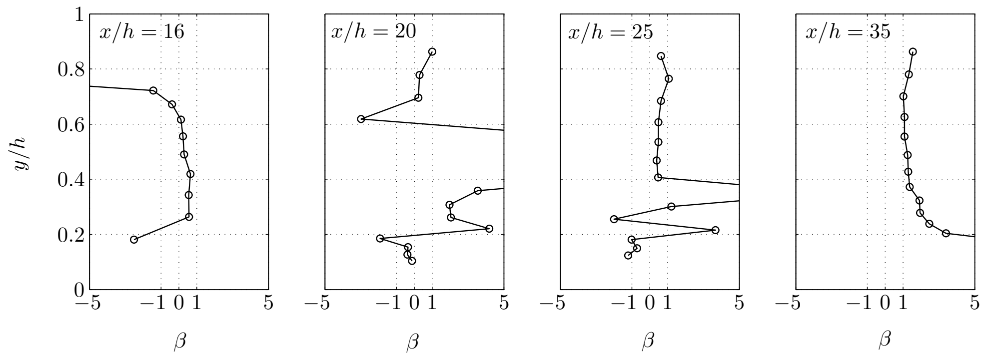

Figure 5.8: Profiles of β, the ratio between eddy diffusivity and eddy viscosity

At $x/h = 20$ and 25, we see the asymptote propagating downwards with increasing distance from the sediment introduction. Above the asymptote, β is also smaller than one. Especially, at $x/h = 20$, large values of β exist, caused by the fact that the concentration profile is constant here over a significant part of the water column ($0.2 < y/h < 0.6$), and hence the concentration gradient is zero. Because of this, the estimated β value in this area is probably quite unreliable. At $x/h = 35$, the asymptote seem to have disappeared. Here, β already shows some characteristics of the fully developed situation in being larger than one over the whole water column.

The sensitivity on the influence of the choice of the vertical velocity was investigated , and it appeared that for $x/h = 16$ and 35, similar results were obtained (respectively, $\beta < 1$, and $\beta > 1$ in the middle of the water column, where the concentrations are most reliable), when the measured vertical fluid velocity was used, rather than a value of zero, to calculate the drift velocities. For the other two profiles $x/h = 20$ and 25, the influence is larger, because the vertical fluid velocity is larger here. In case $x/h = 20$ a similar changing shape remains, but the asymptote has moved downward when using the measured fluid velocity, rather than a value of zero. This profile does not give any conclusive information. The most substantial change appears in the $x/h = 25$ profile, where β changes from being smaller than one to being larger than one in the middle of the water column when using the measured fluid velocity to determine the drift. In addition, the asymptote moves downward, when the measured vertical fluid velocity is used to determine the drift velocity.

One might expect, that the changed value of β is due to the increased settling velocity related to the fact that the particles move downward at the downstream side of the vortices (section 2.2.3). When the increased settling is explicitly taken into account, the value of β is equal to the value in the fully developed situation. In order to verify whether the decreased values of β are related to an increased settling, we write the particle velocity as:

$$\langle v_p \rangle_p = \langle v_f \rangle_f - (v_T + \Delta v_T) - \beta_{FD} \frac{\epsilon_{xy}}{C} \frac{dC}{dy} \tag{5.2}$$

Here, the increase in the settling velocity is written as Δv_T, and βFD is the value of β in the fully developed situation (section 4.3.4). If the extra settling implicitly is included in the value of β (now denoted as β_{NE}), one can write the particle velocity as:

$$\langle v_p \rangle_p = \langle v_f \rangle_f - v_T - \beta_{NE} \frac{\epsilon_{xy}}{C} \frac{dC}{dy} \tag{5.3}$$

Solving these equation for Δv_T leads to:

$$\Delta v_T = (\beta_{NE} - \beta_{FD}) \frac{\epsilon_{xy}}{C} \frac{dC}{dy} \tag{5.4}$$

Since in this situation, $dC/dy > 0$, and $\beta_{FD} > \beta_{NE}$, one finds that $\Delta v_T < 0$, thus that the apparent settling velocity decreases rather than increases. This is in contradiction with the proposed explanation. Hence, one can conclude that the increased apparent settling velocity does not explain the decreased values of β in the non equilibrium situation.

From the preceding, it can be concluded that the ratio of the diffusion coefficient to the eddy viscosity (β) depends on the sediment concentration profile, and is not a universal coefficient. This peculiar behavior of the eddy diffusivity makes the whole concept of gradient diffusion in this situation somewhat awkward and it shows clearly that good results of gradient diffusion models cannot be expected in situations that are not close to equilibrium. Only in the developed situation, a gradient diffusion provides a reasonable estimate in combination with a calibrated Prandtl-Schmidt number.

5.3.3. *Streamwise velocity*

In the following, the streamwise velocities of the particles are analyzed in more detail. It is well known that in a fully developed situation, the mean velocity of the particles is lower than the mean fluid velocity (see chapter 4 and Kaftori *et al.*, 1995b; Best *et al.*, 1997; Muste & Patel, 1997; Kiger & Pan, 2002; Righetti & Romano, 2004; Nezu & Azuma, 2004; Muste *et al.*, 2005). This is attributed to the fact that in the fully developed situation, the particles come from the near wall region, where the velocity is relatively low. A comparison of the fluid and particle velocity by comparing the relative velocity (fig. 5.5) shows that in the present situation, the particles are faster than the fluid close to the injection point. For example at $x/h = 16$, the mean particle velocity is up to $0.25u_*$ faster than the mean fluid velocity, but as close as 25 water depths from the introduction point, the particles have slowed down to a value lower than the fluid velocity. They continue to slow down up to a velocity difference of up to $0.5u_*$ in the fully developed situation.

As already shown in the preceding section, the particles are mainly found in the downward flow structures ($\langle v'_f \rangle_p < 0$) close to the sediment injection point. These structures are the ones that are faster than the mean fluid velocity (i.e. sweeps). It can be seen from the streamwise drift velocity (fig. 5.6) that the presence of particles in fast structures is indeed causing the particle velocity to be larger than the fluid velocity. This figure also shows that at $x/h = 16$, the vertical fluid velocity seen by the particles is downward, which means that the particles are found more often in sweeps than in ejections, thus in fluid structures where the fluid velocity is higher than the mean streamwise velocity, which is also obvious from figure 5.6. The fact that particles are mainly found in downward moving flow structures results in a larger number of particles moving down than moving up (fig. 5.9). In situations that more or less represent a fully developed situation on the other hand, the number of upward and downward moving particles is found to be equal (fig. 5.9), which is in agreement with the findings of Kiger & Pan (2002). Rather interestingly, the absolute values of the drift velocity in both streamwise and wall normal directions show the same pattern (i.e. the largest streamwise drift corresponds to the largest wall normal drift). This could be expected, because the structures responsible for the vertical transport, are also responsible for the horizontal drift, because the horizontal and vertical fluid velocity fluctuations are related through the correlation coefficient R_{uv}. In order to quantify this, we use an expression for the streamwise drift obtained from a gradient diffusion formulation:

$$\langle u'_f \rangle_p = D_{xx} \frac{1}{C} \frac{\partial C}{\partial x} + D_{xy} \frac{1}{C} \frac{\partial C}{\partial y} \tag{5.5}$$

As with eq. 5.1, we neglect the $\partial C/\partial x$ term because it is an order of magnitude smaller than the $\partial C/\partial y$ term. Simonin *et al.* (1993) derived an algebraic model for the drift velocities (similar to a Reynolds flux model), which yields (when the crossing trajectory effect is neglected) the following diffusion coefficient for a stationary uniform flow:

$$D_{xy} = \langle u'_f v'_f \rangle_f T_L + \langle v'^2_f \rangle_f T_L^2 \frac{d\langle u_f \rangle}{dy} \tag{5.6}$$

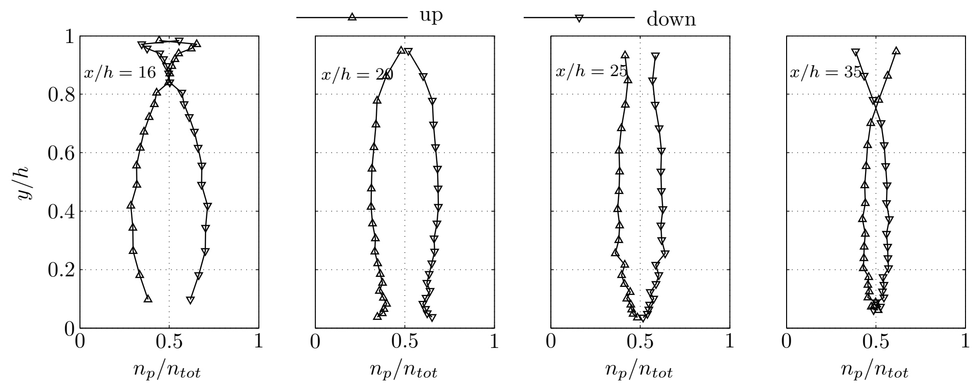

Figure 5.9: Percentage upward and downward moving particles

Now, the Lagrangian time scales can be eliminated using equation 2.13. In this way, the streamwise drift can be estimated to be related to the wall normal drift as:

$$\frac{\langle u'_f \rangle_p}{\langle v'_f \rangle_p} = 2\frac{\langle u'_f v'_f \rangle_f}{\langle v'^2_f \rangle_f} = 2R_{f,uv}\frac{u_{f,rms}}{v_{f,rms}} \tag{5.7}$$

Substituting the empirical expressions from Nezu & Nakagawa (1993) for the fluid velocity fluctuations in eq. 5.7 and a constant value of 0.4 for $R_{f,uv}$, which is good approximation for a large part of the water column (at least for $y/h < 0.7$), one finds that the ratio between the horizontal and the vertical drift velocity is equal to 1.45. Hence the streamwise drift depends on the wall normal drift, which is indeed what we see in the experimental data (fig. 5.10). Rather surprisingly, the two different terms in the equation for D_{xy} appear to be equal when eq. 2.13 is substituted to calculate the Lagrangian time scale. Therefore, using Taylor's diffusion coefficient (such as done by Greimann *et al.*, 1999), which is derived for a homogeneous situation and thus only contains the first term on the right hand side of eq. 5.6, gives half the value for the streamwise drift velocity, and this is not in agreement with the measured data. The physical interpretation of the two terms in equation 5.6 is that the first term shows that the particles have a different velocity than the fluid because they are mainly found in either upward or downward structures, depending on the vertical drift (i.e. the direction of the turbulent diffusion flux). These upward or downward structures have a different velocity depending on the correlation between the horizontal and vertical fluid velocity fluctuations. The second term shows that the particles that are moving upward come from below, where the mean fluid velocity is lower, and therefore these particles move slower. More details of the structures that cause these two processes is given in chapter 6.

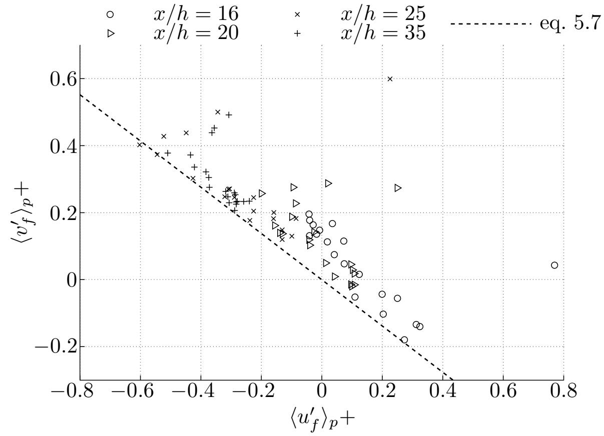

Figure 5.10: Streamwise versus wall normal drift velocity, in combination with eq. 5.7

5.3.4. *Turbulence characteristics*

In this section, the particle and fluid velocity fluctuations will be discussed. In section 2.2.2, it was shown theoretically that the particle velocity fluctuations are approximately equal to the fluid velocity fluctuations at the particle's location, because the particle's inertia is very small (see eq. 2.28). This was confirmed experimentally in section 4.3.3. In this section, it was also shown that there is still a difference between the particle and fluid velocity fluctuations in the fully developed situation, because the particles sample the turbulent structures selectively. It will be investigated whether this also applies to the present situation where the particles are developing toward an equilibrium situation. Especially, this might give some more information about which structures the particles sample in this situation, i.e. depending on the distance traveled from the sediment entrance (and thus on the mean sediment concentration profile).

The fluctuating fluid and particle velocities are shown in figure 5.11 and 5.12. The streamwise fluctuating particle velocities do not differ much from the fluctuating fluid velocities. They are slightly smaller close to the injection point (at $x/h = 16$, most clear for $0.4 < y/h < 0.6$) and slightly larger further away. Larger differences occur in the wall normal fluid and particle velocity fluctuations. Here, the fluid velocity fluctuations are larger than the particle velocity fluctuations for $x/h = 16$ and 20 above $y/h = 0.3$, whereas they are significantly smaller at $x/h = 25$ and 35.

The fluid and particle Reynolds shear stresses are shown in figure 5.13. At $x/h = 16$, the particle Reynolds shear stresses are well below the fluid Reynolds shear stresses for $y/h > 0.2$ and they clearly do not follow a straight line. During its development to a stationary profile, the particle Reynolds shear stress profile increases and straightens until it becomes equal to the fluid Reynolds shear stress profile. This can also be seen very clearly (fig. 5.14) in the correlation function of the streamwise and wall normal fluctuations $R_{uv} = \langle u'v' \rangle / u_{rms} v_{rms}$. Note that the

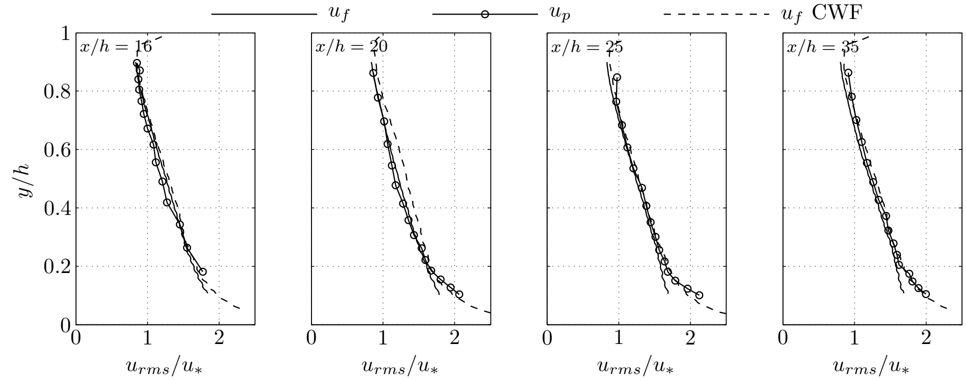

Figure 5.11: Streamwise turbulence profiles of particles (u_p), fluid phase (u_f) and clear water flow (u_f CWF).

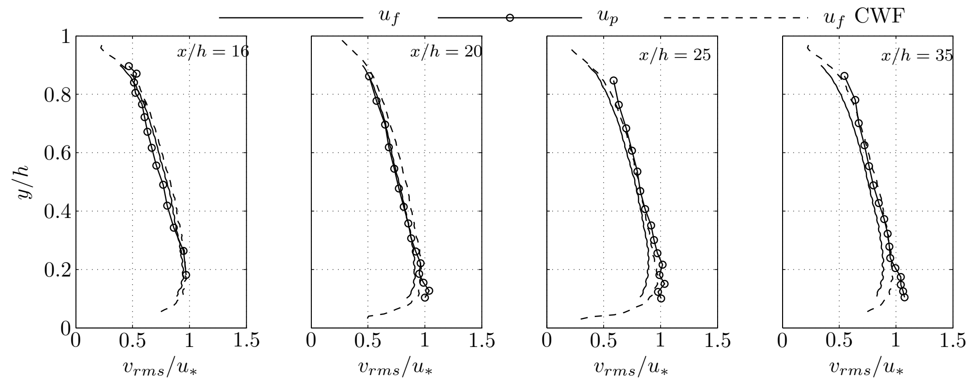

Figure 5.12: Wall normal turbulence profiles of particles (u_p), fluid phase (u_f) and clear water flow (u_f CWF)

comparison of the different cases can be done more easily for the latter quantity, because it is not affected by any errors in the shear velocity u_*.

The previously mentioned effects can be seen much clearer in fig. 5.15, 5.16 and 5.17, where the transfer functions γ_p and γ_f are plotted, which are defined as:

$$\gamma_f = \langle u'_{p,i} u'_{p,j} \rangle_p / \langle u'_{f,i} u'_{f,j} \rangle_f \tag{5.8}$$

$$\gamma_p = \langle u'_{p,i} u'_{p,j} \rangle_p / \langle u'_{f,i} u'_{f,j} \rangle_p \tag{5.9}$$

Thus, γ_f is the ratio between the particle and fluid Reynolds stresses, whereas γ_p is the ratio between the particle Reynolds stresses and fluid Reynolds stresses seen by the particle. According to what was shown in 2.2.2, the latter quantity should be approximately equal to one for sediment particles. From fig. 5.15, 5.16 and 5.17, it indeed appears that γ_p is approximately equal to one, except close to the bottom, where it is larger than one. The increased value near

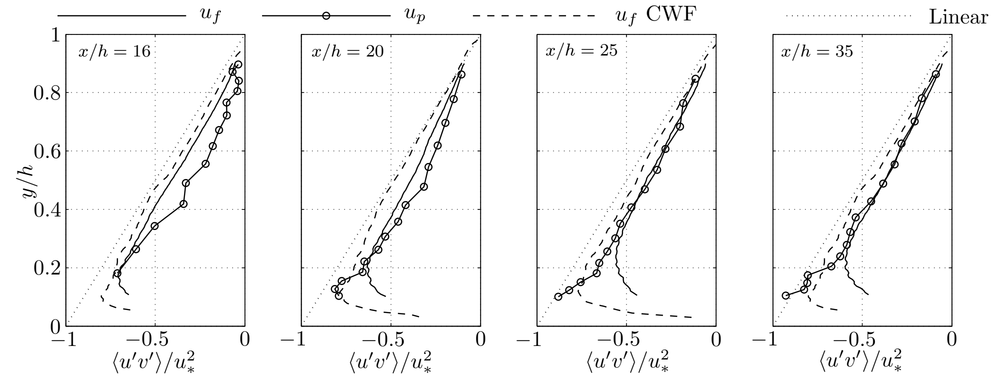

Figure 5.13: Reynolds stress profiles of particles (u_p), fluid phase (u_f) and clear water flow (u_f CWF)

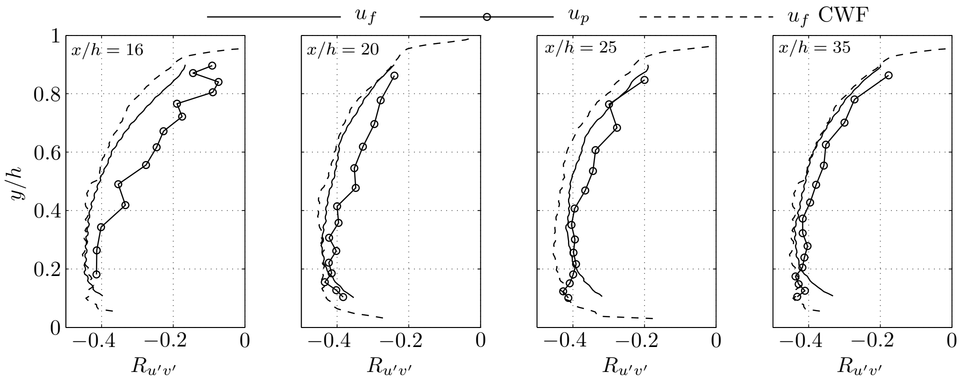

Figure 5.14: Correlation coefficient between horizontal and vertical fluid velocity fluctuations.

the bottom is presumably an artifact of the measurements. Note that the bias in the fluid velocities close to the particles due to the phase discrimination (pp. 78) might result in this value begin biased toward one (section 3.2.4). The ratio γ_f on the other hand is not equal to one. For the streamwise velocity fluctuations, it is clearly smaller than one close to the injection point and it increases to values somewhat larger than one at $x/h = 35$. This is even more clear for the wall normal velocity fluctuations. For the Reynolds shear stresses, the γ_f value is significantly smaller than one close to the injection point (i.e the particle Reynolds stress are significantly lower than the fluid one), but at larger distance from the injection point, this ratio develops to one. The values found here are in agreement with those in section 4.3.3, where it was found that γ_f in the fully developed situation was slightly larger than one for the streamwise velocity fluctuations and significantly larger for the wall normal fluctuations.

Hence it can be concluded that the normal and shear particle Reynolds stresses differ from the ones of the fluid, because the particles sample the flow field selectively. Close to the injection point, the particles are in weaker turbulent structures, than in the fully developed situation. This difference is especially clear for the Reynolds shear stresses. The lower Reynolds shear

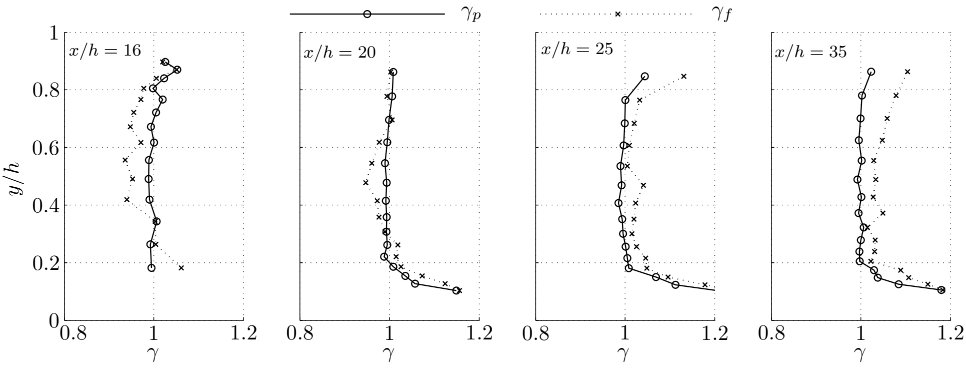

Figure 5.15: Transfer functions for streamwise Reynolds stresses

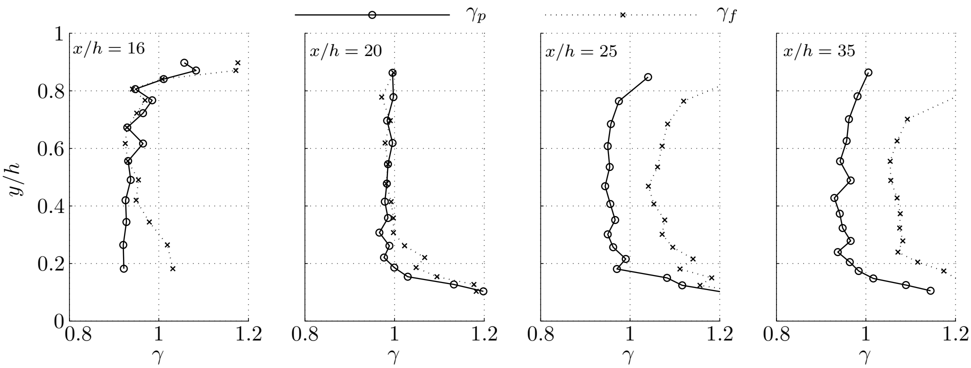

Figure 5.16: Transfer functions for wall normal Reynolds stresses

stresses at small distances from the inlet can be explained by the fact that the particles in this stage are mainly found in sweeps, which although they occur during a larger fraction of time than ejections, contribute less to the Reynolds shear stresses (Nezu & Nakagawa, 1993). Apparently, this is not compensated for by the fact that the particles are located in those sweeps that have the largest vertical velocities.

The difference in the way particles sample the turbulence might partly explain why the β values (the ratio between the turbulent diffusion coefficient for sediment and the eddy viscosity) depend on the distance to the injection point (i.e. on the sediment concentration profile). Close to the injection point, the particles are concentrated in relatively weak turbulent structures, which leads to values of β smaller than one, whereas the opposite happens far from the injection point. Nevertheless the values found here are not strong enough to explain the values of β. The values of β differ strongly from one, whereas the values of γ_f are still quite close to one. In the following section, it is determined which flow structures are sampled by the particles using some conditional averaged quantities.

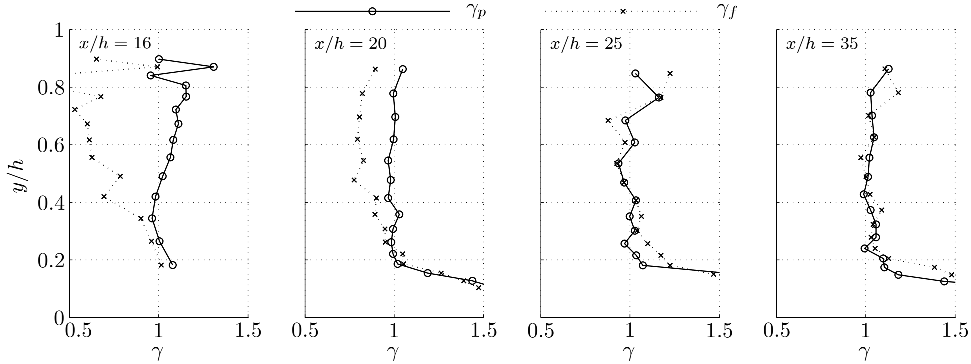

Figure 5.17: Transfer functions for Reynolds shear stresses

5.3.5. *Conditionally averaged quantities*

In section 5.3.4, we have seen that the fluctuating particle velocities differ from the fluctuating fluid velocities, because the particles sample only a subset of the turbulence structures. This means that the fluctuating particle velocity depend on the situation (i.e. the concentration profile), because the particle that move downward sample other (weaker structures) than those that move upward. To investigate this process in more detail, the velocities and turbulence as seen by either upward or downward moving particles are presented.

In fig. 5.18 and 5.19 the difference between the fluid velocity seen by either the upward or downward moving particle and the mean velocity profile is shown. As expected, these profiles clearly show the influence of coherent structures in the sense that downward moving particles are found in faster than average and downward mean flow, and the upward moving particles in a slower upward mean flow.

A comparison of the relative streamwise velocities for all distances from the injection point in fig. 5.18), shows that the downward moving particles decelerate gradually with increasing distance from the injection point, which could be explained by the fact that with increasing distance they less often end up in sweeps (strong downward structures) and more often in weaker downward flow structures. This will be addressed in chapter 6. The upward moving particles on the other hand show a similar streamwise velocity at their location during the whole process. This behavior causes a difference in the absolute value of the streamwise relative velocity, because the streamwise velocity of the upward moving particles differs much more from the average fluid flow velocity than the streamwise velocity from the downward moving particles when approaching the fully developed situation.

The wall normal relative velocities shows similar patterns at each distance from he sediment introduction except for the $x/h = 25$ case (fig. 5.19). This means that the variation with the distance from the injection point in the resulting vertical drift velocity profile patterns mainly occurs because of the difference in the number of upward and downward moving particles (fig.

5.9). Further, this figure shows that the absolute value of the fluid velocity conditioned on the downward moving particles is somewhat smaller than the one conditioned on the upward moving particles. This indicates that the flow structures with an upward directed flow are stronger than the ones with a downward directed flow. However, it is somewhat surprising to find this also for the case close to equilibrium, as it would be expected that the upward and downward conditioned velocities are equal. Hence it seems that this quantity is also somewhat biased by the phase discrimination (p. 78).

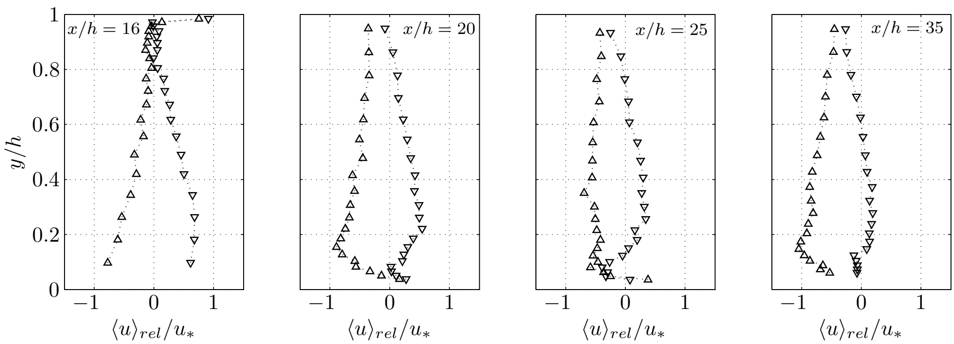

Figure 5.18: Streamwise relative (to mean fluid velocity profile) fluid velocity conditioned on upward and downward moving particles

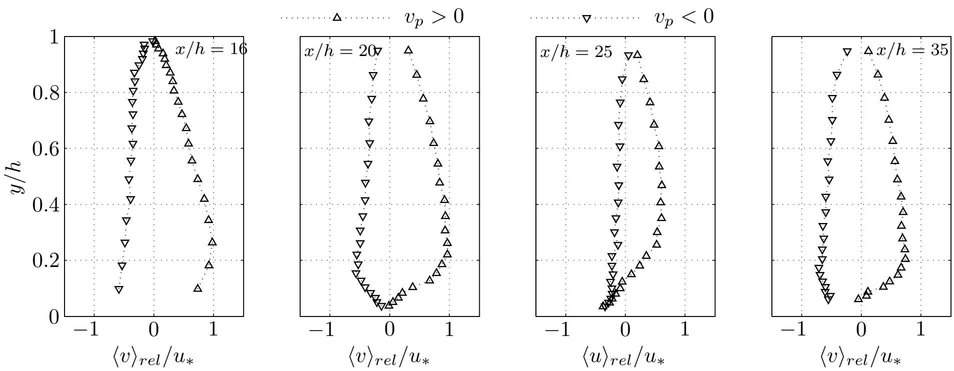

Figure 5.19: Wall normal relative (to mean fluid velocity profile) fluid velocity conditioned on upward and downward moving particles

In order to get an impression of the turbulence seen by either upward or downward moving particles, an extra term needs to be added to the calculated velocity fluctuations at the particle locations:

$$\langle u'_{f,i} u'_{f,j} \rangle_{p+} = \langle u''_{f,i} u''_{f,j} \rangle_{p+} + \Delta u_{f,i} \Delta u_{f,j} \tag{5.10}$$

Here, $\langle u'_{f,i}u'_{f,j}\rangle_{p+}$ is the turbulent Reynolds stress seen by the upward particles, $\langle u''_{f,i}u''_{f,j}\rangle_{p+}$ the fluctuations calculated at the location of the upward moving particles (i.e. $u_{f,i} = \langle u_{f,i}\rangle_{p+} + u''_{f,i}$) and $\Delta u_{f,i} = \langle u_{f,i}\rangle_{p+} - \langle u_{f,i}\rangle_f$. The resulting turbulence profiles seen by either upward or downward moving particles are shown in fig. 5.20, 5.21 and 5.22. From these figures, it appears that the turbulence encountered by the upward moving particles is stronger than encountered by the downward moving particles near the injection point. This difference is strongest in the shear stresses, and weakest in streamwise velocity fluctuations. It is interesting to see that the increase in the fluctuations seen by the upward moving particles is usually larger than the decrease seen by the downward moving particles. Further away from the injection point, the differences between the turbulence seen by the upward and downward moving particles are much smaller and have an equal magnitude for upward and downward moving particles.

This means that the decreased turbulence level (especially in the form of the decreased shear stresses) seen by the particles close to the injection point (as presented in the previous section) is largely determined by the larger number of downward moving particles than upward moving particles (fig. 5.9). The small number of upward particles close to the injection point are apparently only found in strong structures, because the turbulence seen by these particles is the strongest.

A similar increase in the Reynolds shear stress at the location of upward moving particles can be seen in the data presented by Niño & García (1996), who found that in a fully developed situation, the upward moving particles are in those structures that have significantly higher Reynolds shear stresses[3] (up to $4u_*^2$) than average and than found in the present experiment. The difference is that they considered the entrainment of particles at a much lower Rouse number ($u_*/v_T = 0.7$), and only considered the near wall region ($y+ < 150$). For their experiment, the influence of gravity is much stronger than in the present case, and therefore much stronger structures are needed to transport the particles upwards.

5.4. Conclusions and recommendations

In this chapter, the development of the sediment concentration profiles toward a fully developed state was studied for the situation where small particles were released close to the free surface. It was found that the adaptation was very fast at short distances from the sediment injection point ($x/h < 35$), and that the vertical particle velocities in this situation are up to two times larger than the settling velocity due to gravity. Apparently, it is the turbulence, rather than gravity that brings the particles down. The role of gravity is more to determine which structures the particle encounter, similar as was found in the cellular settling experiment of Maxey & Corrsin

3. They calculated the shear stress from the vertical and horizontal particle velocity of the ejected particles, and subtracted the streamwise velocity from the law of the wall in order to get the fluctuating velocity.

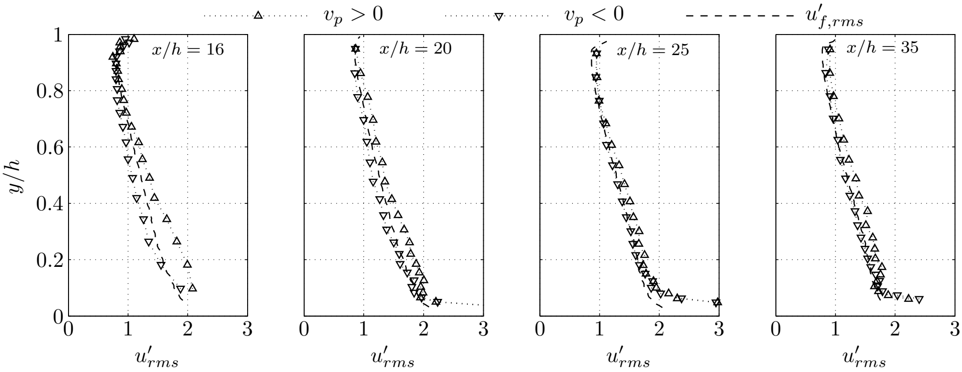

Figure 5.20: Streamwise fluid velocity fluctuations seen by upward and downward moving particles and fluid velocity fluctuation profile.

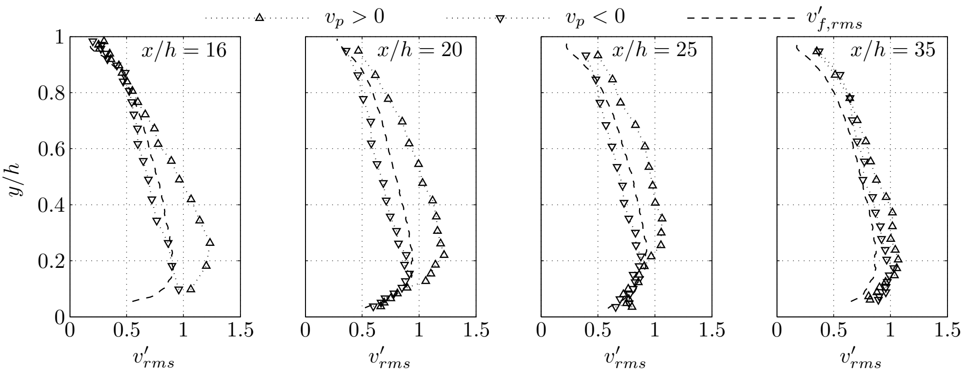

Figure 5.21: Wall normal fluid velocity fluctuations seen by upward and downward moving particles and fluid velocity fluctuation profile.

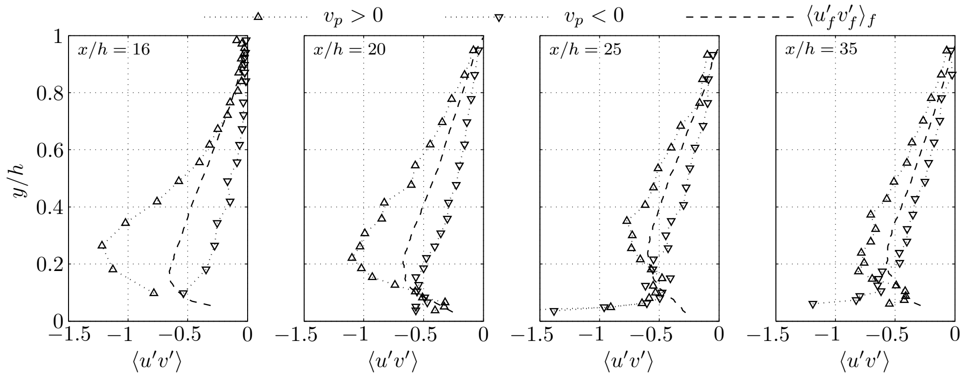

Figure 5.22: Reynolds shear stresses seen by upward and downward moving particles and fluid Reynolds shear stress profile

(1986) as discussed in section 2.2.3. After this fast adaptation period, it takes up to 160 water depths for the particles to reach a completely fully developed state. The second stage of the adaptation, which goes very slow, depends mainly on gravity. This means that the traditional adaptation length scales, determined as the distance a particle travels while it settles from the free surface to the bottom due to gravity, are not adequate to describe the physics of such adaptation processes completely.

The use of a gradient diffusion model in combination with an inverse Prandtl-Schmidt number (β) to relate the eddy viscosity and eddy diffusivity in non-equilibrium situations was shown to be rather cumbersome, because the Prandtl-Schmidt number is case dependent, rather than a universal constant. With most of the sediment high up in the water column, the diffusivity is significantly smaller than the eddy viscosity, whereas when most of the sediment is near the bottom, the eddy diffusivity is larger. This seems to be influenced by the fact that the particles sample weaker turbulent structures, when most sediment is near the free surface.

During the development toward equilibrium, particles are found more often in downward going fluid structures (sweeps), which have a streamwise velocity higher than the mean fluid velocity causing the mean particle velocity to be faster than the fluid velocity. The excess particle velocity decreases gradually together with the decrease of the downward particle velocity, to reach a velocity lower than the fluid velocity in the fully developed situation. It is demonstrated that there is a strong relation between the streamwise and the wall normal drift velocities.

In the non-equilibrium situation, the streamwise fluid and particle turbulence profiles were found to be approximately equal, whereas the particle wall normal turbulence intensities are slightly smaller than the fluid ones. Also, the absolute value of the particle Reynolds stresses are lower than fluid Reynolds stresses in the center of the flow, due to the fact that the particles are located in sweeps, rather than ejections, the latter of which contribute more to the total Reynolds stresses.

Chapter 6

The role of turbulent flow structures in suspended sediment transport[1]

6.1. Introduction

To be able to improve models for the turbulent diffusion of sediment particles, it is important to obtain a better insight in turbulent transport of sediment particles. In the present chapter, this is done by studying the coherent structures of which the turbulence consists and the way in which the individual structures contribute to the transport of individual sediment particles. It was already shown in section 2.3.3 based on the insight from Taylor (1921) that the turbulent diffusion flux of sediment is actually the net average result of the random movement of many particles by many flow structures with different velocities, length and time scales. The coherent structures in a turbulent boundary layer flows (such as open channel flow) consist mostly of hairpin vortices. These vortices and their length and time scales were described in section 2.1.

In the present chapter, the objective is to understand how coherent structures transport sediment particles and how the combined advection by many of these structures leads to an apparent diffusion of the sediment concentration.

One of the first investigations regarding the influence of turbulent flow structures on suspended sediment transport was done by Sumer & Oguz (1978) and Sumer & Deigaard (1981), who showed that for relatively large values of u_*/v_T, the particles are lifted in upward moving flow structures, which after a certain time break-up. Subsequently, the particles are transported downwards in high speed flow structures. Niño & García (1996) showed for a somewhat lower u_*/v_T that intense ejections (the so-called Q2 events) are responsible for lifting particle up.

1. Parts of this chapter have previously been published as: W.A. Breugem and W.S.J. Uijttewaal (2007), "Sediment transport by coherent structures in a turbulent open channel flow experiment" in Bernard J. Geurts et al. (eds.), Particle Laden Flow: From Geophysical to Kolmogorov Scales, pp. 43–55, Springer Verlag and W.A. Breugem and W.S.J. Uijttewaal (2008), "Detailed measurements of suspended sediment transport in a turbulent open channel flow" pp. 499- 506 in River, Coastal and Estuarine Morphodynamics: RCEM 2007 - Dohmen-Janssen & Hulscher (eds.) Taylor & Francis Group, London

This was confirmed in the probability density functions of the fluid at the particle location by Kiger & Pan (2002).

Nevertheless, the role of the other flow structures (sweeps and inward and outward interactions) is not clear, especially for the downward motion of sediment. Therefore, this will be investigated in this chapter. A quadrant analysis is always limited to single point information, even though the spatial extend of the flow structures can be important for particle transport. The reason is that the spatial extend of these structures determines the Lagrangian integral time scale (section 2.1.4), which on its time determines the diffusion coefficient for sediment (section 2.3.3). Thus more insight is necessary on the relation between the quadrant events and the spatial flow structure as well as on the flow structures seen by the particles. In particular, we aim to use the information on which coherent flow structures are important in order to understand the differences between the eddy viscosity and eddy diffusivity that were observed in the previous chapters. Furthermore, the literature has focused on fully developed situations. At present, there is very limited information on which flow structures are most important for non-equilibrium sediment transport. Because it was suggested in chapter 5 that the flow structures important for transport in non-equilibrium situations are different from those in equilibrium situations, this will be investigated here.

In order to obtain insight in the transport process by coherent structures, the following steps are taken in this chapter. First, a quadrant analysis is performed on the fluid and particles velocities, where the velocities at the particle locations are considered as a separate variable, in order to study which type of coherent structures (quadrants) are responsible for the vertical advection of the particles. This is done for the data of the low concentration experiment, which was described in section 3.2. In this analysis, we consider both situations that were studied in the previous two chapters: the “fully developed situation” (chap 4), and the “settling situation” (chap 5). The results for both of these situations are compared, with the purpose of identifying whether the difference in the sediment velocities and concentrations in these situations are affected by the different coherent structures the particles encounter. The results of this quadrant analysis are used to study which flow structures contribute most to the eddy viscosity and eddy diffusivity. In order to relate the quadrant based information with a spatial view of the flow structures, two-point correlation functions for the different quadrant indicators are studied next, with extra attention to the usually neglected third quadrant events. This is followed by a determination of the spatial flow structure that transports the sediment by using conditional averaging (with Linear Stochastic Estimation, section 3.4). This results in a conceptual model of the particle transport by coherent flow structures (the hairpin vortex packets). Finally, more detailed information on the transport process is obtained from considering the length scales of the flow structures encountered by the particles.

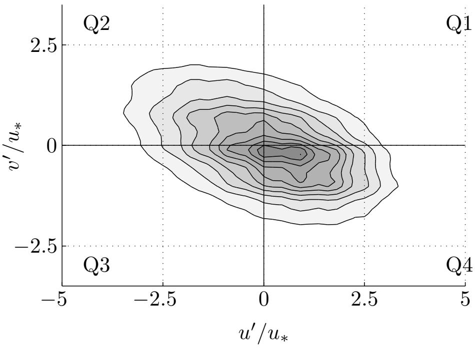

Figure 6.1: Probability density function at $y/h = 0.32$ for the complete fluid velocity in the fully developed situation ($x/h = 160$).

6.2. Quadrant analysis

In the present chapter, the influence of coherent flow structures on the particle transport is studied using a quadrant analysis of the velocity data. In order to do so, the probability density functions (pdf) of the velocity fluctuations ($p(u', v')$) were determined for the fluid velocity at a reference depth, for the fluid velocities at the particle locations, and for the particle velocity. The fluid velocity fluctuations $u'_{f,i}$ were calculated from the instantaneous velocities $u_{f,i}$ with $u'_{f,i} = u_{f,i} - \langle u_{f,i} \rangle_f$, where $\langle\rangle_f$ denotes averaging over the fluid phase. The particle velocity fluctuations were calculated by subtracting the mean particle velocity profile from the individual particle velocities ($u'_{p,i} = u_{p,i} - \langle u_{p,i} \rangle_p$). It is customary to select different quadrants of the pdf to characterize the velocity structures. These quadrants are defined as: Q1 (outward interaction: $u' > 0$ and $v' > 0$), Q2 (ejection: $u' < 0$ and $v' > 0$), Q3 (inward interaction: $u' < 0$ and $v' < 0$), and Q4 (sweep: $u' > 0$ and $v' < 0$). These quadrants are shown schematically in fig. 2.3.

A typical example of a pdf of the fluid velocity fluctuations is shown in figure 6.1. The fluid velocity pdf shows that the second and fourth quadrants are more important than the first and third, with events in the second quadrant that are more extreme than those in the fourth quadrant. These results for the fluid velocities have already been obtained many times (e.g. Willmarth & Lu, 1972; Nakagawa & Nezu, 1981). A consequence of this is that the skewness in the streamwise fluctuations is negative and the skewness in the wall normal ones positive (Wei & Willmarth, 1991). The fluid velocity histograms at the particle location (fig. 6.2) are much less converged, due to the fact that these are taken over much smaller samples as the sediment concentration is low. Despite the scatter in the data, clear differences can be seen in the pdf of the fluid velocity at the particle location between the settling situation and the fully developed situation. The pdf in the developing situation shows an increased number of particles

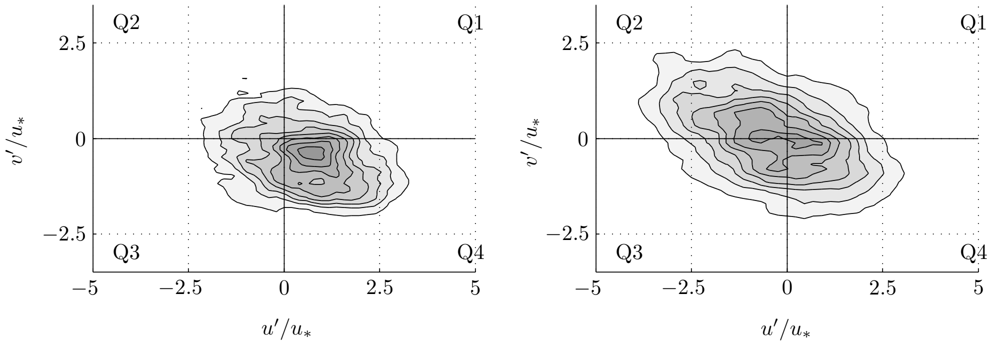

Figure 6.2: Probability density function at $y/h = 0.32$ for the fluid velocity at the particle location. Left: developing situation ($x/h = 16$); Right: fully developed situation ($x/h = 160$).

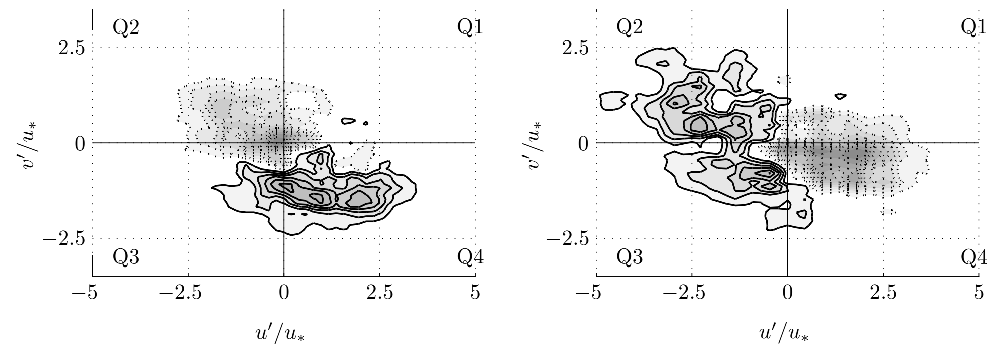

Figure 6.3: Difference in the probability density function of the complete fluid velocity and the fluid velocity at the particle location at $y/h = 0.32$. Negative values are denoted by a dotted line. Left: developing situation ($x/h = 16$); Right: fully developed situation ($x/h = 160$).

in downward flow structures (especially in sweeps), whereas in the fully developed situation, the upward moving particles are mainly found in Q2 events (and hardly any particles are found in Q1), whereas downward moving particles are distributed rather equally over Q3 and Q4 events.

There are also clear differences between these pdfs and the fluid velocity pdf. To show these differences clearer, the fluid velocity was subtracted from the pdf of the fluid velocity at the particle locations (fig. 6.3). In the developing situation, it is shown that the particles are found relatively more often in the downward flow structures especially in Q4 events. There is a smaller increase in the number of Q3 events that the particles encounter. The particles are less often found in Q2 (and to a lesser extend also Q1) structures. For the fully developed situation, figure 6.3 shows an increased occurrence of particles in the second and third quadrants (i.e. the

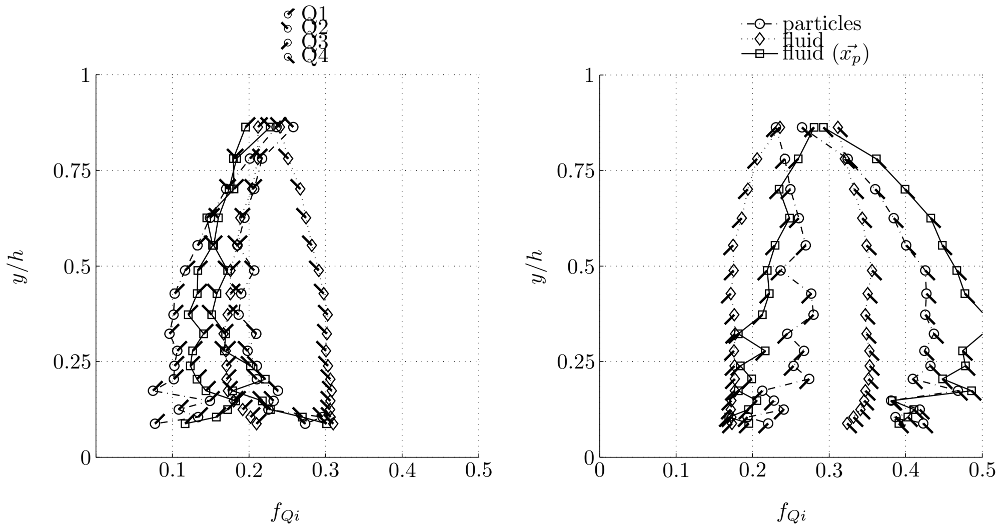

Figure 6.4: Fraction of occurrence in a given quadrant for fluid, fluid at the particle location, and particles. *Settling situation* ($x/h = 16$). Left: quadrants with upward motion; Right, quadrants with downward motion.

ones with a lower than average streamwise velocity) and a decreased occurrence of particles in the first and fourth quadrant events. In fact, the number of fourth quadrant events has decreased to a value that is equal to the number of third quadrant events. Due to this shift, the mean streamwise fluid velocity at the particle location, and hence the mean particle velocity, is lower than the overall mean fluid velocity. This has already been demonstrated many times (e.g. chapter 4 and references therein). The reason for this is that the mean streamwise particle velocity is to a very good approximation equal to the mean fluid velocity at the particle location, as the particle's inertia is too small to cause any streamwise slip velocity (maybe except very close to the bottom; section 2.2.2).

In order to get a view of the occurrence of these processes over the complete water column, we determined the fractional occurrence of a particular event $f(Q_i)$:

$$f(Q_i) = \frac{\int_{Q_i} p(u', v') du' dv'}{\sum_{i=1}^{4} \int_{Q_i} p(u', v') du' dv'} \tag{6.1}$$

This variable is calculated for the overall fluid velocity fluctuations, the fluid velocity fluctuations at the particle location, and the particle velocity fluctuations. The quadrant contributions for the "settling situation" are shown in fig. 6.4. This figure confirms that in this situation, the particles are more frequently found in the downward flow structures (Q3 and Q4). Also, this figure shows that they are found much less frequently in the upward flow events (Q1 and Q2).

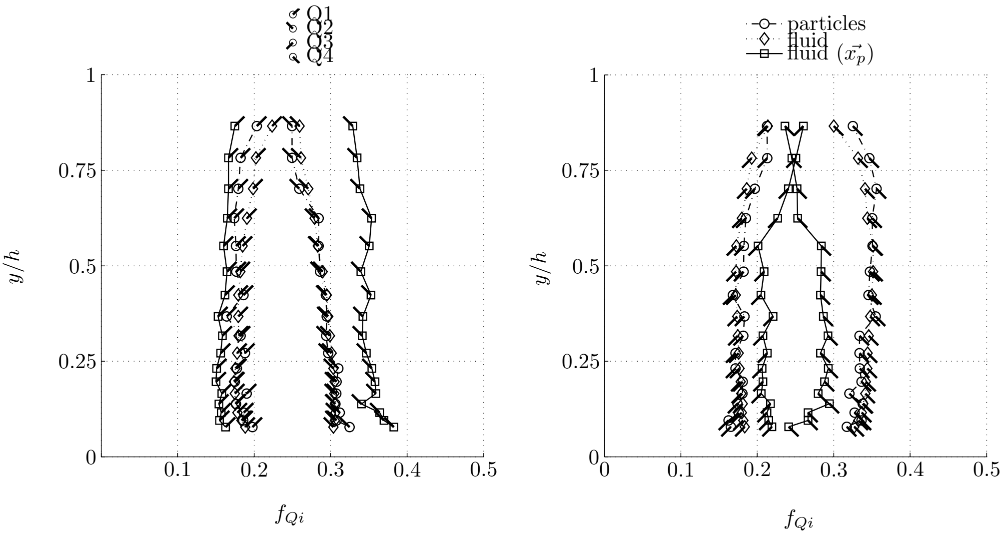

Figure 6.5: Fraction of occurrence in a given quadrant for fluid, fluid at the particle location, and particles. *Fully developed situation* ($x/h = 160$). Left: quadrants with upward motion; Right, quadrants with downward motion.

Especially, in the occurrence of Q2 events, a large difference exists between the fluid velocity data and those seen by the particles. This figure confirms that the increased downward velocity of the particles is caused by an increased occurrence of the particles in the downward moving flow structures (section 5.3). Furthermore, this figure confirms that the increased streamwise particle velocity (compared to the fluid one) is caused by the increased occurrence of particles in Q4 events and a decreased occurrence in Q2 events. In the settling situation, the fraction of occurrence for the particle velocity fluctuations in the different quadrants show a similar pattern as the one of the fluid velocity fluctuations seen by the particles, but they are shifted. The reason for this shift is the difference between the average fluid and the average particle velocity. In other words, if those two average velocities were the same, the profiles for the fraction of occurrence per quadrant would be the same for the particles and the fluid velocity fluctuations at the particles' location, because the velocity lag between the two is negligible (section 2.2.2 and 4.3.3).

The fraction of the occurrence of the different events in the fully developed situation is shown in figure 6.5. This figure confirms what has previously been mentioned for the pdf (fig. 6.2 and 6.3): that the particles encounter Q2 and Q3 structures more frequently than one would expect from a random distribution and that they are found less often in Q4 events. This happens over the complete water column. It appears once more that upward moving particles are found almost uniquely in Q2 event, thus showing the importance of these events for the turbulent

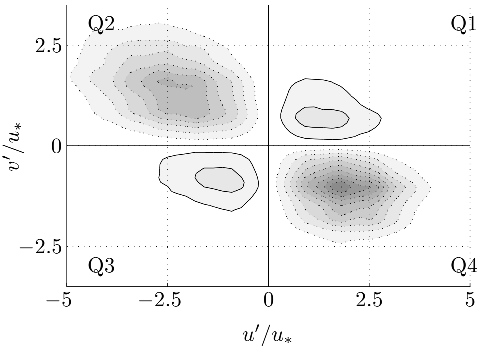

Figure 6.6: Probability density function of the contributions to the fluid Reynolds shear stresses $y/h = 0.32$ in the fully developed situation ($x/h = 160$). Negative contributions are denoted by a dotted line.

transport of sediment particles. The increase of the occurrence of particles in Q3 events and the decrease of the occurrence in Q4 events makes that downward moving particle are divided almost equally over these two quadrants. In the fully developed situation, there is a difference in the fraction of the occurrence of an event between the particle velocities and the fluid velocity at the particle locations. The reason is that for a quadrant analysis on the particle velocities, a lower mean velocity is subtracted (the particle velocity), than for an analysis of the fluid velocity at the particle location, where the mean fluid velocity was subtracted. Because of this, some events are shifted from the third quadrant to the fourth, and from the first to the second. In case one's interest is in determining which flow structures are important for entrainment, obviously the correct definition is the one concerning the fluid velocity fluctuations at the particle location. When doing so, the fluctuations must be obtained by subtracting the overall mean fluid velocity from the instantaneous velocity at the location of the particles. The significant difference between the quadrant fraction distribution of the fluid on the particle locations and the one of the particles explains the difference of the present conclusions with those from Nezu & Azuma (2004), Cellino & Lemmin (2004) and Righetti & Romano (2004), who all perform their quadrant analyses on the sediment particle velocities. Therefore, they did not find the increased occurrence of third quadrant events and the decreased occurrence of fourth quadrant events in a fully developed situation.

In order to understand the importance of these quadrants to the vertical transport of momentum and sediment, we study the contributions of each quadrant to the fluid Reynolds shear stresses and to the vertical drift velocities. An example of the contribution of the different fluid flow structures to the Reynolds shear stresses is shown in fig. 6.6. This contribution is calculated as $u'_f v'_f p(u'_f, v'_f)$. It is an important quantity to show, because the two-dimensional integral of this quantity is equal to the fluid Reynolds shear stress at this height. Fig. 6.6 shows that the largest contributions to fluid Reynolds shear stresses (which are negative) come from Q2 events and to a slightly lesser extend from the Q4 events. Opposite contributions come from the Q1 and Q3 events, but these are much weaker than the contributions from the Q2 and Q4 events.

The drift velocity is the average of the fluid velocity fluctuations at the particle location (see section 2.3.2). It is an important quantity, because it is equal to the turbulent diffusion flux per unit of concentration (Simonin *et al.*, 1993). A pdf of the contributions to the vertical drift velocity is shown in fig. 6.7 for the settling and the fully developed situation. These contributions are defined as $v'_f p(u'(x_p), v'(x_p))$. Fig. 6.7 shows that the main contribution to the drift velocity in the settling situation comes from the Q4 events and to a lesser extend from the Q3 events. The contribution of the upward flow structures (Q1 and Q2) to the drift velocity are limited. In the fully developed situation, the contribution to the upward drift velocity comes largely from the Q2 events. It is counterbalanced by negative contribution to the drift for Q3 and Q4 events, which both contribute a similar amount. This shows that the flow structures that are important for vertical particle transport are quite different in different situation.

The differences between the structures that contribute to the drift velocity (fig. 6.7) and those that contribute to the Reynolds shear stresses (fig. 6.6) are dramatic. The main contribution to the fluid Reynolds stresses (momentum transport from high to low fluid velocity regions) occurs in Q2 and Q4 events. However, these two quadrants always give opposite contributions to the drift velocity. Which of these quadrants (Q2 or Q4) is important for sediment transports from high to low concentration regions, depends on the direction of the concentration gradient. It further appears that Q3 events, which are not important for momentum transport can be important for downward sediment transport. Moreover, the contributions per quadrant (i.e. the contribution per u',v' point) are rather different. There are no contributions to the Reynolds shear stresses if either u' or v' are zero. In contrast, a non-negligible contribution to the drift velocity is obtained from structures that have a u' that is close to zero. A consequence is that the peaks in fig. 6.7 and 6.6 occur at different combinations of u' and v'. The peak in the fluid Reynolds shear stresses can be found rather in middle of each quadrant, where both u' and v' are rather larger. The peaks in the pdf of the drift velocity are found closer to $u' = 0$.

6.2.1. Implications for suspended sediment transport modeling

In the previous section, it was shown that the quadrants responsible for the vertical transport of fluid momentum and those responsible for particle transport are different. In order to get a more accurate and quantitative view of these processes, we study the influence of the different quadrants on the eddy diffusivity and eddy viscosity. We will consider this especially from the viewpoint of the third hypothesis about the difference between the eddy viscosity and eddy diffusivity (section 2.3.3): there are differences between the eddy viscosity and eddy diffusivity, because particles and momentum are transported by different flow structures. In order to do

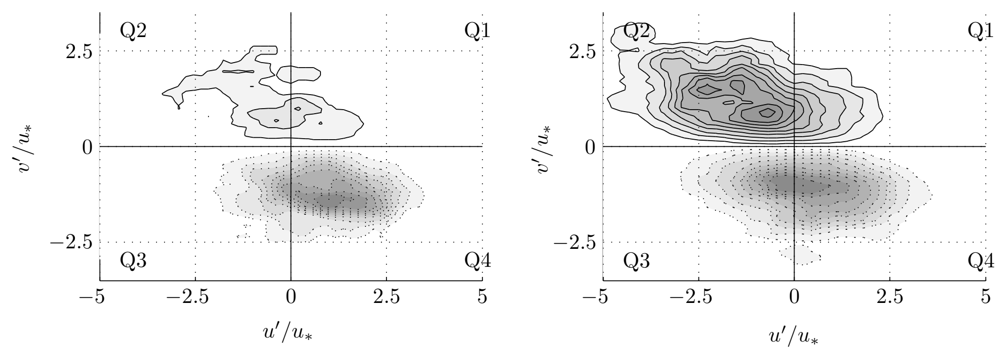

Figure 6.7: Probability density function of the drift velocity contribution at $y/h = 0.32$. Left: developing situation ($x/h = 16$); Right: fully developed situation $x/h = 160$. Negative contributions are denoted as a dotted line.

so, we determine the contribution to the eddy viscosity and eddy diffusivity from the different quadrants. These contributions are calculated (in analogy with eq. 4.5 and 4.4) respectively by:

$$\langle \tilde{\epsilon}_{xy}(Q_i) \rangle = - \left(\frac{\partial \langle u_f \rangle}{\partial y} \right)^{-1} \int_{Qi} u'_f v'_f p(u'_f v'_f) du'_f dv'_f \tag{6.2}$$

$$\langle \tilde{D}_{yy}(Q_i) \rangle = - \frac{C}{dC/dy} \int_{Qi} v'_f p(u'_f(x_p) v'_f(x_p)) dv'_f \tag{6.3}$$

In these equations, the only terms that depend on the quadrants are respectively the Reynolds shear stresses per quadrant and the drift velocity per quadrant. Thus it could be considered as a different normalization of the fluid Reynolds shear stresses and vertical drift velocity per quadrant, which both were discussed in section 6.2. In this way, they represent the turbulent fluxes of streamwise momentum and particles per quadrant, which are normalized in such a way that the influence of the concentration gradient or fluid velocity gradient is compensated for. We used this distinction (that we are representing turbulent fluxes, rather than diffusion coefficients), since the concept of a diffusion coefficient per quadrant seems in some sense at odds with the whole concept of gradient diffusion. However, it is a convenient way in which the momentum and particle fluxes can be compared. Because of the signs that are used, these equations give positive contributions for transport from high to low concentration regions. Thus upward transport of low momentum fluid and downward transport of high velocity fluid have a positive sign, as do upward sediment fluxes when most sediment is found near the bed.

The results are shown in fig. 6.8 for the settling situation and in fig. 6.9 for the fully developed situation. These figures show that Q2 and to a lesser extend Q4 events contribute to the eddy viscosity. The Q1 and Q3 events contribute to momentum transport in the opposite direction.

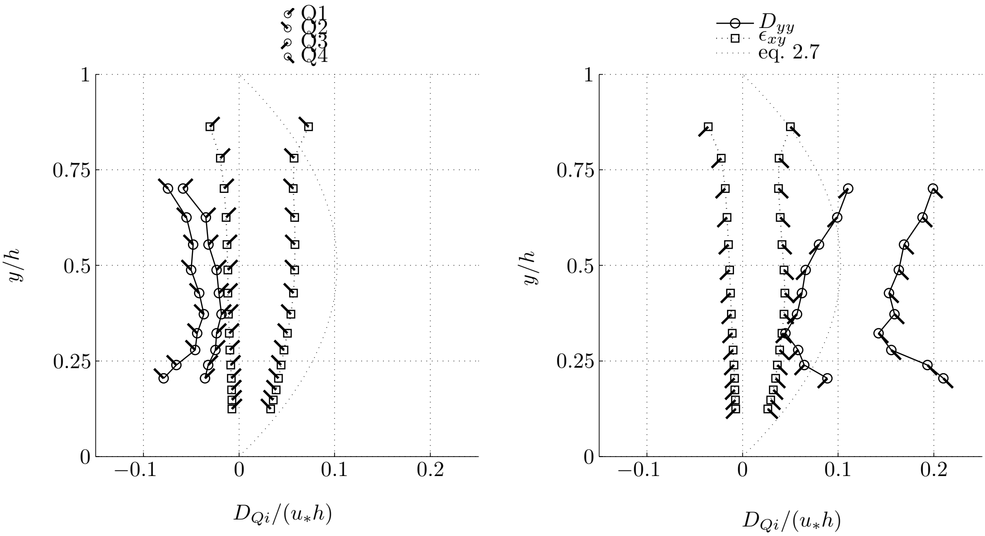

Figure 6.8: Contribution to the eddy viscosity (dotted line with crosses) and eddy diffusivity (dashed line with circles) for a given quadrant in the settling situation ($x/h = 16$). For comparison, the parabolic eddy viscosity profile (eq. 2.7) is also shown (dotted line). The quadrants are indicted by an arrow showing the fluid direction in a quadrant with respect to the mean fluid. Left: quadrants with upward motion; Right: quadrants with downward motion;

However, the magnitude of their contributions is much less than those of the Q2 and Q4 events. For sediment motion, the balance is quite different. In the settling situation, positive contributions to the eddy diffusivity come from Q3 and Q4 event. From these contributions, the one coming from Q4 is twice as large as the one from Q3. Negative contributions come from Q1 and Q2 events, with Q2 events significantly larger than Q1. In fact the contribution from Q2 events has a rather similar magnitude as the contribution from Q3 events. When we compare the magnitude of the contributions to the eddy viscosity and eddy diffusivity per quadrant, the differences between those are large. It appears that each of the quadrants separately is much more effective in transporting sediment particles than momentum (i.e. there is a larger contribution to the eddy diffusivity than to the eddy viscosity).

In the fully developed situation (fig. 6.9), the contributions to the eddy diffusivity are rather different from those in the settling situation. Now, positive contributions come almost completely from Q2 events, which are up to four times larger than the contribution from Q1 events. Negative contributions comes from both Q3 and Q4 events, where the contribution of the Q4 events is 50% larger than the one of the Q3 events. However, both these contributions have a magnitude that is clearly less than those of the Q2 events. In the fully developed situations, the contributions of the individual quadrants to the eddy diffusivity are much larger than those to

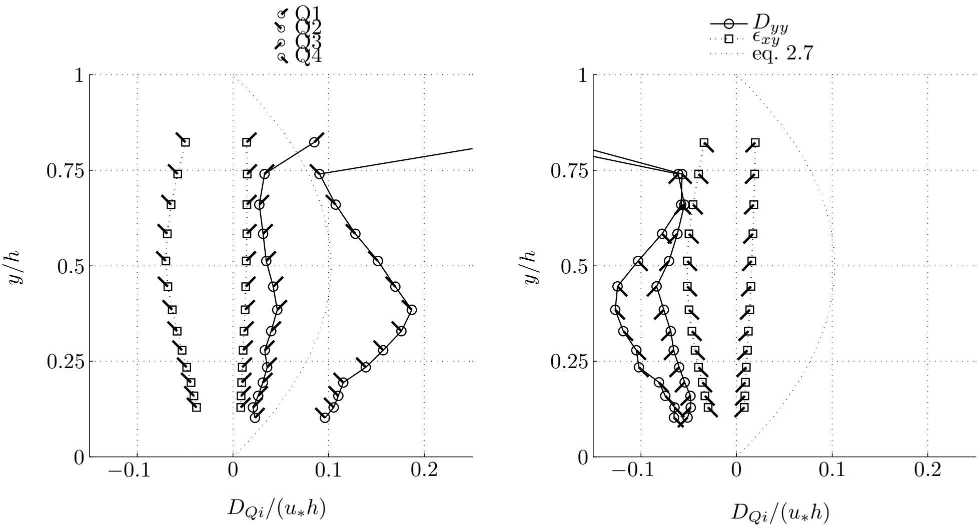

Figure 6.9: Contribution to the eddy viscosity (dotted line) and eddy diffusivity (dashed line with circles) for a given quadrant in the fully developed situation ($x/h = 160$). Symbols as in fig. 6.8

the eddy viscosity, similar as what was found in the settling situation.

The results of $\tilde{D}_{yy}(Q_i)$ are to some extend influenced by the bias error due to the phase discrimination (section 4.3.4, pp. 78), which leads to a fluid velocity at the particle location that is biased to the particle velocity. Since the slip velocity between fluid and particle is zero in the horizontal direction and equal to the settling velocity vertically, the bias error is of the order of magnitude of the settling velocity. The drift velocities per quadrant are all significantly larger than the settling velocity. Therefore, the results for the drift velocity per quadrant, and thus those for the eddy diffusivity per quadrant, are only moderately affected by the bias error. Due to this bias error, contributions to Q1 and Q2 will be underestimated, and those to Q3 and Q4 will be overestimated.

However, since the vertical drift velocity is significantly biased (section 4.3.4), the net results of the analysis (obtained by adding the contributions of all four quadrants) are also strongly biased. Thus we are not able to determine β directly from fig. 6.8 and fig. 6.9. Nevertheless, one can infer from this data that in the settling situations, the largest negative contribution to the eddy diffusivity cancels out some of the largest positive contributions, whereas the contribution of Q2 and Q4 to the eddy viscosity (the largest ones) add up to the final eddy viscosity. In the settling situations, the positive contributions to the eddy diffusivity are overestimated and the negative contributions underestimated. Hence, the net result (i.e. the sum of all those contributions) is in this case larger for the eddy viscosity than for the eddy diffusivity (section 5.3.2). In the fully developed situation, the positive contributions to the eddy diffusivity are underestimated and the negative contributions are overestimated. In this situations, the particles are mainly in the Q2 structures, which are more effective in transporting sediment particles than the other quadrants. Therefore, this leads to a net contribution of the different quadrants that is larger for the eddy diffusivity than for the eddy viscosity (section 4.3.4).

Thus we can conclude that the observed value of β (the ratio of the eddy diffusivity and the eddy viscosity) is the result of the net contributions of the different quadrants. These are substantially different in magnitude for contributions to the eddy viscosity and eddy diffusivity. Therefore, it is not surprising that β is not equal to one. From this, one can conclude that the main weakness in the current modeling approach is the use of the analogy of the transport of sediment and fluid momentum. It appears that modeling can be improved by developing models for the eddy diffusivity that are not explicitly based on this assumption (using the proportionality coefficient β), but instead reflect the role of the four quadrants in transporting sediment.

6.3. Relation between vortices and quadrants

In the preceding section, the relation between the vertical sediment transport and coherent structures in the turbulence was discussed using a quadrant analysis. This type of analysis is a single point analysis, which does not provide any spatial information. In the present section, the information of the quadrant analysis is linked to the spatial structure of the flow and especially to the occurring hairpin vortices (section 2.1.3). Already much research has been performed on the relation between vortices and the second and fourth quadrant events (e.g. Nezu & Nakagawa, 1993; Robinson, 1991; Adrian *et al.*, 2000), because these are the quadrants that are important for understanding the Reynolds shear stresses. However, the first and third quadrants have received much less attention, even though it appeared in the preceding section that the third quadrant is important for the downward transport of sediment particles in the fully developed situation. Therefore, we will consider the spatial relation between vortices and all four quadrants, as well as the relation of quadrants with respect to each other, with some emphasis to the third quadrant.

In order to study the spatial relation between different quadrant events, we use the quadrant indicator function $Q_i(x, y)$, which is one at a certain location for a certain quadrant if the velocity fluctuations occur inside this quadrant at this location, and which is zero otherwise. There are four of these quadrant indicator functions, one for each quadrant. To give an example, if at a location $u' < 0$ and $v' > 0$, then $Q_2(x, y) = 1$ and the other quadrant indicator functions are zero. The two-point correlation functions between the swirling strength λ_s (section 3.4) at a given reference location and the quadrant indicator function obtained from the measured velocity field in a vertical plane are shown in fig. 6.10. In doing so, it is assumed that a vortex head is defined as a point in the measured velocity field with a high value of the swirling strength value. Any effects of the size of the vortex head is neglected. However, since the size of the vortex head is generally small, the swirling strength is strongly peaked, the error in doing so is small. A positive correlation coefficient implies that at this location a certain quadrant event occurs more often than average when a vortex head is present. A negative correlation coefficient means that this event occurs less frequently than average.

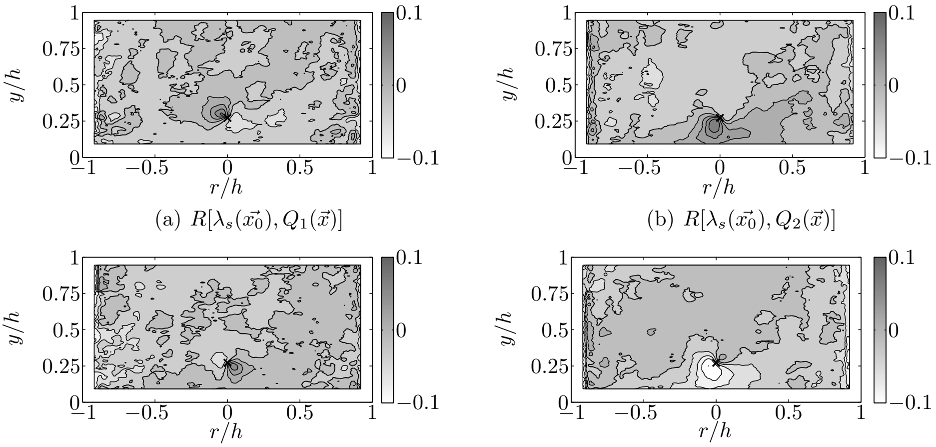

(a) $R[\lambda_s(\vec{x_0}), Q_1(\vec{x})]$ (b) $R[\lambda_s(\vec{x_0}), Q_2(\vec{x})]$

(c) $R[\lambda_s(\vec{x_0}), Q_3(\vec{x})]$ (d) $R[\lambda_s(\vec{x_0}), Q_4(\vec{x})]$

Figure 6.10: Correlation (gray scale) between swirling strength and quadrant indicator function for $y_{ref}/h = 0.27$ (marked with a cross). The zero contour line is indicated with a bold line.

From fig. 6.10, it can easily be seen at which locations the different quadrants occur with respect to the head of a hairpin vortex. The results from this figure are in agreement with what is known from the literature (section 2.1.3), which has mainly been focused on ejections and sweeps. Sweeps (Q4) are found above the hairpin with the most frequent occurrence downstream of the vortex head, whereas ejections (Q2) are found upstream and below the head of the hairpin vortex. The first and third quadrant events have received much less attention in literature. It appears that both these events occur at the locations that could be inferred from the induced flow field of a hairpin vortex packet. First quadrant structures appear above and downstream of the hairpin vortex. Third quadrant structures appear to be located below the hairpin vortex. The figure also clearly reveals the triangular structures of the hairpin vortex packets (section 2.1.3). Note that the values of the correlation coefficient are quite low. Thus the patterns only give a slight tendency, but also reveal that individual hairpin vortices are quite variable (also shown by del Álamo *et al.*, 2006). However, this is in line with other correlations using swirling strength (such as those between swirling strength and velocities; Christensen & Adrian, 2001), which also tend to be quite low. This is also related to the intermittent character of the swirling strength function. Because of this, the two-point correlation functions are mainly determined by a relatively small number of very strong vortices.

From this figure, one can infer the spatial relation between the different quadrants. Especially one might expect that the second and third quadrant events occur side by side, with the third quadrant upstream of the second quadrant. To verify this, the correlations between two different quadrant indicator functions are plotted in fig. 6.11 with the second and fourth quadrant at the reference position. In this figure, the first quadrant event is not plotted, because of its small importance for sediment transport (section 6.2). The autocorrelation functions of the second and fourth quadrant give an indication of the size of these events. They show some similarity with autocorrelation functions of the wall normal velocity fluctuations (such as shown in Liu *et al.*, 2001). The correlations are almost circular for high values of the correlation. This could be expected, because the separation between two different quadrants occurs because of a sign change in the wall normal direction. However, at lower values of the correlation function, the cross correlation between the quadrant indicator functions are more elongated in the streamwise direction than in the wall normal direction. Basically, the second and fourth quadrant functions have similar sizes.

The correlation function between the Q2 and Q4 and the one between Q4 and Q2[2], reveals that the two quadrants do not occur side by side (large regions of negative correlations are found around the reference point)[3]. Thus, if there is a sweep, then there is usually not an ejection present in the nearby flow field and vice versa. The correlation function between Q2 and Q3 on the other hand, reveals a small region of negative correlation and a relatively large region of slightly positive correlations. Thus Q2 and Q3 events do occur side by side and thus they seem to be induced by the same hairpin vortex packet.

6.4. Sediment transport in a turbulent flow structure

In this section, we will study the spatial structure of the sediment transporting flow structures for the two different situation that were also considered in the previous sections. We will study this from conditional averages of the flow field in the vicinity of a vortex head. The conditional averages are obtained by calculating the average of the velocity fluctuations ($u'(\vec{x_0}+\vec{r})$ and $v'(\vec{x_0}+\vec{r})$) conditioned on the swirling strength (λ_s) at location $\vec{x_0}$ (see section 3.4.2 for an explanation of the use of the swirling strength as an indicator of a vortex). The conditional averages are obtained from two-point correlation functions by using linear stochastic estimation (LSE). More details on this technique can be found in section 3.4 and appendix B.

2. These two correlation functions are not symmetric. They would be if the flow were homogeneous, but the inhomogeneity in the wall normal direction breaks the symmetry, except for the streamwise correlation function at $y = y_{ref}$, where one can find $R\left[Q_2(\vec{x_0})Q_4(\vec{x0}+\vec{r})\right] = R\left[Q_4(\vec{x_0})Q_2(\vec{x0}-\vec{r})\right]$.

3. Note that the correlation at the reference point does not need to be equal to -1, as one might naively expect. In fact, one can calculate that at this point, the correlation between quadrants i and j is equal to: $R[Q_i\vec{x_0}Q_j\vec{x_0}] = -\left(\frac{\langle Q_i\rangle\langle Q_j\rangle}{(1-\langle Q_i\rangle)(1-\langle Q_j\rangle)}\right)^{1/2}$

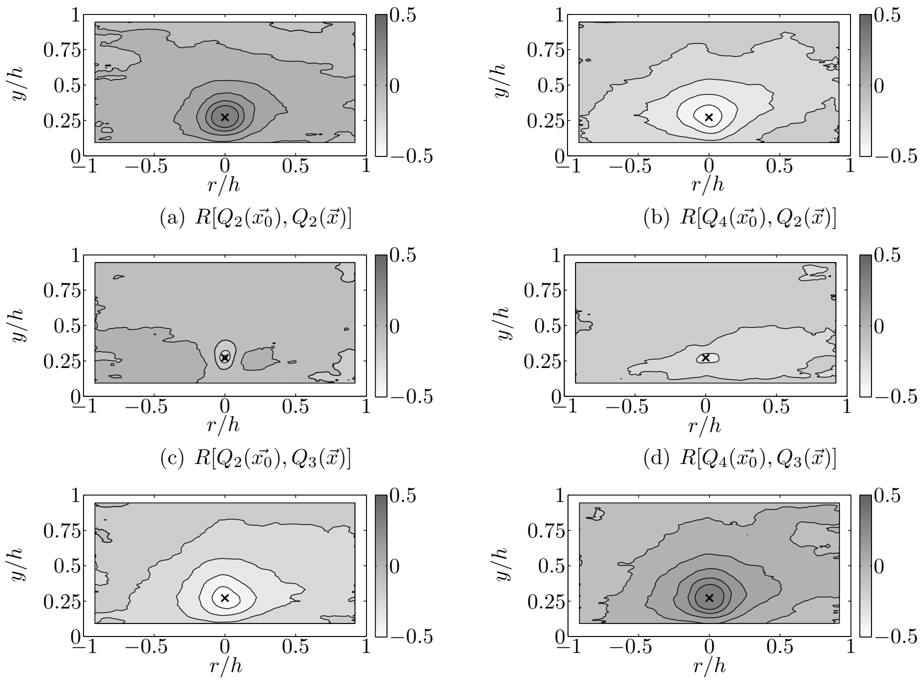

(a) $R[Q_2(\vec{x_0}), Q_2(\vec{x})]$ (b) $R[Q_4(\vec{x_0}), Q_2(\vec{x})]$

(c) $R[Q_2(\vec{x_0}), Q_3(\vec{x})]$ (d) $R[Q_4(\vec{x_0}), Q_3(\vec{x})]$

(e) $R[Q_2(\vec{x_0}), Q_4(\vec{x})]$ (f) $R[Q4(\vec{x_0}), Q_4(\vec{x})]$

Figure 6.11: Correlation function between two quadrant indicator functions with $y_{ref}/h = 0.27$ (marked with a cross). The zero contour line is indicated with a bold line.

An example of a conditionally averaged fluid flow field around a vortex head at $y_0 = 0.56h$ is given in figure 6.12. This conditional average was calculated from the fluid velocity fluctuations, thus the mean flow was subtracted from this flow field. A streamline plot[4] was used to visualize the flow direction clearly even at large distances from the hairpin vortex. This was preferred above the normalized vector map Christensen & Adrian (2001) used. A vector plot without normalization is used, which gives a clear impression of the size of the flow structures. A swirling flow pattern is clearly visible at this location, and it is also clear that a strong Q2 event that extends to the bed can be found below the vortex head. This means that the whole flow structure (vortex and the induced flow) can be classified as an attached eddy (Perry & Chong, 1982). It is also interesting to note the absence of strong Q4 events in the conditional average. A small Q3 event is visible upstream and below the vortex head, and another weaker one downstream of the vortex head.

The conditionally averaged drift velocity (i.e. fluid velocity at the location of the sediment

4. Note that by plotting the streamlines using the conditional average of the fluctuating velocities (u' and v'), it is assumed that the flow structure moves with the average flow velocity. This seems a rather crude assumption, and more research seems necessary to obtain the convection velocity of individual flow structures.

particles) around a vortex head at $y_0 = 0.5h$ is shown in figure 6.13. Note that the drift velocity, is not a zero-mean quantity (chap 4 and 5). It appears that in the settling case, the particles encounter large scale sweeps upstream and above the vortex head. Around the vortex, it can be seen that the particles see an even intenser drift at the downstream side of the vortex pulling the particles down around it. This pattern of particles was previously encountered in section 2.2.3. Specifically, the motion of sediment particles shows some similarity with fig. 2.8, where it is shown that particles (with a small settling velocity) can take a downward path around a vortex. In this way, they encounter a downward velocity, which leads to an increased settling velocity (Maxey & Corrsin, 1986). Indeed, it was found in section 5.3.2 that there is a downward drift velocity in this situation, which leads to a mean vertical particle velocity that is larger than the still water setting velocity. In the fully developed case, the drift velocity looks very similar to the fluid velocity structure. It appears that the downward drift in the streamwise direction (section 5.3.3) that was found in this situation seems thus to be related with the induced flow field beneath the hairpin vortex heads. In section 6.3 is was shown that the quadrants that correspond to the location beneath a hairpin vortex head are Q2 and Q3. In this way, the strong influence that Q2 and Q3 events have on particle transport are encountered once more, and it can be related to the transport of particles in hairpin vortex packets. Note that some care should be taken in interpreting these results, because the figures do not show the number of particles at a location and some results therefore might be coming from a rather small number of sediment particles and at the same time contribute little to the actual transport, as there are no particles at those locations.

The clear difference between the conditional average of the drift velocity in the settling case and the conditional average of the fluid velocity means that apparently only some vortices are important for transporting the particles down. Although the downward and upward drifts are both related to a spanwise vortex, the three-dimensional vortical structure causing this transport is presumably very different. The different structure of the sweeps and ejection has been mentioned before in this chapter (par 6.3). There it was suggested that sweeps (Q4) and ejections (Q2) are indeed related to different flow structures, with sweeps mainly occurring above a hairpin vortex head and ejections beneath them. To obtain more insight into the difference between the spatial coherent structure related to ejections and inward interactions (Q2 and Q3) on the one hand and sweeps (Q4) on the other hand, a LSE is used with two conditions rather than one. Using this technique proposed by Guezennec (1989), a conditional average of the fluid velocity fluctuations is calculated based on two different conditions at two different locations. The two variables that were applied as conditions were the swirling strength and the vertical velocity. The mathematical background of this technique is described in more detail in appendix B. It was chosen to use two conditions that were relatively closely spaced (the velocity condition is $0.07h$ upstream and $0.07h$ below the vortex head), and it was chosen to make the condition imposed on the wall normal velocity relatively weak compared to the one imposed on the swirling strength. Thus we use a similar technique as was used previously

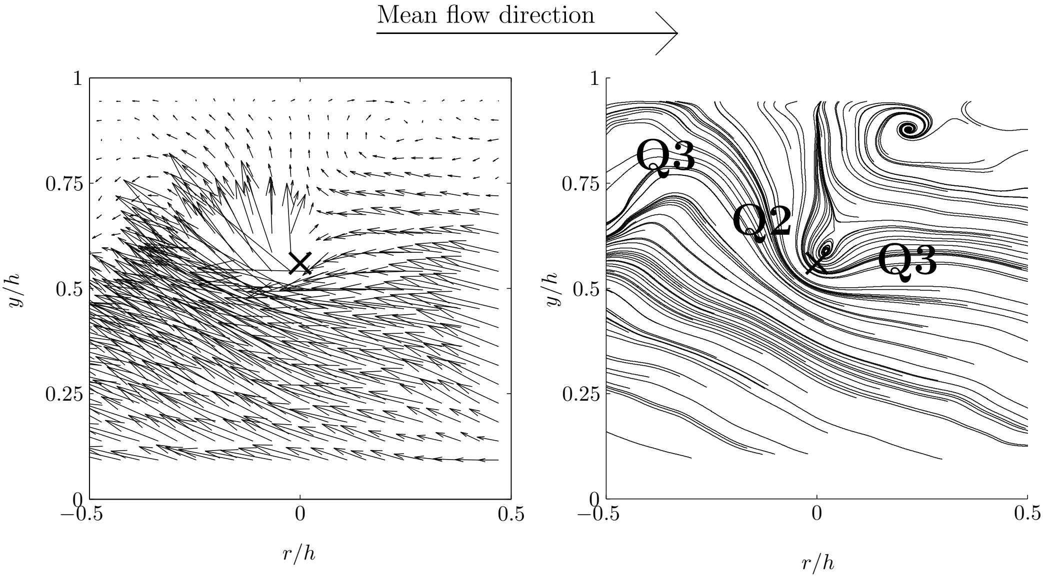

Figure 6.12: Conditionally averaged *fluid flow* structure at $y_0 = 0.56h$ calculated using LSE (mean velocity is subtracted). Left: vector plot; Right: streamline plot.

in the chapter for determining the flow field in the vicinity of the vortex head, but now it is conditioned to only those events, where a downward velocity exists upstream and below the vortex head. The results of applying an LSE with two conditions are shown in fig. 6.14. Now, the encountered turbulent structures are quite different from those found using only swirling strength. In fig. 6.14 the stronger velocities appear above the vortex head, rather than beneath it as was found in fig. 6.12. In this situation, there are increased streamwise velocities above the vortex head (sweeps). The decreased streamwise flow velocities beneath the hairpin vortex (ejections), which were encountered using an LSE with one condition are not found in this figure. The characteristics of this flow structure bear some resemblance to the ones that were found to be important for the increased settling velocity in the settling situation (fig. 6.13). In particular, in both these figures, we find regions of increased streamwise velocities above the vortex head (a Q4 structure), and we see the strongest velocities next to the vortex head on the downstream side, which are directed downwards.

The previous results were presented only for one reference height approximately in the middle of the water column. Similar data calculated close to the wall and close to the free surface showed qualitatively similar flow structures for the fluid velocity as well as for the drift velocity and the settling and fully developed situations (not shown). The low velocity flow structures extend down from the vortex head to the wall for the calculation using the fluid velocity and for the drift velocity in the fully developed situation. Hence this shows that the structures responsible for upward sediment transport are structures that are attached to the wall. The

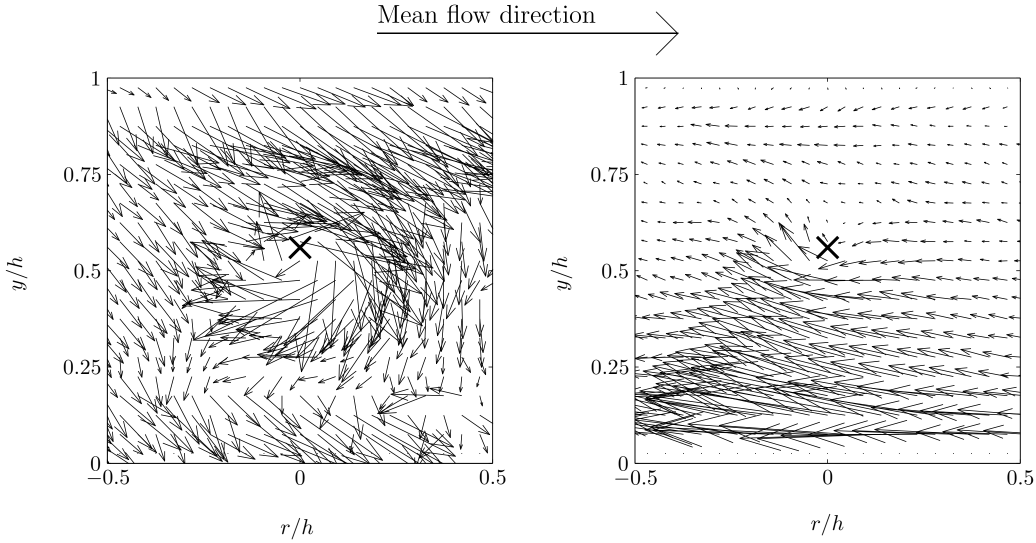

Figure 6.13: Conditionally averaged *drift velocity* structure at $y_0 = 0.56h$ calculated using LSE (mean velocity is subtracted). Left: settling case; Right: fully developed situation.

similarity between the results at different heights suggests that the results found here are valid over the complete water column.

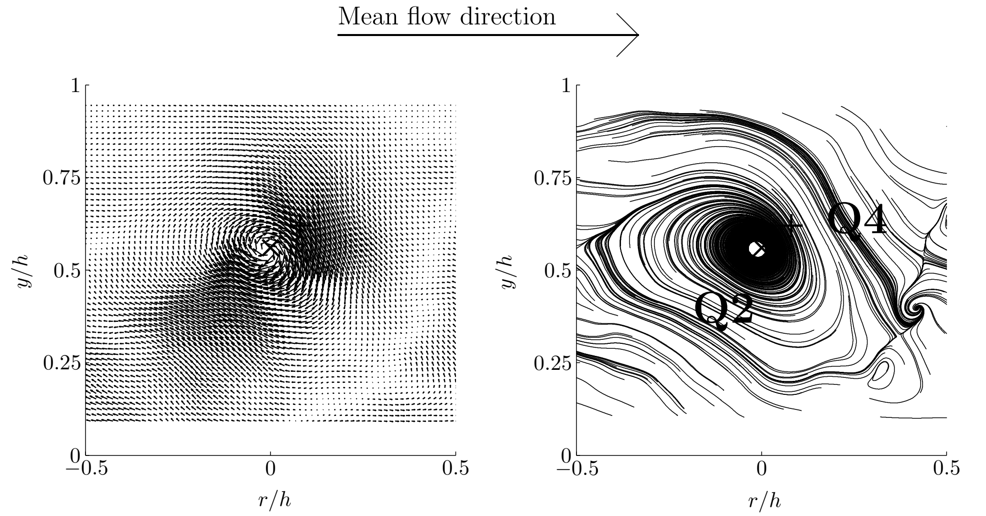

Figure 6.14: LSE of the fluid velocity fluctuations using two conditions, swirling strength at $x_0/h, y_0/h = (0, 0.56)$ (marked with an 'X') and vertical velocity at $x_0/h, y_0/h = (0.08, 0.62)$ (marked with a '+'). $\frac{v_{cond}/v_{rms}}{\lambda_{s,cond}/\lambda_{s,rms}} = -0.20$

From the previous data, it appears that the structures, which are important for the increased settling velocity of sediment particles in the settling situation, consists of a vortex head with a sweep downstream and above it. There are two conceptual models to explain this. The first of them (fig. 6.15) is based on the fact that sweeps have a size that is so large that they need to be induced by the sides of a hairpin vortex (as Biot-Savart's law shows that the induced velocity due to a vortex core decreases quickly as r^{-1}; appendix A). Then, the vortex head, with an induced sweep above it can either exist if an hairpin vortex extends to the side, or if two different sized hairpin vortices are found side by side (fig. 6.15). The second model to explain these sweeps are vortices like the type B eddies of Perry & Marusic (1995), which consists of an spanwise oscillating vortex tube, inclined 45 degrees in the streamwise direction and rotating with the mean shear. However, this model seems less probable as this model was proposed in order to obtain a better comparison with experimental data without claiming their existence, and it has never been observed in experimental or numerical data of wall bounded flows.

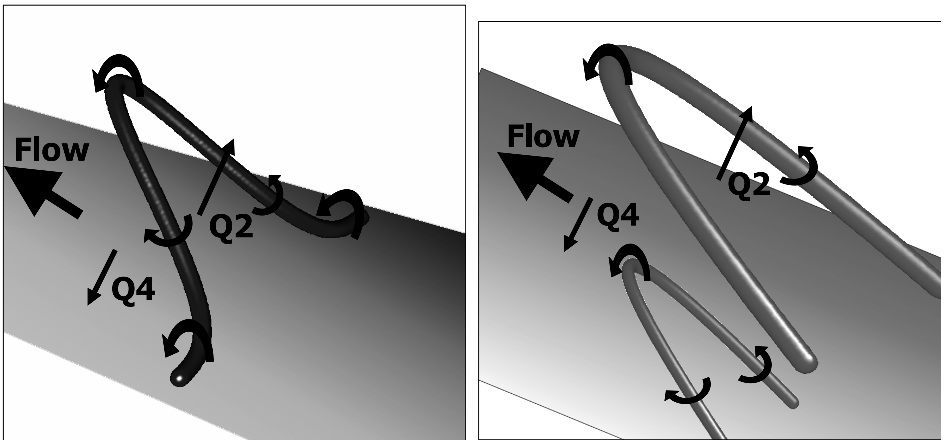

(a) One hairpin vortex (b) Two hairpin vortices side by side

Figure 6.15: Conceptual image of a hairpin vortex and the induced flow structures

Using the results obtained before, we infer the following conceptual model for the transport of sediment particles in the fully developed situation (fig. 6.16). Particles from near the bottom, where the largest concentration exists, are transported upwards by an ejection related to a hairpin vortex. Some of these particles are ejected relatively far upward (above the internal shear layer that connects two vortex heads). However, other particles are not ejected that far, and they remain beneath the hairpin vortex head. Because these hairpin vortices travel in packets (Adrian *et al.*, 2000), these particles encounter a Q3 event related to an upstream hairpin vortex (see also section 6.3), which then transports these particles downwards (dotted in fig. 6.16). This mechanism explains why the particles are encountered significantly more often in Q3 structures than one would expect if they were randomly distributed over the flow structures. Particles (filled circles in fig. 6.16) that are transported above the internal shear

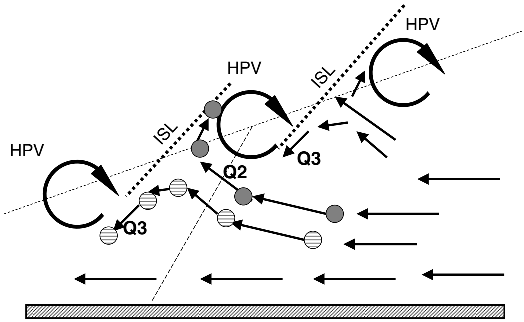

Figure 6.16: Physical mechanism of particle transport in the fully developed situation. The image shows a hairpin vortex packet and two typical particles in a frame moving with the hairpin vortex packet's convective velocity. ISL: Internal shear layer, HPV: Hairpin vortex

layer do not increase the occurrence of particles in Q3 events. If they are transported out of the hairpin vortex packet, some of them may remain at the same vertical location (Niño & García, 1996), because their settling velocity is very small. Others may be transported further upwards by another hairpin vortex packet above. These particles might encounter either a strong Q2 event and thus be transported to an even higher hairpin vortex packet, or a weaker Q2 event followed by a Q3 event. Still others are transported down by a sweep. It seems plausible that the mechanism for this downward transport is similar as in the settling case, viz. the particles are swept down at the downstream side of the vortex related to the sweep. Note that the main contribution of the downward motion of these light particles does not come from gravity (although gravity has a very important effect on the concentration distribution), but from the downward transport by coherent structures (also found by Sumer & Deigaard, 1981), whose velocity magnitude is an order of magnitude larger than the still water settling velocity.

The use of a small mean velocity (made possible by the use of polystyrene as pseudo-sediment) in combination with a relatively large measurement area makes it possible to observe the turbulent structures being advected through the measurement area[5], and in this way, we can obtain an instantaneous example of the previous mentioned mechanism (fig. 6.17). In this figure, a near bottom ejection due to a hairpin vortex is being advected through the measurement area while picking up some particles. It is clear that the velocities of the particles hardly differ from the local fluid velocities. We can see that these particles are transported upward behind the hairpin vortex head (thus they correspond to the filled circles in fig. 6.16). We see that the particles travel a significant vertical distance in this event.

In this section, we have seen that upward and downward transport of sediment particles are governed by different flow structures, and we have made a conceptual model of the flow struc-

5. With a velocity of 0.20 m/s, a flow structure remains during 0.25 s in the measurement area. This corresponds to 3 to 4 consecutive frames when the maximum measurement frequency of 15 Hz is used.

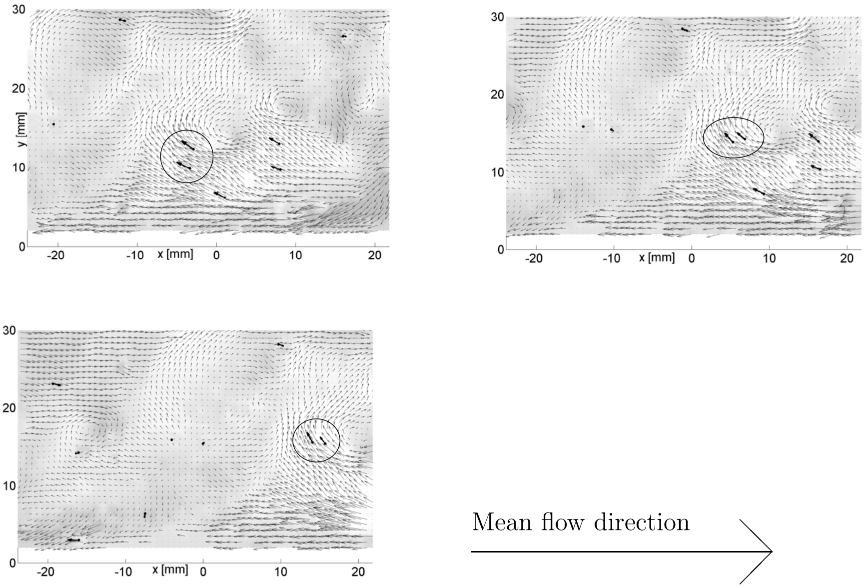

Figure 6.17: Three consecutive flow fields with sediment particle motion ($\Delta t = 0.067s$). Fluid velocities (every other vector) in gray, and particle velocities in black. At every location, a convection velocity of 0.15 m/s is subtracted.

tures that transport the particles. It is not straightforward to translate this conceptual model of the flow structures into a mathematical model that can be used in engineering practice. Instead, we distill some remarks and recommendations for the development of models for the turbulent fluxes of sediment.

The conceptual model clearly shows that the vertical motion of the sediment is mainly governed by the motion close to the head of the vortex. Further away from the vortex head, the vertical component of the transport is small. Therefore, the most important flow structures for transporting particles are those closest to the location of the head of the hairpin and the strongest ones. For larger values of v_T/u_* than the current experiment, the flow due to the vortex head needs to be large enough (larger than v_T) at the location of the particles. Otherwise, the particles cannot be entrained by the flow structure. Therefore, the particles are only transported by the strongest flow structures, which leads to a stronger turbulence at the location of the particles and thus to higher values of β. The settling velocity thus determines by which flow structures the particles are transported, and in this way it determines the strength of the turbulent diffusion process (i.e. β). The influence of the settling velocity in determining which structures transport the particles can also be seen for downward moving particles. There, the settling velocity drives the particles to downward flow structures (fig. 2.8).

With respect to the streamwise velocity of the sediment particles, the conceptual model (fig.

6.16) clearly shows the two different processes (described by eq. 5.6) that drive the particles toward an area in the flow with a velocity that is lower than the average value in a fully developed situation. First, the particles are more often in upward than in downward flow structures, which have a lower than average streamwise velocity (the term containing $\langle u'v' \rangle$ in eq. 5.6). This can be seen in fig. 6.16 as the particle that is transported outward in the Q2 event upstream of the vortex head. Second, the particles (both upward and downward moving) have a velocity lower than average, because they come from the near wall regions, where the streamwise velocity is lower (the term containing the velocity gradient in eq. 5.6). This can be seen in fig. 6.16 as the particle that is transport in an undulating up and down movement in Q2 and Q3 structures.

6.5. Length scales

The preceding section has focused on the turbulent fluxes of sediment (in the form of the drift velocity). In order to obtain information that is more easily applicable for modeling purposes, we study statistical information regarding the length scales as obtained from the fluid velocity data, in order to understand the influence of the size of the coherent structures on the turbulent diffusion coefficients. This is important, because it is shown in section 2.1.4, that the integral time scale on which the diffusion coefficient ($D_{yy} = \langle v_f'^2 > T_L$) for sediment depends (section 2.3.3) can be written as the ratio of a length scale and a velocity scale ($T_L \sim L_y/v_f'$ thus $D_{yy} \sim v_f' L_y$). An increase of length scales of the eddies encountered by the particles, leads to an increased integral time scale and therefore to an increased sediment diffusivity. Specifically, we want to show in the present section that the length scales of the structures encountered by the particles can change because they do not sample all the flow structures equally.

In order to study the length scales in inhomogeneous turbulence, we define the two-point correlation function R of the velocity g as:

$$R\left[g(y_0), g(y)\right) = \frac{\langle g(y_0)g(y)\rangle}{(\langle g(y_0)^2\rangle \langle g(y)^2\rangle)^{1/2}} \tag{6.4}$$

Here, $\langle g \rangle$ is used to denote ensemble averaging combined with spatial averaging in the streamwise direction. From this autocorrelation, the integral length scale in the wall normal direction at a wall normal distance y_0 can be calculated. This quantity gives an indication of the wall normal size of the turbulent eddies. Because of the inhomogeneity, there are two different integral length scales (Carlotti & Drobinski, 2004), one below y_0, defined as:

$$L_{y-}[g, g] = \int_0^{y_0} R\left[g(y_0), g(y)\right] dy, \tag{6.5}$$

and one above y_0, defined as:

$$L_{y+}[g, g] = \int_{y_0}^{h} R\left[g(y_0), g(y)\right] dy \tag{6.6}$$

Both were determined for the streamwise velocity fluctuations u' and for the wall normal ones v'. Carlotti & Drobinski (2004) suggested that the mixing length L_m in a shear flow should be proportional to L_{y-} of the wall normal velocity fluctuations, which would physically mean that the mixing length is a good indicator of the mean size of the eddies that are responsible for upward particle transport. To test this, we plot in fig. 6.18 L_{y-} versus the Bakhmetev distribution with $\kappa = 0.41$ for the mixing length given by eq. 2.9.

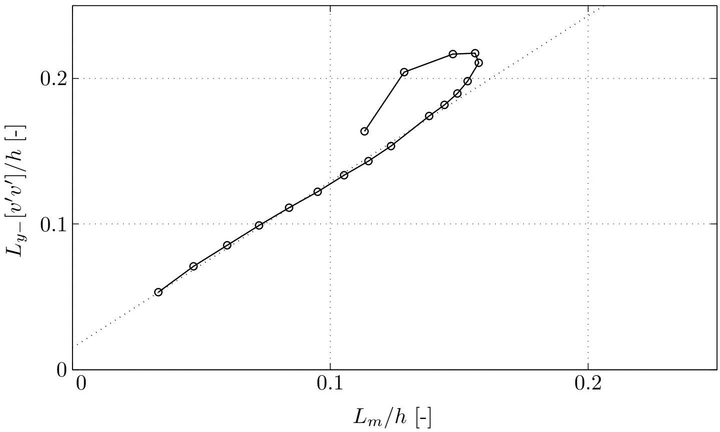

Figure 6.18: Downward length scale () of the wall normal velocity fluctuations versus mixing length. The fitted line is for $L_m/h = 1.14 L_{y-}[v', v']/h + 0.015$.

Here, the Bakhmetev distribution was used rather than the experimentally obtained mixing length. The reason for this is that the experimentally obtained mixing length suffered from a bias error, caused by a dip in the mean streamwise velocity near the free surface. The Bakhmetev distribution provides an excellent fit with L_{y-} in the lower part of the flow. It appears that the proportionality is valid for $y/h < 0.53$. The integral length scales are plotted in fig. 6.19 together with the Bakhmetev length. It further appears that the length scales of the streamwise and wall normal velocity fluctuations have a similar size, which is in clear contrast to the length scales in the streamwise direction (e.g Liu *et al.*, 2001). The latter are much larger for the streamwise than for the wall normal fluctuations.

In order to compare the direct influence of the length scales of the flow on the transport of the particles and their diffusion coefficient D_{yy}, we calculated the vertical correlation function of the fluid velocities as seen by the particles (using eq. 6.4) and from these correlation function we computed the integral length scales (using eq. 6.5 and 6.5). Here, the fluid velocity as seen by the particles is determined by interpolating the fluid velocities at a vertical transect from the bottom to the free surface that passes through a particle. Thus, the fluid velocity as seen by the particles is an Eulerian quantity, and the trajectory of the particle is not taken into account. This quantity only provides information on the size of the flow structures in which

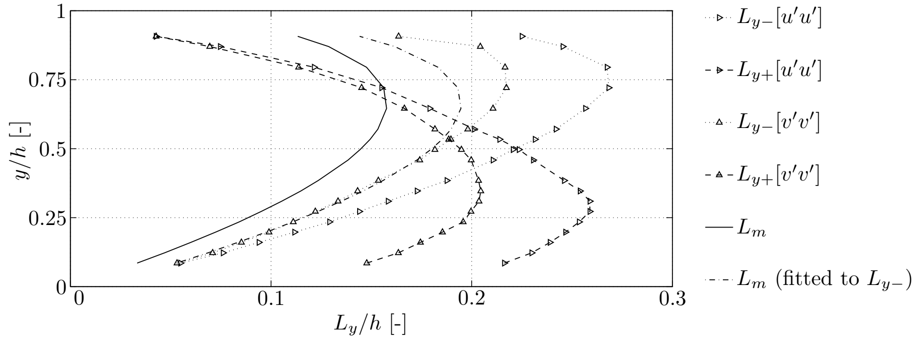

Figure 6.19: Integral length scales in the clear water flow.

the particles are found. The results are shown for the settling situation and the fully developed situation in fig. 6.20. For comparison, the vertical length scales determined for the fluid velocity are also shown in this figure.

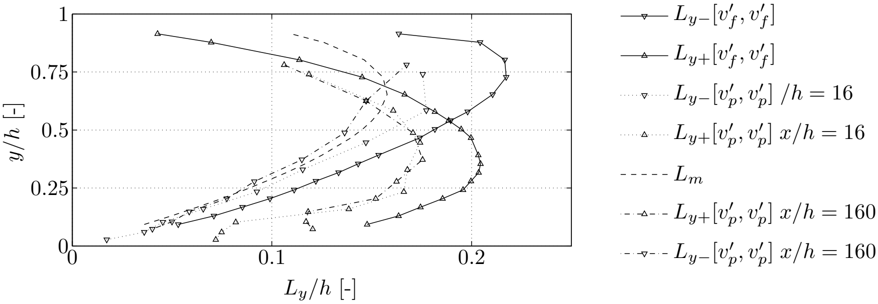

Figure 6.20: Vertical fluid integral length scales as seen by the particles ($L_{vv,p}$), in combination with the fluid integral length scale $L_{vv,f}$ and the mixing length (L_m)

.

It can be seen that the fluid structures that are encountered by the particles are relatively small compared to the length scales of the complete flow field (both for L_{y+} and L_{y-}). This occurs in the settling situation as well as in the fully developed situation. One might expect, that this would lead to a larger diffusivity of momentum than of the particles ($\beta < 1$), since $D_{yy} \sim v'_f L_y$ and L_y is larger for vertical momentum transport than for vertical sediment transport. However, in section 6.2.1, it was shown that characteristic vertical velocity fluctuations that are responsible for sediment transport are much larger than those responsible for momentum transport, and this effect dominates over the influence of the length scale.

It can further be seen that the integral length scale of the fluid velocity above the particles (L_{y+}) has the same size in the settling situation and fully developed situation. The integral length scale of the fluid velocity beneath the particles (L_{y-}) on the other hand is significantly larger (up to 20%) in the fully developed situation than in the settling situations. This means that total length of the eddies that transport particles are larger in the fully developed situation than in the settling situation. This explains the larger diffusion coefficient for sediment in the fully developed situation than in the settling situation.

6.6. Summary and conclusions

In the present chapter, the transport of suspended sediment has been studied from the perspective of coherent structures. In order to do so, first a quadrant analysis was performed on the fluid velocity field, on the particle velocities and on the fluid velocity field as seen by the particles. It was shown that in order to study which flow structures are responsible for the transport of particles, one should use the velocity field at the particle location, rather than the particle velocities. Using a quadrant analysis on the velocity field encountered by the particles, it was found that it depends on the sediment concentration profile, which flow structures are responsible for the vertical motion of the particles. Close to the sediment injection point, when most particles are still close to the free surface, the particles are encountered relatively more often in the downward flow structures (Q3 and especially Q4), which explains both the net downward turbulent flux and the mean particle velocity that is faster than the mean fluid velocity (chapter 5). In a fully developed situation, the particles are mostly found near the bottom of the flume. In this situation, the upward moving particles tend to concentrate strongly in Q2 structures, whereas downward moving particle are found equally often in Q3 and Q4 structures. This is a clear difference with the fluid flow structures, where Q4 events are much more common than Q3 events.

The importance of the various quadrant events on the eddy viscosity and eddy diffusivity has been studied. The eddy viscosity (interpreted as the vertical flux of streamwise momentum normalized by the velocity gradient) gets its main contribution from both Q2 and Q4 events. The opposite contributions from Q1 and Q3 have a smaller magnitude than the contribution from the former two quadrants. The events that are important for transport from high concentration to low concentration regions differ per situation. In the settling situation, transport of sediment from high to low concentration regions comes from Q4 and to a lesser extend Q3 events, while Q2 events provide opposite contributions to the transport. In the fully developed situation, the contribution to transport from high to low concentration regions comes almost exclusively from Q2 events, while opposite contributions come from Q4 and Q3 events. The individual quadrant events are more efficient in transporting sediment than momentum, as can be seen from the larger contributions to the eddy diffusivity than to the eddy viscosity. However, the total contribution to the eddy diffusivity can be either smaller or larger than the contribution to the eddy viscosity. This depends on how the individual contributions counterbalance each other. Thus the inherent difference in the effectivity of transporting sediment and momentum by the flow structures leads to values of β different from one. From this, it appears that the Reynolds analogy (which hypothesizes that the eddy viscosity and eddy diffusivity are proportional) is the main weakness in modeling suspended sediment transport, because the individual structures on which the eddy viscosity and eddy diffusivity depend are different ones.

In order to understand the reason why the particles see different flow structures, an analysis of the spatial structure of the sediment transport was performed using linear stochastic estimation (LSE). It was found that in the settling situation, the particles are encountered mainly in Q4 events that have their induced flow field above the head of a hairpin vortex, and that these structures can transport particles downward at the downstream side of the hairpin vortex. In the fully developed situation, the upward transport of particles is caused by Q2 events that have an induced flow field beneath the hairpin vortex head. As a consequence of the occurrence of hairpin vortices in packets, Q3 events are found mainly next to Q2 events. Thus particles picked up in Q2 events, can relatively easily end up in Q3 events, which transport the particles down again. This explains the increased importance of Q3 events for particle transport (compared to the fluid flow field).

The conceptual model for transport of particles in the fully developed situation is that they are transported upwards by Q2 events. A part of these particles appears to remain in the hairpin vortex packet and is then subsequently transported down in a Q3 event. These particle can then be picked up again by a new Q2 event. However, another part of the particles is picked up by a strong Q2 event and is then transported upwards to an hairpin vortex packet situated above the original hairpin vortex packet. Depending on the flow structure of this packet, a particle can then be transported down in a Q4 event (they are swept down at the downstream side of the vortex head, which is similar to the mechanism that explains the increased settling velocity; Maxey & Corrsin, 1986), or start another upward motion in a Q2 event. Once again, the particle can be transported down in a Q3 event or end up in a even higher hairpin vortex packet.

Chapter 7

Two-way coupling in high concentration flows

7.1. Introduction

In most practical sediment transport situations, sediment concentrations might become quite high, especially near the bottom. Therefore, a good understanding of the physics of high concentration flows is important. However, this is very difficult to obtain, because most experimental techniques that permit detailed measurement are limited to low concentrations. Nevertheless, in some experiments with volume concentrations as low as 10^{-4}, changes in the mean fluid velocity (Kaftori *et al.*, 1998) and turbulence profiles (Best *et al.*, 1997) have been observed. However, many experimental results are contradictory, showing e.g. both increased and decreased turbulence intensities.

In the present chapter, the range of concentrations for which experimental turbulence data exists is extended up to bulk volume concentrations of 0.42 %, which is at least two orders of magnitude larger than the experiment in the previous chapters. This concentration could also be high enough, for hydrodynamic interactions (i.e. four way coupling) to become important (see section 2.4.3). Measurements with these high concentrations were performed using refractive index matching (see 3.3 for a description of the experiment). The experimental conditions are different from most experiments in the literature, because the density ratio is quite low ($\rho_p/\rho_f = 1.14$), whereas the Rouse parameter and non-dimensional particle diameters are quite high ($u_*/v_T = 5$ and $d_{p+} = 10$). The consequences of this choice of parameters is that a relatively large amount of sediment is suspended and hence density stratification and an increased bottom roughness due to the sediment will be limited compared to other experiments in the literature. Furthermore, large particle diameters have in the past been related to increased turbulence intensities (Gore & Crowe, 1989), whereas small particle diameters might lead to decreased turbulence intensities.

In this chapter, first a comparison of the friction velocity between cases with different sediment concentrations is presented. The influence of the experimental artifact of peak locking on the results is discussed in a subsequent section. Then the velocity and turbulence profiles for different concentrations are compared. This is followed by an analysis of the size and shape of the coherent structures in these flows. This chapter is ended with conclusions and recommendations.

7.2. Determination of the friction velocity

In the present chapter, three high concentration sediment laden flow measurements are presented. These experiments were performed on two separate days. Each day, the measurements were started with a clear water flow for comparison.

The friction velocity in this chapter was determined from a fit of the mean velocity profile to the law of the wall (eq. 2.6), as this has proved to be the most suited method in the low concentration experiment. Here, the friction velocity is defined as $\tau_b = \rho_m u_*^2$ with τ_b the shear stress at the bottom and ρ_m the depth averaged density of the mixture. The friction velocities determined in this way differ at most 2 % between sediment laden and clear water flows. Naturally, it is somewhat problematic to use the friction velocity determined from a fit to the log-law in a sediment laden flow, where two-way coupling is known to alter the shape of the velocity profile (e.g. Villaret & Trowbridge, 1991). The most common alternative method for determining the friction velocity in sediment laden flows is from a force balance using the bed slope or the water level slope (maybe in combination with a side wall correction), i.e. $u_* = \sqrt{ghi}$. Using this method for the clear water flow, friction velocities were found that were too low in comparison with those found from the log-law approach, probably due to uncertainties in the determination of the free surface slope and the bottom slope. Therefore, this method was not used. However, the bottom slope was held constant during the experiments, which means that friction velocity in a sediment laden flow can be calculated using the friction velocity from the clear water flow (determined with log-law approach) in combination with the change in the water depth:

$$\frac{u_{*SED}}{u_{*CWF}} = \sqrt{\frac{h_{SED}}{h_{CWF}}} \tag{7.1}$$

Here, the subscripts “CWF” and “SED” were used to indicate quantities from the clear water flow and the sediment laden flow. Using this approach, similar values for the friction velocity in the sediment laden flows were found as for the log-law approach which indicates that the log-law approach is indeed valid in the present situation. The small changes in the friction velocity between sediment laden and clear water flows agree with the fact that changes in the water depth were small (a decrease of at most 3 % of the water depth for the sediment laden flow, see table 3.3).

The complete streamwise momentum balance is equal to the balance of the sediment (from eq. 2.34) added to the one for the fluid (eq. 2.51) and in a fully developed situation (thus no streamwise gradients and time derivatives), it reduces to:

$$-\frac{d\langle p_f\rangle}{dx} + (1-C)\nu_f\rho_f\frac{d\langle u_f\rangle}{dy} + (1-C)\rho_f\langle u_f'v_f'\rangle + C\rho_p\langle u_p'v_p'\rangle = 0 \qquad (7.2)$$

In this equation, particle collisions have been neglected, because these are unimportant except very near the bottom (section 2.4.3). Four-way coupling due to hydrodynamic interactions is implicitly included, but falls out the total momentum balance, because these terms in the equation for the fluid and particles counterbalance each other (although its effect enters the equation, when four-way coupling changes the sediment concentration profile). Note that damping/generation of turbulence is not explicitly visible in this equation (section 2.4.2). The terms responsible for turbulence modification can be found in the Reynolds stress equations (eq. 2.56). Turbulence modification can lead to a change in the fluid Reynolds stresses in eq. 7.2. This has to result in a change of the viscous stress near the wall, and thus in a changed mean fluid velocity profile. This change in the fluid velocity profile in flows with large sediment concentrations have been observed often (e.g. Coleman, 1981; Best *et al.*, 1997; Cellino & Graf, 1999; Righetti & Romano, 2004). Eq. 7.2 shows that a part of the Reynolds shear stresses is now carried by the particles ($\langle u_p'v_p'\rangle$). Therefore, a determination of the friction velocity from the fluid Reynolds stress profile needs to be corrected for the presence of the particles, whose concentrations profiles were not measured in the present experiment. Hence, a determination of the friction velocity using this method is rather cumbersome, and this partly explains the errors in the friction velocity using this method in table 3.3. Furthermore, this method is stronger influenced by statistical errors (as the statistical convergence of the Reynolds stress profile is slower than that of the mean velocity profile; section 3.4.1) and by secondary currents, although the flume is wide enough not to be affected strongly by those currents.

7.3. Influence of peak locking on the measurement results

The high concentration measurements suffered from a substantial amount of peak locking, which increased with increasing sediment concentrations. This is clearly visible in fig. 7.1, where the probability density of the streamwise and wall normal fluid velocity fluctuations are plotted for two different heights. These figures show a great similarity with the histograms from Angele & Muhammad-Klingmann (2005), who developed a simple model to simulate the effect of peak locking on turbulence statistics. From fig. 7.1, it appears that the wall normal velocity fluctuation suffer stronger peak locking than the streamwise ones, and that peak locking is stronger close to the wall, where the sediment concentrations are highest. This makes sense, because the higher near wall sediment concentration will have a larger affect on the transfer of the light scattered from the tracers. Especially the velocity fluctuations in the $C = 0.67$ % case are strongly affected by peak locking. The histograms for this case show additional peaks that are higher than the main peak. This might also be an effect of changes in the flow due to two-way coupling, but it is impossible to show from the present data whether or not this is true.

However, the strong peak locking does not mean that large errors are made in the determination of the mean velocity profile and the turbulence statistics. Christensen (2004) investigated the effects of peak locking on the turbulence statistics measured with PIV in an open channel flow by using three different estimators for subpixel interpolation of the peak of the correlation function. In this way, he obtained velocity data with no, moderate, and strong peak locking, where the strong peak locking case corresponded to absolute peak locking (i.e. no subpixel interpolation). He found that the calculation of the mean velocity profile was not affected by peak locking in all three cases. For the rms velocity fluctuations, the amount of peak locking depended on the total displacement of the tracer particles between two image frames. If this was large enough (16 pixels per frame), peak locking did not affect the turbulence profiles and two-point correlation functions. For too small displacements (8 pixels per frame), the turbulence profiles were affected, with a stronger effect on the wall normal than on the streamwise turbulence profiles. In this case, the two-point correlation functions were affected as well. He also found that the Reynolds shear stress profile was more sensitive to peak locking than either the streamwise or the wall normal turbulence profiles. Angele & Muhammad-Klingmann (2005) developed a simple analytical model to determine the bias error in the turbulence profiles in case peak locking is present and found that this bias is negligible (less than 1 %) if the rms velocity is larger than 0.67 pixels/frame.

In the present measurements, the time interval between two PIV images was set such that the mean velocity was approximately 25 pixels/frame, which corresponds to a wall normal rms velocity of at least 0.9 pixels/frame and hence, the errors in the turbulence profiles will be negligible, at least for the two cases with the lowest concentrations. However, quantities that depend on the determination of the velocity histograms (such as a quadrant analysis) are affected by peak locking and are therefore not meaningful for the present dataset. In the 0.67% concentration case, the peak locking is too strong (the locked peak is higher than the peak around $v' = 0$) for the model of Angele & Muhammad-Klingmann (2005) to be applied. Hence in this case, the turbulence statistics are affected strongly by peak locking. Therefore, the results of this case are not presented in the following.

7.4. Velocity and turbulence profiles

The mean velocity profiles for both cases up to $C_{vol} = 0.42\%$ are shown in fig. 7.2a. For comparison, the law of the wall (eq. 2.6) is shown as well. It is clear in this figure that all velocity profiles collapse using inner scaling, except for an small increase in the flow velocities near the bottom, which increases with increasing concentrations. Together with the fact that the friction velocity also hardly changed with the addition of sediment, this means that two-way

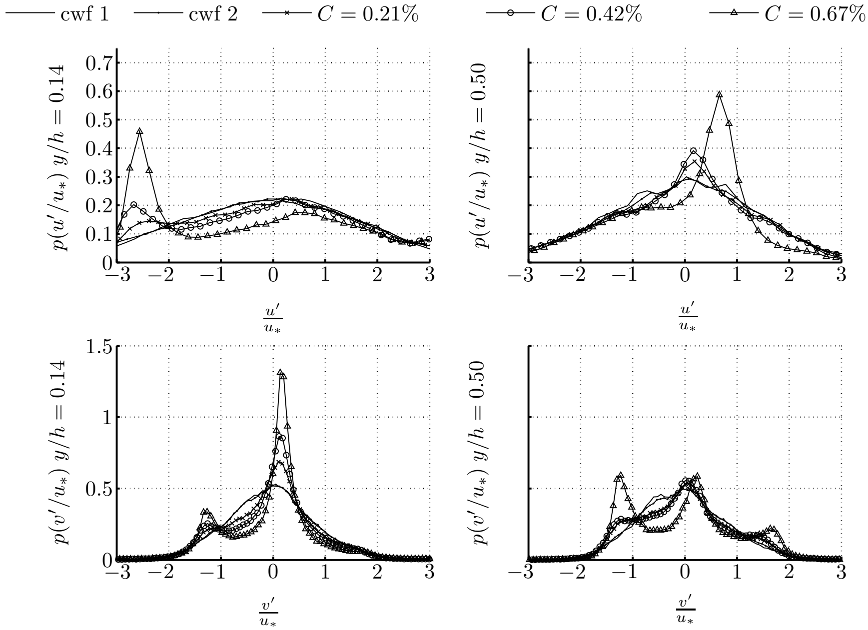

Figure 7.1: Velocity fluctuation histograms. Left: $y/h = 0.14$; Right: $y/h = 0.50$;

coupling in these cases does not have a large effect on the fluid velocity profiles. To show the relative difference between the velocity profiles, the (dimensional) velocity profile in a particle laden flow is divided by the (dimensional) velocity profile in the clear water flow and plotted in fig. 7.2b. This figure confirms that in both cases, the streamwise fluid velocity does not change due to the addition of the sediment particles up to experimental accuracy. The fact that no changes occur in the mean velocity and that the water level decreases at most 3%, means that the Darcy-Weisbach bottom friction factor c_f in this flow also decreases less than 3% with the addition of sediment, because $\langle u_f \rangle_f = \sqrt{ghi_b/c_f}$ thus $c_{f,SED}/c_{f,CWF} = h_{SED}/h_{CWF}$.

The fluid Reynolds shear stress profile (non-dimensionalized with u_* and h) is shown in fig. 7.3a, together with a comparison of the two by dividing the sediment laden Reynolds shear stress profile by the clear water Reynolds shear stress profile in fig. 7.3b. As could be expected from eq. 7.2, the Reynolds shear stresses hardly change with the addition of sediment in the two lowest concentration cases. There is a slight decrease of $\langle u'_f v'_f \rangle$ to approximately 90 % of its value in the clear water flow, which is within the experimental accuracy. The relative decrease in the Reynolds shear stresses near the free surface is stronger.

From the measured Reynolds shear stress and velocity profiles, one can determine the eddy viscosity. The results are shown in fig. 7.4. There is a slight decrease in the eddy viscosity (5 % in the lower concentration case and 10 % in the higher concentration case) for $0.2 < y/h < 0.7$. Above $y/h = 0.8$, there is a strong decrease in the eddy viscosity. There is an increase in

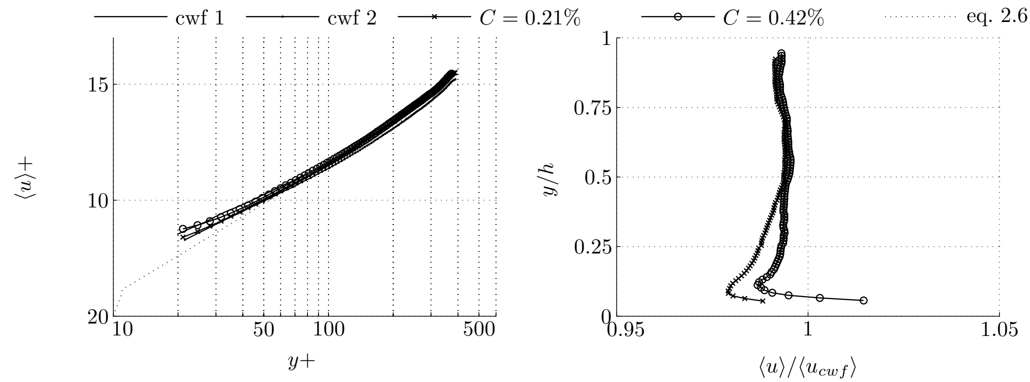

Figure 7.2: Mean velocity profiles. Left: wall units; Right: Comparison to CWF

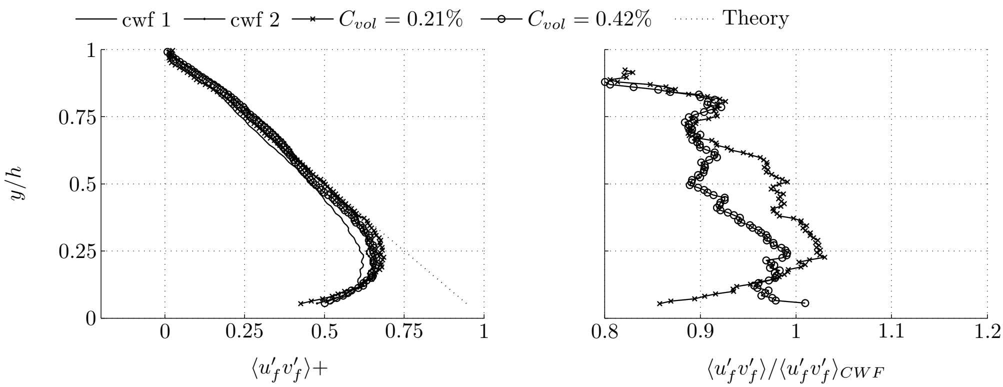

Figure 7.3: Reynolds shear stresses. Left: Outer scaling; Right: Comparison to CWF

the eddy viscosity below $y/h = 0.2$ in the $C_{vol} = 0.42\%$ case. The small changes in the eddy viscosity is somewhat surprising, as even in these conditions with a low density ratio, some stratification effects were expected. To illustrate this, we use the easiest available modeling approach for stratified flows, originally developed in meteorological applications, which is the use of damping functions. Such functions were applied by Villaret & Trowbridge (1991) in their reanalysis of several sediment transport experiments:

$$\frac{\epsilon_{xy}}{\epsilon_{xy,cwf}} = 1 + \beta_1 Ri_f \tag{7.3}$$

Here, Ri_f is the flux Richardson number (eq. 2.58) , and β_1 an empirical parameter, for which Villaret & Trowbridge (1991) found a value of about 4 to 5, and they found that β_1 decreased slightly with increasing concentrations. The flux Richardson number for the present experiment is shown in fig. 7.4. In this figure, the concentration profile was estimated, using the Rouse equation for $y > 2d_p$ (eq. 2.32 with $\beta = 1/0.7$) and following Einstein, we used a constant concentration C_0 for $y < 2d_p$ in order to calculate the absolute concentration values from the bulk concentrations. The velocity and Reynolds stresses were estimated from eq. 2.6 and eq. 2.5. The application of eq. 7.3 for the present experiment shows the expected damping of the eddy viscosity, which should be at most 20 % in the $C_{vol} = 0.4\%$ case. Nevertheless, the experiments do not show such a change in the eddy viscosity. Quite some assumptions had to be made to get the results of fig. 7.4, especially in the determination of the concentration profiles, for which the Rouse equation is used and no correction was made for the change in the shape due to two-way coupling. However, this approximation seems not unreasonable, since the changes found experimentally in the eddy viscosity are small. More doubtful is the assumption that the concentration is constant in a layer of two particle diameters, but unfortunately, there are no methods to verify this assumption. Therefore, this figure represents a quite rough estimate and one cannot conclude with certainty from the measured eddy viscosities in combination with the calculated Richardson numbers that stratification effects are weaker than predicted by eq. 7.3.

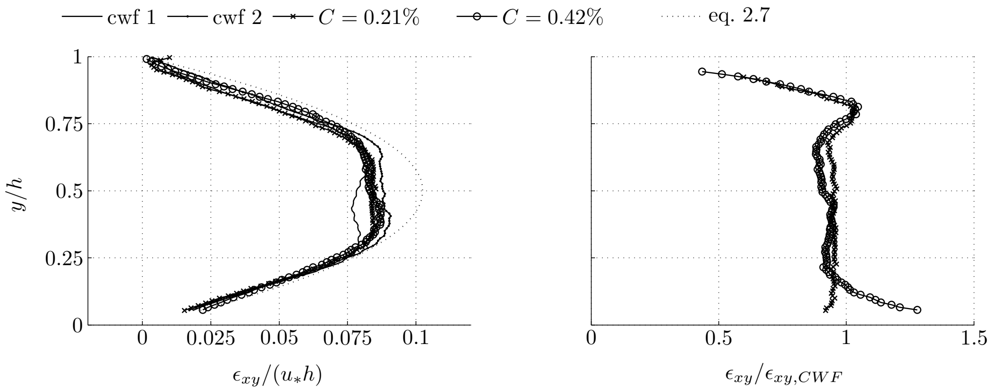

Figure 7.4: Eddy viscosity. Left: outer scaling; Right: comparison to CWF;

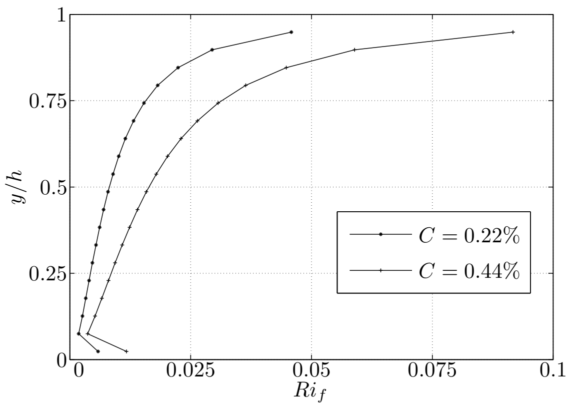

Figure 7.5: Estimated flux Richardson profile.

The streamwise velocity fluctuations are shown in fig. 7.6a and b. From this figure, it appears that these fluctuations hardly change with the addition of sediment. There is a decrease visible (to 95 to 98 % of the clear water value) for the two lowest concentration cases. The decrease is slightly more pronounced for the higher concentration case. Near the bottom ($y/h < 0.2$), there is a slight increase (2 %) of the turbulence intensity in the lowest concentration case. A similar increase in the turbulence intensity can be seen in the higher concentration case near the free surface ($y/h > 0.8$). These results (only a very slight decrease in the streamwise turbulence intensity) compare well with those found before at significantly lower concentrations by Kiger & Pan (2002), Rashidi *et al.* (1990) and Muste *et al.* (2005).

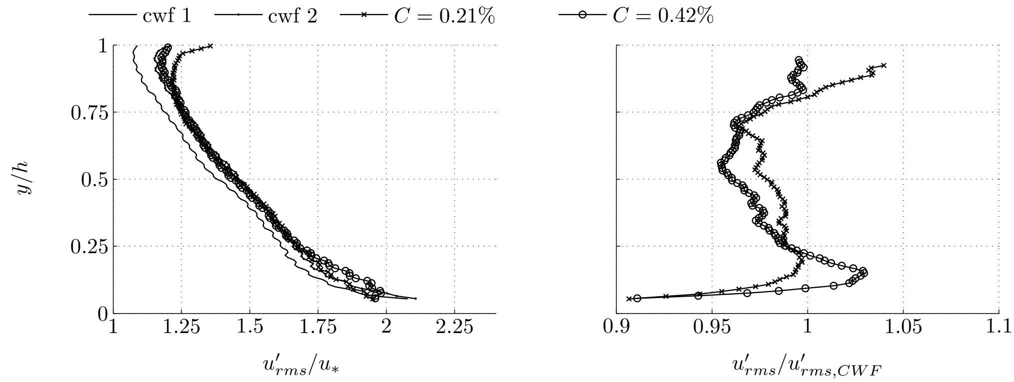

Figure 7.6: Streamwise velocity fluctuations. Left: Outer coordinates; Right: Comparison to CWF

The wall normal velocity fluctuations (fig. 7.7 a and b) on the other hand, increase over most of the water depth when sediment is added. The increase becomes larger near the free surfaces, but nevertheless, the maximum increase is never larger than 10 %. Only below $y/h = 0.25$, there is a slight decrease in the wall normal velocity fluctuations to 95 % of the clear water value. This increase in the wall normal velocities has previously only been found by Muste *et al.* (2005) in their highest concentration case for what they call neutrally buoyant particles. These where quite large particles ($d_p/\lambda_{kolm} = 3.6$), with a very small fall velocity ($u_*/v_T \approx 70$) and thus similar as in our experiment, these particles were well mixed over the vertical. It might be the effect of the interaction of the particles with the energy cascade thus transferring energy from the streamwise to the wall normal direction. If so, this appears to be a very small effect. Note that the observed increase in the wall normal turbulence intensities cannot be explained by an increased bottom roughness due to the addition of sediment, because the bed shear stress did hardly change in this experiment.

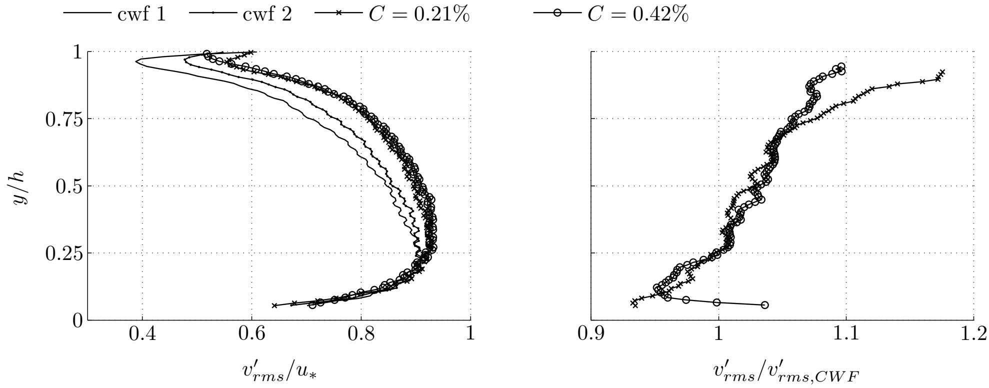

Figure 7.7: Wall normal velocity fluctuations. Left: Outer scaling; Right: Comparison to CWF;

7.5. Two-point correlations

In the previous section, it was shown that the particles have a limited effect on the turbulence and velocity profiles. However, it is possible that the particles modify the turbulence, but in such a way that the total turbulent energy of the fluid does not change, but the time and the length scales of the flow do change. Such an effect was found by Ferante & Elghobashi (2003) in their two-way coupled DNS simulations of heavy particles. They found that particles with $St_{kolm} = 0.25$ do not modify the kinetic energy of isotropic turbulence, but do change the turbulence spectra. Because these particles cannot be detected just by measuring the turbulent kinetic energy, they called these particles “ghost particles”. Now, it is investigated whether such a phenomenon also occurs in the present experiment. In order to do so, we calculated the two-point correlation functions for the streamwise and the wall normal velocity fluctuations. These are defined (for the streamwise velocity fluctuations) as:

$$R\left[u'_f(\vec{x_0}), u'_f(\vec{x_0}+\vec{r})\right] = \frac{\langle u'_f(x_0,y_0)u'_f(x_0+r,y)\rangle}{\langle u'_f(x_0,y_0)^2\rangle^{1/2}\langle u'_f(x_0+r,y)^2\rangle^{1/2}} \tag{7.4}$$

The two-point correlation functions are shown in fig. 7.8 and 7.9 for a reference hight of $y_0/h = 0.47$. From these figures, it appears that both the streamwise and the wall normal correlation functions have a similar shape over the whole domain. Thus it appears that the largest flow scales, which are the ones important for turbulent transport of sediment, did not change when increasing the sediment concentrations (the differences far away from the location of the peak is just experimental noise). This applies to the streamwise as well as the wall normal correlation functions. Also close to the peak at the correlation function, the shapes are very similar between the three different data sets that were analyzed (this could be appreciated more clearly in a detailed plot of the peak; not shown). This suggests that the small flow scales were also not strongly affected by the presence of the sediment particles. Of course, one cannot be completely sure that no changes occurred at the smallest flow scales, because the resolution of the PIV measurements is not high enough to resolve the smallest flow scales. On the other hand, it is not very likely that these scales are largely affected, because in that case, there would have been some influence of the turbulent energy cascade, which would also have been visible at larger flow scales. The results have only been shown for one reference height. However, an inspection of the data at different reference heights confirmed that this conclusion was valid over the complete outer layer. There were no reliable data to compute the correlations very close to wall.

From the previous, it can be concluded that in the present situation, the particles do not behave as “ghost particles”. Instead, the effect from the particles on the flow is even at these concentrations very limited. Given that the changes in the turbulence at the smallest flow levels are small as well, one can conclude that two-way coupling effects at the micro scales (as proposed by Crowe, 2000) such as extra dissipation by the interaction of the flow field induced by the particles with the turbulence (section 2.4.2) are very limited. Therefore, the largest two-way coupling influence for these kind of sediment transport flows seems to come from density stratification effects, but even this effect is quite limited in this experiment with relatively low values of ρ_p/ρ_f.

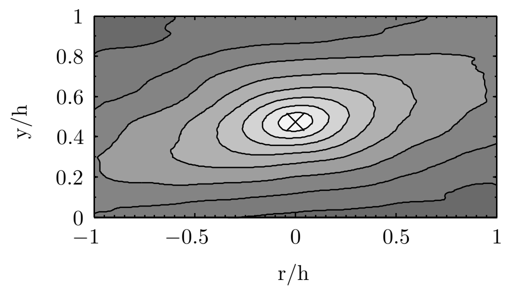

(a) CWF

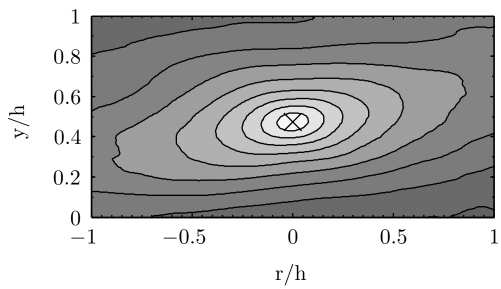

(b) $C = 0.21\%$

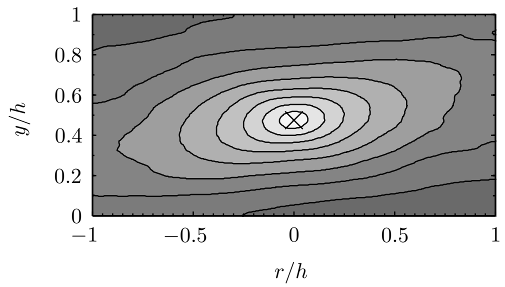

(c) $C = 0.42\%$

Figure 7.8: Two-point velocity correlation function for the streamwise velocity fluctuations. $y_0/h = 0.47$ (marked with an ‘x’).

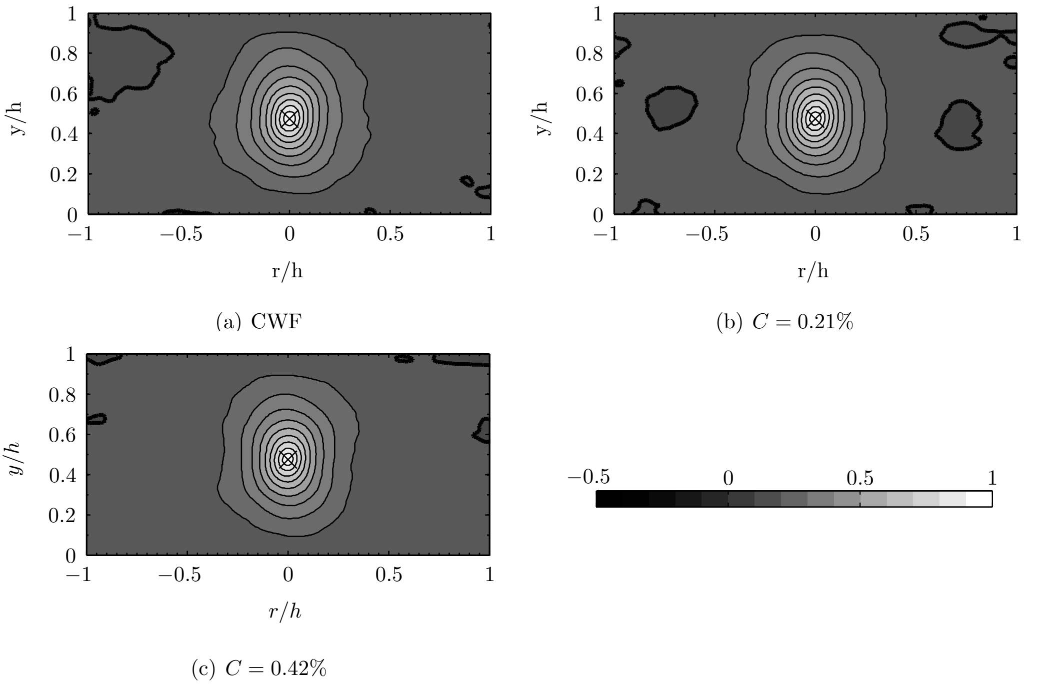

Figure 7.9: Two-point velocity correlation function for the wall normal velocity fluctuations. $y_0/h = 0.47$ (marked with an 'x'). Zero contour lines are indicated with a bold line.

7.6. Conclusion and recommendations

An experiment to study two-way coupling in a sediment laden flow was performed using refractive index matching in combination with PIV. This experiment was different from most previous detailed sediment experiments, in that the sediment concentration was quite high (reliable measurements up to a volume concentration of 0.42 %), the density ratio was quite low ($\rho_p/\rho_f = 1.14$), the particles were well suspended ($u_*/v_T \approx 4$) and the particles were quite large $d_p/\lambda_{kolm} \approx 4.2$. For these specific conditions, it was found that the mean flow and turbulence hardly changed with the addition of sediment. The bottom friction coefficient remained constant within 3 %. There was a slight decrease in the streamwise turbulence intensity and a slight increase in the wall normal one. There was a decrease in the eddy viscosity of maximal 10 % in the case with a $C_{vol} = 0.42\%$, which is less than was expected from previous studies (Villaret & Trowbridge, 1991), whose parametrization based on previous experimental investigations predict a 20 % decrease in the eddy viscosity due to density stratification effects caused by the suspended sediment. Thus it seems that density stratification is not very important at the present low ρ_p/ρ_f ratio. However, this effect can still be important at higher flux Richardson numbers.

The present experiments show that it is not to possible to apply known results from particles in gases directly to sediment transport processes. For example, the well-known diagram of Elghobashi (1994) suggests that two-way coupling would occur at volume concentrations as low as 10^{-6}, and four-way coupling at concentrations of 10^{-3}. Hence one would expect strong two-way coupling and even four-way coupling in the present experiments (with concentrations up to 6.7 10^{-3}. It cannot be determined from the present measurements whether four-way coupling effects are important, because the main effects of four-way coupling would be visible in the dispersed phase (especially changes in the sediment concentration profile), whereas in the experiment only information on the fluid phase was obtained. However, the expected strong two-way coupling effects were not encountered in the experiment.

The absence of strong two-way coupling effects in the mean velocity and turbulence profiles as well as in the two-point correlation functions shows clearly that some effects that are considered to be important, are in fact negligible. One of these effects, which is important in many studies on turbulence modification by particles in a gas (such as Squires & Eaton, 1990; Elghobashi & Truesdall, 1993; Boivin *et al.*, 1998), but negligible for sediment transport is turbulence damping due to the sediment particle lagging the fluid flow. This could have been expected (section 2.4.2), because the Stokes number is low and hence the relative velocity between the fluid and the particles is very small (section 2.2.2). Another effect, which appeared to be negligible for suspended sediment transport from the present experiments, is the turbulence modification by the interaction of the flow field generated by the particle with the turbulent energy cascade (Crowe, 2000). Furthermore, sediment particles are shown not to behave as “ghost particles” (Ferante & Elghobashi, 2003), which are particles that do not influence the kinetic energy level of the turbulence, but do change its length and time scales. From the previous it seems that for higher concentrations and density ratios (such as typically found in real world applications) density stratification is the most important two-way coupling effect.

The use of refractive index matching (RIM) in order to perform PIV velocity measurements of the fluid in flows with high sediment concentrations performed quite well. The main limitation encountered, was that a high concentrations, the light intensity coming from the tracers decreased, which resulted in increased peak locking, which at a certain concentration prohibited accurate measurements. The Sodium Iodide has proved to be an excellent working fluid, providing a high enough refractive index, while still having a viscosity that was low enough for the present type of experiment. Furthermore, it appeared safe and easy to use. The used silica gel particles, provided an adequate, but by no means ideal material. Especially the fact that they absorb fluid complicates the experiments. Furthermore, it seemed that the inhomogeneity of the used silica gel particles had a strong influence on the maximum concentrations that could be obtained in the current experiments.

The need for strong temperature control and the high costs of the Sodium Iodide solution prescribed the use of a small experimental facility. However, the experiments showed that the obtained fluid flow statistics in the clear water flow did not differ from those obtained in the larger facility (at a similar Reynolds number), at least in the center of the flume. Specifically, the occurrence of a supercritical flow in the small scale facility did not have an influence of the velocity and turbulence profiles. Thus, such small facilities can provide a viable alternative for large scale facilities if circumstances require.

Chapter 8

Conclusions and recommendations

8.1. Introduction

In this thesis, the transport of suspended sediment particles in a turbulent open channel flow was studied. The objectives of this study were:

- To obtain more insight into the vertical transport process of suspended sediment particles and in particular into the role of turbulent flow structures in transporting these particles. This insight may be used to develop better Reynolds averaged sediment transport models.
- To get a clear view on the transport of suspended sediment in a non-equilibrium situation.
- To compare the data generated by a direct numerical simulation (DNS) that calculated the trajectories of individual particles to simulate the sediment to experimental data without using any scaling.
- To develop better experimental methods for studying sediment transport in high concentration flows, and to use these in order to obtain more insight into two-way coupling.

In order to achieve these objectives, two different experiments were performed, one considering low concentrations and one considering high concentrations. The low concentration experiment used PIV (particle image velocimetry) to measure the fluid velocity field. The velocities of individual sediment particles were measured simultaneously using particle tracking velocimetry (PTV). To discriminate between sediment particles and tracer particles in the recorded images such that their velocities could be determined separately, a median filtering technique (Kiger & Pan, 2000) was used. A separate experiment used refractive index matching (RIM) in order to make the sediment particles transparent. In this way, the fluid velocities were measured using PIV in a flow with high sediment concentrations. In this way, two-way coupling effects in high concentration flows (with volume concentrations up to 0.42%) could be measured.

In this section, the findings of these two experiments are presented. This is followed by a discussion of the consequences of these findings for sediment transport modeling in civil engineering practice. Finally, some recommendations are given for future research with respect to the low concentration experiment and the high concentration experiment.

8.2. Conclusions

8.2.1. Insight in vertical transport process

In order to obtain insight in the vertical transport process of sediment, an experiment was performed for a fully developed situation. It was obtained by feeding the particles to the flow at a sufficiently large distance upstream of the measurement section.

Importance of fluid velocity at the particle locations

Insight in the vertical transport process was obtained by studying various statistics of the velocities encountered by the sediment particles. This was done, because two-fluid theory shows that the turbulent diffusion processes are governed by the fluid velocities encountered by the particles. Also, it is according to our physical intuition that it is important to regard the fluid velocities only at the particle location, if one wants to understand how the particles are transported by the fluid. The particle velocities, which are important in order to obtain the net particle fluxes, are merely an effect, caused by the fluid velocity encountered by the particles in combination with gravity and buoyancy forces.

It is important to distinguish between the fluid velocity at the particle location and the particle velocities, because the statistics applied to these quantities are different (especially in case of a quadrant analysis). The reason for this difference is that the average particle velocities differ from the average fluid velocity.

The flow structures that transport particles in a fully developed situation

A schematic picture of the turbulent flow structures that transport particles is shown in fig. 8.1. In this picture a hairpin vortex packet, consisting of multiple aligned hairpin vortices, is shown. The trajectories of two particles are also shown. This figure shows how particles from near the bed can be transported upwards by Q2 events (ejections). This leads to the observed increased occurrence of upward moving particles in Q2 events. Some of these particles are transported above the hairpin vortex packets. Only those particles can end up in Q4 events (sweeps), thus leading to a decrease of the number of particles in Q4 events. Others end up in Q3 events induced by an upstream hairpin vortex, which leads to the increased occurrence of downward moving particles in Q3 events. Because the particles that were studied have a settling velocity that is much lower than the vertical fluid velocity fluctuations, the motion of the particles, both upward and downward, have a velocity that is of similar magnitude as the vertical fluid velocity fluctuations.

Influence of flow structures on horizontal particle velocity statistics

Because the sediment particles are found more often in Q2 and Q3 events compared to a completely random distribution and less often in Q4 events, they encounter relatively more often

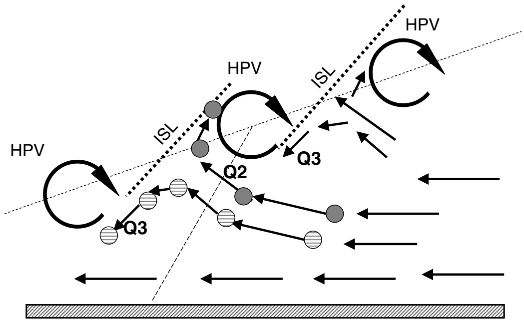

Figure 8.1: Physical mechanism of particle transport in a fully developed situation. The image shows a hairpin vortex packet and two typical particles in a frame moving with the hairpin vortex packet's convective velocity. ISL: Internal shear layer, HPV: Hairpin vortex head

low velocity flow structures. Since there is no instantaneous horizontal slip velocity between the particles and the fluid, this leads to an average horizontal particle velocity that is lower than the average horizontal fluid velocity. One can describe the occurrence of particles in low velocity flow structures by two effects. The first effect, related to the increased occurrence in Q2 events, is that the net upward velocity that the particles encounter is correlated with a lower than average flow velocity. The second one, related to the increased occurrence in Q3 events, is that particles come from the near wall region where the mean velocity is lower.

Influence of flow structures on vertical particle velocity statistics

The particles appeared to be encountered in flow structures that are slightly stronger than average. The reason is that Q2 events, where the particles end up more often, are stronger than Q4 events, which are less often encountered by the particles. Therefore the fluid velocity fluctuations at the location of the particles were slightly larger than the fluid velocity fluctuations (averaged over the complete flow field). The inertia of the sediment particles is so low that the particles can follow all fluid velocity fluctuations at a scale larger than the Kolmogorov time scale. This led to vertical particle velocity fluctuations that were larger than the fluid velocity fluctuations and particle Reynolds shear stresses that had a larger magnitude than the fluid Reynolds shear stresses.

Influence of settling velocity

It is quite surprising that the settling velocity has such a large influence on the resulting concentration profiles[1], even though its magnitude is much smaller than that of the typical vertical

1. This can be seen from the fact that the Rouse profile, which depends on the settling velocity, gives a rather good description of the observed concentration profiles

fluid motion. The reason is that although particles move with the typical fluid velocities of the structures they encounter, it is the settling velocity that determines in which flow structures the particles end up. This can happen in two different ways:

- The settling velocity can bias the particles to trajectories downstream of a vortex head, which have a downward vertical fluid velocity (see also fig. 8.2).
- Particles can only be transported up by those flow structures with an upward vertical velocity larger than the settling velocity. The vertical fluid velocity fluctuations are strongly determined by motion in the vicinity of the head of the hairpin vortex. Closer to the bed, the vertical velocity fluctuations in a flow structure are much smaller and they may be of comparable magnitude as the settling velocity. However, this is also the location where the particles enter the flow structure. In this way particles can be filtered out of weak or downward directed flow structures.

Influence of bed load layer

Two different situations were compared, with different values of u_*/v_T. In the situation with the lowest flow velocity, streaks of sediment were observed to move slowly over the bottom of the flume, whereas no such streaks were encountered in the high velocity case. From this, one can infer that in the former situation bed load occurs, whereas in the latter situation no bed load occurs. Nevertheless, the results in the outer layer of both these experiments were the same when the data were properly scaled. Therefore, one can conclude that the bed layer and the outer layer are decoupled with respect to the motion of sediment particles. This on its turns confirms that the often used separation of total sediment transport in suspended load and bed load is a physical plausible concept, and does not lead to any inconsistencies in modeling sediment transport.

Relation between vertical transport of sediment and momentum

Different hypotheses for the difference between the eddy viscosity and eddy diffusivity were tested. The most important effect is that individual coherent flow structures transport sediment particles differently than they transport momentum. Low momentum fluid is transported upwards by Q2 and Q4 events (in the latter case actually by transporting high velocity downward). Sediment particles are transported up (thus from high concentrations to low concentrations) by Q2 events and down by Q4 and Q3 events. Hence Q4 events have a different effect for momentum transport, than for sediment transport. Furthermore, it appears that each quadrant individually is more efficient in transporting sediment than momentum, but some flow structures (especially Q2) are more efficient in transporting sediment than others. The net transport of sediment and momentum is the combined result of all four quadrant events. The increased occurrence of particles in flow structures that are more efficient than the others in transporting sediment leads to the increased eddy diffusivity (compared to the eddy viscosity).

This means that the weak point in the current modeling approach is the assumption that the eddy diffusivity and eddy viscosity are proportional.

There is a secondary effect, because the particles sample vertical flow structures that are stronger than average. This leads to fluid velocity fluctuation at the particle locations that are larger than the total fluid velocity fluctuations, and hence results in an increased diffusivity for the sediment particles (of approximately 10 %). Other effects that are sometimes thought to be important (particle inertia, turbophoresis and crossing trajectories) were shown to be unimportant for the situations studied in this thesis. It was also shown that the gradient diffusion hypothesis provided to be an adequate approximation for the processes studied here. Correction terms that account for the concentration profile being non-linear over the typical vertical size of a turbulent flow structure are not important for the presently studied situation.

8.2.2. Insight in non-equilibrium transport processes

In addition to the fully developed situation, non-equilibrium sediment transport was studied. This was done by changing the location where the sediment was added to the flume from 16 to 280 water depths upstream of the measurement section. At each of these locations, the sediment was added at the centerline of the channel close to the free surface.

Transport regimes

Close to the point of sediment introduction, the sediment is mainly located close to the free surface. Here, the sediment particles are descending rapidly, until a sediment distribution was obtained with already most sediment near the bed. After this, the sediment descended slowly until a completely developed situations was established. It appeared that the two processes were caused by different mechanisms. The rapid descend of the particles close to the sediment introduction was caused by the turbulence, while the slow descend further away was caused by gravity.

Flow structures encountered by the particles

The sediment close to the point of sediment introduction, where it is still mostly close to the free surface, encounters different flow structures than the sediment in the fully developed situation (fig. 8.2). In this situations, there are more particles in downward fluid flow structures than in upward ones. Now, Q4 events (sweeps) are the flow structures, in which most particles are encountered, followed by Q3 and Q2 events. These sweeps are located above the hairpin vortex heads, rather than below them. The particles are mostly found in Q4 structures because their settling drives them to the downstream side of a hairpin vortex head.

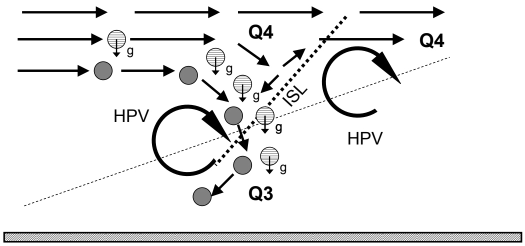

Figure 8.2: Physical mechanism of particle transport in a non-equilibrium situation. The image shows a hairpin vortex packet and two typical particles in a frame moving with the hairpin vortex packet's convective velocity. ISL: Internal shear layer, HPV: Hairpin vortex head; g: gravity.

Influence of flow structures on horizontal particle velocity statistics

Because the particles are mostly encountered in Q4 events, they are located in flow structures with a higher than average streamwise velocity. Therefore, the average streamwise particle velocity is higher than the average streamwise fluid flow velocity. This is a clear contrast to the fully developed situation.

Influence of flow structures on vertical particle velocity statistics

The upward directed Q2 events (which are less often encountered by the particles) are stronger than the downward Q4 events (that are more often encountered by the particles). Therefore, the particle velocity fluctuations are lower than the fluid velocity fluctuations in the non-equilibrium situation, and the particle Reynolds shear stresses have a lower magnitude than the fluid Reynolds shear stresses.

Relation between vertical transport of sediment and momentum

The particles end up in flow structures that are relatively less efficient in transporting particles vertically (compared to those flow structures that are encountered by the particles in the fully developed situation), because the particles encounter flow structures that are smaller in size. Therefore the ratio between the eddy diffusivity and eddy viscosity (β) is lower than one in this case, which is a clear contrast with the fully developed case. The fact that the value of β is situation dependent rather than a universal constant means that modeling concept using the equivalence of turbulent transport of sediment particles and momentum is doubtful and could benefit from an approach accounting for these effects.

8.2.3. Validation of particle laden DNS for simulating sediment transport

The experiment was set up specially to allow a comparison with the data from a DNS (performed by M. Cargnelutti of the Kramers' laboratory of TU Delft) without any scaling. In this DNS, each particle was simulated using the Maxey & Riley (1983) equation, where the fluid velocity at the particle location is interpolated from the DNS data. It appeared that the sediment concentration profiles from the DNS agreed well with the experimental data, provided that a resuspension mechanism near the wall is used. Surprisingly, the details of this resuspension mechanism do not matter as long as it is sufficiently strong, i.e. strong enough to lift particles to a level, where the vertical velocity fluctuations are comparable to the settling velocity. This confirms that also in the simulations, the bed load layer and the outer layer are decoupled (section 8.2.1). The agreement between experiment and simulations in the concentration profiles was that good that similar values of the ratio between eddy viscosity and eddy diffusivity (β) were observed in experiment and simulation.

8.2.4. Development of experimental methods for high concentration experiments

An experiment was performed to measure two-way coupling effects in sediment laden flow with bulk volume concentrations up to 0.42%. The used methodology (a combination of refractive image matching and PIV) proved to be an adequate tool to study two-way coupling effects in sediment laden flows. In particular, the sodium iodide appeared to be a very useful fluid for performing refractive index matching without increased safety hazards while still showing a water-like behavior (i.e. a Newtonian viscosity with the same order of magnitude as water). The use of a very small experimental facility necessary for a feasible refractive index matching experiment was found to give similar results for flow and turbulence (without sediment) as the large scale set-up that was used for the low concentration experiment.

8.2.5. Two-way coupling in sediment laden flows

In the refractive index matching experiment it was found that for the present experiment with a low density ratio $\rho_p/\rho_f = 1.14$, large particles $d_{p+} \approx 9$ and a relatively large amount of suspended particles $u_*/v_T \approx 4$, two-way coupling effects were hardly detectable. No changes were observed in the bed shear stress and average fluid velocity profiles for volume concentrations up to 0.42 %. Changes in the streamwise and wall normal velocity fluctuations as well as the Reynolds shear stresses were limited to experimental precision. The eddy viscosity decreased up to 10% in sediment laden flow compared to the unladen flow. The observed decrease is less than estimated from the relations developed in Villaret & Trowbridge (1991).

Two-point correlation functions of the streamwise and wall normal velocity fluctuations did not show significant differences between the sediment laden and the unladen flows, both at the small and the large scales. This implies that the particles do not behave as "ghost particles" (particles that change the length scales of the turbulence without changing the total amount of turbulent kinetic energy).

From this one can conclude that the most important two-way coupling effect is density stratification. Changes in the turbulence because of the interaction of the particles wakes with the turbulent energy cascade are negligible. The physical mechanisms that lead to two-way coupling are different from those responsible for two-way coupling in gas-particle flows. In the latter, momentum is transfered between the phases by drag forces, which exist because the particles cannot follow the fluid velocity fluctuations due to their inertia. This mechanism is negligible for sediment laden flows, and hence results obtained for gas-particle flows cannot be used to make any predictions for sediment laden flows.

8.3. Implications for sediment transport modeling

8.3.1. The use of two-fluid models

Using some simplifications, it was shown that the two-fluid modeling approach is consistent with the traditional advection-diffusion modeling approach. For sediment transport, both approaches result in the Rouse equation for describing the vertical sediment concentration profile in an equilibrium situation. Therefore, the current approach to use the advection-diffusion equation to model sediment transport in large scale models seems justified. The use of an advection-diffusion model is advantageous, because this approach is computationally less expensive than the two-fluid approach. However, the two-fluid approach shows that the current modeling approach can be improved rather easily by using a particle velocity that differs from the fluid velocity (see section 8.3.2).

Nevertheless, the use of the two-fluid modeling approach in this thesis was advantageous, because this approach is physically more sound, and less based on ad-hoc assumptions. Furthermore, the two-fluid approach as a mean to derive the advection-diffusion equation has the advantage that two-way and four-way coupling effects can be included straightforwardly, rather than on an ad-hoc basis (see section 8.3.4).

8.3.2. Modeling of the horizontal drift velocity

When a distinction is made between the horizontal fluid and particle velocities, a closure relation is needed for the velocity differences between fluid and particles. Based on the work by Simonin *et al.* (1993), an expression was used that gives the velocity difference (eq. 5.5 and 5.6) as a function of the vertical concentration gradient. This expression gives adequate results in equilibrium as well as non-equilibrium situations.

8.3.3. Modeling of the vertical processes

For highly accurate results, the models for simulating the vertical transport processes should be able to take the distribution of the particles over the flow structures into account. This is fulfilled when large eddy simulation (LES) is used, even when the particles are simulated using a scalar-advection equation provided that the sediment fraction has a settling velocity. Since the inertia of the particles is not important, the added value of using separate particle tracking for the sediment is limited. However, at present, LES is still too computationally expensive for use in practical sediment transport calculations.

In Reynolds averaged models, the distribution of the particles over the flow structures is parametrized. It has been shown in this thesis that the gradient diffusion hypothesis provides an adequate tool for modeling particle fluxes, when the sediment concentrations are low. Especially, the often heard criticism (e.g. Libby, 1996; Nielsen & Teakle, 2004) that it is assumed that turbulent eddies are small considered to the length scale over which the concentration varies, did not appear to pose a problem for the situations considered here. This has the consequence that the use of an (algebraic) Reynolds-flux model will not lead to important improvements over modeling using gradient diffusion models (as the k-epsilon model), because it has been shown that the main advantage of Reynolds flux models is that they take large distance transport into account (Wyngaard & Weil, 1991; van Dop & Verver, 2001). Note that algebraic Reynolds stress models can be a large improvement for higher sediment concentrations, since they are better at representing buoyancy effects on the turbulence.

The assumption that the turbulent transport of momentum and sediment are related appeared the most problematic one. For modeling purposes, it is thus recommended to develop new relations for the "diffusivity" of sediment, which are not related directly on the proportionality between the eddy viscosity and the eddy diffusivity. These relation should take the turbulent transport direction (that depends on $\partial C/\partial y$) explicitly into account.

8.3.4. Modeling high concentration effects

For many practical situations, the effects of high sediment concentrations are important. This is especially so near the bed, where the sediment concentrations are largest. The effects of two-way and four-way coupling can be incorporated straightforwardly in the two-fluid modeling approach. However using an advection-diffusion approach, these effects can be included automatically by modifying the equation of state in order to include the influence of sediment on the mixture density. Then, stratification effects can be modeled by using a buoyancy destruction term in the turbulence model. Changes in the settling velocity (due to changes in the fluid pressure gradient working on the particles) are also accounted for by the decrease of the settling velocity due to increase of the mixture density. If a separate parametrization is used for modeling hindered settling, this effect is counted double, and the settling velocities will be underestimated. Furthermore, using a parametrization for hindered settling is not in agreement with the continuity equations of a two-fluid model. It was shown that a hindered settling model that correctly accounts for the return flow generated by the settling sediment, should depend on the net particle flux. A decreased settling velocity should only occur when deposition occurs, whereas in case of upward net particle fluxes (erosion), the settling velocity increases.

Four-way coupling effects by hydrodynamic interactions can be modeled by a change in the drag force, and hence the settling velocity, although accurate theoretical models for this change in drag force do not exist for arbitrary particle Reynolds numbers. A separate term needs to be included to model contact forces. However, the latter are only important for concentrations close to complete packing, which only occur for bed load, not for suspended load.

8.3.5. Consequences of fast vertical transport

The fast vertical transport in the non-equilibrium situation is at first rather surprising. However, because turbulent diffusion is the reason for this fast transport, it can be simulated well using an advection-diffusion model with a sufficient vertical resolution, (although for accurate simulations, an eddy diffusivity is needed that is lower than the eddy viscosity, section 8.2.2). There are however larger consequences when simulating this situation with a 2D depth averaged model. In such a depth-averaged model, the time scale in which the concentration adapts to the equilibrium situation needs to be prescribed. This is often done using a time scale based on the settling velocity and water depth. However, this time scale does not take the rapid settling into account, and therefore it will give time scales that are too large and thus an adaptation of the depth-averaged concentrations that is too slow. Better results will be obtained, when this fast settling is taken into account, by using an adaptation time scale that depends on the difference between the actual depth averaged concentration and the equilibrium concentration.

8.3.6. Effects of high Reynolds numbers

The present investigation was limited to low Reynolds numbers. In practical situations, where sediment transport is important, the Reynolds number is some orders of magnitude larger. This might have consequences on the findings in this thesis, especially for the near bed layer (because this becomes relatively thinner when the Reynolds number increases). However, further away from the bed (i.e. the region that was considered in this thesis), it is expected that the conclusions in this thesis do not change with the increase of the Reynolds number. Two arguments for this can be given:

- In this thesis, the vertical transport by hairpin vortex packets was studied. It is known that hairpin vortex packets occur in low Reynolds number as well as high Reynolds number flows, and in both situations, they have similar characteristics (Adrian *et al.*, 2000; Hommema & Adrian, 2003).
- Vertical sediment transport depends on the vertical velocity fluctuations, and the scaling of these fluctuations ($< v'_f >_{RMS} / u_*$) in a boundary layer is independent of the Reynolds number (De Graaff & Eaton, 2000; Nickels *et al.*, 2007), in contrast to horizontal velocity fluctuations, where $< u'_f >_{RMS} / u_*$ increases with increasing Reynolds number.

8.4. Recommendations for future research

8.4.1. Low concentration experiment

In this thesis, it was shown that the vertical transport of sediment particles depends on the main direction of the flux. In particular, it was shown that the downward turbulent transport when most particles are near the free surface (in a non-equilibrium situation) differs from the upward turbulent transport when most particles are near the bed. In order to verify this and to obtain more insight in the differences between these two processes, it is recommended to perform an extra experiment in order to show the influence of the direction of the turbulent flux on the magnitude of the diffusion coefficient. This experiment could be performed as an open channel flow experiment, with particles slightly lighter than the fluid (for example using polystyrene particles in a salt water solution). In such an experiment, most particles will move toward the surface due to the buoyancy force, and hence the turbulent diffusion flux will be directed downwards and sweeps rather than ejections determine the (downward) entrainment process. In this situation, one expects to find an upside-down Rouse profile for the measured concentrations. From this data, it can be determined whether β is larger or smaller than one in this situation. Such an experiment could either be done using a DNS with particle tracking or preferably with a flume experiment.

8.4.2. High concentration experiment

Extension of the parameter space

In order to come to a general description of the sediment transport, more insight into the physical processes that are important at high sediment concentrations is highly necessary. Refractive index matching was shown to be a promising tool for this kind of research. It is therefore recommended to extend the experiments presented in this thesis in order to obtain a more complete data set. This data set should cover a wide parameter range with respect to four non-dimensional parameters (u_*/v_T, d_{p+}, Re_p and ρ_p/ρ_f) in order to assess the importance and effect of each of these. These experiments should not only measure the two-way coupling effects (changes in the mean fluid flow and turbulence) but also the effect of two-way and four-way coupling on the particle distribution and velocities. Ideally, similar experiments are also performed in simpler situations than open channel flow, such as homogeneous, isotropic turbulence. From these experiments, constitutive relations for changes in the drag force on the particles as function of the concentration could be derived

Improvements to the experimental setup

The experimental setup that was used in the present experiment could be improved in two ways:

- It can be extended to measure both phases (fluid and sediment) simultaneously by adding a small percentage of sediment particles with a fluorescent coating to the fluid. By doing so, a physically high concentration experiment can be converted into an optically low concentration one, similar to the one described in section 3.2. In this situation, care needs to be taken that both the visible and invisible particles have the same hydrodynamic and collisional properties.
- The experiment can be extended to higher sediment concentrations. In the present experiments, the main limitation that prevented measurements at higher concentrations was the amount of light that was recorded by the camera. Thus in order to perform experiments at higher concentrations, the amount of light recorded by the camera must be increased. This can be done in several ways. First of all it is recommended to change the position of the laser to let the light penetrate the flow from above, rather than from below. This can be done much more easily when the experiment is changed from an open channel to a closed channel flow. Secondly, the refractive index matching can still be improved. It seems that the major deficiency in the refractive index matching was related to the inhomogeneity of the used sediment particles. Hence, the use of other materials for the dispersed phase should be considered such as for example fused silica or calcium fluoride. It is important that the used material is as pure as possible and thus that it does not posses any inhomogeneities, dust or other optical disturbances (such as air bubbles trapped inside the material). Furthermore, an increased light scattering can be obtained by adapting the used light sheet optics to those more suitable for small scale experiments. Finally, it is recommended to use larger tracer particles in future experiments, because these scatter more light and will be less sensitive to blurring by the suspended sediment.

References

Abdulagatov, I.M., Zeinalova, A.B., & Azizov, N.D. 2006. Viscosity of Aqueous Electrolyte Solutions at High Temperatures and High Pressures. Viscosity B-Coefficient. Sodium Iodide. *Journal of Chemical Engineering Data*, **51**, 1645–1659.

Admiraal, D.M., García, M.H., & Rodríguez, J. F. 2000. Entrainment response of bed sediment to time-varying flows. *Water Resources Research*, **36**(1), 335–348.

Adrian, R.J. 1994. Stochastic estimation of Conditional Structure: a Review. *Applied Scientific Research*, **53**, 291–303.

Adrian, R.J., Meinhart, C.D., & Tomkins, C.D. 2000. Vortex organization in the outer region of the turbulent boundary layer. *Journal of Fluid Mechanics*, **422**, 1–54.

Angele, K.P., & Muhammad-Klingmann, M. 2005. A simple model for the effect of peak-locking on the accuracy of boundary layer turbulence statistics in digital PIV. *Experiments in Fluids*, **38**, 341–347.

Ardekani, A.M., & Rangel, R.H. 2006. Unsteady motion of two solid spheres in Stokes flow. *Physics of Fluids*, **18**(103306), 1–14.

Armenio, V., & Fiorotto, V. 2001. The importance of the forces acting on particles in turbulent flows. *Physics of Fluids*, **13**(8), 2437–2440.

Batchelor, G. K. 1972. Sedimentation in a dilute dispersion of spheres. *Journal of Fluid Mechanics*, **52**(2), 245–268.

Batchelor, G.K. 1967. *An introduction to fluid dynamics*. Cambridge university press.

Bazant, M.Z. 2005. *Random Walks and Diffusion*. MIT Open Course Ware.

Best, J., Bennett, S., Bridge, J., & Leeder, M. 1997. Turbulence Modulation and Particle Velocities over Flat Sand Beds at Low Transport Rates. *Journal of Hydraulic Engineering*, **123**(12), 1118–1129.

Boivin, M., Simonin, O., & Squires, K.D. 1998. Direct numerical simulation of turbulence modulation by particles in isotropic turbulence. *Journal of Fluid Mechanics*, **375**(235-263).

Budwig, R. 1994. Refractive index matching methods for liquid flow investigations. *Experiments in Fluids*, **17**, 350–355.

Cargnelutti, M.F., & Portela, L.M. 2007 (July). Influence of the resuspension on the particle sedimentation in wall-bounded turbulent flows. *In: 6th International Conference on Multiphase Flow, ICMF 2007, Leipzig, Germany*. submitted.

Carlotti, P., & Drobinski, P. 2004. Length Scales in Wall-Bounded High-Reynolds-Number Turbulence. *Journal of Fluid Mechanics*, **516**(239-264).

Cellino, M., & Graf, W.H. 1999. Sediment-Laden Flow in Open-Channels under Noncapacity and Capacity Conditions. *Journal of Hydraulic Engineering*, **125**(5), 455–462.

Cellino, M., & Lemmin, U. 2004. Influence of Coherent Flow Structures on the Dynamics of Suspended Sediment Transport in Open-Channel Flow. *Journal of Hydraulic Engineering*, **130**(11), 1077–1088.

Chen, R.-C. 1991. *Experimental and numerical studies of solid-liquid multiphase flow in pipes*. Ph.D. thesis, Case Western Reserve University.

Chen, R.C., & Fan, L.-S. 1992. Particle Image Velocimetry for Characterizing the Flow Structure in Three-Dimensional Gas-Liquid-Solid Fluidized Beds. *Chemical Engineering Science*, **47**(13/14), 3615–3622.

Cherukat, P., & McLaughlin, J.B. 1994. The inertial lift on a rigid sphere in a linear shear flow field near aflat wall. *Journal of Fluid Mechanics*, **263**, 1–18.

Christensen, K.T. 2004. The influence of peak-locking errors on turbulence statistics computed from PIV ensembles. *Experiments in Fluids*, **36**, 484–497.

Christensen, K.T., & Adrian, R.J. 2001. Statistical evidence of hairpin vortex packets in wall turbulence. *Journal of Fluid Mechanics*, **431**, 433–443.

Coimbra, C.F.M., & Rangel, R.H. 2001. Spherical Particle Motion in Harmonic Stokes Waves. *AIAA Journal*, **39**(9), 1673–1682.

Coleman, N.L. 1981. Velocity profiles with suspended sediment. *Journal of Hydraulic Research*, **19**(3), 211–229.

Crowe, C.T. 2000. On models for turbulence modulations in fluid-particle flows. *International Journal of Multiphase Flow*, **26**, 719–727.

Csanady, G.T. 1963. Turbulent diffusion of Heavy Particles in the Atmosphere. *Journal of the Atmospheric Sciences*, **20**, 201–208.

Cui, M.M., & Adrian, R.J. 1997. Refractive index matching and marking methods for highly concentrated. *Experiments in Fluids*, **22**, 261–264.

Dávila, J., & Hunt, J.C. 2001. Settling of small particles near vortices and in turbulence. *Journal of Fluid Mechanics*, **440**, 117–145.

De Graaff, D.B., & Eaton, J.K. 2000. Reynolds-number scaling of the flat-plate turbulent boundary layer. *Journal of Fluid Mechanics*, **422**, 319–346.

del Álamo, J.C., Jiménez, J., Zandonade, P., & Moser, R.D. 2006. Self-similar vortex clusters in the turbulent logarithmic region. *Journal of Fluid Mechanics*, **561**(329-358).

Eaton, J.K., & Fessler, J.R. 1994. Preferential concentration of particles by turbulence. *International Journal of Multiphase Flow*, **20**(Suppl), 169–209.

Elghobashi, S. 1991. Particle-laden turbulent flows: direct simulation and closure models. *Applied Scientific Research*, **301-314**.

Elghobashi, S. 1994. On Predicting Particle-Laden Turbulent Flows. *Applied Scientific Research*, **52**, 309–329.

Elghobashi, S., & Truesdall, G.C. 1993. On the two-way interaction between homogeneous turbulence and dispersed solid particles. I: Turbulence modification. *Physics of Fluids*, **5**(7), 1790–1801.

Enwald, H., Peirano, E., & Almstedt, A.-E. 1996. Eulerian two-phase flow theory applied to fluidization. *International Journal of Multiphase Flow*, **22**(Suppl.), 21–66.

Epanechnikov, VA. 1969. Non-parametric estimation of a multivariate probability density. *Theory of Probability and its Applications*, **14**, 153.

Ferante, A., & Elghobashi, S. 2003. On the physical mechanisms of two-way coupling in particle-laden flow. *Physics of Fluids*, **15**(2), 315–329.

Fessler, J.R., Kulick, J.D., & Eaton, J.K. 1994. Preferential concentration of heavy particles in a turbulent channel flow. *Physics of Fluids*, **6**(11), 3742–3749.

Galappatti, G., & Vreugdenhil, C.B. 1986. A depth-integrated model for suspended sediment transport. *Journal of Hydraulic Research*, **23**(4), 359–375.

Ganapathisubramani, B., amd W.T. Hambleton, N. Hutchins, & Marusic, E.K. Longmireand I. 2005. Investigation of Large-Scale Coherence in a Turbulent Boundary Layer UsingTwo-Point Correlations. *Journal of Fluid Mechanics*, **524**, 57–80.

García, M., & Parker, G. 1991. Experiment of bed sediment into suspension. *Journal of Hydraulic Engineering*, **117**(4), 414–435.

Gore, R.A., & Crowe, C.T. 1989. Effect of particle size on modulating turbulent intensity. **15**(2), 279–285.

Greimann, B.P., Muste, M., & Holly Jr., F.M. 1999. Two-phase formulation of suspended sediment transport. *Journal of Hydraulic Research*, **37**(4), 479–500.

Guezennec, Y.G. 1989. Stochastic estimation of coherent structures in turbulent boundary layers. *Physics of Fluids*, **1**(6), 1054–1060.

Haam, S.J., Brodkey, R.S., Fort, I., Klaboch, L., Placnik, M., & Vanecek, V. 2000. Laser Doppler anemometry measurement in an index of refraction matched column in the presence of dispersed beads Part I. *International Journal of Multiphase Flow*, **26**, 1401–1418.

Hagen, J.P., & Kurosaka, M. 1993. Corewise cross-flow transport in hairpin vortices - The “tornado effect”. *Physics of Fluids*, **5**(12), 3167–3174.

Head, M.R., & Bandyopadhyay, P. 1981. New aspects of turbulent boundary-layer structure. *Journal of Fluid Mechanics*, **107**, 297–338.

Hetsroni, G. 1989. Particles-turbulence interaction. *International Journal of Multiphase Flow*, **15**(5), 735–746.

Hinze, J.O. 1975. *Turbulence*. Second edn. McGraw-Hill.

Hofland, B. 2005. *Rock & Roll Turbulence-Induced Damage to Granular Bed Protections*. Ph.D. thesis, Technische Universiteit Delft.

Hommema, S.E., & Adrian, R.J. 2003. Packet structure of surface eddies in the atmospheric boundary layer. *Boundary-Layer Meteorology*, **106**, 147–170.

Hutchins, N., & Marusic, I. 2007. Evidence of very long meandering features in the logarithmic region of turbulent boundary layers. *Journal of Fluid Mechanics*, **579**, 1–28.

Hutchins, N., Hambleton, W.T., & Marusic, I. 2005. Inclined cross-stream stereo particle image velocimetry measurements inturbulent boundary layers. *Journal of Fluid Mechanics*, **541**, 21–54.

Jansen, P.Ph., van Bendegom, L., van den Berg, J., & de Vriesand A. Zanen, M. 1994. *Principles of River Engineering*. facsimile edition edn. Delftse Uitgevers Maatschappij.

Kaftori, D., Hetsroni, G., & Banerjee, S. 1995a. Particle behavior in the turbulent boundary layer. I. Motion, deposition,and entrainment. *Physics of Fluids*, **7**(5), 1095–1106.

Kaftori, D., Hetsroni, G., & Banerjee, S. 1995b. Particle behavior in the turbulent boundary layer. II. Velocity and distributionprofiles. *Physics of Fluids*, **7**(5), 1107–1121.

Kaftori, D., Hetsroni, G., & Banerjee, S. 1998. The effect of particles on wall turbulence. *International Journal of Multiphase Flow*, **24**(3), 359–386.

Khalitov, D.A., & Longmire, E.K. 2002. Simultaneous two-phase PIV by two-parameter phase discrimination. *Experiments in Fluids*, **32**, 252–268.

Kiger, K.T., & Pan, C. 2000. PIV Technique for the Simultaneous Measurement of Dilute Two-Phase Flows. *Journal of Fluids Engineering*, **122**, 811–818.

Kiger, K.T., & Pan, C. 2002. Suspension and turbulence modification effects of solid particulates ona horizontal turbulent channel flow. *Journal of Turbulence*, **3**(019), 1–21.

Kim, K.C., & Adrian, R.J. 1999. Very large-scale motion in the outer layer. *Physics of Fluids*, **11**(2), 417–422.

Koh, C.J., Hookham, P., & Leal, L.G. 1994. An experimental investigation of concentrated suspension flows in a rectangular channel. *Journal of Fluid Mechanics*, **266**, 1–32.

Kraichnan, R.H. 1964. Relation between Lagrangian and Eulerian Correlation Times of a Turbulent Velocity Field. *Physics of Fluids*, **7**(1), 142–143.

Krishnan, G.P., & Leighton, Jr., D.T. 1995. Inertial lift on a moving sphere in contact with a plane wall in a shear flow. *Physics of Fluids*, **7**(11), 2538–2545.

Kurose, R., & Komori, S. 1998. Drag and lift forces on a rotating sphere in a linear shear flow. *Journal of Fluid Mechanics*, **384**, 183–206.

Lavelle, J.W., & Thacker, W.C. 1978. Effects of hindered settling on sediment concentration profiles. *Journal of Hydraulic Research*, **16**(4), 347–355.

LaVision. 2002 (February). *FlowMaster Manual. PIV Hardware Manual for Davis 6.2*. Tech. rept. LaVision GmbH.

Leighton, D., & Acrivos, A. 1985. The lift on a small sphere touching a plane in the presence of a simple shear flow. *Journal of Applied Mathematics and Physics*, **36**, 174–178.

Lesieur, M., Begou, P., Briand, E., Danet, A., Delcayre, F., & J.L.Aider. 2003. Coherent-vortex dynamics in large-eddy simulations of turbulence. *Journal of Turbulence*, **4**(016), 1–24.

Libby, P.A. 1996. *Introduction to Turbulence*. Combustion: An International Series. Taylor & Francis.

Liu, C. H., Vafidis, C., Whitelaw, J. H., & Margary, R. 1990. Flow in the coolant passages of an internal combustion engine cylinder head. *Experiments in Fluids*, **10**(1), 50–54.

Liu, Z., Adrian, R.J., & Hanratty, T.J. 2001. Large-scale modes of turbulent channel flow: transport and structure. *Journal of Fluid Mechanics*, **448**, 53–80.

Maxey, M.R., & Corrsin, S. 1986. Gravitational Settling of Aerosol Particles in Randomly Oriented CellularFlow Fields. *Journal of the Atmospheric Sciences*, **43**(11), 1112–1134.

Maxey, M.R., & Riley, J.J. 1983. Equation of motion for a small rigid sphere in a nonuniform motion. *Physics of Fluids*, **26**(4), 883–889.

McLaughlin, J.B. 1993. The lift on a small sphere in wall-bounded linear shear flows. *Journal of Fluid Mechanics*, **246**(249-265).

Mei, R., Adrian, R.J., & Hanratty, T.J. 1991. Particle dispersion in isotropic turbulence under Stokes drag and Basset force with gravitational settling. *Journal of Fluid Mechanics*, **225**, 481–495.

Michaelides, E. 2003. Hydrodynamic Force and Heat/Mass Transfer From Particles, Bubbles, and Drops-The Freemann Scholar Lecture. *Journal of Fluids Engineering*, **125**, 209–238.

Michaelides, E.E. 1997. Review — The Transient Equation of Motion for Particles Bubbles, and Droplets. *Journal of Fluids Engineering*, **119**, 233–247.

Minier, J.-P., & Peirano, E. 2001. The PDF approach to turbulent polydispersed two-phase flows. *Physical Review*, **352**, 1–214.

Muste, M., & Patel, V.C. 1997. Velocity Profiles for Particles and Liquid in Open-Channel Flow with Suspended Sediment. *Journal of Hydraulic Engineering*, **123**(9), 742–751.

Muste, M., Yu, K., Fujita, I., & Ettema, R. 2005. Two-Phase versus Mixed-Flow Perspective on Suspended Sediment Transportin Turbulent Channel Flows. *Water Resources Research*, **41**(10402), 1–22.

Nakagawa, H., & Nezu, I. 1981. Structure of space-time correlations of bursting phenomena in an open-channelflow. *Journal of Fluid Mechanics*, **104**, 1–43.

Nakagawa, S., & Hanratty, T.J. 2001. Particle image velocimetry measurements of flow over a wavy wall. *Physics of Fluids*, **13**(11), 3504–3507.

Narrow, T.L., Yoda, M., & Abdel-Khalik, S.I. 2000. A simple model for the refractive index of sodium iodide aqueus solutions. *Experiments in Fluids*, **28**, 282–283.

Nezu, I., & Azuma, R. 2004. Turbulence Characteristics and Interaction Between Particles and Fluid in Particle-Laden Open Channel Flows. *Journal of Hydraulic Engineering*, **130**(10), 988–1001.

Nezu, I., & Nakagawa, H. 1993. *Turbulence in Open-Channel Flows*. A.A. Balkema.

Nezu, I., & Rodi, W. 1986. Open-channel Flow Measurements with a Laser Doppler Anemometer. *Journal of Hydraulic Engineering*, **112**(5), 335–355.

Nickels, T.B., Marusic, I., Hafez, S., Hutchins, N., & Chong, M.S. 2007. Some predictions of the attached eddy model for a high Reynolds number boundary layer. *Philosophical Transactions of the Royal Society*, **365**, 807–822.

Nielsen, P., & Teakle, I.A. 2004. Turbulent diffusion of momentum and suspended particles: A finite-mixing-lengththeory. *Physics of Fluids*, **16**(7), 2342–2348.

Niño, Y., & García, M.H. 1996. Experiments on particle-turbulence interactions in the near-wall region of an open channel flow: implications for sediment transport. *Journal of Fluid Mechanics*, **326**, 285–319.

Niño, Y., López, F., & García, M. 2003. Threshold for particle entrainment into suspension. *Sedimentology*, **50**, 247–263.

Oesterlé, B., & Zaichik, L.I. 2004. On Lagrangian time scales and dispersion modeling in equilibrium turbulent shear flows. *Physics of Fluids*, **16**(9), 3374–3384.

Perry, A.E., & Chong, M.S. 1982. On the mechanism of wall turbulence. *Journal of Fluid Mechanics*, **119**, 173–217.

Perry, A.E., & Marusic, I. 1995. A wall-wake model for the turbulence structure of boundary layers. Part1. Extension of the attached eddy hypothesis. *Journal of Fluid Mechanics*, **298**, 361–388.

Philip, J.R. 1967. Relation between Eulerian and Lagrangian Statistics. *Physics of Fluids*, S69–S71.

Poelma, C. 2004. *Experiments in Particle-Laden Turbulence Simultaneous Particle/Fluid Measurements in Grid-Generated Turbulence*. Ph.D. thesis, Technische Universiteit Delft.

Portela, L.M., & Oliemans, R.V.A. 2003. Eulerian-Lagrangian DNS/LES of particle-turbulence interactions in wall-bounded flows. *International Journal for Numerical Methods in Fluids*, **43**(9), 1045–1065.

Portela, L.M., Cota, P., & Oliemans, R.V.A. 2002. Numerical study of the near-wall behaviour of particles in turbulent pipeflow. *Powder Technology*, **125**, 149–157.

Raffel, M., Willert, C., & Kompenhans, J. 1998. *Particle Image Velocimetry*. Springer.

Rashidi, M., Hetsroni, G., & Banerjee, S. 1990. Particle-turbulence interaction in a boundary layer. *International Journal of Multiphase Flow*, **16**(6), 935–949.

Raudkivi, A.J. 1976. *Loos boundary hydraulics*. 2nd edn. Pergamon Press.

Richardson, J.F., & Zaki, W.N. 1954. Sedimentation and fluidisation: Part I. *Transactions of the Institution of Chemical Engineers*, **32**, 35–53.

Righetti, M., & Romano, G.P. 2004. Particle-fluid interactions in a plane near-wall turbulent flow. *Journal of Fluid Mechanics*, **505**, 93–121.

Robinson, S.K. 1991. Coherent motions in the turbulent boundary layer. *Annual Review of Fluid Mechanics*, **23**, 601–639.

Saffman, P.G. 1965. The lift on a small sphere in a slow shear flow. *Journal of Fluid Mechanics*, **22**, 385–400.

Sato, Y., & Yamamoto, K. 1987. Lagrangian measurement of fluid-particle motion in an isotropic field. *Journal of Fluid Mechanics*, **175**, 183–199.

Schmeeckle, M.W., Nelson, J.M., Pitlick, J., & Bennett, J.P. 2001. Interparticle collision of natural sediment grains in water. *Water Resources Research*, **37**(9), 2377–2391.

Simonin, O., Deutsch, E., & Minier, J.P. 1993. Eulerian Prediction of the Fluid Particle Correlated Motion in TurbulentTwo-Phase Flows. *Applied Scientific Research*, **51**(1-2), 275–283.

Squires, K.D., & Eaton, J.K. 1990. Particle response and turbulence modification in isotropic turbulence. *Physics of Fluids*, **2**(7), 1191–1203.

Squires, K.D., & Eaton, J.K. 1991. Lagrangian and Eulerian statistics obtained from direct numerical simulation of homogeneous turbulence. *Physics of Fluids*, **3**(1), 130–143.

Sumer, B.M., & Deigaard, R. 1981. Particle motions near the bottom in turbulent flow in an open channel. Part2. *Journal of Fluid Mechanics*, **109**, 311–337.

Sumer, B.M., & Oguz, B. 1978. Particle motions near the bottom in turbulent flow in an open channel. *Journal of Fluid Mechanics*, **86**(1), 109–127.

Taylor, G.I. 1921. Diffusion by continuous movements. *Proceedings of the London Mathematical Society*, **20**, 196–212.

ten Cate, A., Derksen, J.J., Portela, L.M., & van den Akker, H.E.A. 2004. Fully resolved simulation of colliding monodisperse spheres in forces isotropicturbulence. *Journal of Fluid Mechanics*, **519**, 233–271.

Thacker, W.C., & Lavelle, J.W. 1977. Two-phase flow analysis of hindered settling. *Physics of Fluids*, **20**(9), 1577–1579.

Tomkins, C.D. 2001. *The structure of turbulence over smooth and rough walls*. Ph.D. thesis, University of Illinois at Urbana-Champaign.

Uijttewaal, W.S.J., & Oliemans, R.V.A. 1996. Particle Dispersion and Deposition in Direct Numerical and Large Eddy Simulationsof Vertical Pipe Flows. *Physics of Fluids*, **8**(10), 2590–2604.

van der Plas, G.A.J., Zoeteweij, M.L., Bastiaans, R.J.M., & Rindt, R.N. Kieftand C.C.M. 2003 (April). *PIV, PTV and HPV User's Guide 1.1.* Eindhoven University of Technology. Draft.

van Dop, H., & Verver, G. 2001. Countergradient Transport Revisited. *Journal of the Atmospheric Sciences*, **58**, 2240–2247.

Van Rijn, L. C. 1984. Sediment transport, Part II: Suspended Load Transport. *Journal of Hydraulic Engineering*, **110**(11), 1613–1641.

van Wageningen, W.F.C. 2006. *Design of a static mixer reactor for copper recovery from waste streams*. Ph.D. thesis, Delft University of Technology.

Vanoni, V.A. 1946. Transportation of suspended sediment by water. *American Society of Civil Engineers Transactions*, **2267**, 67–133.

Villaret, C., & Trowbridge, J.H. 1991. Effects of Stratification by Suspended Sediments on Turbulent Shear Flows. *JGR*, **96**, 10659–10680.

Wang, L.-P., & Maxey, M.R. 1993. Settling velocity and concentration distribution of heavy particles in homogeneous isotropic turbulence. *Journal of Fluid Mechanics*, **256**, 27–68.

Wang, L.-P., & Stock, D.E. 1993. Dispersion of Heavy Particles by Turbulent Motion. *Journal of the Atmospheric Sciences*, **50**(13), 1897–1913.

Wang, Q., Squires, KD, Chen, M., & McLaughlin, JB. 1997. On the role of the lift force in turbulence simulations of particle deposition. *International Journal of Multiphase Flow*, **23**(4), 749–763.

Wei, T., & Willmarth, W.W. 1991. Examination of v-velocity fluctuations in a turbulent channel flow in the context of sediment transport. *Journal of Fluid Mechanics*, **223**, 241–252.

Willmarth, W.W., & Lu, S.S. 1972. Structure of the Reynolds Stress Near the Wall. *Journal of Fluid Mechanics*, **55**(1), 65–92.

Wu, J., & Manasseh, R. 1998. Dynamics of dual-particle settling under gravity. *International Journal of Multiphase Flow*, **24**, 1343–1358.

Wu, Y., & Christensen, K.T. 2006. Populations Trends of Spanwise Vortices in Wall Turbulence. *Journal of Fluid Mechanics*, **568**, 55–76.

Wyngaard, J.C., & Weil, J.C. 1991. Transport asymmetry in skewed turbulence. *Physics of Fluids*, **3**(1), 155–162.

Yang, T.S., & Shy, S.S. 2003. The settling velocity of heavy particles in an aqueous near-isotropic turbulence. *Physics of Fluids*, **15**(4), 868–880.

Young, J., & Leeming, A. 1997. A theory of particle deposition in turbulent pipe flow. *Journal of Fluid Mechanics*, **340**, 129–159.

Zhou, D., & Ni, J.R. 1995. Effects of dynamic interaction on sediment-laden turbulent flow. *Journal of Geophysical Research*, **100**(C1), 981–996.

Zhou, J., Adrian, R.J., Balachandar, S., & Kendall, T.M. 1999. Mechanisms for generating coherent packets of hairpin vortices in channel flow. *Journal of Fluid Mechanics*, **387**, 353–396.

Appendix A

Self induction of vortices

The most important process in understanding the behavior of a vortex is induction. We refer to induction to indicate that whenever there is vorticity, the regions surrounding this region of vorticity will show a flow around it. A mathematical way of expressing this velocity $\vec{u_v}$ at location $\vec{x}$ due to vorticity $\vec{\omega}$ at $\vec{x'}$ is Biot-Savarts's law (e.g. Batchelor, 1967, page 87), where $\vec{s} = \vec{x} - \vec{x'}$:

$$\vec{u_v}(\vec{x}) = \frac{1}{4\pi} \int \frac{\vec{s} \times \vec{\omega}(\vec{x'})}{s^3} dV(\vec{x'}) \tag{A.1}$$

The derivation of equation A.1 only used the continuity equation and hence, it is a kinematic description of a vortical flow. Note that a potential (i.e. rotation free) flow field $\vec{u_p}(\vec{x})$ should still be added to $\vec{u_v}(\vec{x})$ in order to find the total velocity field. We apply equation A.1 to a line vortex with vortex strength $\Gamma = \int \omega dA$ and constant curvature c in a plane normal to the vortex axis and find as asymptotic form for $r \to 0$ (thus close to the vortex core) , (Batchelor, 1967, par 7.1):

$$\vec{u_v}(\vec{x}) = \frac{\Gamma}{2\pi r} \left(\vec{b} \, \cos(\theta) - \vec{n} \, \sin(\theta) \right) + \frac{\Gamma c}{4\pi} \log \left(\frac{L}{r} \right) + O(r^0) \tag{A.2}$$

Here, we used cylindrical coordinates (r, θ) and $\vec{n}$ is the normal and $\vec{b}$ the binormal to the vortex line, L is the length of the vortex. The first term is the same for a straight vortex, and it is also valid for large values of r. It shows that the induced velocity decreases as r^{-1} away from the vortex core for both straight and curved vortices. The second term, shows the tendency of a curved vortex to move in the direction of the flow in its inner bend. In the inner bend, the induced flow from a larger part of the vortex is concentrated than in the outer bend, thus the induced flow is concentrated here and therefore causes the vortex to move in this direction. This process is called self-induction (fig. A.1), and it applies only to the vortex itself as the limit $r \to 0$ was taken in the derivation.

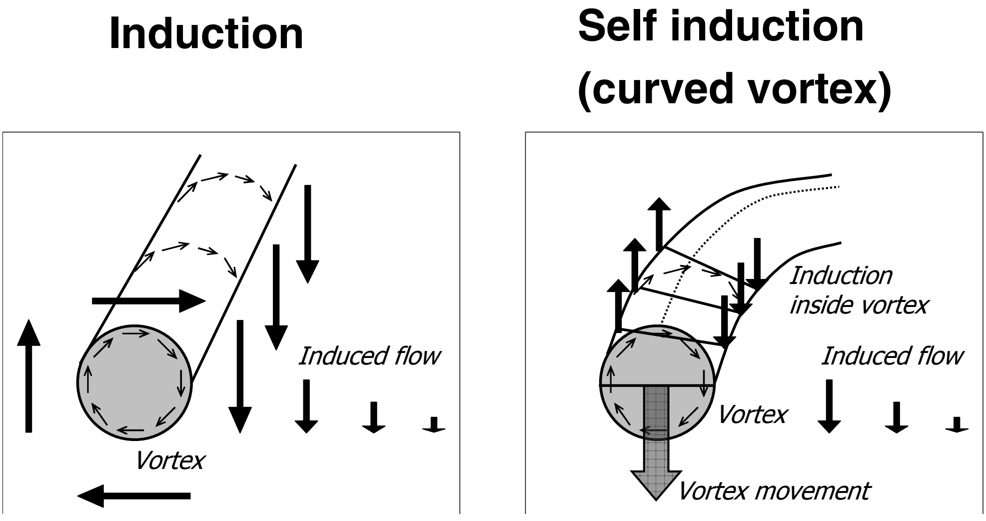

Figure A.1: Self induction of a vortex

Appendix B

Linear stochastic estimation

In this thesis, conditional averages where calculated using Linear Stochastic Estimation (LSE; see Adrian, 1994, for a review). In this appendix, the derivation of the used equations for performing LSE are given.

Using conditional average of a quantity g under a certain condition A is defined as

$$\langle g|A\rangle = \int_{-\infty}^{\infty} g f_{g|A} dg \tag{B.1}$$

with the conditional probability density function $f_{g|A}$ defined as:

$$f_{g|A} = \frac{f(g, A)}{f(A)} \tag{B.2}$$

Here, $f(g, A)$ is the joined probability density function of g and A, and $f(A)$ is the probability density function of the conditional event A. In fact, the conditional average is just the calculation of the first-order moment of g of the joined probability density function $f_{g|A}$.

In Stochastic Estimation, a conditional average of g at $\vec{x}_0 + \vec{r}$ is approximated by a series expansion in the condition A_j at x_0 (see Guezennec, 1989).

$$\langle g_i(\vec{x}_0 + \vec{r})|A_j(\vec{x}_0)\rangle = B_{ij}(\vec{x}_0 + \vec{r})A_j(\vec{x}_0) + O(A^2) \tag{B.3}$$

A least-square fit is performed in order to minimize the difference ΔSE between the conditional average and the Stochastic Estimation.

$$\Delta SE = \langle [\langle g_i(\vec{x}_0 + \vec{r})|A_j(\vec{x}_0)\rangle - B_{ij}(\vec{x}_0 + \vec{r})A_j(\vec{x}_0)]^2\rangle \tag{B.4}$$

Equation B.4 is differentiated to B_{ij} and the derivative is set equal to zero in order to perform the minimization. This leads to the following equation for the coefficient B_{ij}, from which the conditional average can be determined using equation B.3:

$$B_{ij}(\vec{x}_0 + \vec{r}) = \frac{\langle g_i(\vec{x}_0 + \vec{r}) A_k(\vec{x}_0) \rangle}{\langle A_j(\vec{x}_0) A_k(\vec{x}_0) \rangle} \tag{B.5}$$

It is clear from the preceding that correlation functions are needed for the calculation of a LSE. In fact the linear stochastic estimate is a weighted version of the correlation function:

$$\langle g_i(\vec{x}_0 + \vec{r}) | A_j(\vec{x}_0) \rangle = \frac{R_{gi,Ak}(\vec{x}_0 + \vec{r})}{R_{Aj,Ak}(\vec{x}_0)} \left(\frac{g_{i,rms}(\vec{x}_0 + \vec{r})}{A_{k,rms}(\vec{x}_0)} \right) A_j(\vec{x}_0) \tag{B.6}$$

In this equation:

$$R_{gi,Aj}(\vec{x}_0 + \vec{r}) = \frac{\langle g_i(\vec{x}_0 + \vec{r}) A_j(\vec{x}_0) \rangle}{g_{i,rms}(\vec{x}_0 + \vec{r}) A_{j,rms}(\vec{x}_0)} \tag{B.7}$$

In this thesis, we are interested in what happens when there is a vortex at the reference location $\vec{x}_0$. In order to recognize the vortex, we use the fluctuating part of the swirling strength λ'_s (see section 3.4.2), which is a scalar quantity. Then the equations for the LSE reduce to (Christensen & Adrian, 2001):

$$\langle u'_j(\vec{x}_0 + \vec{r}) | \lambda'_s(\vec{x}_0) \rangle = B_j(\vec{x}_0 + \vec{r}) \lambda'_{s,cond}(\vec{x}_0) \tag{B.8}$$

In this equation:

$$B_j(\vec{x}_0 + \vec{r}) = R_{uj,\lambda}(\vec{x}_0 + \vec{r}) \frac{u'_{j,rms}(\vec{x}_0 + \vec{r})}{\lambda'_{s,rms}(\vec{x}_0)} // R_{uj,\lambda}(\vec{x}_0 + \vec{r}) \quad = \frac{\langle \lambda'_s(\vec{x}_0) u'_j(\vec{x}_0 + \vec{r}) \rangle}{\lambda'_{s,rms}(\vec{x}_0) u'_{j,rms}(\vec{x}_0 + \vec{r})} \tag{B.9}$$

Guezennec (1989) extended the LSE technique to situations, where multiple conditions are used. Then, it is possible determine the conditionally averaged structure under two simultaneous conditions, one for the swirling strength $\lambda_s(\vec{x_1})$ at location $\vec{x_1}$ and another for the vertical velocity $v(\vec{x_2})$ at $\vec{x_2}$ as:

$$\langle u'_i(\vec{r}) | \lambda_s(\vec{x_1}) \wedge v'(\vec{x_2}) \rangle \approx A_i \lambda'_{s,cond}(\vec{x_1}) + B_i v'_{cond}(\vec{x_2}) \tag{B.10}$$

In this equation:

$$A_i = \frac{u_{i,rms}(\vec{r})}{\lambda_{s,rms}(\vec{x_1})} \frac{R_{\lambda,ui}(\vec{x_1}, \vec{r}) - R_{v,ui}(\vec{x_2}, \vec{r}) R_{\lambda,v}(\vec{x_1}, \vec{x_2})}{1 - R^2_{\lambda,v}(\vec{x_1}, \vec{x_2})} \tag{B.11}$$

$$B_i = \frac{u_{i,rms}(\vec{r})}{v_{rms}(\vec{x_2})} \frac{R_{uy,ui}(\vec{x_2}, \vec{r}) - R_{\lambda,ui}(\vec{x_1}, \vec{r}) R_{\lambda,v}(\vec{x_1}, \vec{x_2})}{1 - R^2_{\lambda,v}(\vec{x_1}, \vec{x_2})} \tag{B.12}$$

The disadvantage of using two conditions is that the number of adjustable parameters increases. In addition to the height of the swirling event y_{ref}, one now has to specify a ratio between the relative strength of the two conditions (multiplying both conditions with the same number once again does not change the results because of linearity), thus weighting the importance that is given to these. Also the distance $\vec{x_1} - \vec{x_2}$ between the two locations, where the conditions are imposed, needs to be specified. Thus adding two adjustable parameters making the results less general.

An example of the use of LSE with two conditions is shown in fig. B.1. It is clear from this figure that the LSE using two conditions is a linear combination of the two LSE estimations using one condition, with a correction for the correlation between the two separate conditions. The importance attributed to each condition is determined by the ratio of the two conditions. This figure also shows the potential of this technique. In fig. B.1c. d. and e., a strong sweep can be found downstream and above the vortex head, which was not found when only swirling strength was used as a condition (fig. B.1f.). So using this technique, there is less probability that significant coherent structures are not recognized because they are averaged out.

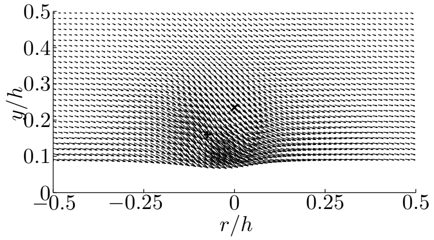

(a) LSE using only v_{cond}

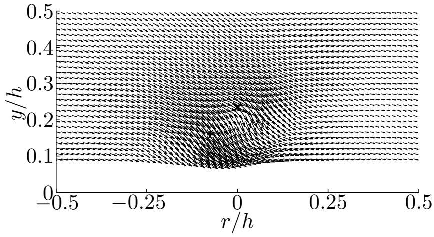

(b) $\frac{v_{cond}/v_{rms}}{\lambda_{s,cond}/\lambda_{s,rms}} = -0.5$

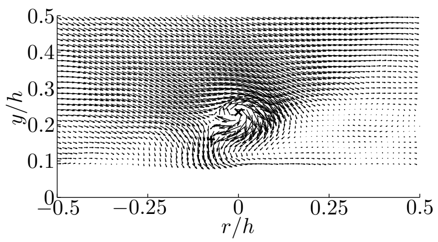

(c) $\frac{v_{cond}/v_{rms}}{\lambda_{s,cond}/\lambda_{s,rms}} = -0.1$

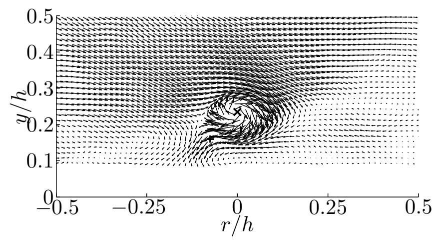

(d) $\frac{v_{cond}/v_{rms}}{\lambda_{s,cond}/\lambda_{s,rms}} = -0.05$

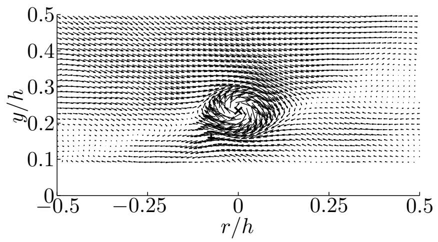

(e) $\frac{v_{cond}/v_{rms}}{\lambda_{s,cond}/\lambda_{s,rms}} = -0.01$

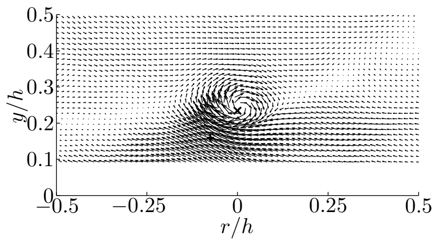

(f) LSE using only $\lambda_{s,cond}$

Figure B.1: LSE using two conditions, swirling strength at $x_0/h, y_0/h = (0, 0.23)$ (marked with an 'X') and vertical velocity at $x_0/h, y_0/h = (-0.07, 0.16)$ (marked with a '+').

List of Figures

List of Tables

List of Symbols

In the following tables, the most important variables, subscripts, acronyms and operators are explained.

Roman Symbols

A, B	Log-law constants	$-$
C	Volumetric sediment concentration	$-$
d_p	Particle diameter	m
F	Flatness/kurtosis	$-$
F	Force	N
F	Particle Flux	$1/s$
Fr	Froude number $\equiv u/\sqrt{gh}$	$-$
g	Acceleration due to gravity	m/s^2
h	Water depth	m
i_b	Bed slope	$-$
l_m	Mixing length	m
L	Integral length scale	m
m	Mass	kg
u, v, w	Velocity in the streamwise, wall normal and spanwise direction	m/s
R	Correlation/ correlation function	$-$
Re	Reynolds number; $\equiv uh/\nu_f$	$-$
Re_*	Reynolds number; $\equiv u_*h/\nu_f$	$-$
Re_G	Shear Reynolds number; $\equiv \lvert du/dy \rvert d_p^2/\nu_f$	$-$
Re_p	Particle Reynolds number; $\equiv u_{rel}d_p/\nu_f$	$-$
$\vec{r}$	Relative distance $\equiv \vec{x} - \vec{x}_0$	m
S	Skewness	$-$
St	Stokes number, ratio of partic to fluid time scale	$-$
t	Time	s
T	Integral time scale	s
u_*	Friction velocity	m/s
v_T	Terminal velocity (with respect to the fluid)	m/s
x, y, z	Streamwise, wall normal and spanwise coordinate	m

Greek symbols

β	Inverse Prandtl-Schmidt number $\equiv D_{yy}/\epsilon_{xy}$	$-$
β	$\equiv \frac{3\rho_f}{2\rho_f\rho_p}$	$-$
γ	$\equiv \frac{\langle u_p'^2\rangle}{\langle u_f'^2\rangle}$	$-$
ϵ	Dissipation	m^2/s^3
ϵ_{xy}	Eddy viscosity	m^2/s
η	Spectral response of the particle fluid velocity fluctuations	$-$
κ	Von Karman's constant	$-$
λ	Micro length scale	m
λ_s	Swirling strength	$1/s^2$
ν_f	Kinematic viscosity of the fluid	m^2/s
ρ_f	Fluid density	kg/m^3
ρ_p	Particle density	kg/m^3
τ	Micro time scale	s
τ	Relative time $\equiv t - t_0$	s
τ	Shear stress	N/m^2
τ_b	Bed shear stress	N/m^2
τ_p	Particle time scale	s
ω	(Angular) frequency	$1/s$

Subscripts

$_*$	Star units; Non-dimensionalizing using u_* and h
$_+$	Wall units; Non-dimensionalizing using u_* and ν_f
$_a$	Indicator of phase a (no summation)
$_{CWF}$	Clear water flow
$_d$	Drift
$_E$	Eulerian
$_{FD}$	Fully developed
$_f$	Fluid phase
$_{f\rightarrow p}$	Working from the fluid on the particles
$_{p\rightarrow f}$	Working from the particles on the fluid
$_{i,j}$	Spatial index (using Einstein summation convention)
$_{kolm}$	Kolmogorov
$_L$	Lagrangian
$_l$	Lift
$_{M,E}$	Eulerian, in a frame moving with average velocity
$_{NE}$	Non-equilibrium
$_p$	Particle phase
$_{rel}$	Relative

SED	Sediment laden flow
T	Terminal
0	Undisturbed/ one-way coupled

Operators

$\langle\rangle_f$	Concentration weighted ensemble average over fluid phase
$\langle\rangle_p$	Concentration weighted ensemble average over particle phase
$'$	Fluctuation with respect to the average over the fluid phase ($u'_f = u_f - \langle u_f \rangle_f$)
$''$	Fluctuation with respect to the average over the particle phase ($u''_f(x_p) = u_f(x_p) - \langle u_f \rangle_p$)
$\frac{D}{Dt}$	$\equiv \frac{\partial}{\partial t} + u_{f,i}\frac{\partial}{\partial x_i}$ Material derivative with respect to the fluid
$\frac{d}{dt}$	$\equiv \frac{\partial}{\partial t} + u_{p,i}\frac{\partial}{\partial x_i}$ Material derivative with respect to a particle

Acronyms

CCD	Charge-coupled device
CWF	Clear water flow
DNS	Direct numerical simulation
FEP	Fluorinated Ethylene Propylene
LDV	Laser Doppler velocimetry
LES	Large eddy simulation
LSE	Linear stochastic estimation
PDF	Probability density function
PIV	Particle image velocimetry
PMMA	Polymethylmethacrylaat
PTV	Particle tracking velocimetry
Q1	Outward interaction $u' > 0$, $v' > 0$
Q2	Ejection $u' < 0$, $v' > 0$
Q3	Inward interaction $u' < 0$, $v' < 0$
Q4	Sweep $u' > 0$, $v' < 0$
RANS	Reynolds-averaged Navier-Stokes
RIM	Refractive index matching
RMS	Root mean square
U-RANS	Unsteady Reynolds-averaged Navier-Stokes

Acknowledgements

There are many people, without whom this thesis would not have been what it currently is. First of all, I would like to thank my daily supervisor and promotor Wim Uijttewaal for his continuing support and assistance in preparing this thesis. Also warm thanks to Guus Stelling. Furthermore, I also would like to thank Luis Portela and Rob Mudde and especially Marcos from the Kramers' laboratory for the fine collaboration and the many discussions that always provided a source of inspiration. I also thank Jan Vreeburg and Rob Uittenbogaard from the STW user committee for their continuous involvement in the project.

I am very much indebted to the staff of the Laboratory, without whom experimental research would not be possible and who have always supported me in the design and construction of whatever was needed for my research. So many thanks to Karel, Jaap, Arie, Hans, Sander, Frank, Michiel and Fred. Also many thanks to Rob and Harry for their advices and the inspiring discussions I had with them about my work.

The period at the laboratory would not have been the same without my fellow PhD students and Postdocs. So many thanks to Gerben, Federico, Petra, Francesca, Maarten, Stephan, Harmen, Shaid, Mohammed, Bas, David, Walter, Michel, Wim, Olga, Claire, Bas, Tim, Pauline, Bram, Martijn and André for making these four years an unforgettable period.

Finally, I would like my family and friends for their support during the period in which I worked on my thesis and especially I would like to thank Esther for here patience and encouragement while I was making this thesis.

Curriculum Vitae

Alexander Breugem was born on the 15th April 1979 in Schiedam, the Netherlands. After completing his secondary education at the Marnix Gymnasium in Rotterdam, he studied Civil Engineering at TU Delft from 1997 to 2003. During his studies, he performed his traineeship at the "Instituto de Ingeniería" of the UNAM (Universidad Autónoma de México) in Mexico City. His master's thesis, performed under supervision of Leo Holthuijsen of the Environmental Fluid Mechanics Section of the Civil Engineering Faculty of TU Delft, treated the development of wind generated water waves in a shallow lake using both numerical simulations (SWAN) and analysis of a database of existing field measurement data.

From October 2003 to December 2007, he worked as a PhD student at the Environmental Fluid Mechanics Section of TU Delft, during which he investigated the transport of sediment particles in a turbulent open channel flow. This investigation was performed in collaboration with the Kramers' Laboratory of the Physics faculty of TU Delft, where Alexander Breugem performed the experimental part of the study, whereas the numerical part was performed by Marcos Cargnelutti of the Kramer's laboratory. This work resulted in the present thesis.

In April 2007, he married Esther in Comalcalco, México. After the marriage, they moved together to live in Antwerp. Since February 2008, he is working there as a project engineer at IMDC, where he is involved with field measurements and mathematical modeling of flow and transport. Especially, he is heavily involved in the development of a sediment transport and morphology module in the existing coastal ocean model Coherens.

List of publications

W.A. Breugem and W.S.J. Uijttewaal, (2006) “A PIV/PTV experiment on sediment transport in a horizontal open channel flow”, River Flow 2006, Lisboa, Portugal, pp. 789–798

W.A. Breugem and W.S.J. Uijttewaal (2007), “PIV/PTV for suspended sediment transport measurements in an open channel flow”, Hydraulic Measurements & Experimental Methods Conference (HMEM 2007), Lake Placid, NY, USA

W.A. Breugem and W.S.J. Uijttewaal (2007), “Sediment transport by coherent structures in a turbulent open channel flow experiment” in Bernard J. Geurts et al. (eds.), Particle Laden Flow: From Geophysical to Kolmogorov Scales, pp. 43–55, Springer Verlag

W.A. Breugem and W.S.J. Uijttewaal (2008), “Detailed measurements of suspended sediment transport in a turbulent open channel flow” pp. 499- 506 in River, Coastal and Estuarine Morphodynamics: RCEM 2007 - Dohmen-Janssen & Hulscher (eds.) Taylor & Francis Group, London

M. Cargnelutti, W.A. Breugem, L. M. Portela, R.F. Mudde, W.S.J. Uijttewaal, and G.S. Stelling (2006), “Particle sedimentation in wall-bounded turbulent flows” in European Conference on Computational Fluid Dynamics ECCOMAS CFD 2006 P. Wesseling, E. Oñate and J. Périaux (Eds.) TU Delft, The Netherlands